Sparse array 3D ultrasound imaging

Mohamed Tamraoui

Université Claude Bernard Lyon 1

THÈSE de DOCTORAT DE L'UNIVERSITÉ DE LYON
Opérée au sein de :
l'Université Claude Bernard Lyon 1

Ecole Doctorale N° 162
MÉCANIQUE, ÉNERGÉTIQUE, GÉNIE CIVIL, ACOUSTIQUE

Spécialité de doctorat : Acoustique

Soutenue publiquement le 22/10/2024, par :

Mohamed TAMRAOUI

Sparse Array 3D Ultrasound Imaging

Devant le jury composé de :

Chris L. de Korte Professeur/ Université de Twente	**Président**
Denis Kouamé Professeur/Université Paul Sabatier, Toulouse 3	**Rapporteur**
Alessandro Ramalli Professeur assistant/Université de Florence	**Rapporteur**
Diana Mateus Professeur/École Centrale Nantes	**Examinatrice**
Claire Prada DR CNRS/Institut Langevin	**Examinatrice**
Giulia Matrone Professeur assistant/University of Pavia	**Examinatrice**
Adrian Basarab Professeur/Université Claude Bernard Lyon 1	**Examinateur**
Hervé Liebgott Professeur/Université Claude Bernard Lyon 1	**Directeur de thèse**
Emmanuel Roux Maître de conférences/Université Claude Bernard Lyon 1	**Co-directeur**

This research is part of an ANR (Agence National de la Recherche) project named SPARse array TECHniques FOR 3D medical UltraSound (SPARTECHUS). SPARTECHUS is a collaborative project between our laboratory, CREATIS, and IMASONIC, an ultrasound transducer manufacturer, with the aim of developing the next generation of sparse arrays for 3D ultrasound imaging.

Abstract

Three-dimensional (3D) medical ultrasound imaging systems provide a full representation of the 3D anatomy allowing the clinician to access volumetric information in the observed scene (anatomy, flow, ...). Ideally, 2D matrix arrays are used to acquire 3D images of the whole volume. However, the use of 2D matrix arrays presents significant technological challenges, primarily due to the large number of transducer elements that must be individually controlled. To address this issue, various techniques have been developed to reduce either the number of elements or the volume of data transmitted to the ultrasound system.

Sparse arrays present several notable advantages over other element reduction techniques for 3D ultrasound imaging. One of the most promising benefits is their ability to freely steer the ultrasound beam in all directions, which significantly enlarges the field of view. This capability opens up possibilities for implementing advanced imaging sequences, such as diverging waves, which are particularly beneficial for applications like echocardiography. Additionally, sparse arrays use fewer elements, reducing the complexity and cost of manufacturing and operating the transducer arrays. This reduction in hardware can also simplify the system design and decrease power consumption. Despite their advantages, sparse arrays face two significant challenges: low sensitivity and reduced image contrast.

The primary objectives of this thesis are twofold: first, to increase the signal-to-noise ratio (SNR) of sparse arrays; second, to enhance image contrast. My first contribution consisted of developing coded excitation sequences, with the goal of improving the SNR of sparse arrays. Based on this contribution, a new sparse array prototype has been developed, incorporating transducer elements with higher sensitivity and divergence. To tackle the issue of poor image contrast caused by high sidelobes level of this prototype, my second contribution focused on the development of a new reconstruction algorithm based on deep learning and specifically trained for the new prototype. This algorithm optimizes the beamforming processes to produce high-quality ultrasound images. Collectively, these contributions aim to address the major challenges associated with sparse arrays, advancing their application in 3D ultrasound imaging.

Résumé

Les systèmes d'imagerie ultrasonore médicale en trois dimensions (3D) fournissent une représentation complète de l'anatomie 3D, permettant aux cliniciens d'accéder à des informations volumétriques dans la scène observée (anatomie, flux, etc.). Idéalement, des sondes matricielles 2D sont utilisées pour acquérir des images 3D de l'ensemble du volume. Cependant, l'utilisation de matrices 2D pose des défis technologiques significatifs, principalement en raison du grand nombre d'éléments qui doivent être contrôlés individuellement. Pour résoudre ce problème, diverses techniques ont été développées pour réduire soit le nombre d'éléments, soit le volume de données transmises au système ultrasonore.

Les sondes sparses offrent plusieurs avantages notables par rapport à d'autres techniques de réduction d'éléments pour l'imagerie ultrasonore 3D. L'un des avantages les plus prometteurs est leur capacité à orienter librement le faisceau ultrasonore dans toutes les directions, ce qui agrandit considérablement le champ de vision. Cette capacité ouvre des possibilités pour la mise en œuvre de séquences d'imagerie avancées, telles que les ondes divergentes, particulièrement bénéfiques pour des applications comme l'échocardiographie. De plus, les sondes sparses utilisent moins d'éléments, réduisant ainsi la complexité et les coûts de fabrication et d'exploitation des sondes. Cette réduction de nombre d'éléments peut également simplifier la conception du système et diminuer la consommation d'énergie. Malgré leurs avantages, les sondes sparses sont confrontées à deux défis majeurs : une faible sensibilité et un contraste d'image réduit.

Les objectifs principaux de cette thèse sont doubles : premièrement, augmenter le rapport signal sur bruit (SNR) des sondes sparses; deuxièmement, améliorer le contraste des images. Ma première contribution a consisté à développer des séquences d'excitations codées, dans le but d'améliorer le SNR des sondes sparses. Sur la base de cette contribution, un nouveau prototype de sonde a été développé, incorporant des éléments avec une sensibilité et une divergence élevée. Pour résoudre le problème du faible contraste d'image causé par les niveaux élevés de lobes secondaires de ce prototype, ma deuxième contribution s'est concentrée sur le développement d'un nouvel algorithme de reconstruction basé sur l'apprentissage profond et spécifiquement entraîné pour le nouveau prototype. Cet algorithme optimise les processus de beamforming pour produire des images ultrasonores de haute qualité. Collectivement, ces contributions visent à relever les principaux défis associés aux sondes sparses, faisant progresser leur utilisation dans l'imagerie ultrasonore 3D.

Table of contents

General Introduction

According to the World Health Organization, up to two-thirds of the global population lacks easy access to diagnostic imaging equipment. Among the available modalities, medical ultrasound is likely the only one that could be widely accessible to this underserved population, making it the imaging modality with the greatest potential for future health benefits. Ultrasound imaging offers a rapid and accurate diagnostic tool, providing real-time images of the human body at low cost and without the use of ionizing radiation.

Currently, conventional 2D ultrasound imaging systems are the standard in clinical practices, capturing real-time 2D slices of the the human body using 1D probes. However, the main drawback of conventional 2D ultrasound is that it uses 2D imaging techniques to capture slices from a 3D anatomy. As a result, the accuracy of the diagnosis largely depends on the ability of clinicians to mentally reconstruct the 3D anatomy from the 2D images, which can be particularly challenging during diagnosis or surgery.

In contrast, 3D ultrasound imaging offers significant advantages over traditional 2D modalities by revolutionizing how medical professionals acquire, visualize and interpret anatomical structures. One of the primary benefits of 3D imaging is that it provides a complete representation of the anatomy, eliminating the need for mental reconstruction of the scene. This comprehensive visualization reduces the dependency on the expertise of the operator and allows for the re-examination of the organ from different perspectives even after the patient has left, making it easier to share acquisitions for input from specialists located in distant hospitals.

3D ultrasound imaging also enhances the accuracy of measurements, such as sizes or volumes of anatomical structures, which are inherently three-dimensional or too complex to capture with 2D modalities. For instance, determining the size and exact location of lesions or calcifications becomes more straightforward with 3D imaging [1]. Similarly, measuring the volumes of cardiac chambers is simplified [2]. Moreover, any application involving dynamic phenomena, particularly in cardiovascular imaging, benefits from 3D imaging due to the presence of out-of-plane motion in biological tissues, especially when pathologies are involved. With 3D dynamic acquisition, it becomes possible to distinguish physiological changes from out-of-plane motion artifacts.

Furthermore, the potential to achieve high frame-rate 3D ultrasound imaging at several thousand frames per second, as demonstrated in 2D imaging [3], promises substantial benefits. Although not yet part of clinical guidelines, several emerging applications hold great promise for the future. For example, 3D vector flow and 3D micro-vascularization imaging can capture the complex organization of blood vessels during normal and patho-

logical development, helping in the characterization of cancer tissues or heart muscle post-infarction. Additionally, 3D ultrasound will enable the visualization of the 3D architecture of heart muscles , as described by [4], and the quantification of skeletal muscle contraction properties, as shown by [5]. Shear-wave elastography, a technique used to assess tissue stiffness, also stands to benefit significantly from 3D imaging. Current methods are limited to in-plane tissue movement; however, 3D imaging could provide a more comprehensive assessment of tissue properties.

Despite the numerous advantages of 3D imaging, it has not yet become the standard clinical approach. This is likely due to two primary factors: either the image quality provided by current systems is insufficient, or the systems are prohibitively expensive. A key determinant of image quality in 3D ultrasound imaging is the ultrasound probe used to acquire the volume. Ideally, 2D matrix arrays are used to scan the entire anatomical volume. Scanning the volume with these arrays requires individual control of each transducer element in the array to steer the ultrasound beam in both the elevation and lateral directions.

To design an ultrasound array that avoids artifacts such as sidelobes and grating lobes in the reconstructed images, the array configuration must respect the Nyquist criterion, which dictates that the spacing between elements should not exceed half the wavelength. Additionally, to achieve the same resolution as a conventional 1D array, the 2D matrix array must contain a sufficient number of elements to cover the same footprint size in both dimensions, which leads to a high number of active elements. For example, to match the image quality of a 128-element linear array, a matrix array would need $128 \times 128 = 16{,}384$ elements.

Since each element needs to be controlled individually in order to freely steer the ultrasound beam, the same number of channels as number of elements is required. However, most current ultrasound systems are equipped with only 256 channels, meaning it would take 64 systems to control such an array. From a technical perspective, manufacturing an array with thousands of elements is highly complex and expensive. Furthermore, connecting several thousand elements in a one-element-to-one-channel configuration increases the complexity of the system electronics, data transfer, and storage requirements. This also results in a large probe cable, making the system impractical for clinical use.

Sparse arrays have emerged as a promising candidate for 3D ultrasound imaging, addressing the limitations associated with the large number of elements in 2D matrix arrays. By optimally distributing a reduced number of elements across the aperture of the array, sparse arrays allow for the use of fewer beamforming channels. Typically, sparse arrays with 256 elements are designed to match the number of channels available in most state of the art ultrasound systems, enabling continuous control of each element by an individual channel. This configuration allows existing ultrasound systems to be used to transmit and receive focused beams at different angles, offering high flexibility in beamforming and steering capabilities. Moreover, using fewer elements significantly reduces the complexity and cost of manufacturing and operating the transducer arrays.

However, sparse arrays face two significant challenges: low sensitivity and reduced image quality, particularly in terms of contrast. Thus, the primary objectives of this thesis are to enhance the sensitivity and contrast of sparse arrays. My first contribution involves developing coded excitation sequences aimed at improving the signal-to-noise ratio (SNR), thereby addressing the inherent low sensitivity of sparse arrays. Concurrently, my second

contribution focuses on overcoming the problem of poor image contrast caused by high sidelobes level. To this end, I developed a new reconstruction algorithm based on deep neural networks, specifically trained for a newly developed sparse array prototype, to produce high-quality ultrasound images. Together, these contributions aim to address the key challenges associated with sparse arrays, paving the way for significant innovations as 3D ultrasound imaging becomes the new standard in clinical practice.

Chapter 1

Arrays for 3D Ultrasound Imaging

In this chapter, I will explore the theoretical aspects of the radiated beam pattern of ultrasound transducer arrays. Understanding the beam pattern is crucial for optimizing resolution and image quality in 3D ultrasound imaging. Subsequently, I will examine the different types of transducers used for 3D ultrasound imaging, with a particular focus on sparse arrays. Sparse arrays offer unique advantages in terms of flexibility and reduced element count, but they also present challenges such as lower sensitivity and higher side-lobes level. Finally, the chapter will conclude by presenting the primary objectives of this thesis. These include increasing the signal-to-noise ratio (SNR) of sparse arrays using coded excitation sequences and enhancing image contrast through the development of a new image reconstruction algorithm.

1.1 Ultrasound beam pattern

1.1.1 Beam pattern description

The transmit beam pattern of an ultrasound transducer array describes the spatial distribution of the emitted ultrasound energy, playing a crucial role in determining the resolution and image quality in ultrasound imaging. The beam pattern is influenced by the array geometry, the spacing between elements, and the excitation signals applied to each element. This section discusses the theory for calculating the beam pattern of an array transducer. In the frequency domain, the beam pattern can be derived using the far-field approximation and the Fourier transform of the aperture function [6]. This approach simplifies the analysis and provides insights into the spatial characteristics of the ultrasound beam. Under the far-field approximation, the distance from the transducer to the point of observation is much larger than the aperture size, allowing the spherical wavefronts to be approximated as plane waves [6, 7].

For simplicity, we will consider a linear array since the theory is extendable to a 2D array. Assuming the elements of the array have similar rectangular shapes with a width D and height H, and a monochromatic wave is used to excite each individual element, the aperture function in the real domain is given by [7]:

$$\mathcal{A}(x,y) = \text{Rect}\left(\frac{y}{H}\right)\left[\left\{\text{Rect}\left(\frac{x}{D}\right) \times \sum_{n=-\infty}^{\infty} \delta(x-nd)\right\} * \text{Rect}\left(\frac{x}{W}\right)\right] \tag{1.1}$$

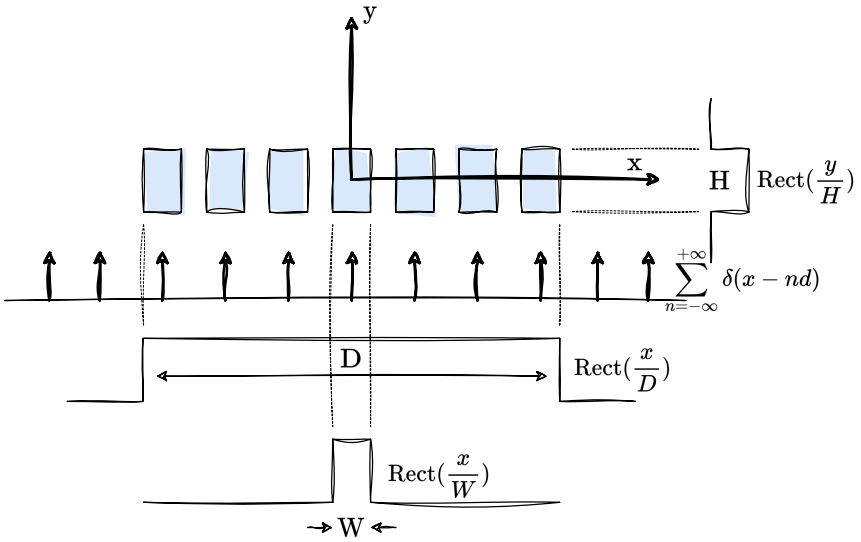

Figure 1.1: Representation of the aperture function geometry in the real domain. The aperture function is obtained by multiplication and convolution operations.

Where D is the size of the aperture given by $D = (N-1)d + W$ for an odd number of elements, x and y are the coordinates on the source plane $z = 0$, and d is the spacing between the elements (pitch). The aperture function is modeled as the product of a rectangular function corresponding to the array aperture shape and a comb function representing a series of delta functions modeling the center of each transducer element. To replicate the element in each delta function, a convolution with the rectangular function modeling each transducer element is used (Figure 1.1).

Beam steering and apodization can be incorporated into the equation of the beam pattern. To steer the beam, a phase shift $\Delta\phi$ of the signal applied to each element must vary linearly with the element position [7]. This can be achieved by multiplying the aperture function by $e^{j\Delta\phi x/d}$. Apodization, which involves varying the amplitude applied to each element to reduce sidelobes and improve image quality, can be accounted for by introducing a function $A(x)$ that describes the amplitude applied to each individual element of the array. Combining both beam steering and apodization, the aperture function becomes :

$$\mathcal{A}(x,y) = \text{Rect}\left(\frac{y}{H}\right)\left[\left\{\text{Rect}\left(\frac{x}{D}\right) \times A(x)e^{j\Delta\phi x/d} \sum_{n=-\infty}^{\infty} \delta(x - nd)\right\} * \text{Rect}\left(\frac{x}{W}\right)\right] \tag{1.2}$$

Using the Fraunhofer approximation, the far-field beam pattern of an ultrasound transducer array can be calculated by taking the Fourier transform of the aperture function. The radiated beam pattern $\mathcal{P}(x, y; \omega)$ is given by [6, 7]:

$$\mathcal{P}(x,y;\omega) = \frac{j\omega\rho_0\nu_0}{2\pi r} e^{-jkr} \mathcal{FT}(\mathcal{A}(x,y)) \tag{1.3}$$

where ρ_0 is the density of the medium, ν_0 is the vibration amplitude, ω is the angular frequency, k is the wavenumber, r is the distance from the transducer to the observation point, $\mathcal{FT}$ denotes the Fourier transform.

Considering a rectangular apodization function, the radiated beam pattern $\mathcal{P}(x, y; \omega)$ is modeled as :

$$\mathcal{P}(x, y; \omega) = \frac{j\omega\rho_0\nu_0}{2\pi r} e^{-jkr} \frac{HDW}{d} \text{sinc}\left(\frac{y_0 H}{\lambda r}\right) \text{sinc}\left(\frac{x_0 W}{\lambda r}\right) \times \sum_{n=-\infty}^{\infty} \text{sinc}\left[D\left(\frac{x_0}{\lambda r} - \frac{n}{d} - \frac{\Delta\phi}{2\pi d}\right)\right] \tag{1.4}$$

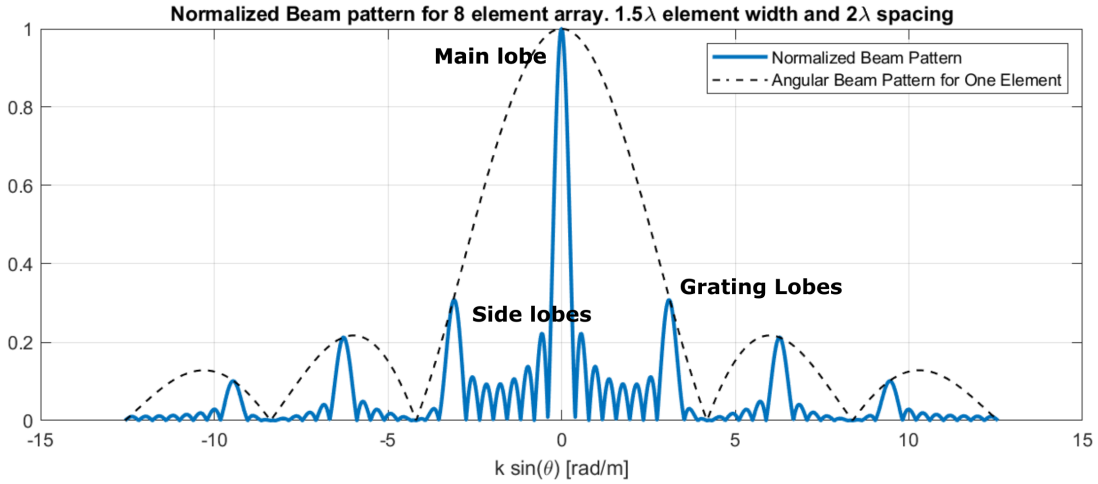

Figure 1.2: The radiated beam pattern for 8 element array with elements of width 1.5λ and an inter-element spacing of 2λ. The figure highlights the position of the main lobe, side lobes and grating lobes.

From the derived expression, it is evident that the beam pattern exhibits a sinc-like shape, characterized by a high-amplitude central lobe, known as the main lobe, and low-amplitude lobes surrounding the main lobe, referred to as sidelobes (Figure 1.2). The main lobe is the primary area of interest as it represents the focused ultrasound energy, essential for high-resolution imaging. Additionally, high-amplitude lobes, which are replicas of the main lobe, can appear in the beam pattern. These replicas arise due to the convolution of the Fourier transform of the array aperture with the Fourier transform of the comb function.

1.1.2 Characteristics of the beam pattern

Main lobe width

The width of the main lobe in the beam pattern is a critical parameter that indicates the lateral resolution of an ultrasound array. Typically, the width of the main lobe is measured at the -6 dB point below the main lobe peak, corresponding to the Full Width at Half Maximum (FWHM). A narrower main lobe corresponds to better resolution. The width of the main lobe is inversely proportional to the aperture size. For a rough approximation, the main lobe width can be considered as :

$$\text{FWHM} = \frac{\lambda r}{D} \tag{1.5}$$

From this expression, it is obvious that the beam width becomes narrower with an increase in the aperture size, resulting in improved lateral resolution. However, the resolution degrades as the focus distance r increases, moving further away from the array.

Grating lobes

The periodic distribution of the array elements gives rise to grating lobes [6, 7]. These lobes correspond to copies of the main lobe and can occur at different angles depending on the inter-element spacing. The presence of grating lobes can lead to errors in ultrasound detection, as they differ from side lobes, which have low amplitudes and are generally part of the main lobe structure. Grating lobes, on the other hand, have the same structure as the main lobe and appear at regular intervals from the main lobe. They arise due to spatial aliasing when the sampling of the array does not adhere to the Nyquist criterion [8]. In the context of the derived equations, the last summation term indicates the positions of the main lobe and the grating lobes, which can be determined by:

$$\sin(\theta) = \frac{\lambda}{d}\left(\pm n - \frac{\Delta\phi}{2\pi}\right) \tag{1.6}$$

The positions of the main lobe is given by $n = 0$, and the diffrent orders of grating lobes are given by $n = (1, 2, 3, ...)$. The angles θ_g of appearance of grating lobes can the determined by :

$$\theta_g = \sin^{-1}\left(\sin(\theta_s) \pm \frac{n\lambda}{d}\right) \tag{1.7}$$

Where θ_s is the steering angle. From this equation, it can be concluded that if no grating lobes appear in the beam pattern when the array is steered to the extreme angles corresponding to $\pm 90°$, then grating lobes can be avoided for all steering angles below this value. According to the equation, when the array is steered at an angle $\theta_s = 90°$, the first grating lobe appears for $n = -1$:

$$\theta_g = \sin^{-1}\left(1 - \frac{\lambda}{d}\right) \tag{1.8}$$

If the inter-element spacing $d < \lambda/2$, then $\left|1 - \frac{\lambda}{d}\right| > 1$, which means that the grating lobe will not be visible in the corresponding beam pattern [8]. This condition ensures that grating lobes are suppressed for all steering angles, thereby enhancing the quality of the ultrasound image by preventing the occurrence of spatial aliasing artifacts.

1.2 Two-Dimensional Arrays

1.2.1 2D Matrix arrays

To perform 3D ultrasound imaging, a 2D array is typically employed to scan the entire volume without the need for mechanically moving the ultrasound probe [9–11]. This approach allows the ultrasound beam from the array to be steered throughout the region of interest (ROI), achieving a two-way focus in all directions. Duke University was the first to introduce a real-time 3D imaging system using 2D matrix arrays consisting of

20×20 elements [12,13]. The system was limited by the number of available beamforming channels, allowing only 32 elements to be used for transmit and receive to create a 3D pyramid scan. Parallel beamforming was then employed to achieve a high volume rate [14]. To avoid artifacts such as sidelobes and grating lobes in the reconstructed images, the configuration of the array must respect to the Nyquist criterion. This criterion states that the pitch of the elements in the array should be no greater than half the wavelength. Ensuring this condition is met is crucial for maintaining image contrast and minimizing artifacts. Additionally, to achieve the same resolution as that provided by a conventional 1D array, the 2D array must contain a sufficient number of elements in both dimensions. For instance, to match the image quality of a 128-element linear array, a matrix array with $128 \times 128 = 16384$ elements is required. Since each element needs to be controlled individually in order to freely steer the ultrasound beam, the same number of channels as number of elements are required. Most of the current ultrasound system have only 256 channels, it will take 64 system to controls such array. In a technical point of view, connecting several thousands of elements in a one-element-to-one-channel design increases the complexity of the electronics required to control the array and produces a huge size probe cable making it unsuitable to clinical practices.

Another major challenge with 2D arrays is that packing a large number of elements into the probe footprint requires each element to be very small, resulting in extremely high electrical impedance [15,16]. In current linear arrays, the electrical impedance ranges from around 100Ω to $1k\Omega$, depending on the central frequency and array size [17]. However, in 2D arrays, the much smaller elements can have impedance up to 64 times higher, making it difficult to couple energy from the imaging system. This small element size and the impedance mismatch between the elements and the driving system cause low transmitted energy and poor sensitivity, leading to a low SNR [18]. This problem becomes more challenging when higher frequency are used since the element size scales inversely with the frequency and they are packed more densely.

2D matrix arrays are also very demanding in terms of data transfer and storage due to the large number of channels. For example, a 40x40 (1600 element) array generates a data transfer rate of 1500 Gb/s with a 12-bit ADC at an 80 MHz sampling frequency, requiring around 2 TB of storage per second of acquisition [19]. Additionally, the computational load needed to reconstruct volumetric data from these signals is extremely high. To overcome the limitations associated with 2D matrix arrays, various techniques have been proposed to reduce the number of elements or the number of signals transferred to the ultrasound system. The most prominent techniques include micro-beamforming, multiplexing, row-column addressing, and 2D sparse arrays. These techniques will be discussed in detail in the next section.

1.2.2 Micro-beamforming

Micro-beamforming, also known as sub-aperture beamforming, was proposed to reduce the amount of data transferred from the probe to the ultrasound system and consequently decrease the number of required beamforming channels [20–23]. This technique involves performing an initial beamforming step within the probe itself, thereby reducing the number of signals transmitted through the connection cable to the ultrasound system. Figure 1.3 illustrates the two stages involved in the micro-beamforming approach. In

the first stage, inside the ultrasound probe, multiple adjacent elements of the 2D matrix array are grouped into sub-groups. Each element within a sub-group has electronic circuits that apply specific fine delay to it to achieve a desired tilt angle. The signals that result from these delays are referred to as pre-steered signals. These signals are then summed together and transferred throughout the cable to the ultrasound system where the second beamforming stage is taking place. In the second stage, the ultrasound system applies coarse delays to focus the signals, which are then summed to beamform the image. In this approach, the channel count is reduced by a factor equal to the number of elements in each sub-group [24]. This reduction decreases the cable size and the complexity of the electronic systems driving the probe, as well as the amount of data that needs to be processed and stored. Several commercial solutions implement micro-beamforming for 3D ultrasound imaging. However, most of these are available only for transesophageal echocardiography applications, such as the Philips X7-2t [25] and the GE 6VT-D [26].

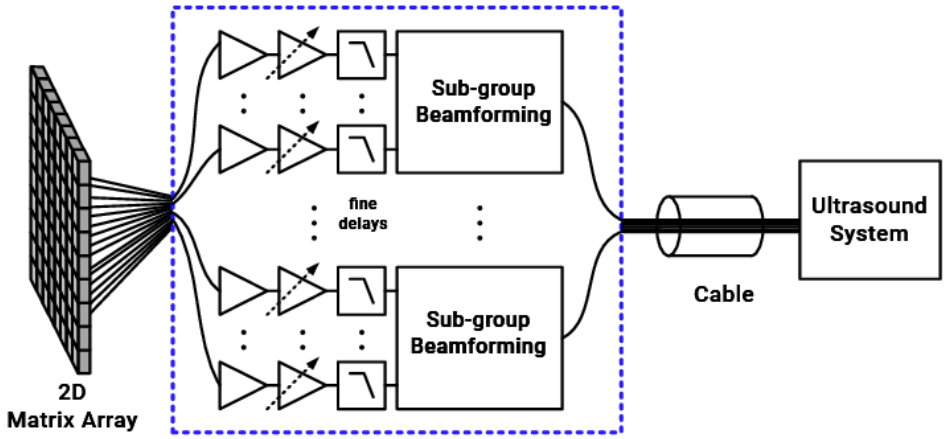

Figure 1.3: Micro-beamforming system design for 2D matrix arrays [27].

The implementation of micro-beamforming can be achieved using a front-end application-specific integrated circuit (ASIC) within the probe itself [28]. These circuits not only apply delays to the sub-groups but also include high-voltage transmitters to drive the transducer elements for beam generation and low-voltage receivers that provide proper signal amplification and time-gain compensation to each transducer element before beamforming [29]. Designing such front-end ASICs presents several challenges. The first challenge is related the complexity of the interconnection between the ASIC and the transducer array. The ASICs should be mounted with the same pitch as the one used for the transducer elements, such requirement leads to highly-compact and complex circuit inside the probe [30, 31]. Another significant challenge involves managing the power consumption of ASICs. High power consumption of both the ASICs and the transducer elements leads to self-overheating, which can cause tissue overheating and probe damage [32, 33]. To prevent excessive tissue temperature rise, power consumption must be kept below 0.5W, translating to 0.5 mW per element for a 1000-element array [31]. However, current state-of-the-art ASICs consume at least 1.4 mW per element, exceeding this limit which means that cooling strategies must be implemented [27, 34–36]. Additionally, the micro-beamforming approach is only relevant for arrays with low frequencies (2-5 MHz) and the complexity of the circuit gets more difficult with increased frequencies [37].

1.2.3 Multiplexing

Channel multiplexing is an effective solution for reducing the number of required electronic channels while retaining all the transducer elements of a matrix array [38–41]. In a multiplexed 2D matrix array, a set of elements are connected through a switch to the same electronic channel. In this configuration, only one of the interconnected elements can be activated during transmission or reception.

One widely used multiplexed 2D matrix array is the 32-by-35 matrix array developed by Vermon (Vermon, Tours, France). In this probe, the 9th, 17th, and 25th lines are not connected, resulting in a 32x32 matrix array (Figure 1.4). The aperture is divided into four sub-apertures, with elements controlled by an external 4:1 multiplexer that connects four elements from different sub-apertures to the same electronic channel. Consequently, this probe can be connected to a 256-channel ultrasound system, such as Verasonics (Verasonics, Inc., Kirkland, WA, USA) or Pioneer platform from TPAC (West Chester, OH, USA), and has demonstrated good results in various applications, including ultrafast ultrasound imaging [42–45] and super-resolution microscopy [46–49].

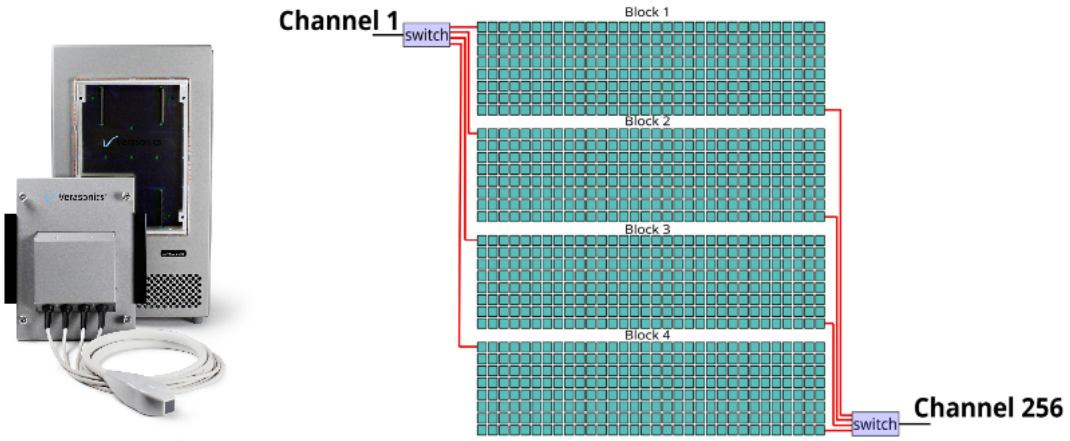

Figure 1.4: 32-by-35 2D multiplexed matrix array developed by Vermon (Vermon, Tours, France) connected to the Verasonics scanner.

Another commercially available probe is the MUXHEAD, developed by the Fraunhofer Institute for Biomedical Engineering (IBMT) [39]. Unlike the Vermon array, the MUXHEAD is a 32x32 matrix array without gaps and includes an integrated 4:1 multiplexing stage within the probe itself. Additionally, an amplification stage is embedded in the probe to amplify the weak signals from the small matrix elements and to match the cable impedance.

Although 2D multiplexed arrays have demonstrated good imaging performance in 3D ultrasound imaging, they face several challenges. First, multiplexed elements are not continuously connected to the ultrasound system, and they (the four elements) inherently share delay and amplitude when transmitting, which affects beamforming [50]. Additionally, since the elements cannot be activated simultaneously, there are restrictions on the frame rate. For example, to perform a single acquisition with the 1024-element multiplexed Vermon array, 16 acquisition events (4 transmit x 4 receive) are needed to obtain all possible element permutations in the transmit and receive apertures [47, 51].

1.2.4 Row-Column Addressing

Another channel reduction technique that has recently been studied intensively is the row-column addressing (RCA) [52]. In this approach, elements of 2D matrix arrays are driven by their row or column index, making them function similarly to a single large element (Figure 1.5). Instead of addressing individual elements, an entire row or column is addressed. The RCA approach treats an $N \times N$ 2D matrix array as an orthogonal set of N elements in 1D arrays. Consequently, the number of electronic channels required to drive the array is reduced to $2N$ instead of N^2. For example, a 128x128 matrix array using row-column addressing would require only 256 electronic channels, reducing the number of required connections by a factor of 64. In practice, to beamform a 3D B-mode image, only rows (or columns) are used to create a transmit-focused beam, while the columns (or rows) create a receive focus, resulting in one-way focusing in each of the azimuth and elevation directions.

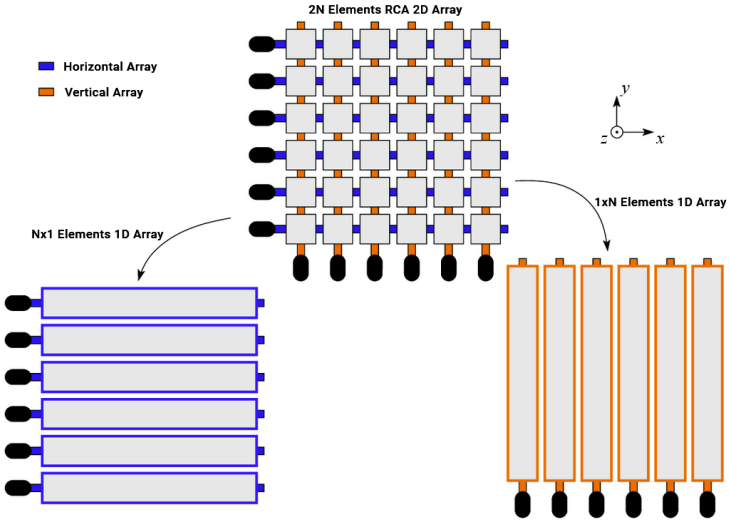

Figure 1.5: A row-column-addressed 2-D transducer array functions as two orthogonal 1-D arrays, where each element is accessed by its row or column index [53].

One notable advantage of RCA arrays is their ability to provide a very large aperture surface area without increasing the number of electronic channels. This large aperture allows for the acquisition of high-resolution images, outperforming a 2D matrix array with an equivalent number of active channels [53–55]. Additionally, the transmitting surface area of a single RCA array element is N times larger than that of a 2D matrix array element. As a result, the transmitted and received energy is significantly greater, leading to an improved SNR and increased penetration depth [52, 55].

The first RCA array, referred to as crossed electrode arrays, was introduced at Queen's University in Kingston [56, 57]. Subsequent research has extensively explored this approach using PZT-based arrays and CMUT arrays. A 64x64 PZT RCA array with a central frequency of 5.6 MHz was introduced and characterized in [58], and later, the same group developed a 256x256 2D RCA array with dimensions of 38.4x38.4 mm, operating at a central frequency of 5.3 MHz and exhibiting a -6 dB fractional bandwidth of 53% [59]. High-frequency and high-bandwidth RCA arrays have also been developed using CMUT technology. For instance, in [60] and [61], a 32x32 element RCA array with

central frequencies of 5 MHz (with a -6 dB bandwidth of 135%) and 12 MHz (with a -6 dB bandwidth of 110%) was introduced.

Various RCA arrays have also been developed under the name of top-orthogonal-to-bottom electrode (TOBE) [62]. A 64x64 TOBE array was fabricated using CMUT technology, allowing for single-element control rather than single-column or row control, distinguishing it from other RCA arrays [63, 64]. Other research groups have also contributed to the development of RCA arrays and their applications [53,54,65–69], including Doppler imaging [70, 71] and super-resolution imaging [72, 72, 73].

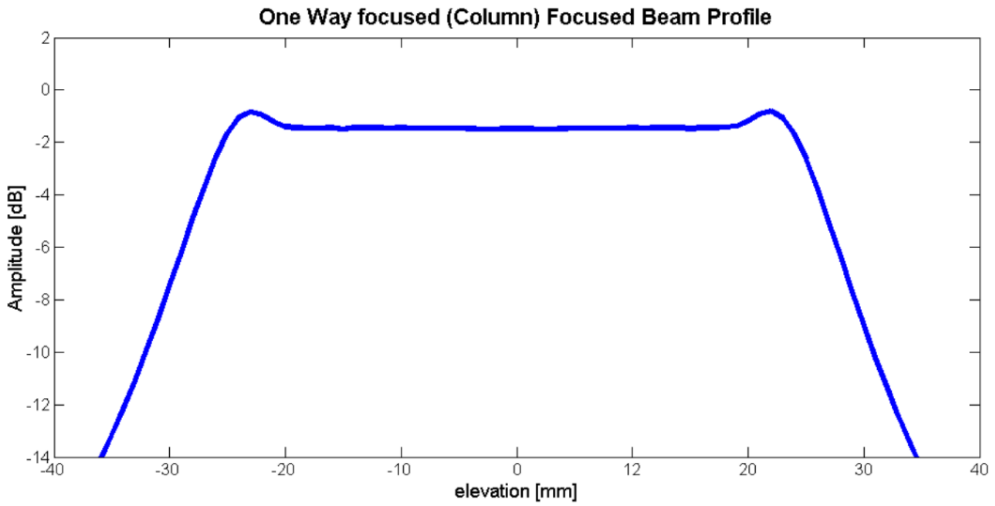

Figure 1.6: Simulated pressure profile of the RC-array showing side lobes in the elevation direction due to higher pressure at the edges of the elongated elements [74, 75].

In the RCA arrays, there is no electronic control over the length of the elements, preventing the application of electronic apodization [55]. This lack of control leads to significant edge effects due to the long row and column elements, which degrade image quality [52, 53, 55, 75–77]. A simulated pressure field of a RCA arrays is depicted in Figure 1.6. The high pressure produced by the edges of the long elements creates two sidelobes in the edges of the pressure wave in the elevation direction. These side lobes are responsible of ghost echoes in the beamformed image [75]. It was shown in [53] that the two-way impulse response in a row-column system generates up to nine echoes from a single scatterer. While only the initial echo is used for imaging, the additional, weaker echoes still negatively impact the image quality by causing ringing artifacts. Standard apodization can be applied to the array to reduce these artifacts; however, this comes at the cost of reducing the field of view [74]. Another proposed solution involves integrating apodization directly into the array, which adds complexity to the design and fabrication process [53, 54].

Additionally, the focusing power of the RCA array beamforming scheme is inherently limited. The two-way focusing achieved is equivalent to the one-way focusing of either the transmit or receive array alone, as the array only focuses in azimuth during transmission and in elevation during reception. Consequently, each transmission event captures spatial information from only two of the three dimensions, resulting in a Point Spread Function (PSF) that exhibits artifacts in the lateral and elevation directions, giving it a cross-like

shape with sidelobes level up to -30 dB [77, 78]. Coherent compounding with multiple transmission angles can mitigate these cross-shaped artifacts, but they remain particularly visible with fewer transmissions. This focusing limitation also affects the -6 dB resolution, which deteriorates as the focus moves further from the aperture [77].

1.2.5 Sparse arrays

An interesting candidate for 3D ultrasound imaging is the sparse arrays approach. This approach tackles the limitations associated with the large number of elements of 2D matrix arrays by optimally distributing a reduced number of elements over the aperture of the array, allowing the use of a reduced number of beamforming channels [79, 80]. The first studies on sparse arrays were introduced by Turnbull in [79] and they showed that the elements of a 2D matrix array can be reduced up to 1/6 of the initial number while preserving a descent image quality. In most cases, 256 elements sparse arrays are designed to match with the number of beamforming channels available in most ultrasound systems, allowing each element to be continuously controlled by an individual channel. As a consequence, the ultrasound system can transmit and receive focused beams at different angles, enabling a high flexibility in beamforming and steering capabilities [81]. Additionally, reducing the number of elements lowers manufacturing and instrumentation costs while allowing for larger element sizes, which allows for higher transmitted energy and increased system SNR performance [82].

Ideally, a sparse array should be designed to match the size of a 2D matrix array, thereby achieving high image resolution with significantly fewer beamforming channels. Consequently, the transducer elements should be distributed strategically across the aperture in order to maximize its effective size and minimize the main lobe width of the beam pattern. However, this distribution increases the distance between the elements and the inter-element spacing becomes larger than $\lambda/2$ resulting in (if distributed regularly) the introduction of grating lobes decreasing as a consequence the ultrasound image quality in terms of contrast [7, 79]. Therefore, designing a sparse array typically involves balancing the reduction in the number of elements with maintaining acceptable image contrast.

In addition to the number of elements, their distribution over the aperture significantly affects the beam pattern and image quality. As the inter-element spacing becomes larger when sampling the 2D matrix array, the distribution of the elements must be carefully chosen to minimize side lobes and grating lobes in the beam pattern while preserving a narrow beam width. Based on the manufacturing processes involved in their design, two main strategies for the development of sparse arrays exist: gridded strategies and non-gridded strategies. Gridded strategies are the most commonly used in practice, as many dense 2D arrays consist of regular grids with a pitch of approximately $\lambda/2$, from which the active elements are selected. These arrays present fewer fabrication challenges since they can be realized through conventional dicing procedures.

Non-gridded strategies, on the other hand, have been investigated and shown to improve the beam pattern's performance by significantly reducing grating lobes [81]. However, the fabrication processes involved are more complex and costlier. Regardless of whether gridded or non-gridded strategies are used, several element distribution strategies have been proposed, including periodic arrays, random arrays, optimized arrays, and deterministic arrays. These distribution strategies will be discussed next.

Periodic arrays

The simplest and most straightforward approach for designing a sparse array is to periodically distribute the elements over the aperture. This can be achieved either by placing the elements in a periodic pattern within the aperture or by activating the elements with a periodic distance in both dimensions of a 2D matrix array [83–85]. However, in periodic sparse arrays, the inter-element spacing is usually greater than $\lambda/2$, leading to the introduction of grating lobes in the beam pattern, with the distance to the main lobe decreasing as the inter-element distance increases (Figure 1.7).

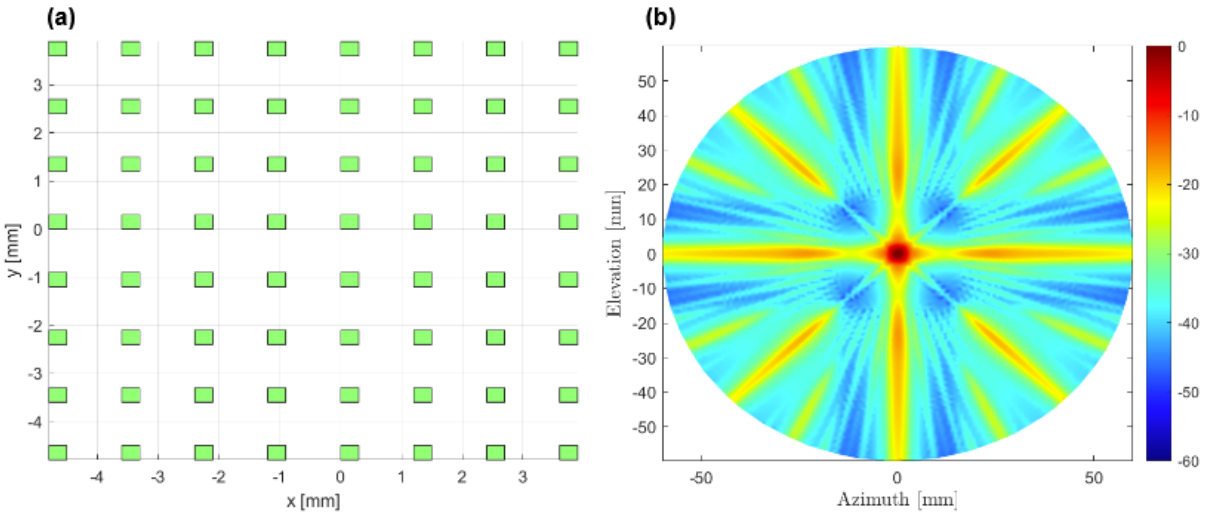

Figure 1.7: Periodic sparse array. (a) 8×8 elements periodic sparse array. (b) The corresponding radiated beam pattern highlighting grating lobes.

Although periodic sparse arrays generally show poor performance in terms of image quality, significant improvements can be achieved when different periodic arrays are used for transmission and reception. These types of arrays, known as Vernier arrays, will be discussed in a later section.

Random arrays

In periodic sparse arrays, fixed and regular spacing between the elements leads to the formation of grating lobes, which degrade image contrast. On the other hand, random sparse arrays mitigate this issue by selecting active elements through a stochastic process, resulting in a non-uniform distribution of elements across the aperture [86–92]. This approach can be applied to both gridded and non-gridded apertures, where elements are distributed according to a probability density function [87, 91]. The lack of periodicity suppresses the constructive interference responsible for high grating lobes, although the energy of the grating lobes is redistributed into the sidelobe region around the main lobe, increasing the sidelobe level floor (Figure 1.8) [86,93]. The sidelobe level floor is influenced by several factors, including the number of elements, element directivity, pulse bandwidth, and focusing parameters [87].

A study [86] designed a random 2D sparse array by randomly removing elements from a fully populated 65 × 65 dense array. The sparse array, maintaining the same 10 mm × 10

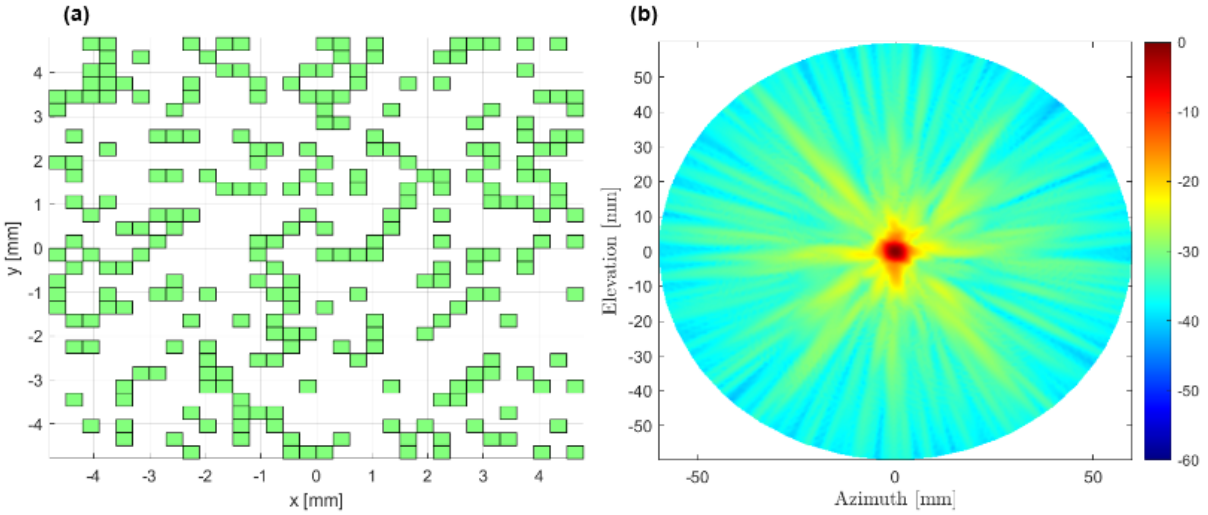

Figure 1.8: Random sparse array. (a) random distribution of 256 elements (b) The corresponding radiated beam pattern highlighting the high sidelobe level floor.

mm aperture as the dense array, consisted of only one-sixth of the original elements. The findings indicated that while the main lobe width remained stable despite the reduction in the number of elements, the sidelobe level floor increased proportionally to the reduction in elements, ranging from -70 dB to -50 dB. Similar observations were reported in an earlier study [92] where different random gridded sparse arrays (comprising 256, 180, and 110 elements) were compared.

An alternative method, known as the random binned array approach [88], involves dividing the array aperture into several non-overlapping bins of equal size, with elements selected randomly within each bin. This strategy demonstrated improved sidelobe level performance in the near field compared to completely random arrays. This approach was later adapted [89] to design non-overlapping sparse arrays with distinct transmit and receive apertures, using a bin size of 2×2.

Another study [87] compared two random sparse arrays designed with different random distributions, each with 192 transmit elements and 64 receive elements. The first array employed a uniform random distribution for both transmit and receive elements, while the second array applied spatial tapering with a Gaussian-weighted random distribution for the transmit elements and a uniform distribution for the receive elements. Broadband simulations of the radiation pattern for 400 arrays were performed, and arrays with optimal mainlobe beam width were selected. Results indicated that the array with Gaussian distribution for the transmit elements and uniform distribution for the receive elements exhibited better sidelobe level performance, however showed a wider mainlobe width due to spatial transmit tapering [94].

Testing only 400 arrays among the vast number of possible combinations is not sufficient for identifying the optimal random sparse array configuration. Moreover, generated arrays must be carefully evaluated to prevent element overlap, which complicates fabrication. However, exhaustively testing all potential arrays is infeasible. The number of possible combinations for designing a sparse array with M elements from a gridded 2D matrix array with N elements is given by :

$$\frac{N!}{(N-M)!M!} \tag{1.9}$$

For instance, in a 50×50 matrix array, the number of possible random sparse arrays with 250 elements exceeds 10^{350} combinations, surpassing the number of atoms in the observable universe [91]. This immense combinatorial space necessitates the use of optimization methods to identify sparse array layouts that meet specific criteria.

Optimized arrays

Random sparse arrays exhibit varied performance when testing different array configurations. Because the elements are selected randomly, optimization algorithms can be used to identify the optimal array configuration that satisfies a certain fixed criterion. These algorithms can adjust the array based on various parameters, including the number of elements, apodization weights, element positions, element sizes, etc.

In [95] a method was proposed to optimize the positions and apodization weights of sparse arrays through the solution of a set of nonlinear equations and a generalized eigen decomposition problem. The optimization procedure focuses on the maximization of the Integrated Sidelobe Ratio (ISLR), which is the ratio of the energy in the main lobe to the energy in the sidelobes within the radiation beam pattern. The advantage of maximizing the ISLR is that it enhances both contrast and resolution without broadening the main lobe width, which is a common issue when focusing solely on sidelobe ratio optimization [95]. The optimized array configuration is determined by maximizing the ISLR with respect to positions and apodization weights, separately and recursively. During each iteration of the process, the apodization weights are initially kept constant while the optimal positions of the array elements are identified by solving a set of nonlinear equations. Subsequently, for the optimal found element positions, the optimal apodization weights are calculated by addressing a generalized eigen decomposition problem. This iterative approach continues until convergence, resulting in finely tuned positions and apodization weights that achieve maximum ISLR.

A similar study [96–98] used linear programming as the optimization procedure for determining the positions and weights of sparse arrays. The optimization aimed to minimize the Chebyshev norm of the sidelobe level by varying the element weight vector while maintaining a normalized mainlobe. This method was applied to both 1D and 2D arrays, demonstrating enhanced performances. In [99], complex weights, rather than real weights, were optimized. However, because complex weights are phase-dependent and vary with frequency, they are less effective for broadband waveforms compared to real weights [91]. Although linear programming and approaches based on generalized eigen decomposition provide optimal solutions, they are limited by memory constraints, restricting their use to arrays with fewer than approximately 100 elements and they are only capable of designing symmetric arrays. Furthermore, apodization is generally undesirable in 2D sparse arrays because the elements typically exhibit high impedance and low sensitivity, which can degrade the SNR. Thus, most of the optimization works focuses on the elements number and layout rather than optimization of the apodization weights.

Since the selection of active elements from a set of elements can be described stochastically, stochastic optimization algorithms are suitable for optimizing sparse arrays. Among

these, genetic algorithms and simulated annealing are the most commonly employed. Genetic algorithms (GAs) simulate the process of natural selection and evolution, where a population of solutions competes for resources, and only the fittest survive to pass their "genes" to the next generation [100, 101]. This method can optimize problems involving multiple parameters by encoding these parameters. Based on the encoding involved we can differentiate binary and continuous genetic algorithms [102].

In binary genetic algorithms, parameters are represented as binary strings (genes). These encoded parameters correspond to potential solutions to the optimization problem. Each potential solution is evaluated using a fitness function, which assesses its quality. The best-performing solutions are selected to reproduce through crossover, where their genetic information is combined to create new offspring. Additionally, a mutation operation introduces random variations to maintain genetic diversity. The genetic algorithm proceeds iteratively by initially selecting a population of possible solutions, evaluating their fitness, selecting the best candidates, applying crossover and mutation, and replacing the old population with a new generation of solutions. This process continues until an optimal or satisfactory solution is achieved.

Another algorithm suitable for the design of sparse arrays is the simulated annealing algorithm [103, 104]. This algorithm is inspired by the annealing process in metallurgy, where a metal is heated to a high temperature and then slowly cooled to form a low-energy, stable crystalline structure [105]. Simulated annealing applies this principle to optimization problems by making an analogy between the molecular states during annealing and the parameters to be optimized, which are represented by a cost function. For sparse array optimization, the cost function typically depends on the beam pattern of the array. And just like the annealing process that aims to find the best arrangement of molecules, the simulated annealing algorithm aims to find the best configuration of parameters that minimizes the cost function. The algorithm begins with a high "temperature" and a random initial solution then introduces random perturbations iteratively to this solution. A distinctive feature of simulated annealing is its ability to accept not only perturbations that lower the cost function but also those that increase it, with a probability dependent on the current temperature. This mechanism allows the algorithm to escape local minima making it useful for problems with several local minima [106]. Thus, the higher the temperature the more likely bad configuration are accepted, facilitating exploration of the solution space. As the temperature decreases, the algorithm becomes more stable, increasingly rejecting configurations that increases the cost function until it reaches convergence.

For the design of sparse arrays, multiple studies have explored genetic algorithms and simulated annealing as optimization tools. In [107], genetic algorithms were employed to optimize the number of elements included in a sparse array through a process known as array thinning. Thinning involves selectively deactivating certain elements in a 2D matrix array to achieve a desired distribution of active elements across the aperture. The goal is to maintain an decent beam pattern while minimizing the number of active components. In this approach, a genetic algorithm was used to identify which elements to deactivate in a 2D matrix array to achieve a specified sidelobe level. The elements of the array were encoded as a binary sequence, with a "1" indicating an active element and a "0" indicating a deactivated element. A fitness function based on the maximum relative sidelobe level was used to evaluate the different binary sequences. The algorithm optimized an 83%-

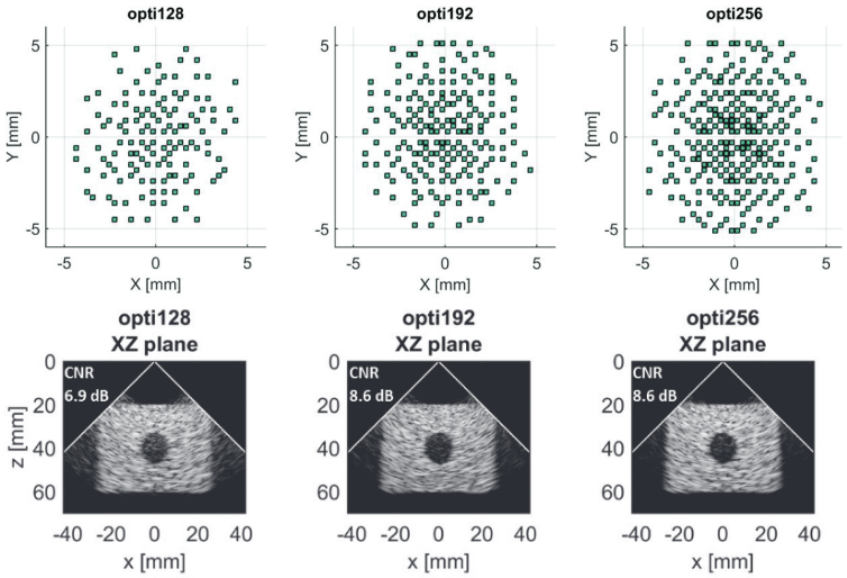

Figure 1.9: Beamformed images from sparse arrays with different element counts (128, 192 and 256) show that increasing the number of elements improves image contrast. [108]

filled sparse array from a 20x10 matrix array, achieving a maximum sidelobe level below -20 dB. However, for computational reasons, the method assumed a symmetric array and the optimization was conducted by computing the beam pattern only along two axes.

A similar study refrenced in [106] used simulated annealing to optimize both the number of elements and their weights by thinning a fully sampled 2D matrix array. The main advantage of their approach lies in its ability to effectively optimize very large sparse arrays while simultaneously optimizing both the weights and the number of active elements, even though weight optimization is often less desirable. Moreover, the method allows the desgin of asymmetric arrays, offering a greater number of degrees of freedom. During optimization, the cost function was defined over the entire narrowband 3D beam pattern, allowing for precise control over the radiation characteristics. When tested on the same 2D matrix array as in [107], the method successfully optimized a sparse array of 101 elements, corresponding to a reduction of 7 elements and achieving a sidelobe level reduction of approximately 5.4 dB compared to [107]. A larger 64x64 element array was also optimized, resulting in a thinned array with 359 elements and a sidelobe level of -21.2 dB. Compared to another study [98], where the same large array was randomly thinned to 404 elements, this approach achieved a sidelobe level reduction of 3.8 dB and decreased the element count by 45.

Although the methods demonstrated that reducing the number of elements resulted in decreased sidelobes level, this improvement is attributed not to the reduced element count but to the optimized array's asymmetric nature and the comprehensive consideration of the entire beam pattern during optimization. In fact, reducing the number of elements generally has the opposite effect on sidelobes level.The impact of reducing the number of elements was investigated in [81, 108] by designing sparse arrays with 128, 192, and 256 elements from a 32x32 (1024 elements) array. These arrays were compared in terms of beam pattern and 3D imaging capability, revealing that increasing the number of elements in the sparse arrays enhances image contrast (Figure 1.9). However, for a fixed

probe active aperture, the number of active elements has a lesser impact on the main lobe width; instead, it is the array energy that is primarily affected, which consequently influences the image contrast. It has been stated in [81] that the energy loss of the array is proportional to the ratio of active elements to the array aperture, with a reduction ratio of 68% resulting in an energy loss of -23dB.

Even if several methods investigated the optimization of the number of elements in the sparse array arrays [90,106,107,109–112], several other studies choose to fix the number of active elements to be non greater than the number of channels available in most commercial ultrasound (e.g 128 or 256 channels). A study conducted by our group investigated for the first time the impact of non-gridded sparse arrays on the beam pattern, specifically focusing on sidelobes level [113–115]. Unlike traditional methods, this technique allows elements to move freely during simulated annealing optimization, provided they do not overlap, rather than being confined to a regular grid. However, the study was limited to narrowband simulations of the radiated beam pattern to compute the cost function. The study initially compared non-gridded sparse arrays with randomly placed elements against standard gridded arrays, examining the effects of changing the number of active elements and element sizes. Additionally, optimized arrays using both strategies were compared. Non-gridded sparse arrays demonstrated superior performance in terms of sidelobes level, especially as the number of elements increased, showing reductions from -3 dB to -15 dB lower than the standard gridded array. Regarding element size, the study revealed that for a sparse array with 256 elements, sidelobes level increased with the number of elements in the standard gridded array, whereas for a non-gridded array, sidelobes level remained stable (Figure 1.10). Comparisons between optimized standard gridded and non-gridded sparse arrays indicated that the optimized non-gridded arrays exhibited better sidelobe level performance in both steered and non-steered beam patterns.

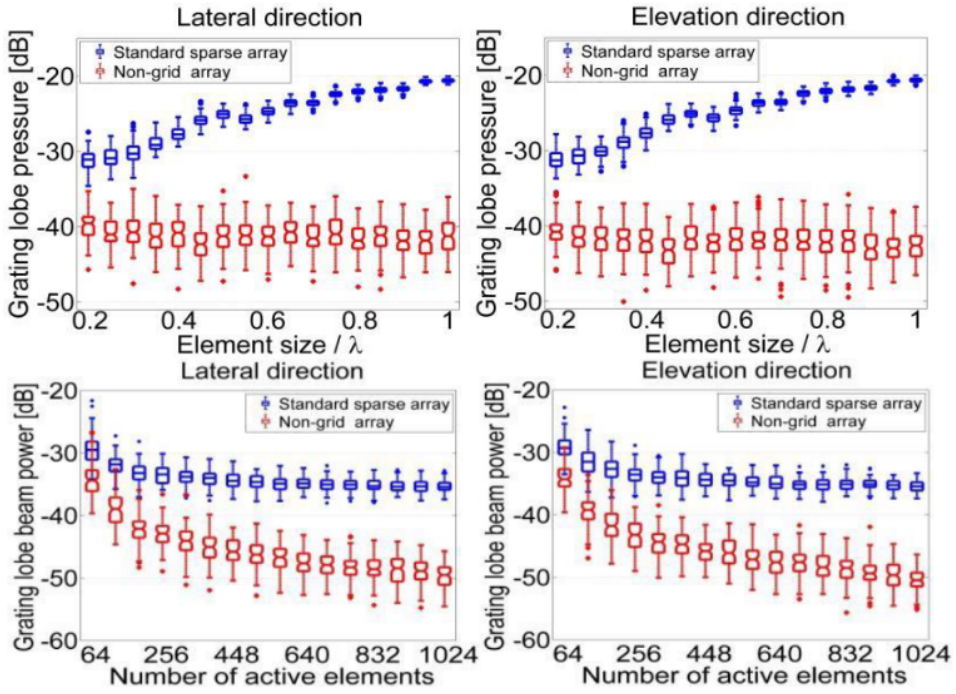

Figure 1.10: Grating-lobe level as a function of (top) the element size (bottom) number of active elements. [81]

The use of narrowband signals assumes monochromatic transmission, which does not reflect realistic excitation scenarios and wave propagation conditions. In practice, signals generally possess finite bandwidths rather than being purely monochromatic. Consequently, the use of narrowband signals can affect the accuracy of optimization techniques. To address these limitations, our group extended previous narrowband work to a fully wideband optimization setup [108, 116, 117]. Integrating wideband beam pattern simulations into the simulated annealing optimization process increases the computational resources and algorithm convergence time. To speedup this process while integrating the wideband ultrasound simulator Field II [118, 119] for beam pattern computation, two methods were proposed [120]. The first method reduces the number of pressure measurement points (PMPs) required to evaluate the beam pattern by arranging these points in a spiral-like distribution on a half-sphere at the measurement depth. This approach results in a uniform, non-periodic distribution of PMPs, enabling faster computation of the beam pattern with good precision. The second method leverages the assumption of linear propagation in Field II pressure field computations to accelerate simulations. Given this assumption, during simulated annealing optimization, only the pressure field of the perturbed elements is computed with an update in the PMPs to account for focusing delays.

By speeding up the wideband pressure field computation, a simulated annealing-based optimization method for non-gridded sparse arrays was proposed, which calculates the pressure field at three different depths during the optimization process [116]. This method uses three hemispheres with spiral-distributed PMPs and introduces a multi-depth cost function to optimize the pressure field across these depths. The results showed that optimizing the pressure field at multiple depths rather than a single depth leads to a reduction in sidelobes level across all three depths and better control over the array's steering capability at each depth. The same optimization setup was subsequently applied to the design of a gridded sparse array, incorporating specific fabrication constraints. Three sparse arrays, with 128, 192, and 256 elements respectively, were optimized from an original 32×32 array that included three deactivated lines to accommodate cable connections. The optimization algorithm, by considering these fabrication constraints, effectively reduced the sidelobes introduced by the deactivated lines.

Deterministic arrays

Deterministic arrays, often referred to as aperiodic arrays, represent another category of sparse array design where no computational costs due to optimization is involved. One of the earliest examples of such deterministic arrays is the mills cross array, designed specifically for compatibility with the Duke University system [121, 122]. Due to the system's limitation of 32 independent transmit and receive channels, the array was designed with 32 elements, which inludes the central row of transmitters along the azimuth direction of a 2D matrix array and the central row in the elevation direction for receivers. Two types of transducers were proposed: a right cross array for transmission and a 45° oriented cross for reception. This configuration achieved a sidelobe level of -15 dB. Different array variations incorporating apodization to the transmit elements were also proposed and reduced the sidelobe level to approximately -30 dB. However, thanks to their nature, the transmit beam remains narrow in the azimuth dimension but becomes significantly wide in elevation, and conversely for the receive beam.

Following the same idea of different transmit and receive aperture, Vernier arrays were proposed in as an novel approach for designing 2D sparse arrays [123, 124]. These arrays use a periodic spacing with differing periodicities for the transmit and receive elements. This unique distribution strategically places the grating lobes of the transmit and receive apertures such that their contributions to the array beam pattern effectively cancel each other out. Specifically, the grating lobes of the transmit beam pattern are aligned with the nulls of the receive beam pattern, and vice versa [89]. This design principle is based on the assumption that, in the far field, the radiated beam pattern is equivalent to the Fourier transform of the effective aperture, which is the convolution of the transmit and receive aperture functions [125]. By configuring the effective aperture to closely approximate that of a 2D matrix array, Vernier arrays can be designed in an optimal way for suppressing grating lobes.

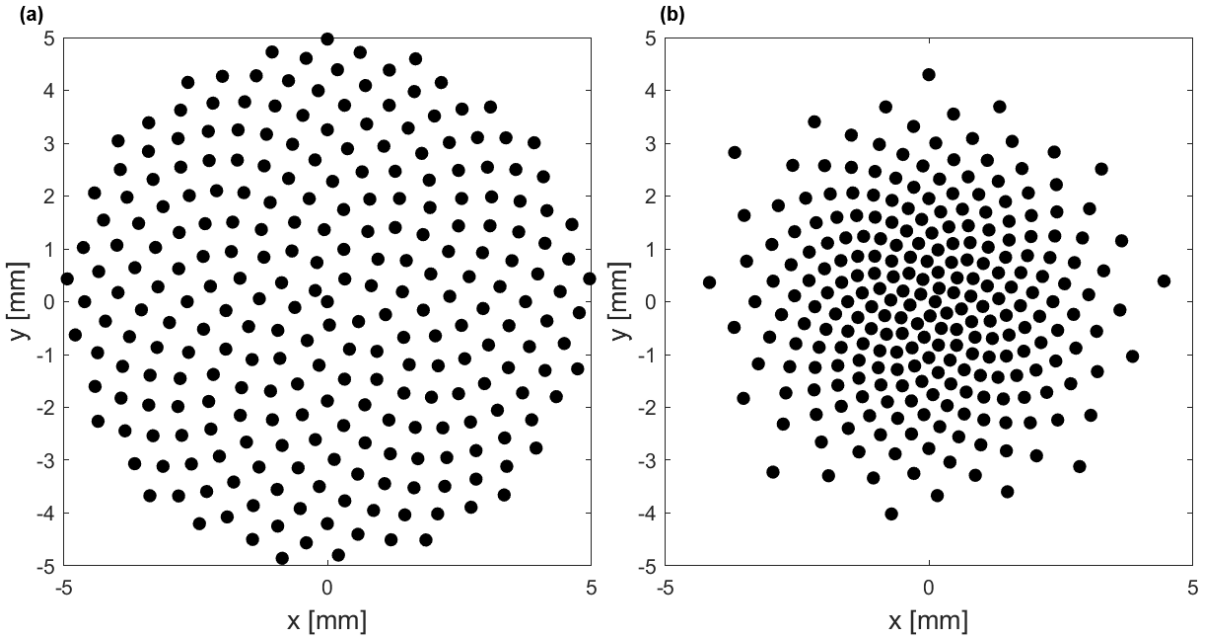

Figure 1.11: Fermat's spiral array distributions with 256 element. (a) No tapering (b) Blackman window tapering.

A sparse array consisting of 517 transmit and receive elements was developed from a 64x64 array with $\lambda/2$ inter-element spacing [123]. The elements of the Vernier array were confined within a circular aperture and employed a cosine radially symmetric apodization function to remove the concentration of secondary lobes along the array's axis, resulting in a smoother radiation pattern. To achieve an effective aperture with the same inter-element spacing as the 64x64 array, an interpolation method was applied, producing a transmit array with $3 \times (0.9)\lambda/2$ and a receive array $2 \times (0.9)\lambda/2$ inter-element spacing. The pitch of $0.9\lambda/2$ was selected to reduce grating lobes generated by high frequencies in the transmitted pulse. Simulations using a point scatterer indicated that the sidelobe level of the beam pattern was around -75dB. However, the use of different distributions for the transmit and receive arrays in Vernier arrays means that some elements are common to both the transmit and receive arrays, introducing technological challenges in their design and implementation [126]. Additionally, the authors noted a decrease in the SNR due to the required apodization and a need of more elements to obtain the required

effective aperture [123]. In a comparative study, a Vernier array was evaluated against a random array, a Mills cross array, and a fully populated 2D matrix array with 128x128 elements [122]. The Vernier array was significantly sparsified, keeping only 2% of the elements of the fully populated array. The results indicated that the highly sparse Vernier array was unsuitable for imaging due to the presence of high grating lobes, especially when compared to the random array and Mills cross array. The study concluded that the Vernier array becomes more advantageous for imaging applications when less sparsity is applied in its design [122].

Recent investigations have focused on the use of spiral arrays as non-periodic sparse arrays for 3D ultrasound imaging. The initial study on spiral arrays, however, was conducted earlier, where elements were arranged along an exponential spiral path [127]. This array, intended for transthoracic cardiac imaging, used 128 odd elements for transmission and 127 elements for reception, resulting in a configuration similar to a Vernier array [125]. When compared with random and periodic arrays, the spiral array demonstrated comparable beam pattern width but with significantly lower sidelobes level. Specifically, it achieved a sidelobe level of -40 dB in non-steered simulations and -28 dB when the beam was steered to a 40° angle.

More recently, a study proposed the use of a specific type of spiral distribution known as Fermat's spiral for designing sparse arrays (Figure 1.11 (a)) [128]. In this design, elements are arranged according to a divergence angle that determines the distance between adjacent elements. The radial position of each element follows the square root of its angular position. The radial positions of the Fermat spiral array are given by the following formula [128]:

$$\theta_n = n.\alpha \tag{1.10}$$

$$R_n = \frac{D\sqrt{n\alpha}}{2\sqrt{(N_e - 1)\alpha}} \tag{1.11}$$

Where α is the divergence angle, D is the desired aperture size and N_e is the number of elements. A special case where the divergence angle equals the golden angle results in a sunflower Fermat spiral array, so named because the element distribution resembles sunflower seeds. According to [94], since the golden angle is an irrational number, each element has a unique angular position, enhancing the beam pattern performance by reducing grating lobes level.

In [128], two different spiral arrays were simulated with a minimum distance between elements set to λ and a divergence angle equal to the golden angle, with aperture diameters of 40λ, 50λ, and 60λ. The first configuration involved two different spiral arrays, each with 128 elements, to form an effective aperture by adding a phase displacement to the receive array, reducing the grating lobe level. An exhaustive search was conducted for divergence angles in the interval (0°:0.005°:180°). The second configuration used 256 elements, with the same elements employed for both transmission and reception. The results indicated that using different apertures for the 128-element array configuration improved performance, achieving a sidelobe level of -42 dB. However, the 256-element array, despite using the same aperture for both transmit and receive functions, demonstrated superior performance with a sidelobe level of -50 dB, regardless of the aperture size.

Using amplitude apodization on already less sensitive sparse arrays can drastically reduce the array's sensitivity and overall SNR. To preserve array sensitivity while employing apodization, a different approach for designing Fermat's spiral arrays was proposed in [94], utilizing spatial apodization rather than amplitude apodization (Figure 1.11 (b)). This approach, known as density tapering, was first introduced for antenna array design and results in increased array sensitivity while simplifying control system design, as no electronic apodization is needed [129]. Unlike amplitude apodization, which adjusts the weights of array elements, density tapering involves varying the element density across the array according to a tapering window (e.g., Blackman window). Typically, a higher element density is used near the center of the array, decreasing towards the edges. The central density depends on the tapering window used. In [94], this approach was used to design large Fermat's spiral sparse arrays with 256 elements. The wideband 3D beam patterns focused at 127λ were simulated for 105 sparse arrays using different large apertures of sizes 40λ, 60λ, and 80λ and element sizes of 0.5λ, 0.7λ, 1λ, 1.2λ, and 1.5λ. Various tapering windows, including rectangular, Tukey, cosine, Taylor, sinc, Hanning, and Blackman, were studied. The tapered spiral arrays were compared to 2D matrix arrays with the same aperture size and element size but varying element numbers to create a dense matrix.

For different simulated steering angles, the spiral arrays and matrix arrays showed similar beamwidths; however, the spiral arrays exhibited higher sidelobes level. The study concluded that smaller elements provided better uniformity of sidelobes level over the simulated steering angles, although the sensitivity of the elements deteriorated. Sensitivity was increased by tapering, achieving up to +3 dB. Additionally, the use of tapering reduced lateral resolution because the elements were densely packed in the center of the probe, reducing the active footprint, although larger apertures increased resolution. The depth of field also increased with apodization, and smaller aperture sizes yielded better values.

A different spiral array was proposed for anomaly detection in transcranial blood flow based on the logarithmic spiral distribution [82]. The array had a small aperture size of 30 mm with circular elements to preserve rotational symmetry. The array pattern consisted of several non-overlapping spiral arms with an element at the center of the array. The increasing gap between successive turns of a logarithmic spiral prevented grating lobes, creating an aperiodic structure and simplifying fabrication. The designed logarithmic spiral array matched the size of the temporal bone window in the skull and consisted of 13 arms, each with 6 elements, and an additional central element, totaling 79 elements. Each element had a radius of 0.95 mm, with a gap of 0.5 mm between adjacent elements along the same arm. Narrowband simulation was conducted to evaluate the performance of the logarithmic spiral array against a random array and Fermat's spiral array. The comparative analysis showed that the logarithmic spiral array achieved the lowest peak sidelobe level, with an improvement of around -3 dB compared to the other two configurations.

The effect of using different spiral arrays for transmit and receive to spread the energy of the sidelobes was studied in [130]. In this approach, a Fermat's spiral array with 280 elements and a golden angle was assumed to be a dense array, and the goal was to create two different arrays—one for transmit and one for receive—by specifying the dense spiral array. The active elements for each array were chosen based on the method proposed for the design of sparse linear arrays [131]. The results showed that the number of elements

in the spiral array could be reduced while maintaining good sidelobe performance. By choosing appropriate element distributions for transmit and receive, concentrations of sidelobes could be mitigated, and the results could match the performance of a dense spiral array.

To acquire images from a large field of view, different images can be acquired by different probes and coherently compounded by means of registration. In 3D, a method that uses two different Fermat's spiral transducers was proposed to achieve a large field of view [132]. Instead of performing image registration, this method coherently combines the RF signals received by two synchronized transducers based on a method called coherent-multi transducer ultrasound (CoMTUS) imaging [133]. CoMTUS imaging uses only the RF signals to estimate the beamforming parameters with high precision. Cross-correlation of signals is used to maximize the coherence between the received RF signals, which allows the estimation of the transducers locations and speed of sound. A density-tapered spiral array (50% Tukey) of 512 elements was implemented on 1024-element matrix probes (Vermon S.A., Tours, France) by deactivating the elements that do not belong to the spiral pattern. This array was further divided into two spiral arrays. The two arrays were placed in two different spatial locations following a geometric transformation. The RF signals were acquired by transmitting plane waves with the arrays sequentially, and both arrays were used to collect the signals. The images were beamformed by coherently compounding the RF signals based on the CoMTUS algorithms and compared to the images obtained with the dense 512 spiral array. The CoMTUS images demonstrated better lateral resolution and contrast compared to the dense spiral array.

More recently, Costas arrays have been proposed as an alternative for designing sparse arrays [134]. A Costas array is a 2D array characterized by each row and column containing only a single non-zero element, with the vector distance between any pair of elements being distinct. This feature results in an aperiodic distribution of elements, which helps reduce grating lobes level. For a 256-order Costas array, there exist 65,534 different array combinations. They were all simulated under narrowband conditions, and the array with the best sidelobe level performance was chosen for the study. The selected array had a wide aperture of 96λ and was compared to a random array, a Fermat's spiral array, a density-tapered version of the spiral array with the same aperture size, and a smaller 2D matrix array. PSF and cyst phantom images were simulated, and the results showed that the Costas array offers the same lateral resolution as the random array and the spiral array, as they have almost the same active aperture. Additionally, the Costas array has a lower sidelobe level than the random array; however, it exhibits a higher sidelobe level compared to the spiral array, especially in the region around the main lobe. Despite the slightly higher sidelobe level compared to the spiral array, its gridded nature makes it a good candidate for 3D ultrasound imaging. Since only a single element is present in each row and column, the fabrication process of these arrays is much simpler than that of the spiral array. The authors state that these arrays can be manufactured with bulk or composite piezoelectric material, which can offer a good backing layer, enhancing the bandwidth of the array [134].

Manufactured sparse array prototypes

The most commonly used 2D matrix probe is the PZT-based 32x32 elements probe manufactured by Vermon S.A., Tours, France. Two probes with the same dimensions of $10mm$,

element size of $249\mu m$, and pitch of $300\mu m$ in both directions were developed, but with different frequencies: 3.5MHz and 7.5MHz. Based on these probes, several sparse arrays were developed by selecting the active elements among the 32x32 matrix. However, since the sparse arrays are designed from an already manufactured probe, only the elements' positions can be chosen with a fixed element pitch and size. Additionally, since this probe is multiplexed, these constraints must be taken into account in the array design. In [135], the sparse array optimized using a simulated annealing algorithm in [108] was implemented on the 3.5MHz matrix probe. To drive the elements of the optimized array, a total of four Vantage-256 research scanners (Verasonics, Inc., Kirkland, WA, USA), each having 256 beamforming channels, were used in synchronization. By doing so, each element of the sparse probe is continuously connected to the same beamforming channel in transmission and reception. This setup was used to experimentally evaluate the optimized array in focused and diverging wave imaging.

Experimental validation of the Fermat's spiral array was initially conducted using the Vermon 32x32 matrix probe [136]. In [137, 138], a 512-element density-tapered spiral array was designed on the 3.5 MHz matrix array by combining two spiral arrays, each with 256 elements, since an ultrasound system with only 256 channels was used. The two 256-element spiral arrays followed a 50% Tukey tapered window. Since the spiral array is ungridded, the elements of the designed arrays were selected to be as close as possible to the matrix grid. The two spiral arrays were designed to have no overlapping elements. Additionally, two 256-channel Ultrasound Advanced Open Platform (ULA-OP 256) [139] systems were synchronized to control the resulting 512-element spiral array. The same technique was used in order to experimentally validate the performance of 3D CoMTUS imaging where two probes are required [140]. The same 256 spiral probes were used but this time two different 32x32 matrix arrays were used with two synchronous 256-channel ULA-OP systems.

The first implementation of an ungridded Fermat's spiral array for Non-Destructive Evaluation (NDE) with Bulk piezoelectric (PZT) material technology was presented in [141]. The array was designed based on Fermat's spiral with a diverging angle of 141.59 degrees and comprised 96 elements. The central frequency of the array was 1.5 MHz, and it featured a wide aperture of 70λ. Initially, the element size was set to $\lambda/2 \times \lambda/2$, but this configuration reduced the active area by approximately 99% due to diminished element sensitivity. To address this, larger elements of $2\lambda \times 2\lambda$ were used. However, this adjustment decreased the element divergence, resulting in degraded steering capabilities of the array. Despite this, such a compromise can be acceptable in NDE applications if the steering angle is limited to less than 8 degrees. The array was manufactured using a new technique called Fused Filament Fabrication (FFF). Post-manufacturing tests revealed that more than half of the elements had a -6 dB fractional bandwidth of 50%, while 3% of the elements were non-functional.

For medical ultrasound imaging applications, a study designed a prototype of the density-tapered spiral array proposed in [142]. Two prototype 2D tapered spiral arrays following a 50% Tukey window were designed with center frequencies of 2.5 MHz (low-frequency) and 5 MHz (high-frequency), based on piezoelectric material built directly on printed circuit boards (PZT-on-PCB). The use of PCB facilitated the manufacturing process by utilizing PCB traces to position the elements accurately. Both arrays had 256 elements distributed over the same aperture size of 13 mm but featured different element

sizes. The arrays were manufactured by fully populating a grid of elements and connecting only the 256 elements whose positions were closest to the ideal spiral distribution to the PCB. High element impedance and cable attenuation were mitigated using preamplifiers to amplify the received signals, thereby increasing the SNR of the array. Characterization of both probes revealed that the low-frequency array had 30 dead elements, while the high-frequency probe had 15 dead elements. The frequency response of single elements showed a fractional -3 dB one-way bandwidth of 26% ± 13% for the low-frequency array and 32% ± 11% for the high-frequency array. While these bandwidths are adequate for fundamental mode imaging, they might be insufficient for contrast imaging at higher harmonics.

A prototype for the logarithmic spiral array was also manufactured [82]. After comparing three arrays—random array, Fermat spiral array, and a log spiral array—the latter was chosen for fabrication based on its superior performance. The array consists of 79 elements distributed in a 30 mm aperture and operates at a central frequency of 2 MHz for transcranial imaging applications. A piezoelectric ceramic structure referred to as composite element composite array transducer (CECAT) was used for the manufacturing of the array. The CECAT elements consist of piezocomposites, where piezoelectric fibers are randomly distributed within the array element area, providing performance similar to that of conventional 1–3 composite structures. Along with the CECAT array, a conventional 1–3 composite structure was also manufactured with the same characteristics for comparison. Electrical impedance measurements showed that the 1–3 array has lower electrical impedance, indicating that, with the same driving voltage, the 1–3 array would have higher vibration velocity than the CECAT array and, consequently, better sensitivity. However, mechanical cross-talk was measured to be lower for the CECAT array, although its values were acceptable for both arrays. In terms of bandwidth, the -6 dB pulse-echo bandwidth was larger for the CECAT array, with a value of 47.44%, while the 1–3 array had a bandwidth of 30.95%.

An ellipsoidal array based on the spiral array with 256 elements was developed for transperineal ultrasound imaging of the prostate. The shape was chosen for geometrical considerations of the imaging window, as a circular array cannot fit the available window. The array was manufactured by first dicing a PZT 1-3 composite to create a 2D matrix with 25x49 elements with a pitch of 513 μm. Only the elements that corresponded to the ellipsoidal array geometry were connected. The single-element acoustic characterization of the array showed that 25% of the elements were non-functional. Spectral analysis results revealed a central frequency of 4.3 MHz and a -6 dB pulse-echo bandwidth of 32%.

To mitigate the severe ultrasound attenuation caused by the skull in 2D transcranial ultrasound imaging, a large 2D sparse array with 2024 elements, distributed following a density-tapered (Taylor window) Fermat spiral pattern, was manufactured in [143]. The aperture size was chosen to be 65 mm to average out aberrations and reduce sensitivity to phase aberration. To penetrate the skull and improve the imaging depth of brain tissue, a frequency of 1.25 MHz was selected. The element size was set to 0.75λ to balance low sidelobes level and array sensitivity. The fabrication involved creating a 1–3 piezo composite with PET5H, featuring a 64% volume fraction of piezoelectric material to balance bandwidth and sensitivity. Using the dicing process, elements were electrically isolated, and an alumina-doped epoxy matching layer was added to the front face. The piezo composite was then assembled with a custom flexible PCB, which had cutouts aligned to each

element and connected via 25μm diameter gold wire bonds. An epoxy backing layer was added to attenuate back-propagated signals and protect the wire bonds. The transducer shell was 3D printed and included a protective silicone layer across its front face. Finally, cables were attached to the PCB, facilitating interface with Verasonics Vantage systems. Acoustic characterization of the array was performed using a hydrophone. Four Verasonics Vantage systems, totaling 1024 beamforming channels, were synchronized to drive the array. The array demonstrated a sidelobe level of -27.5 dB and a beamwidth of 1.5 mm. Additionally, acoustic characterization in the presence of the skull showed a 12.5 dB drop in measured pressure due to strong reflections from the skull.

All the previously mentioned prototypes were fabricated using PZT technology. Other studies have also investigated the use of CMUT technology in the design of sparse arrays. The advantage of CMUT technology over PZT technology is the ease of manufacturing ungridded arrays. PZT technology usually relies on the dicing process, which imposes regular grids on the definition of element positions. In contrast, CMUT technology, with its small cell size, enables the design of arrays with arbitrary element positions and shapes, offering greater flexibility in array configuration. In [144], a new packing method was used to design a 256-element sparse array based on CMUT technology. The elements were distributed over a 45λ aperture following a density-tapered Fermat's spiral array with a Blackman window. The elements were designed with a hexagonal shape composed of 19 CMUT membranes operating at a central frequency of 7 MHz. To mitigate the electrical impedance of the CMUT elements, a 256-channel analog front-end ASIC was integrated, containing pulsers, a low-noise receiver, and a TX beamformer. The acoustic characterization of the designed prototype was later performed in a separate study using unfocused wave transmissions for high volume rate imaging [145].

Experimental applications of sparse arrays

Most applications of sparse arrays in 3D ultrasound imaging have focused on high frame rate acquisition sequences. In [135], the application of sparse arrays for high frame rate volumetric imaging was investigated using diverging wave imaging. Utilizing four synchronized Verasonics Vantage systems, a sparse array of 256 elements was optimized (for focused transmissions) on a 32x32 2D matrix array (Vermon, Tours, France) with a 72% bandwidth at 3 MHz. 25 virtual sources were placed behind the transducer in a spherical cap at 25 mm, yielding a field of view (FOV) of 25.4°. Compounding was performed on the 25 low-resolution volumes obtained by each diverging wave transmission to reconstruct the final high-quality volume at a frame rate of 90 volumes per second. The array was compared to the 32x32 matrix array and a random array, showing better contrast than the random array, while the fully populated matrix array outperformed both arrays (Figure 1.12).

In another experimental study, high frame rate imaging using diverging waves with Sparse Random Aperture Compounding (SRAC) was investigated. Using the same probe as in [146], but instead of employing four Verasonics channels, a single 256-channel system with a 4-to-1 multiplexer was used. The SRAC imaging approach utilizes several complementary random apertures to approximate a full matrix array. A set of SRAC apertures with four complementary random apertures was implemented. For each transmit angle, a different aperture was used for transmission, thanks to the short time delay of the multiplexer switch (2 μs), achieving frame rates up to 750 Hz.

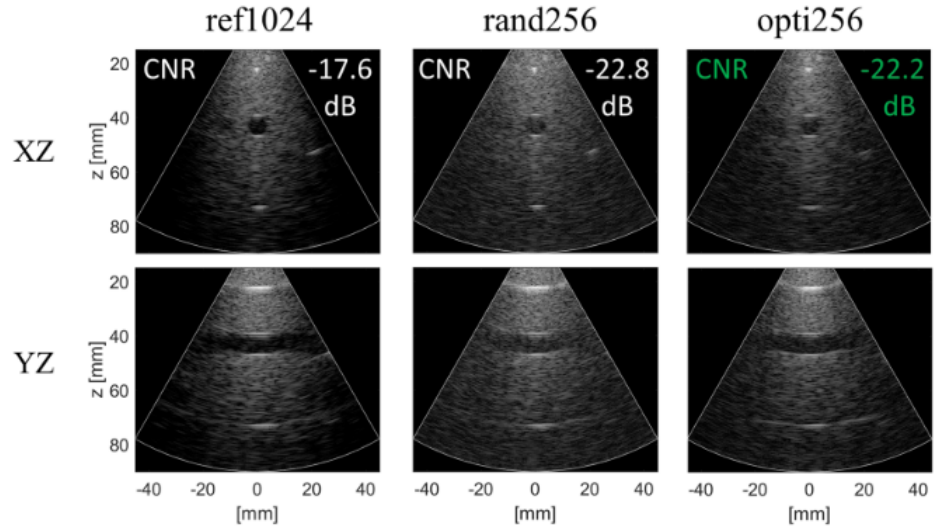

Figure 1.12: Experimental phantom image comparing contrast with a reference matrix array, a random array, and an optimized sparse array using 25 diverging waves [135].

Based on the studies that investigated the feasibility of sparse arrays for high frame rate volumetric imaging, several implementations of sparse arrays have been explored for various applications requiring high imaging rates, such as blood flow imaging and super-resolution imaging. In one study, a spiral sparse array was implemented in a three-plane echocardiography imaging system, achieving frame rates similar to those obtained clinically with 2D echocardiography, albeit with a contrast drop of -3 dB. The feasibility of using sparse arrays for blood flow imaging was investigated in a study focused on spectral Doppler measurements. The study implemented the optimized array on a 3 MHz Vermon matrix probe. The results indicated that the Doppler spectrum shape was not significantly affected by the use of the sparse array compared to the full matrix array. However, a significant drop in SNR was observed with the sparse array, which remains a primary challenge due to the reduced number of elements. Another study partially addressed the SNR issue by using a Linear Frequency Modulated (LFM) waveform, a coded signal that increased the SNR, achieving an average SNR gain of 11 dB [136]. Several other studies focused on the uses of sparse array for blood flow applications, such as vector flow imaging [147] , color flow imaging [148] and transcranial Doppler imaging [85].

1.3 Objectives of the thesis

Sparse arrays present several notable advantages over other element reduction techniques for 3D ultrasound imaging. One of the most promising benefits is their ability to freely steer the ultrasound beam in all directions, which significantly enlarges the field of view. This capability opens up possibilities for implementing advanced imaging sequences, such as diverging waves, which are particularly beneficial for applications like echocardiography. Additionally, sparse arrays use fewer elements, reducing the complexity and cost of manufacturing and operating the transducer arrays. This reduction in hardware can also simplify the system design and decrease power consumption. Sparse arrays provide

flexibility in the design and configuration of the array elements, allowing for optimization specific to various applications and imaging conditions. Despite their advantages, sparse arrays face two significant challenges: low sensitivity and reduced image contrast.

Sparse arrays are typically designed with small apertures because fewer elements are distributed over the array footprint, necessitating smaller footprints to minimize the distance between elements. Consequently, the size of the elements must be small, usually around half the wavelength. Small elements, however, exhibit very low sensitivity and high electrical impedance, significantly reducing the SNR. Moreover, the reduction in the number of elements limits the amount of acoustic energy transmitted and received due to less vibrating surface area compared to a full matrix array. In contrast, increasing the element size in sparse arrays can enhance sensitivity due to the larger inter-element spacing. An optimized sparse array with element sizes varying from 0.4λ to 0.8λ demonstrated a sensitivity increase of 16dB compared to an array with a fixed element size of $\lambda/2$. However, this increase in element size depends on the distribution used, as varying inter-element spacing can lead to element overlap. Additionally, larger element sizes reduce their divergence, thereby diminishing the array's steering capability.

In addition to the low SNR of sparse arrays, the spatial distribution of elements on the array aperture, with interelement spacing larger than $\lambda/2$, significantly degrades the array's beampattern. This degradation manifests as high sidelobes level around the main lobe, causing energy leaks during beamforming and drastically reducing image contrast. The sidelobes level are strongly influenced by the way elements are distributed over the array's aperture. Consequently, much of the research on sparse arrays has focused on addressing this challenge by finding optimal distributions that reduce the number of array elements while maintaining acceptable image quality. One of the most promising distributions is the density tapering of the Fermat's spiral array. This layout can reduce sidelobes level, albeit at the expense of some degradation in image resolution. However, for ultrasound images typically displayed with a dynamic range of -60 dB, artifacts remain visible.

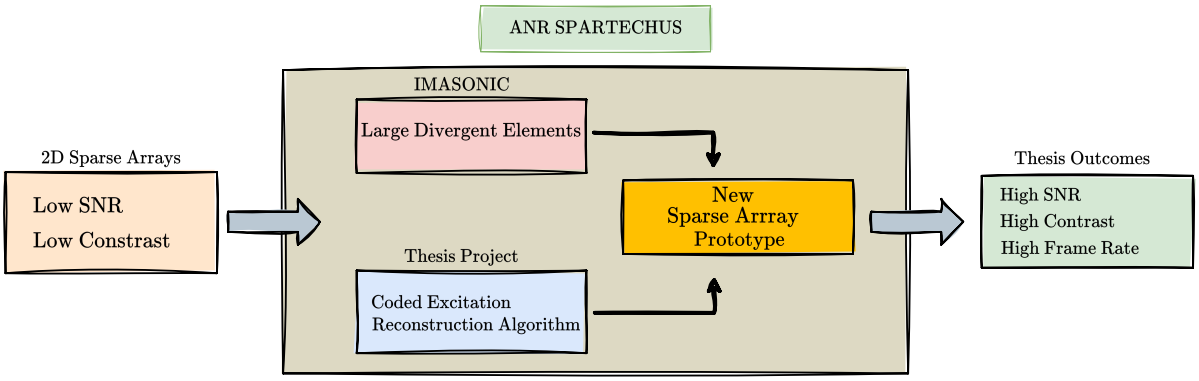

Figure 1.13: A diagram highlighting the objectives of the thesis.

The primary objectives of this thesis are twofold (Figure 1.13): first, to increase the SNR of sparse arrays; second, to enhance image contrast. This research is part of the ANR (Agence National de la Recherche) Project named SPARse array TECHniques FOR 3D medical UltraSound (SPARTECHUS). SPARTECHUS is a collaborative project between our laboratory, CREATIS, and Imasonic, an ultrasound transducer manufacturer,

with the aim of developing the next generation of ultrasound arrays for 3D medical ultrasound imaging. The project is designed to overcome the most significant limitations of current technologies and to open new possibilities, particularly for integrated multi-modal systems.

By hypothesizing that transducer elements with higher sensitivity and equivalent directivity can be developed, Imasonic will focus on creating large transducer elements with integrated lenses to preserve their divergence, thus addressing the low sensitivity limitation of sparse arrays. Our contribution involves combining their technology with innovative coded excitation emissions. By implementing coded excitation sequences, the goal is to enhance the SNR, thereby addressing one of the critical limitations of sparse arrays, which is their inherently low sensitivity. The combination of these two techniques will lead to the development of a new prototype of a 2D sparse array.

Concurrently, to address the problem of poor image contrast due to high sidelobes level, we will develop a new reconstruction algorithm based on deep neural networks, trained specifically for the newly developed sparse array prototype. These algorithms will focus on optimizing the beamforming processes to achieve high-quality ultrasound images. Together, these objectives aim to overcome the principal challenges associated with sparse arrays, paving the way for their more effective use in 3D ultrasound imaging.

Chapter 2

Signal-to-Noise Ratio Increase Of Sparse Arrays Using Coded Synthetic Transmit Aperture

In this chapter, I will explore methods to increase the Signal-to-Noise Ratio (SNR) of sparse arrays using coded excitation, implemented within a synthetic transmit aperture (STA) imaging sequence. Sparse arrays, despite their advantages, often suffer from low SNR, which can significantly degrade image quality. I will begin by examining the causes of low SNR in sparse arrays. Following this, a brief literature review on existing coded excitation methods will be provided to contextualize the development of our approach. Finally, I will introduce a novel coded excitation method based on complete complementary codes, detailing its potential to improve SNR in 2D sparse array in simulation and experimental studies.

2.1 SNR challange of 2D sparse arrays

2.1.1 Number of element and electrical impedance

The primary challenge facing 2D sparse arrays is the necessity to design them with very small elements compared to 1D arrays in order to maintain a good divergence angle in both spatial directions. In contrast, 1D arrays typically have a larger height (greater than 1 mm) and a smaller width (around 0.5 mm), focusing primarily in a single plane in the lateral direction. However, 2D arrays, such as sparse arrays, have much smaller elements. For instance, the 32x32 Vermon probe, which is commonly used as a base for designing sparse arrays, has elements with dimensions of 300x300 μm. The small size of these elements leads to low radiated energy and also increases their electrical impedance, which in turn results in reduced sensitivity. Additionally, reducing the number of elements in the probe to create a sparse array further decreases the array's SNR.

The electrical impedance of piezoelectric elements is directly related to their area through their capacitance. The capacitance of an element is given by:

$$C_0 = \frac{\varepsilon_0 \varepsilon_r A}{t} \tag{2.1}$$

where ε_0 is the dielectric permittivity of vacuum, ε_r is the relative dielectric constant, t is the thickness of the element, and A is its area. From Equation (2.1), it can be observed that as the area A of the element decreases, its capacitance C_0 also decreases. Since the electrical impedance is inversely proportional to the capacitance of an element, a decrease in the area leads to an increase in the electrical impedance.

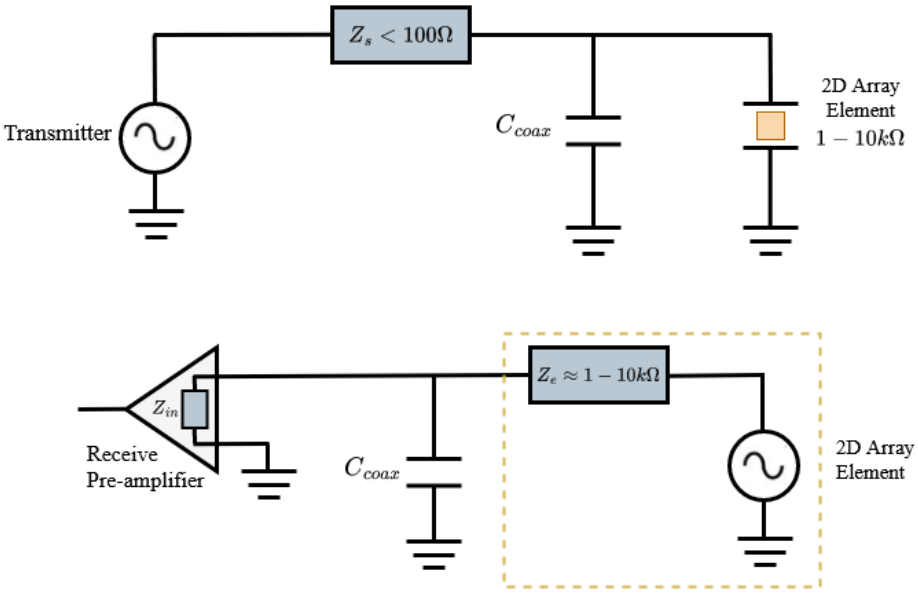

Figure 2.1: Simplified electrical circuit diagrams of an ultrasound system: the top diagram shows the connection to a transmitting channel, and the bottom diagram depicts the connection to a receiving channel with a small 2D array element.

Consider the simplified ultrasound system connected to transmit and receive channels, as represented in Figure 2.1. During transmission, energy transfer is suboptimal due to an impedance mismatch between the transmitter, with an impedance of less than 100Ω, and the small transducer element, which has an impedance of $1k\Omega$. In receiving mode, the 2D array element can be modeled as an ideal voltage source with an output impedance ranging from 1 to $10k\Omega$. A standard coaxial cable, with a capacitance of approximately $200pF$, typically exhibits an impedance of about 150Ω, depending on the ultrasound frequency. Due to the high impedance of the array element, over 80% of the signal is lost through the voltage divider effect between the coaxial cable impedance and the transducer element impedance [149]. This significant signal loss results in a low SNR, particularly when the noise from the pre-amplifier and other amplifiers predominates.

2.1.2 The excitation pulse

In a conventional pulse-echo ultrasound imaging system, short pulses are used as excitation signals for the transducer. These short pulses are transmitted periodically, and the frequency at which they are transmitted is called the pulse repetition frequency (PRF). The benefits of such waveforms are related to their large bandwidth, which provides good axial resolution. However, the use of short pulses results in low transmitted energy, leading to a tradeoff between resolution and penetration depth. The reduced energy associated with short pulses means that the echoes received from deeper tissues are weaker. Conse-

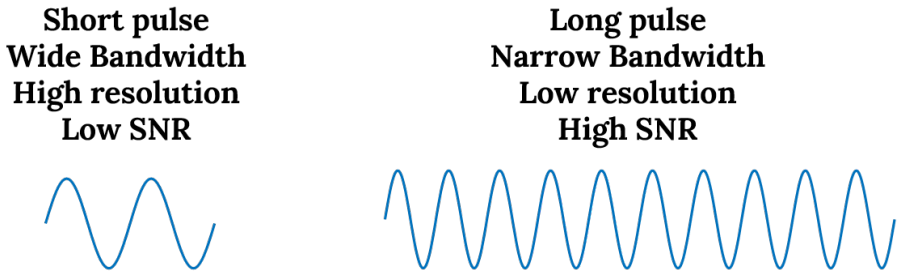

Figure 2.2: A comparison of the characteristics of short pulses vs long pulses.

quently, the deeper the tissue, the lower the SNR. The SNR is defined as the ratio of the maximum received signal power to the noise power at the receiver stage:

$$SNR = \frac{\text{Maximum Received Signal Power}}{\text{Noise Power}} \tag{2.2}$$

Assuming that the noise originating from the transducer element and pre-amplifier is a white Gaussian noise with a noise power N_p . Given that the energy of the received echo is E_r, the SNR is given by [7] :

$$SNR = \frac{2E_r}{N_p} \tag{2.3}$$

When a short sinusoidal pulse with an amplitude A and time duration T is used, the energy of the received signal is $E_r = \frac{A^2T}{2}$ and the SNR becomes :

$$SNR = \frac{A^2T}{N_p} \tag{2.4}$$

From equation (2.4), increasing the SNR of the imaging system can be achieved by either increasing the pulse amplitude or the pulse duration. However, the Food and Drug Administration (FDA) imposes strict safety limitations on the peak pressure and transmitted intensity of ultrasound systems to ensure patient safety. These regulations are in place to prevent potential tissue damage due to excessive acoustic exposure. Specifically, for diagnostic ultrasound applications, the FDA limits the spatial peak temporal average (I_{SPTA}) to 720 mW/cm^2 and the spatial peak pulse average (I_{SPPA}) to less than 240 W/cm^2 [7]. Additionally, the potential for tissue damage and cavitation is taken into consideration by restricting the peak negative pressure. Furthermore, probe and tissue heating must be monitored. These two safety concerns are controlled by the Mechanical Index (MI) and the Thermal Index (TI), respectively.

The MI often reflects the potential bioeffects, such as cavitation due to mechanical disruption, which is proportional to the transmitted waveform voltage. It is given by:

$$MI = \frac{p^-}{C_{MI}\sqrt{f_0}} \tag{2.5}$$

where p^- is the peak rarefaction pressure in MPa, C_{MI} is a constant, and f_0 is the center frequency of the ultrasound in MHz.

The TI provides information on possible probe or tissue damage resulting from overheating due to ultrasound absorption. It can be calculated as follows:

$$TI = \frac{W_p}{W_{deg}} \tag{2.6}$$

where W_p is the power emitted by the ultrasound transducer and W_{deg} is the estimated power required to raise the tissue temperature by 1°C.

In diagnostic medical ultrasound, typical values for the MI range from 0.004 to 1.7. However, when using a short pulse, increasing the amplitude of the pulse to enhance the SNR can increase the peak negative pressure, potentially causing the MI values to exceed safety limits. Consequently, once these MI safety limits are reached, the only viable method to further increase the SNR is by extending the pulse duration rather than the amplitude. Nevertheless, increasing the pulse duration reduces the axial resolution. Coded excitation offers a solution to this trade-off by enhancing the SNR without compromising resolution.

2.2 Coded Excitation

2.2.1 Basic theory

The SNR is proportional to the amount of transmitted energy. To increase the SNR, longer excitation pulses may be used; however, increasing the pulse duration severely affects axial resolution. Coded excitation is a technique commonly used to increase transmitted energy. Initially introduced for radar systems [150] and later applied to ultrasound imaging [151, 152], this technique involves transmitting long modulated waveforms into the medium. These modulated waveforms have the advantage of having a long duration without decreasing the bandwidth compared to non-modulated waveforms. However, even with the preservation of large bandwidth, the resolution would still be compromised. To preserve resolution, a pulse compression step is used in reception to compress the energy, thereby increasing the SNR without affecting resolution (Figure 2.3).

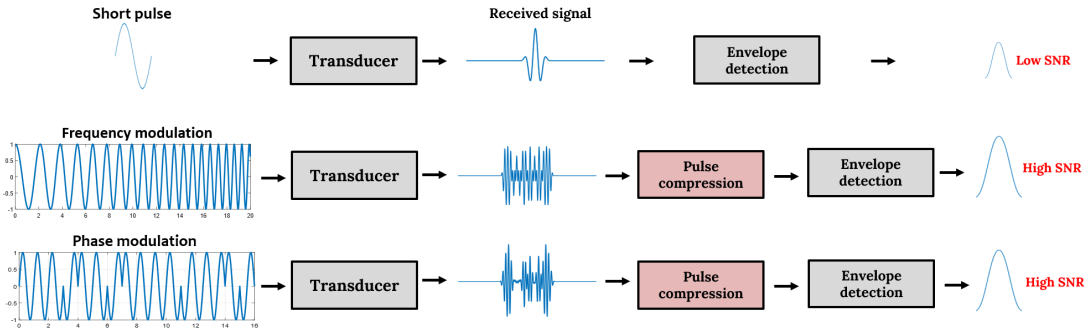

Figure 2.3: A diagram highlighting a comparison between non coded and coded excitations. A pulse compression step is required when using long modulated sequences to improve the SNR while preserving the axial resolution.

Various methods have been proposed in the literature for pulse compression. The most commonly used approach is the matched filter, developed after the Second World War to optimize target detection in radar systems [153]. It provides a solution to the problem

of finding a linear time-invariant filter that maximizes the SNR at the receiver output in the presence of white Gaussian noise. Assuming $e(t)$ is the long modulated excitation waveform, the matched filter is designed with an impulse response $h(t)$ that maximizes the SNR by correlating the received signal with a time-reversed and conjugated version of the transmitted pulse:

$$h(t) = e^*(-T + t) \tag{2.7}$$

where $e^*(t)$ is the complex conjugate of $e(t)$, and T is the duration of the waveform.

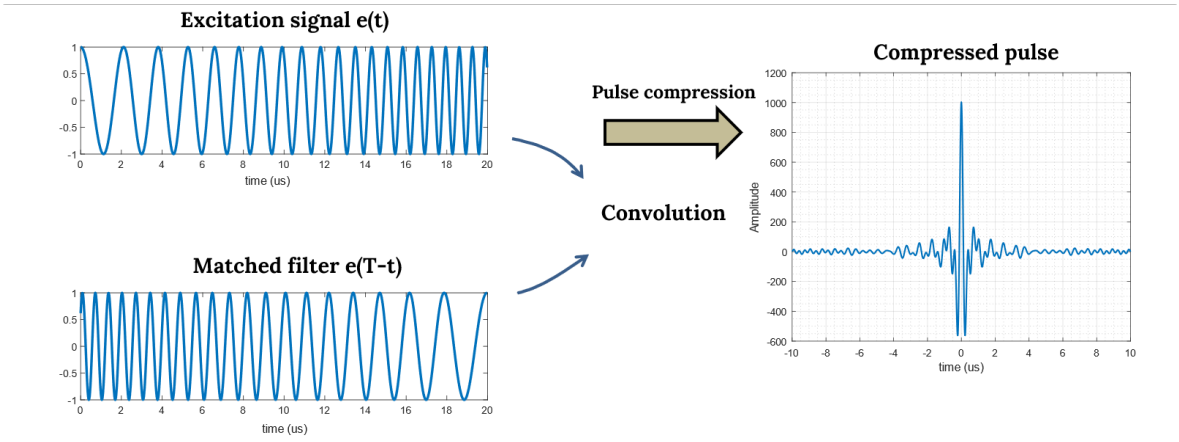

Figure 2.4: A diagram highlighting the pulse compression operation by matched filtering.

The output of the matched filter is obtained by convolving the received RF signals with the matched filter impulse response (Figure 2.4). The result of the compression will have a peak at the corresponding time delay of the reflected signal. As a consequence the matched filter corresponds to the auto-correlation of the excitation waveform. The SNR gain (gSNR) obtained as a result of the matched filter operation is equal to the time-bandwidth (TB) product of the transmitted waveform. For an ideal linear propagation medium, this improvement is quantified by [154]:

$$gSNR = 10 \log_{10}(TB) \tag{2.8}$$

where T is the duration of the transmitted waveform and B is the bandwidth.

2.2.2 Literature review

In the literature, various coded excitation schemes have been proposed in medical ultrasound imaging and can be divided into two categories: frequency modulated schemes and phase modulated schemes.

For frequency-modulated schemes, the most popular technique is using linear frequency-modulated (LFM) chirps [155–158]. In a linear chirp, the instantaneous frequency changes linearly over time, allowing a linear sweep of the entire bandwidth of the transducer. The two crucial parameters of a chirp are its duration and the swept bandwidth. These parameters significantly influence the chirp signal's performance, affecting both resolution and SNR enhancement. A study on the parameter optimization of chirps transmission in

ultrasound imaging can be found in [159]. LFM chirps have been widely used to increase the SNR in STA imaging. They were introduced for the first time as a coded excitation method for ultrasound imaging to increase the SNR of STA imaging and a theroretical SNR gain of 15-20 dB was obtained [151, 152]. It was also used to improve the frame rate of STA imaging by dividing the signal duration into multiple parts and sweeping the available bandwidth with different slopes for each part [160, 161]. In [162, 163], narrow-band LFM waveforms have been designed and assigned to different transducer elements for simultaneous STA transmission, optimizing the use of frequency division. In [164], an LFM chirp was used to enhance the sensitivity of power Doppler ultrasound for imaging meniscus vascularization with plane wave imaging. Furthermore, LFM chirps have been applied to increase the SNR of sparse arrays for 3D ultrasound imaging, achieving an 11 dB SNR gain for spectral Doppler measurements [136].

Despite their proven effectiveness in increasing SNR, LFM chirps suffer from compression sidelobes that can be as high as -13 dB, severely affecting image contrast. Mismatched filtering can reduce the compression sidelobes level to around -40 dB, but this comes at the cost of degrading axial resolution [157]. These sidelobes can still be visible in images because ultrasound imaging typically requires a dynamic range of 60 dB or more. Moreover, chirp waveforms are not well-suited for simultaneous sequence transmission, particularly in STA imaging. Dividing the bandwidth across several chirps can allow for simultaneous transmission, but this is limited by the orthogonality of the chirp waveforms and the restricted bandwidth available in ultrasound imaging [161].

Different from frequency-modulated schemes, phase modulation schemes use binary sequences that are modulated by a pulse at the central frequency of the transducer, where a $+1$ corresponds to a 0° phase and a -1 corresponds to a 180° phase. Binary sequences are primarily characterized by the sidelobes level of their correlation function. One of the most well-known binary sequences is the Barker code [165], characterized by the low autocorrelation sidelobes bounded to unity, offering the best performance in terms of sidelobes among binary sequences of the same length. Barker codes have been used in ultrasound imaging to increase the SNR, mostly in single transmit modulation sequences. Applications include ophthalmological ultrasound imaging [166], blood flow imaging [167, 168], and transcranial imaging [169, 170]. However, their application is still limited due to the presence of axial sidelobes; even though they are bounded to unity, in ultrasound imaging, they can produce artifacts up to 20 dB. The sidelobes can be decreased by using an inverse filtering approach for decoding the signals, but this comes at the expense of a loss in SNR [168]. Moreover, only seven Barker codes exist, with lengths ranging from 2 to 13 bits, which restricts their use in applications requiring diverse sequences. Compounding can be used to create Barker codes longer than 13 bits; however, this increases the level of autocorrelation sidelobes [171, 172].

Another popular binary sequence used in medical ultrasound is the complementary Golay code, introduced by Marcel Golay for his works on infrared spectrometry [173, 174] and has been extensively used in ultrasound imaging [175–181]. These codes consist of two binary sequences of the same length N. The autocorrelation functions of the two sequences have sidelobes with the same level but opposite signs. Summing the compressed signals results in an autocorrelation with a peak magnitude of $2N$ and suppressed sidelobes. A study on the properties of Golay codes can be found in [182]. Since two sequences are used to suppress the axial sidelobes, two different transmit events are required to transmit

each sequence separately, unlike Barker codes, where a single modulated transmit is used. However, the necessity for two separate successive transmissions results in a reduction of the imaging frame rate by a factor of two.

Alternatively, spatial coding methods such as Hadamard encoding can be used to increase the SNR [183–185]. Hadamard encoding was first introduced to enhance the SNR of STA imaging [183]. With this encoding method, instead of single-element STA transmission, all elements transmit simultaneously, each weighted by a coefficient from the Hadamard matrix. The received signals from all transmissions are collected and decoded. Due to the orthogonality of the Hadamard matrix, the contributions from each element can be separated using a decoding process based on addition and subtraction operations to retrieve the conventional STA dataset with higher SNR. The decoding process involves multiplying the received signal matrix by the inverse of the Hadamard matrix. Hadamard encoding has also been shown to improve the SNR and penetration depth of plane wave imaging without sacrificing the frame rate [186]. As stated in the literature , this type of encoding can also be combined with modulated sequences such as LFM chirps and Golay codes to further increase the SNR [187].

2.3 Proposed coded imaging scheme

Although the previously cited coded excitation methods increase the SNR in ultrasound imaging, they suffer from drawbacks such as the presence of axial sidelobes and a reduction in imaging frame rate. We propose a new coded excitation method combined with STA imaging to enhance the SNR of 2D sparse arrays for 3D ultrasound imaging. In its conventional form, STA imaging uses only a single element in each transmission event, with the backscattered echoes recorded by all elements to form a low-resolution image. After all transmissions, these low-resolution images are coherently compounded to create a high-resolution image. To maximize the benefits of STA imaging, instead of transmitting with a single element, we propose to use all elements of the array in transmission, each emitting a coded waveform. In reception, the echoes are decoded to retrieve the STA dataset with a high SNR.

The proposed coded excitation scheme is based on *complete complementary codes* (CCC) that we use to increases the SNR of sparse arrays while suppressing the axial sidelobes and maintaining the frame rate unchanged. The CCC are often referred to as $(\mathrm{M}, \mathrm{N}, \mathrm{L})$-CCC since they are composed of M sets of N binary sequences of length L (i.e., the number of symbols in each sequence is fixed to L). They were proposed for the first time by Suehiro et al. [188] as an extension of the complementary sets proposed in [189] by reaching the upper bound limit (i.e. $\mathrm{M} \leq \mathrm{N}$). As it will be further discussed, reaching this upper bound is of particular interest for US imaging as it minimizes the number of required firing. Indeed, these CCC evolved from the Golay codes by, (1) extending the number of sequences in each set (from two to N), and (2) extending the number of sets (from one to M). Thus, they have the advantages that the sum of the auto-correlations of sequences in each set is zero except for zero shift (i.e., delta impulse) and the sum of cross-correlations of sequences at the same index between any two distinct sets is zero for all shifts. However, the $(\mathrm{N}, \mathrm{N}, \mathrm{N}^2)$-CCC that they proposed in [188] using N-Shift cross-orthogonal sequences were relatively long (N^2). Interestingly, this construction was later improved by the authors of [190] to construct $(\mathrm{M}, \mathrm{N}, \mathrm{MN})$-CCC and $(\mathrm{N}, \mathrm{N}, \mathrm{MN})$-CCC with

($M, N \in Z^+$; $M \leq N$). Hence, the required number of symbols in the sequences decreased from N^2 to MN, and it was even further reduced to MN/P with a method for generating (N, N, MN/P)-CCC with ($M, N, P \in Z^+$; $M, P \leq N$) [191]. A review paper analyzing the applications of CCC can be found in [192]. For ultrasound imaging, having CCC with shorter sequences offers the possibility to transmit shorter excitation signals. Because of their ideal correlation properties, CCC codes have been extensively applied in Code-Division Multiple Access (CDMA) [193–195] and Multiple-input multiple-output (MIMO) [196–198] systems. To my knowledge, this work is the first implementation of CCC in medical ultrasound. I also believe that they are well adapted for 3D ultrasound imaging with sparse arrays, since they offer the possibility of transmitting with all the elements while using STA beamforming. Although, using conventional focused transmission with sparse arrays gives better SNR than conventional STA, the number of transmissions required to reconstruct the 3D volume is quite large since a focused transmission event is required for each volume line.

2.3.1 Mathematical framework

Let $\boldsymbol{s_1} = (s_1(1), s_1(2), ..., s_1(L))$ and $\boldsymbol{s_2} = (s_2(1), s_2(2), ..., s_2(L))$ be two sequences of length L, where each symbol can be $+1$ or -1. The discrete aperiodic correlation function is defined as follows on $\tau \in [1 - L, L - 1]$:

$$R_{\boldsymbol{s_1},\boldsymbol{s_2}}(\tau) = \sum_{t=-\infty}^{+\infty} s_1(t) s_2(t+\tau)^*, \tag{2.9}$$

where $s_2(t+\tau)^*$ denotes the complex conjugate of $s_2(t+\tau)$. If $\boldsymbol{s_1} \neq \boldsymbol{s_2}$, equation (2.9) is called the cross-correlation function of $\boldsymbol{s_1}$ and $\boldsymbol{s_2}$ and, if $\boldsymbol{s_1} = \boldsymbol{s_2} = \boldsymbol{s}$, it is the auto-correlation function denoted by $R_s(\tau)$ and $E_s = R_s(0)$ is called the energy of $\boldsymbol{s}$.

Letting $\mathcal{C}_1 = [\boldsymbol{s}_{1,1}, \boldsymbol{s}_{1,2}, ..., \boldsymbol{s}_{1,N}]$ and $\mathcal{C}_2 = [\boldsymbol{s}_{2,1}, \boldsymbol{s}_{2,2}, ..., \boldsymbol{s}_{2,N}]$ be two indexed sets of N sequences of length L. Each set is called an (N, L)-sequence set. The correlation between the two (N, L)-sequence set is defined by the following sum :

$$\mathcal{R}_{\mathcal{C}_1,\mathcal{C}_2}(\tau) = \sum_{n=1}^{N} R_{\boldsymbol{s}_{1,n},\boldsymbol{s}_{2,n}}(\tau). \tag{2.10}$$

If $\mathcal{C}_1 = \mathcal{C}_2$ then equation (2) sums the N auto-correlations of sequences of the same set; otherwise, if $\mathcal{C}_1 \neq \mathcal{C}_2$ it sums the N cross-correlations between sequences with the same index n in the two sets.

An (N, L)-Complementary set $\mathcal{C}_i$ is defined as an (N, L)-sequence set whose auto-correlation sum $\mathcal{R}_{\mathcal{C}_i}(\tau)$, is zero except for the zero shift :

$$\mathcal{R}_{\mathcal{C}_i}(\tau) = E_{\mathcal{C}_i} \delta(\tau) \tag{2.11}$$

Where $E_{\mathcal{C}_i}$ is the energy of $\mathcal{C}_i$ and $\delta(\tau)$ is the *Kronecker's delta function*.

A collection of M (N, L)-sequencesets $\mathcal{C} = [\mathcal{C}_1, \mathcal{C}_2, ..., \mathcal{C}_M]$ represent a (M, N, L)-sequencefamily with family size M subject to $M \leq N$. A (M, N, L)-sequence family $\mathcal{C}$ is called a *Complete Complementary Code* (CCC) denoted by (M, N, L)-CCC if the two following conditions are satisfied :

1. For every $i \in [1, \mathrm{M}]$, we have :

$$\mathcal{R}_{\mathcal{C}_i}(\tau) = E_{\mathcal{C}_i}\delta(\tau) \tag{2.12}$$

2. For every i, $j \in [1, \mathrm{M}]$, $i \neq j$:

$$\mathcal{R}_{\mathcal{C}_i,\mathcal{C}_j}(\tau) = 0 \tag{2.13}$$

The first condition implies that the sum of the auto-correlations in each sequence set is zero except for the zero shift where it equals $E_{\mathcal{C}_i}$. This means that each sequence set $\mathcal{C}_i$ must be an (N, L)-Complementary set. The second condition implies that, given any two different sets, the sum of the cross-correlations between sequences at the same index is zero at all shifts. In this case, the two sets are then called, cross-complementary sets. Consequently, an $(\mathrm{M}, \mathrm{N}, \mathrm{L})$-sequence family is called $(\mathrm{M}, \mathrm{N}, \mathrm{L})$-CCC, if all the M sets are (N, L)-Complementary set and any distinct pair of which are cross complementary sets.

For example, if $\mathrm{M} = 2$, $\mathrm{N} = 2$ and $\mathrm{L} = 4$ the corresponding $(2, 2, 4)$-CCC $\mathcal{C} = (\mathcal{C}_1, \mathcal{C}_2) = ((\boldsymbol{s}_{1,1}, \boldsymbol{s}_{1,2}), (\boldsymbol{s}_{2,1}, \boldsymbol{s}_{2,2}))$ is given by :

$$\begin{aligned} \boldsymbol{s}_{1,1} &= (+\,+\,+\,-) \quad \boldsymbol{s}_{1,2} = (+\,-\,+\,+) \\ \boldsymbol{s}_{2,1} &= (+\,+\,-\,+) \quad \boldsymbol{s}_{2,2} = (+\,-\,-\,-) \end{aligned}$$

Where $+$ denotes $+1$ and $-$ denotes -1. Then the auto-correlation sum of $\mathcal{C}_1$ and the auto-correlation sum of $\mathcal{C}_2$ are :

$$\begin{aligned} \mathcal{R}_{\mathcal{C}_1}(\tau) &= R_{\boldsymbol{s}_{1,1}}(\tau) + R_{\boldsymbol{s}_{1,2}}(\tau) \\ &= (-1, 0, 1, 4, 1, 0, -1) + (1, 0, -1, 4, -1, 0, 1) \\ &= (0, 0, 0, 8, 0, 0, 0) \end{aligned}$$

$$\begin{aligned} \mathcal{R}_{\mathcal{C}_2}(\tau) &= R_{\boldsymbol{s}_{2,1}}(\tau) + R_{\boldsymbol{s}_{2,2}}(\tau) \\ &= (1, 0, -1, 4, -1, 0, 1) + (-1, 0, 1, 4, 1, 0, -1) \\ &= (0, 0, 0, 8, 0, 0, 0) \end{aligned}$$

And the sum of cross-correlation between $\mathcal{C}_1$ and $\mathcal{C}_2$ is given by :

$$\begin{aligned} \mathcal{R}_{\mathcal{C}_1,\mathcal{C}_2}(\tau) &= R_{\boldsymbol{s}_{1,1},\boldsymbol{s}_{2,1}}(\tau) + R_{\boldsymbol{s}_{1,2},\boldsymbol{s}_{2,2}}(\tau) \\ &= (-1, 0, 3, 0, 1, 0, 1) + (1, 0, -3, 0, -1, 0, -1) \\ &= (0, 0, 0, 0, 0, 0, 0) \end{aligned}$$

A graphical representation of the auto-correlation sum and cross-correlation are represented in Figure 2.5.

2.3.2 Construction of CCC

Because of their interesting correlation properties, many researchers have tried to develop CCC construction algorithms. Among those methods, we have decided to use the one proposed in [191] to generate an $(\mathrm{N}, \mathrm{N}, \mathrm{MN/P})$-CCC because it allows generating CCC

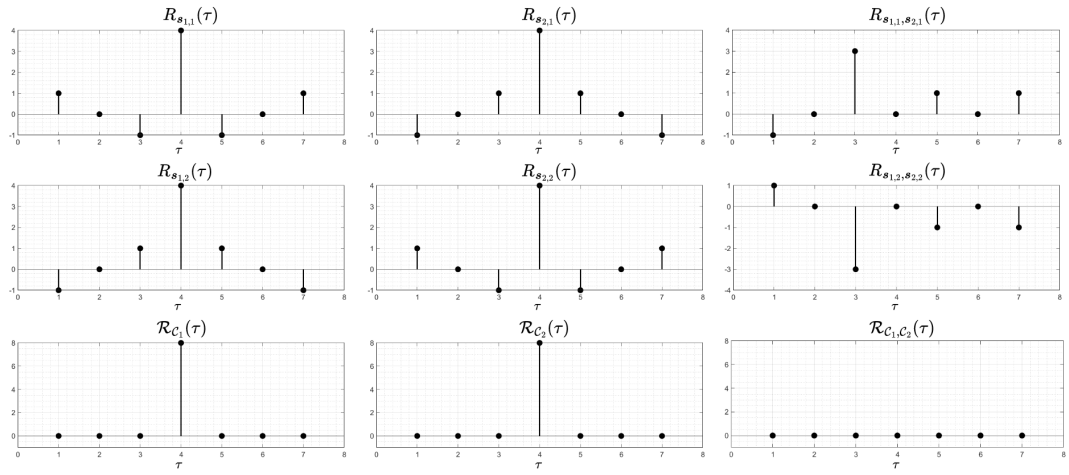

Figure 2.5: Plots of the auto-correlation sums $\mathcal{R}_{\mathcal{C}_2}(\tau)$ and $\mathcal{R}_{\mathcal{C}_1}(\tau)$ along with the cross correlation sum $\mathcal{R}_{\mathcal{C}_1,\mathcal{C}_2}(\tau)$.

with short sequences length which befenical for avoiding large blind zone areas, which is advantageous in avoiding large blind zones.

Following [191], *unitary matrices* are used in order to generate a $(\mathrm{N}, \mathrm{N}, \mathrm{MN/P})$-CCC. An $\mathrm{N} \times \mathrm{N}$ matrix U_{N} is called *unitary* if it satisfies $U_{\mathrm{N}} U_{\mathrm{N}}^t = U_{\mathrm{N}}^t U_{\mathrm{N}} = I_{\mathrm{N}}$, where I_{N} denotes the $\mathrm{N} \times \mathrm{N}$ identity matrix. A good candidate for the *unitary matrix* is the *Hadamard matrix* which is the one used in this work. Additionally, P and M values must be chosen so that P divide into N, and M divide into N/P. After choosing the M, N and P values for the desired $(\mathrm{N}, \mathrm{N}, \mathrm{MN/P})$-CCC, the construction method is divided into four steps :

1. We split column-wise a *Hadamard matrix* of size $\mathrm{N/P} \times \mathrm{N/P}$ into $\mathrm{N/(MP)}$ matrices $A_1, A_2, \ldots, A_{\mathrm{N/(MP)}}$ of size $\mathrm{N/P} \times \mathrm{M}$ (A_i is the i-th block of M columns of A).

2. Then, a matrix $\mathcal{D}$ of size $\mathrm{N^2/P^2} \times \mathrm{MN/P}$ can be constructed as follows :

$$\mathcal{D} = \begin{bmatrix} (B \otimes C).Diag(Vec(A_1)) \\ (B \otimes C).Diag(Vec(A_2)) \\ \vdots \\ (B \otimes C).Diag(Vec(A_{N/MP})) \end{bmatrix} \tag{2.14}$$

   with, B and C two *Hadamard matrices* of respective size $\mathrm{M}\times\mathrm{M}$ and $\mathrm{N/P}\times\mathrm{N/P}$ and with, $\otimes$ the Kronecker product, . the matrix multiplication, $Diag$ the diagonal operator and Vec the vectorization operator.

3. We construct a new matrix $\mathcal{H}$ of size $\mathrm{N/P}\times\mathrm{MN^2/P^2}$ by concatenating the rows of the i-th block of N/P rows of $\mathcal{D}$ to form a single row $\mathcal{H}_i$ of $\mathcal{H}$:

$$\mathcal{H} = \begin{bmatrix} \mathcal{H}_1 \\ \mathcal{H}_2 \\ . \\ \mathcal{H}_{N/P} \end{bmatrix}, \mathcal{H}_i = [d_{1+r_i}, d_{2+r_i}, ..., d_{N/P+r_i}] \tag{2.15}$$

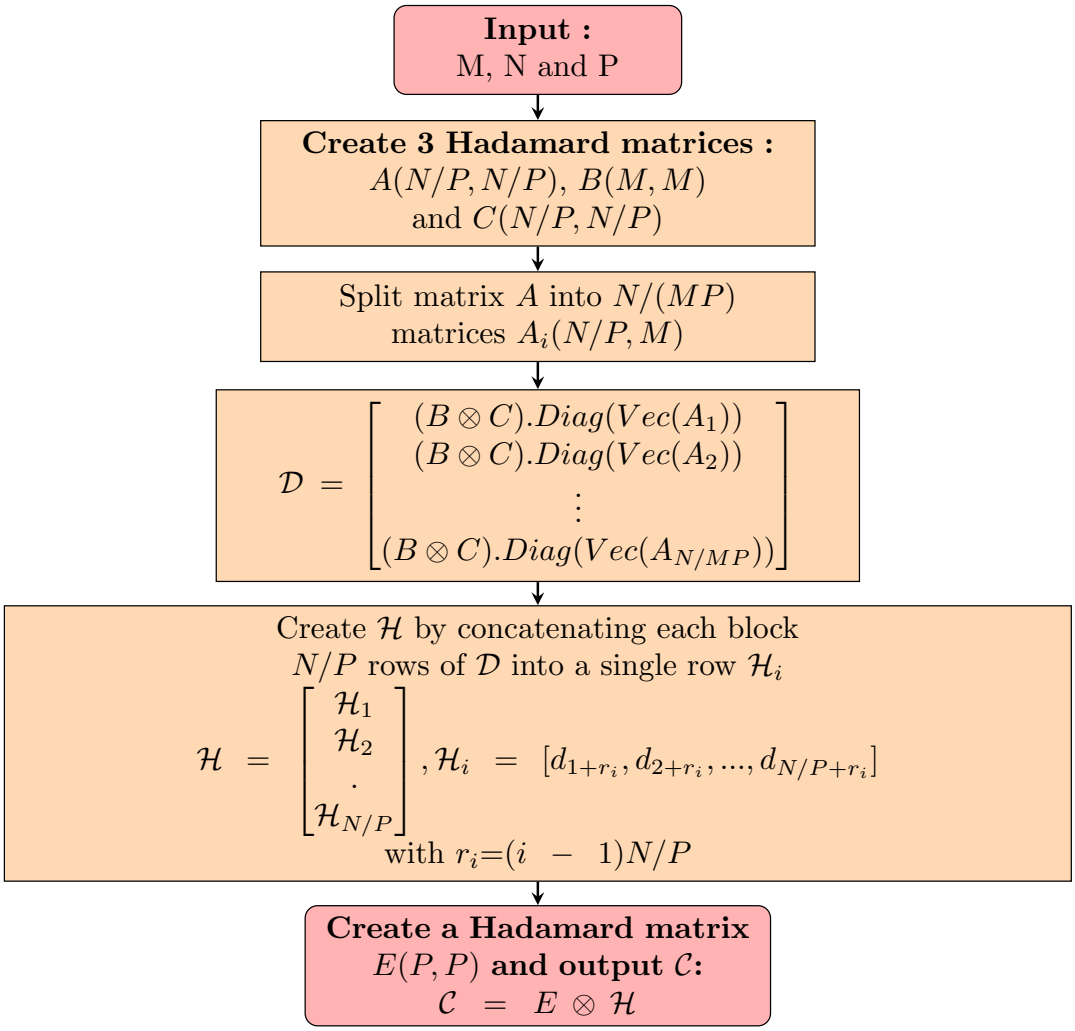

Figure 2.6: Flowchart of the $(N, N, MN/P)$-CCC generation process.

where an indexed d is a single row of $\mathcal{D}$ and $r_i = (i-1)N/P$ with $i \in [1, N/P]$.

4. The final (N, N, MN/P)-CCC matrix $\mathcal{C}$ of size N×MN²/P is obtained with the Kronecker product of a *Hadamard matrix* E of size P×P with matrix $\mathcal{H}$:

$$\mathcal{C} = E \otimes \mathcal{H} = \begin{bmatrix} \mathcal{C}_1 \\ \mathcal{C}_2 \\ . \\ \mathcal{C}_N \end{bmatrix} = \begin{bmatrix} \boldsymbol{s}_{1,1} & \boldsymbol{s}_{1,2} & ... & \boldsymbol{s}_{1,N} \\ \boldsymbol{s}_{2,1} & \boldsymbol{s}_{2,2} & ... & \boldsymbol{s}_{2,N} \\ . & . & ... & . \\ \boldsymbol{s}_{N,1} & \boldsymbol{s}_{N,2} & ... & \boldsymbol{s}_{N,N} \end{bmatrix} \tag{2.16}$$

Where each of the N rows of the $\mathcal{C}$ matrix corresponds to a set of N sequences and each entry $\boldsymbol{s}_{i,j}$ is a sequence of length MN/P. Figure 2.6 represent a flowchart that summarize the generation process $(N, N, MN/P)$-CCC. The code used to generate CCC, including test functions was implemented in MATLAB and is provided publicly through a github repository (https://github.com/Tamraoui/CompleteComplementaryCodes).

2.4 Imaging method

2.4.1 Principal of CCC STA

To increase the SNR of 3D sparse arrays, a CCC excitation scheme is applied to the STA imaging sequence (CCC STA). Unlike Conventional STA, all the elements transmit simultaneously N times. Instead of transmitting the same short pulse, each i-th element transmits the sequence $\boldsymbol{s}_{i,j}$ during the j-th transmission event. So, in this coded excitation scheme, all the elements transmit a different sequence picked from the (N, N, MN/P)-CCC matrix $\mathcal{C}$ at each transmission event. After the N transmissions and thanks to the ideal auto-correlation and cross-correlation properties of CCC, the received signals are then decoded without any mutual interference. Hence, we recover the full STA dataset as would yield the standard STA approach under the assumption of an ideal, linear, propagation medium, but with much higher SNR.

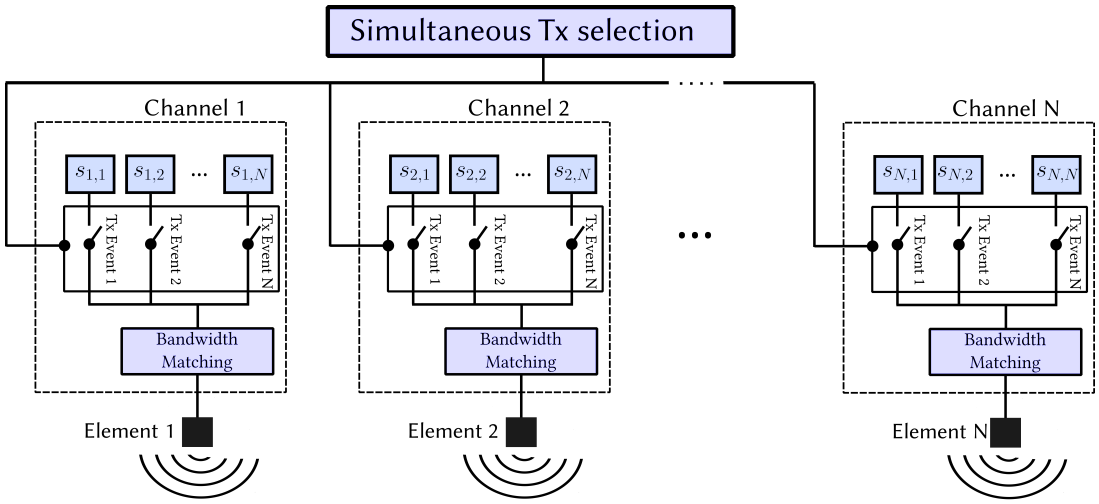

Figure 2.7: CCC STA imaging transmission scheme using (N, N, MN/P)-CCC.

More precisely, equation (2.16) shows that $\mathcal{C}$ is composed of N sequence sets $\mathcal{C}_i$ with $i = (1, 2, \ldots, N)$. And each set $\mathcal{C}_i$ contains N binary sequences $\boldsymbol{s}_{i,j}$ with $j = (1, 2, ..., N)$. Each binary sequence has length MN/P. In the proposed coded excitation scheme each of the N transducer elements will be assigned a sequence set $\mathcal{C}_i$, thus element 1 is assigned the set $\mathcal{C}_1$, element 2 is assigned the set $\mathcal{C}_2$ and so on. Since each set is composed of N sequences, to make profit of the ideal auto-correlation and cross-correlation properties of CCC, all the sequences need to be transmitted requiring N transmit events to be made. In each transmit event, all the elements are activated simultaneously and each one of them will transmit the sequence $\boldsymbol{s}_{i,j}$ from the assigned set $\mathcal{C}_i$.

As depicted in Figure 2.7, the transmission scheme works as follows: in transmit event 1, element 1 transmits the sequence $\boldsymbol{s}_{1,1}$, element 2 transmits the sequence $\boldsymbol{s}_{2,1}$ and element N transmits the sequence $\boldsymbol{s}_{\mathrm{N},1}$. In the second transmit event, element 1 transmits the sequence $\boldsymbol{s}_{1,2}$, element 2 transmits the sequence $\boldsymbol{s}_{2,2}$ and element N transmits the sequence $\boldsymbol{s}_{\mathrm{N},2}$. And the transmit events continue until the last transmit event during which element 1 transmits the sequence $\boldsymbol{s}_{1,\mathrm{N}}$, element 2 transmits the sequence $\boldsymbol{s}_{2,\mathrm{N}}$ and element N transmits the sequence $\boldsymbol{s}_{\mathrm{N,N}}$.

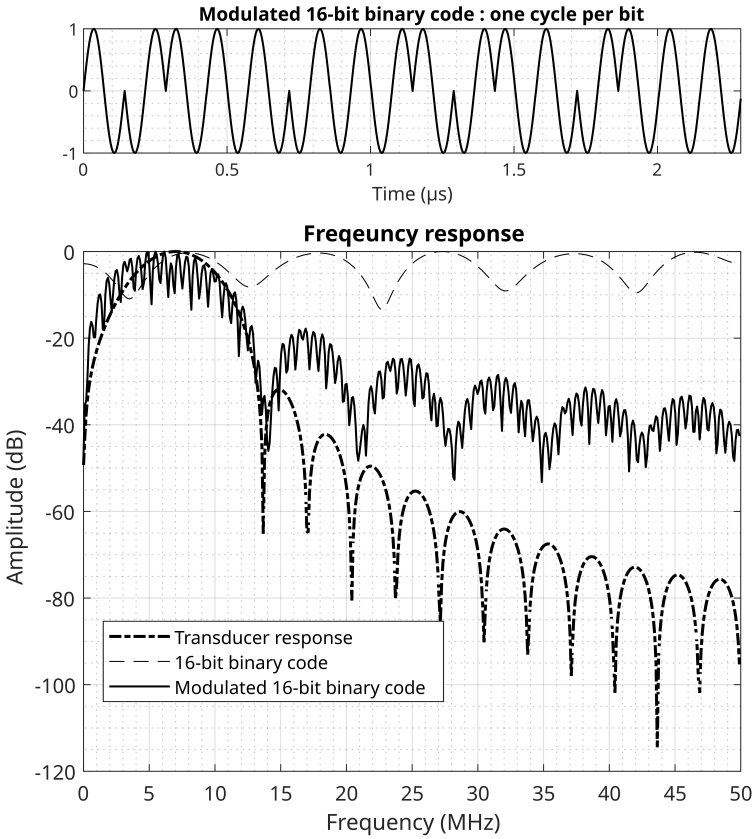

Figure 2.8: Modulation of a 16-bit binary code (top) and its corresponding frequency response plotted against the response of the transducer and an unmodulated binary code (bottom).

In practice, the binary $(\mathrm{N}, \mathrm{N}, \mathrm{MN}/\mathrm{P})$-CCC sequences can not be used directly to drive the transducer because the spectrum of a binary code is much wider than the transducer bandwidth. Instead of a direct sequence transmission, a modulation is applied to make good use of the transducer bandwidth and maximize the transmitted energy: before transmission, a binary phase shift keying (BPSK) modulation is used to make each sequence bandwidth match the bandwidth of the transducer. In (BPSK) each code bit is modulated with a pulse at the central frequency of the transducer with an integer number of cycles and a phase of 0° for a $+1$ bit and a phase of 180° for a -1 bit. The modulation and its effect on the spectrum of a 16-bit binary $(1, -1, 1, 1, 1, -1, -1, -1, 1, -1, 1, 1, -1, 1, 1, 1)$ sequence is illustrated in Figure 2.8. Each bit is modulated by a 1 cycle sine wave at a frequency of 7.2MHz.

In order to recover the STA dataset as if the elements had transmitted one at a time, the received RF signals (recall that all elements are receiving after each transmission events) need to be decoded. In order to recover the data corresponding to a transmission by the i-th element, the RF signals received after each simultaneous transmit event are correlated with the sequence $\boldsymbol{s}_{i,j}$ that was transmitted by the i-th element in that specific event (the j-th) and then summed together. Figure 2.9 illustrates the decoding process for the i-th element. In other words, the received RF signals after each transmit event are correlated with the sequences of the set $\mathcal{C}_i$ assigned to the i-th element. And since the sum of the auto-correlations of sequences in same set is a delta function (equation (2.12)) and

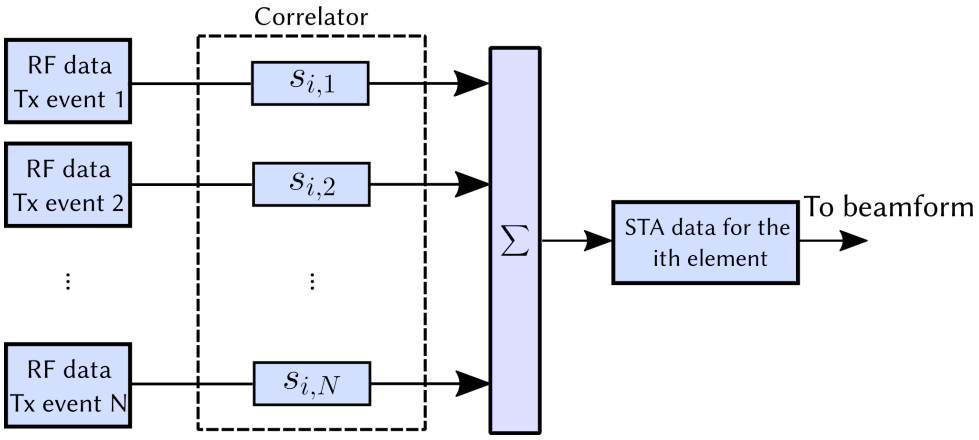

Figure 2.9: Decoding block of the received RF data to retrieve the STA dataset.

the sum of the cross-correlations between each two sets is zero (equation (2.13)), summing the correlated RF signals will ensure that only the echoes from the i-th transmitter are kept with higher SNR and the RF signals from all the other transmitters are eliminated when ideal, linear, propagation medium is considered.

2.4.2 Optimization of the decoding operation

In CCC STA, all N elements of an array transmit different codes simultaneously across N transmit events. However, decoding the resulting STA dataset traditionally involves a computationally intensive procedure that requires N^2 correlation operations, which restricts the practical use of CCC in real-time applications. To address this challenge, we propose a novel method for real-time decoding of CCC STA that reduces the number of correlations from N^2 to $2N$. This approach takes advantage of a unique property of CCC STA transmission events. Specifically, although CCC consists of N sets of N binary codes, during transmission, elements with odd and even indices transmit the same code but with opposite signs (e.g., +1 becomes -1 and vice versa). For instance, if element 1 transmits code $s_{1,1}$, then element 3 will transmit code $s_{3,1} = -s_{1,1}$. Our proposed method leverages this property by using simple addition and subtraction operations in an initial decoding step to partition the received dataset into pairs based on even and odd transmit events. Following this, $2N$ correlation operations are performed on these pairs to individually recover their decoded datasets. The straightforward nature of the mathematical operations in our decoding approach enables efficient GPU acceleration. We have implemented this method on a GPU to enhance processing speed. An example illustrating the decoding operation for $N = 8$ CCC STA transmissions is provided in Figure 2.10.

2.4.3 Simulation and experimental setups

The proposed CCC STA was validated trough simuation and experimental studies on a optimized sparse array. The array was optimized on the 1024-element multiplex Vermon matrix probe (central frequency 7.2 MHz). The matrix array is composed of four blocks of 8x32 elements, separated by three blank rows to facilitate electrical connections. Mul-

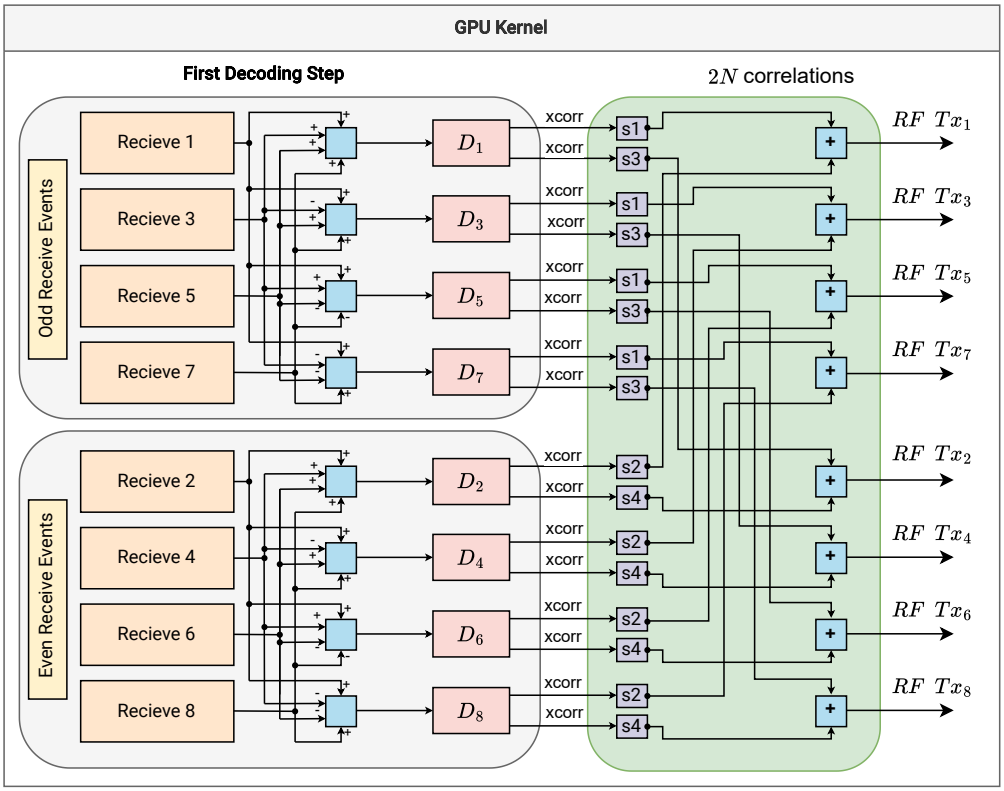

Figure 2.10: A diagram illustrating the GPU kernel of the optimized decoding operation of (N, N, MN/P)-CCC *when N=8.*

tiplexing is achieved by connecting elements with the same index in the four blocks to the same ultrasound beamforming channel (Figure 2.11 (a)). Due to this multiplexing constraint, elements connected to the same channel can be activated simultaneously during transmission but will receive the same transmit delay. However, in reception, only one of the elements can be used to receive the echoes. When optimizing a sparse array on this matrix probe, this multiplexing constraint must be taken into consideration. We have addressed this limitation by adapting previous work conducted by our group [108], optimizing a 256-element sparse array on the 1024-element multiplex Vermon array by incorporating the multiplexing constraint into a simulated annealing optimization process.

To identify the optimal 256-element sparse array among all elements of the multiplexed array, the simulated annealing algorithm was employed with a multi-depth cost function. This cost function evaluates the radiated beam pattern at multiple depths—30 mm, 40 mm (focal depth), and 50 mm—instead of considering only the focal depth. In simulated annealing, state transitions are typically governed by a communication mechanism. In our approach, this mechanism was adapted to account for the multiplexing constraint of the Vermon array, controlling channels instead of individual elements. To satisfy the multiplexing constraint during the optimization process, where each channel can connect to four specific elements, a new array configuration candidate is generated by randomly selecting a channel, determining which element it is connected to in the current state, and then randomly reconnecting it to one of the other three available elements.

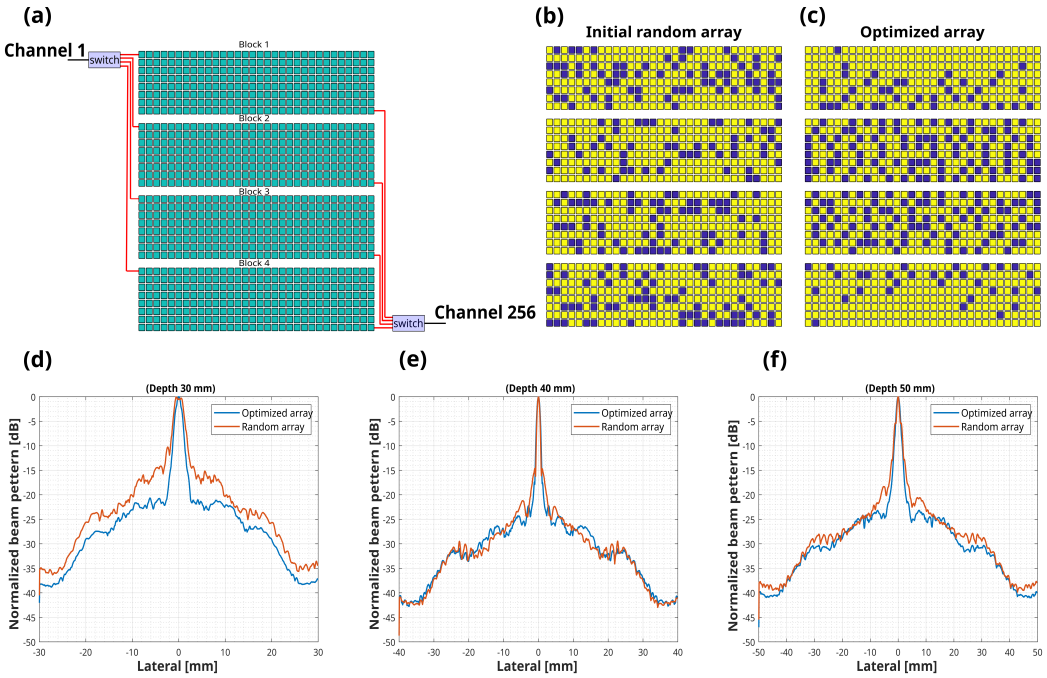

Figure 2.11: Optimization of the multiplex Vermon matrix array (a). The layout of the initial random array (b), the layout of the optimized array, the beam patterns comparison at Depth 30mm (d), 40mm and 50 mm.

Figure 2.11 (b) and (c) show the layout of the initial random array used as input to the simulated annealing algorithm and the final optimized array respectively. The layout of the optimized array confirms that the multiplexing constraint has been respected and only one of the elements controlled by the same channel is activated. Figure 2.11 (d), (e) and (f) shows a beam pattern comparison of the two arrays. At the focal depth (40 mm) the sidelobe level of the optimized array has improved by 6.35 dB compared to the random array thanks to the concentration of the elements to the center of the array. This concentration however, reduces the footprint of the array which in turns degrades slightly the resolution by 0.22mm. Out of the focal depth, the sidelobe level has improved by 10.14 and 3.05 dB and the resolution by 0.74 and 0.32 mm at depth 30 and 50 mm respectively, which highlights the advantage of using a multi-depth cost function. This optimized array will be used for simulations and experiments with the proposed coded imaging scheme.

For simulation, a summary of the parameters of the simulated array are listed in Table 2.1. Simulations were carried out using the Field II ultrasound simulation software [118,119]. Frequency dependent attenuation was not accounted to avoid the computational load associated with it during simulations and in order to test the codes in ideal propagations conditions and to verify the theoretically expected SNR gains. As mentioned in [175], frequency dependent attenuation affects the received signals and the output of the matched filter does not correspond to the autocorrelation of the coded sequence which in turns reduces the SNR gains. Even if not tested in this study, many approaches have been considered in order to reduce the effect of attenuation during decoding [199–201]. The performance of the proposed CCC STA in increasing the SNR was compared with the Hadamard STA, Chirp STA, Golay STA, combined Hadamard-Chirp STA and combined

Hadamard-Golay STA. An additive white Gaussian noise was generated according to the bandwidth of the transducer using a pass-band filter and added to Conventional STA RF data. The same type and level of noise was also added to the RF data simulated with the coded excitation techniques before decoding and beamforming.

Table 2.1: Sparse array parameters

Parameter	Value	Unit
Central frequency	7.2	MHz
Aperture size	10	mm
Number of elements	256	-
Element shape	square	-
Element width	300	μm
Element height	300	μm

For a 256 elements sparse array, an $(256, 256, 16)$-CCC was generated. The generated CCC contains 256 sets, each one is composed of 256 binary sequences. Each element of the array is assigned a set of 256 sequences. To make profit of the ideal auto-correlation and cross-correlation properties of CCC during decoding, all the sequences need to be transmitted, therefore, 256 transmissions are required. Binary sequences of lengths 16 bits were used during the simulations. The sequences were used to modulate a 1 cycle sine wave at the central frequency of the transducer with a sampling frequency of 100MHz giving excitation signals of duration 2.22μs.

Conventional STA was simulated using a short pulse of 0.13μs. The pulse is a 1 cycle sine wave at the central frequency of the transducer. For Hadamard STA a 256 order *Hadamard matrix* is required. In each transmission, elements are excited with the same short pulse used for Conventional STA but weighted by a coefficient from the corresponding row of the *Hadamard matrix*. The inverse of the *Hadamard matrix* is used for decoding. For Chirp STA, a chirp with a duration of 2.22μs tapered by a Tukey window was used. The swept bandwidth of the chirp was chosen as 6.41MHz which is slightly larger than the transducer's bandwidth (6.17MHz) as suggested by [156], in order to minimize the effect of the convolution between the transducer impulse response and the excitation signal. The compression was done using a mismatched filter with Hanning window to reduce side-lobes level. For Golay STA, a complementary Golay pair of length 16bits was generated which will give two complementary excitation signals of same duration (2.22μs) after modulation. The same parameters of the Hadamard STA, Chirp STA and Golay STA codes were used for combined Hadamard-Chirp STA and Hadamard-Golay STA.

The performance of the coded excitation methods was quantified using the *peak signal to noise ratio* (PSNR) and the *contrast ratio* (CR). To assess the PSNR, a *point spread functions* (PSFs) phantom composed of 5 scatterers was simulated. The scatterers have been axially placed in front of the transducer starting from 20mm to 60mm by a step of 10mm between each two scatterers Figure 2.12 (a). The PSNR was then calculated on the beamformed images using the following formula [202]:

$$(\text{PSNR})_{dB} = 20log_{10}(\frac{max(S_{scat})}{\sigma_{noise}}) \tag{2.17}$$

Where $max(S_{scat})$ is the peak signal of the scatterer and σ_{noise} is the root mean square (RMS) of the noise at the same depth as the scatterer.

To assess the CR, a 3D phantom of size 10×10×40mm (xyz) containing three anechoic spherical inclusions placed at depths of $30mm$,$40mm$ and $50mm$ with a diameter of $5mm$ was used. In order to have a fully developed speckle 10 scatterers per resolution cell was chosen with Gaussian distributed amplitudes. The contrast was then calculated as follows :

$$(\mathrm{CR})_{dB} = 20log_{10}(\frac{\mu_{cyst}}{\mu_{bck}}) \tag{2.18}$$

Where μ_{cyst} and μ_{bck} are the mean image intensities respectively inside the cyst and in the surrounding background.

For the experimental setup, the Vantage-256 research scanner (Verasonics, Inc., Kirkland, WA, USA) was used to drive the sparse array. The optimized sparse array was implemented by selecting 256 elements from the gridded layout of a 2-D Vermon matrix array (Vermon S.A., Tours, France). The array has a central frequency of 7.2 MHz, a pitch of 300 μm, and an element size of 300 × 300 μm. The same sequence and parameters that were used for simulation were also implemented in the experimental setup. The evaluation of the implemented sequences in terms of 3D imaging was conducted using a commercial tissue-mimicking phantom (Gammex Sono410 SCG) with the same simulation imaging metrics. The Arbitrary Waveform Generation Toolbox (ArbWave Toolbox in Verasonics), provided by the Vantage scanner was used to implement the different coded excitation methods.

2.5 Results

2.5.1 Simulation results

The simulated PSFs images obtained with Conventional STA and the different coded excitation techniques are shown in Figure 2.12. The images represent the XZ (Y=0) slices extracted from the 3D reconstructed volume. The 5 scatterers have been axially placed in front of the transducer starting from 20mm to 60mm by a step of 10mm between each two scatterers. All of the images are displayed with a dynamic range of −60dB and were simulated with a noise condition of −30dB SNR on the RF data. This noise condition does not seem realistic, especially that only one element is used during each transmit event in the case of Conventional STA, but it was chosen to make sure that the noise will be visible in the images to demonstrate the ability of CCC STA to increase the SNR compared to the other coded excitation methods. Additionally, it aligns with the experimental results obtained using the optimized sparse array, which will be presented later.

The image produced by the Conventional STA is very noisy which makes it difficult to differentiate the scatterers from the noise because of the low SNR of sparse arrays. Compared to the Conventional STA image, it is visually clear that all the coded excitation schemes lowered the noise in the images, confirming the ability of coded excitation to improve the SNR. In spite of a strong noise reduction, the background remains slightly noisy in the cases of a first group made of those three methods: Hadamard STA, Chirp STA and (to a lower extent) Golay STA. On the contrary, a higher SNR improvement is achieved in

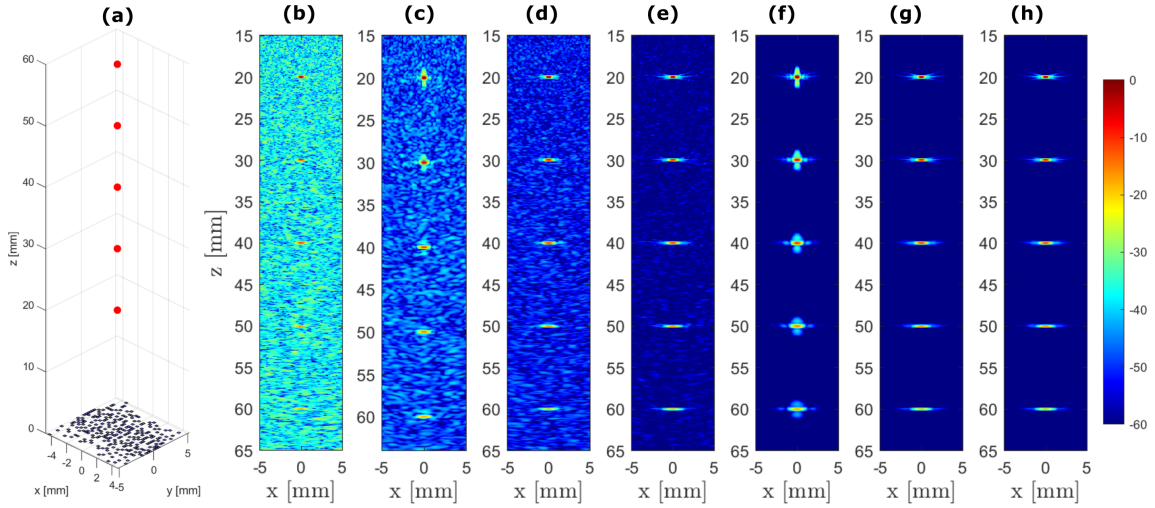

Figure 2.12: Simulated beamformed PSFs (a) images obtained with (b) Conventional STA*, (c)* Hadamard STA*, (d)* Chirp STA*, (e)* Golay STA*, (f)* Hadamard-Chirp STA*, (g)* Hadamard-Golay STA*, (h) proposed* CCC STA*.*

the case of this second group of methods (Hadamard-Chirp STA, Hadamard-Golay STA, CCC STA): the noise seems to be completely removed from the images. As expected with chirps, in Figure 2.12 (f), axial side lobes are visible especially around the scatterers close to the transducer, however, they are less visible around scatterers at greater distance due to depth-dependent attenuation, but they are still around -40 dB compared to the amplitude of the main lobe.

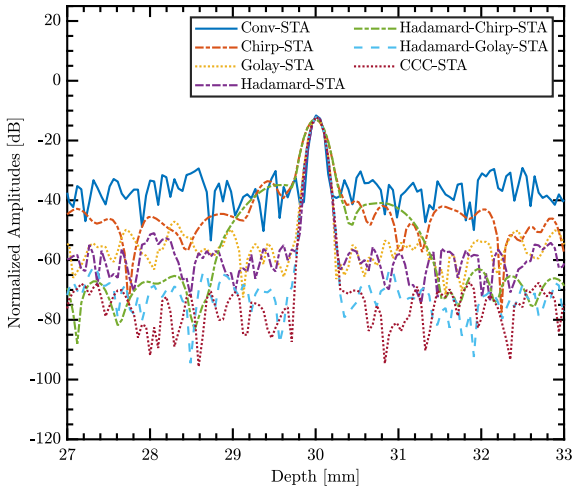

Figure 2.13: Axial line plots of the scatterer at the depth of 30mm *for the different excitation schemes.*

To further demonstrate the results, Figure 2.13 shows an axial line plot over the scatterer placed at 30 mm. As previously, the compared coded excitation techniques cluster into two groups: with the first group (Hadamard STA, Chirp STA, Golay STA), the background noise level higher than -60dB along with the one of Conventional STA. With

Table 2.2: Comparison of the −6dB *axial resolution computed on the scatterer at depth* 30mm. *Values are given in* mm

	−6dB Axial resolution
Conventional STA	0.16
Hadamard STA	0.16
Chirp STA	0.26
Golay STA	0.17
Hadamard-Chirp STA	0.26
Hadamard-Golay STA	0.17
CCC STA	0.17

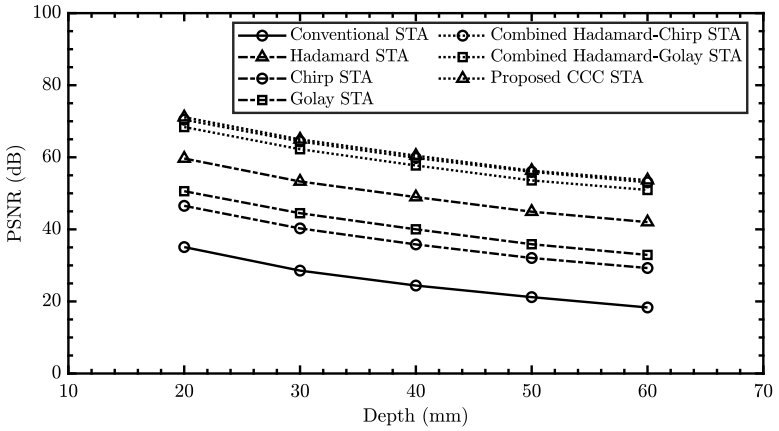

Figure 2.14: PSNR for the compared excitation schemes as a function of depth of the 5 scatterers.

the second group of methods (Hadamard-Chirp STA, Hadamard-Golay STA, CCC STA), the noise level is less that -60dB and thus not visibile in the images. Table 2.2 provides a comparison of FWHM axial resolution calculated on the 30 mm placed scatterer. In accordance with what can be visually seen in Figure 2.13, the table shows that compared to Conventional STA where an axial resolution of 0.16mm was obtained, Hadamard STA, Golay STA, Hadamard-Golay STA and CCC STA coded methods did not affect the axial resolution while a degradation has been observed in the case of Chirp STA and Hadamard-Chirp STA where a value of 0.26mm was obtained.

Furthermore, Figure 2.14 shows a comparison of the PSNRs computed on each of the 5 axially placed scatterers displayed in the images of Figure 2.12. When comparing to Conventional STA, the gain in SNR is constant as a function of depth regardless of the method used since frequency dependent attenuation was not considered. Again, we distinguish two groups of performing methods. On the one hand, Hadamard STA shows a gain of around 24dB, and both Chirp STA and Golay STA yield around 11dB and 15dB of SNR gain respectively. On the other hand, the Hadamard-Chirp STA and Hadamard-Golay STA reaches an SNR gain of 34.60dB and 40.29dB respectively and our proposed CCC STA achieves a 35.95dB SNR gain. In addition, Table 2.4 provides a summary of gSNR obtained by all the compared methods.

To assess the effect of coded excitation on the contrast, B-mode images of 3D cyst phantom were simulated with the different methods under a −20dB SNR noise condition

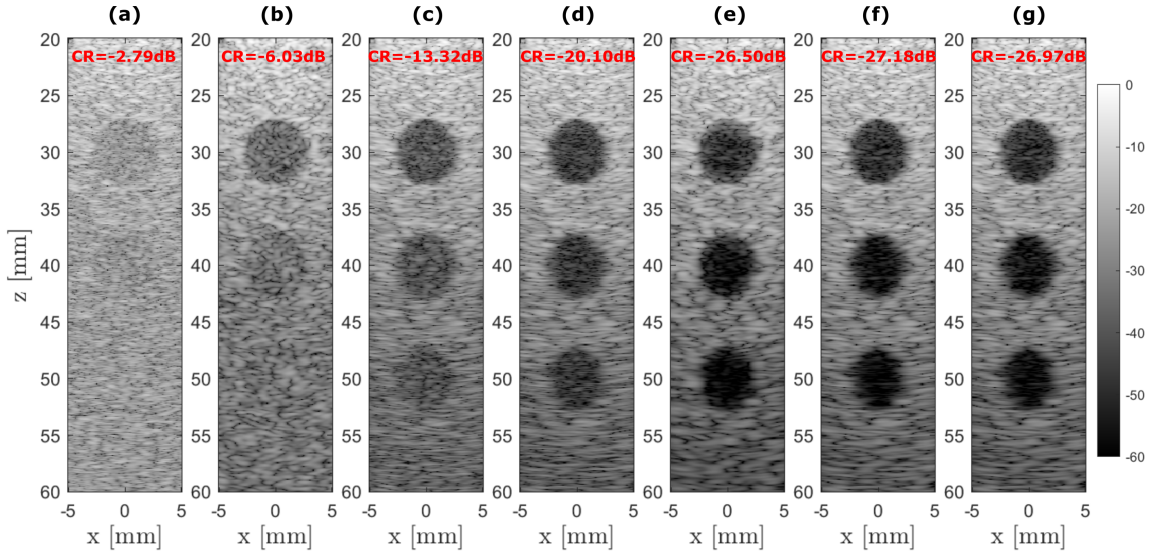

Figure 2.15: Simulated beamformed cyst phantom images obtained with (a) Conventional STA*, (b)* Hadamard STA*, (c)* Chirp STA*, (d)* Golay STA*, (e)* Hadamard-Chirp STA*, (f)* Hadamard-Golay STA*, (g) proposed* CCC STA*.*

Table 2.3: The Simulated gSNR and the expected theoretical gSNR obtained with the different coded excitation methods. Values are given in dB

Methods	**gPSNR**	**Theoretical gSNR**
Hadamard STA	23.56	24
Chirp STA	11.49	11.54
Golay STA	15.23	15.05
Hadamard-Chirp STA	34.60	35.62
Hadamard-Golay STA	40.29	39.13
CCC STA	35.95	36.12

on the RF data. We have chosen a different SNR condition for the cyst phantom compared to the PSFs phantom in order for the anechoic inclusion to be visible. The energy coming from all the scatterers of the cysts is very large compared to the PSFs phantom where we only have 5 scatterers and if the same SNR condition was chosen the quantity of noise would be important making the anechoic inclusion invisible. In Figure 2.15, slices in the XZ plane from the full 3D reconstructed volume are shown with a dynamic range of -60dB. It can be observed that the quality of the reconstructed images improves by using coded excitation compared to Conventional STA. The Conventional STA image is highly degraded by noise making it hard to differentiate the cyst from the background. In the case of Hadamard STA, Chirp STA and Golay STA, the quality of the images has been improved but noise is still present inside the anechoic inclusion because it has not been completely removed. However, the proposed CCC STA, Hadamard-Chirp STA and Hadamard-Golay STA achieve better images quality and the level of artifacts inside the anechoic inclusion has been highly reduced. The artifacts that are still present in the anechoic inclusions are related to the sidelobe level of the sparse array and cannot be removed by coded excitation.

These qualitative results are validated quantitatively by the computed CR values

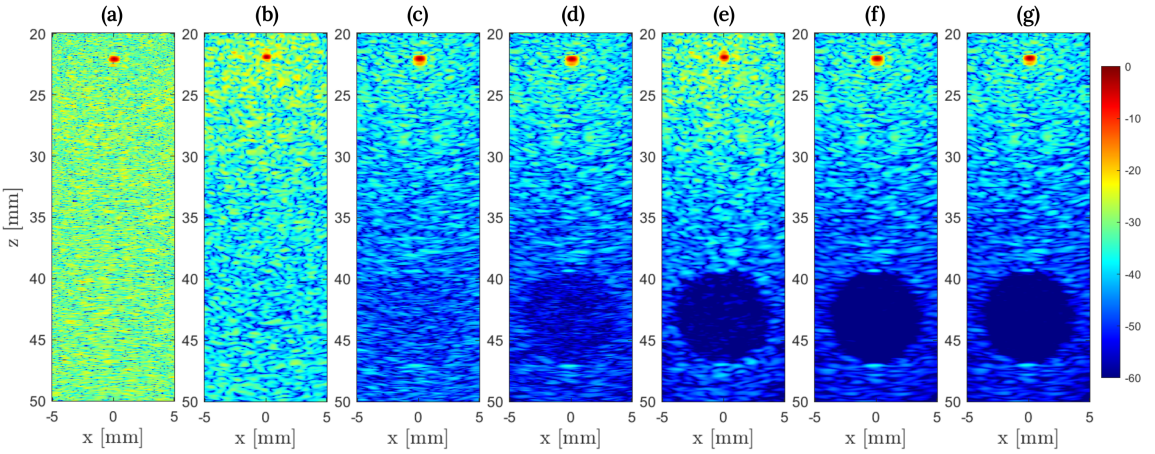

Figure 2.16: Experimental beamformed images on the phantom with Nylon wire obtained with (a) Conventional STA*, (b)* Hadamard STA*, (c)* Chirp STA*, (d)* Golay STA*, (e)* Hadamard-Chirp STA*, (f)* Hadamard-Golay STA*, (g) proposed* CCC STA*.*

reported in Figure 2.15. Conventional STA have the worst CR value compared to the other methods with a value of −2.79dB. Chirp STA, Golay STA and Hadamard STA achieve CR values of −6.03dB, −13.32dB and −20.10dB, respectively. Thanks to the high SNR gains, the proposed CCC STA, Hadamard-Chirp STA and Hadamard-Golay STA present a similar CR with a value around −27dB.

2.5.2 Experimental results

The experimental results on the tissue-mimicking phantom obtained with Conventional STA and various coded excitation techniques are shown in Figure 2.16. The scanned volume comprises a strongly reflecting scatterer represented by a nylon wire surrounded by tissue-mimicking speckle and an anechoic inclusion of 8 mm diameter. For this experiment, the voltage of the Verasonics system was set to 10 volts. The displayed images represent the XZ slice from the 3D beamformed volume and are displayed with a dynamic range of -60 dB.

From visual inspection, the experimental results are in concordance with the simulated results. The image obtained with Conventional STA is very noisy to the extent that the anechoic inclusion is not visible, indicating a very poor penetration depth. The penetration depth is improved by the use of coded excitation methods, with the extent of improvement varying by method. For the Chirp and Golay methods, the noise has been reduced, but not sufficiently to make the anechoic inclusion visible.

Hadamard STA, on the other hand, shows better performance, making the anechoic inclusion visible, although the noise level is still high and can be seen inside the inclusion. For Hadamard-Chirp STA, the SNR appears to be improved, although some noise artifacts are still present. The same performance observed in the simulation is achieved in the experimental study for Hadamard-Golay STA and the proposed CCC STA. The noise level is significantly reduced in the images obtained with these two methods, making the anechoic inclusion clearly visible and indicating a substantial improvement in SNR. Sidelobes artifacts associated with the sparse array are still present in the anechoic inclusion, but, thanks to the strongly reflecting scatterer the dynamic range of the image has shifted

making the artifacts invisible.

Table 2.4: The Experimental SNR and the gSNR obtained with the different coded excitation methods. Values are given in dB

Methods	**PSNR**	**gSNR**
Conventional STA	36.25	-
Chirp STA	44.82	8.57
Golay STA	54.48	18.22
Hadamard STA	60.48	24.22
Hadamard-Chirp STA	63.84	27.59
Hadamard-Golay STA	67.80	31.55
CCC STA	67.50	31.25

These visual observations were qualitatively validated by calculating the PSNR on the images shown in Figure 2.16. The maximum signal was measured on the nylon wire, and the RMS of the noise was calculated inside the anechoic inclusion. The results are represented in Table 2.4, along with the gSNR obtained by the coded excitation methods in comparison to Conventional STA.

In comparison to other coded excitation methods, Chirp STA presented the lowest SNR gain with a value of 8.57 dB. The highest SNR gains were obtained with Hadamard-Golay STA and the proposed CCC STA, both achieving gains of 31.55 dB and 31.25 dB, with a slight advantage to Hadamard-Golay STA at 31.55 dB. It is worth noting that all the coded excitation methods provided SNR gains lower than what is theoretically expected.

To better assess the increase in penetration depth associated with coded excitation, another experiment was conducted using the same coded excitation methods on a region of the tissue-mimicking phantom with three anechoic inclusions at depths of approximately 24 mm, 43 mm, and 63 mm. The Verasonics system voltage was set to 30V, the maximum recommended for the Vermon matrix array. The results are shown in Figure 2.17, highlighting the gain in penetration depth achieved with coded excitation.

Visual inspection of the images reveals that the top anechoic inclusion is visible with conventional STA and all the coded excitation methods. The second anechoic inclusion is not visible with conventional STA and is barely visible in the images obtained with Chirp STA and Golay STA. However, it is clearly visible for the rest of the coded excitation methods. The third and deepest anechoic inclusion is only visible with Hadamard-Chirp STA, Hadamard-Golay STA, and the proposed CCC STA.

These observations were quantitatively validated by computing the contrast for the three anechoic inclusions, as represented in Table 2.5. The contrast values for three anechoic inclusions were compared across the various coded excitation methods. For the first cyst, all coded excitation methods showed similar performance, with values around -15 dB, whereas Conventional STA had a noticeably lower contrast at -7.02 dB. For the second cyst, the advantage of coded excitation methods became more evident; Hadamard-based methods and the proposed CCC STA exhibited better contrast, with values around -15 dB compared to -1.49 dB for Conventional STA. For the third cyst, only Hadamard-Chirp STA, Hadamard-Golay STA, and the proposed CCC STA achieved higher penetration depths with significantly improved contrast values, around -12 dB to -10 dB, whereas Conventional STA showed very poor performance at -0.83 dB.

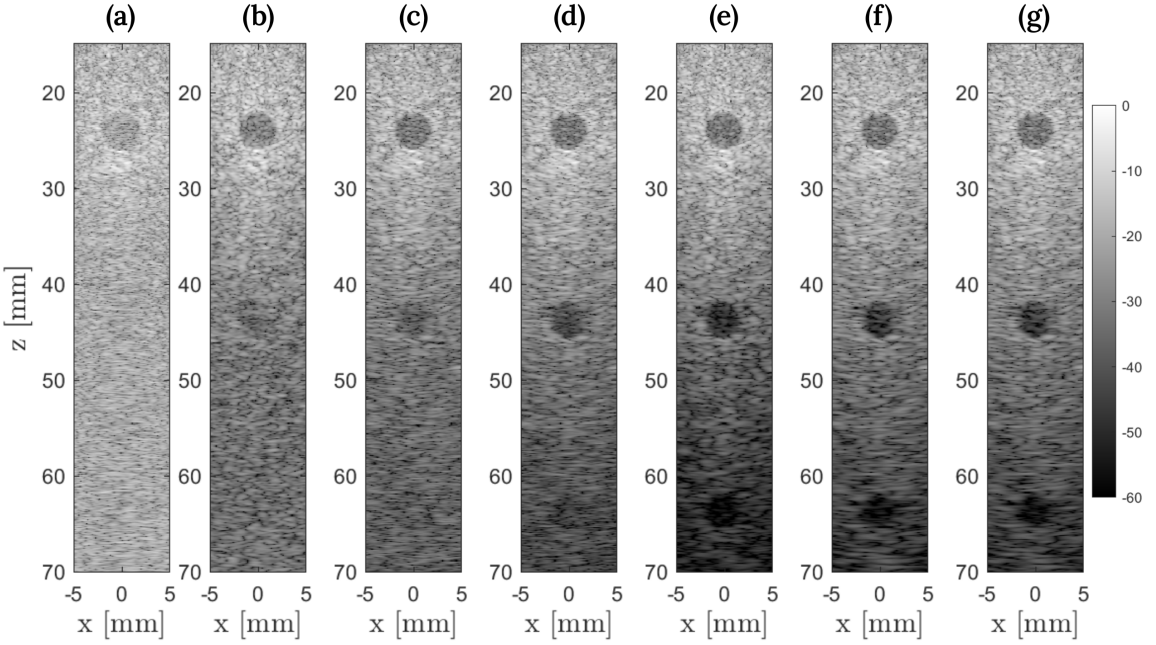

Figure 2.17: Experimental beamformed images on the phantom with three anechoic inclusions obtained with (a) Conventional STA*, (b)* Hadamard STA*, (c)* Chirp STA*, (d)* Golay STA*, (e)* Hadamard-Chirp STA*, (f)* Hadamard-Golay STA*, (g) proposed* CCC STA*.*

Table 2.5: Comparison of the contrast values for coded excitation methods across three anechoic inclusions. Values are given in dB

Method	**Top Cyst**	**Middle Cyst**	**Bottom Cyst**
Conventional STA	-7.02	-1.49	-0.83
Chirp STA	-13.58	-5.08	-1.33
Golay STA	-14.34	-9.04	-0.32
Hadamard STA	-15.57	-12.98	-4.21
Hadamard-Chirp STA	-15.31	-16.38	-10.28
Hadamard-Golay STA	-15.54	-15.46	-12.30
CCC STA	-15.52	-14.72	-11.95

2.6 Discussion

To our knowledge, this study is the first to use complete complementary codes (CCC) to increase SNR for sparse array 3D ultrasound imaging. We compared this approach with five well-known coded excitation schemes: Hadamard STA, Chirp STA, Golay STA, Hadamard-Chirp STA, and Hadamard-Golay STA. Great care was taken to ensure a fair comparison between the different techniques. First, excitation signals of the same duration were used for both simulations and experiments, with short pulses employed for Conventional STA and Hadamard STA as these methods lack a pulse compression step in reception. Second, the same noise level was added to the received RF signals before decoding in simulations. Noise was generated within the array bandwidth using a pass-band filter, resulting in a -30dB SNR for Conventional STA RF signals in PSFs phantom simulations, and -20dB for cyst phantom simulations. This same noise was then added to the RF signals of the other coded excitation techniques before decoding. For

the experimental study, the Verasonics system voltage was set to 10V for acquisitions on the phantom with the nylon wire and 30V for the phantom with only anechoic inclusions.

Theoretically, when comparing Conventional STA with Hadamard STA, an SNR gain of $10\log_{10}(N)$=$10\log_{10}(256)$=24dB is expected, where N is the number of transmissions. The simulation results from Table 2.3 and Figure 2.14 shows a gain around 23.56dB which is close to the theoretical value. The same trend was also observed in the case of Chirp STA, the expected SNR gain corresponds to the Time-Bandwidth product of the Chirp : $10\log_{10}(2.22 * 6.41) = 11.54$dB. From Table 2.3 it can be observed that the SNR gain for Chirp STA corresponds to what was expected.

When using Golay STA an SNR gain of 15.23dB is obtained that matches the theoretical expected value. In fact, the expected theoretical gain in SNR when using Golay codes is $10\log_{10}(N.L) = 10\log_{10}(2 * 16) = 15.05$dB , where $N = 2$ is the number of transmissions required to transmit the two Golay complementary codes, and $L = 16$ is the length of each code. For the Hadamard-Chirp STA, Hadamard-Golay STA, and our proposed CCC STA methods, instead of using only one element in each transmission event, all the elements are used to transmit a long duration waveform: this increases the acoustic energy delivered to the medium which explains the high SNR gains observed for this group of methods (Table 2.3). Theoretically, using the $(N, N, MN/P)$-CCC sequences, an SNR gain of $10\log_{10}(N.L) = 10\log_{10}(256 * 16) = 36.12$dB is expected, where $N = 256$ is the number of transmission and $L = 16$ is length of the binary sequences. This theoretical value is close to the 35.95dB gain reported in Table 2.3. Hadamard-Golay STA gives a SNR gain of 40.29dB which is around 3dB greater than the proposed CCC STA because the transmission events are doubled: this comes at the cost of frame rate divided by two. In a nutshell, the presented results demonstrates the SNR improvement offered by the simultaneous transmission of all the elements during each transmission event.

The experimental results, particularly the PSNR computed on images of the phantom with the nylon wire, corroborate the comparative of different coded excitation methods (Table 2.4). Similar to simulations results, Hadamard-Golay STA, Hadamard-Chirp STA, and CCC STA exhibit the highest SNR gains. However, the observed SNR gains are lower than the theoretical expectations (Table 2.4). The theoretical SNR gains are based on the assumption of an ideal linear propagation medium without frequency-dependent attenuation, which does not hold in practical ultrasound experiments. The propagation medium used is a commercial tissue-mimicking phantom, which is non-ideal and exhibits a frequency-dependent attenuation of 0.5 dB/[MHz cm]. Due to this attenuation, both the peak frequency (the frequency at which the spectral amplitude is highest) and the bandwidth of the received signal decrease with increasing depth. Consequently, the matched filter becomes less suitable for the received signal, leading to reduced SNR gains.

Moreover, one of the limitations of using Chirps in coded excitation is the degradation of the axial resolution and the presence of axial side-lobes. Usually the compressed chirps have axial side-lobes that severely affect the contrast, which can be as high as -13 dB. The axial side-lobes level was reduced by using a tapered chirp and a mismatched filter in compression at the price of degrading the axial resolution as shown in Figure 2.13 and Table 2.2 for Chirp STA and Hadamard-Chirp STA. The axial side-lobes have been reduced to around -40dB but the main-lobe is broader compared to the other techniques. Even if the axial side-lobes are reduced their presence is still observed in the B-mode cyst images as shown in Figure 2.12 (f). The artifacts inside the anechoic inclusion are more

important in the case of Chirp STA and Combined Hadamard-Chirp STA especially in the interface with background speckle as was observed in the simulation (Figure 2.15) and experimental (Figure 2.16 and 2.17) results. However, in the proposed CCC STA, the axial resolution is not affected since each bit of the sequences was modulated by a 1 cycle sine pulse which matches with the short pulse used for Conventional STA and Hadamard STA. The same thing can be said for Golay STA and Hadamard-Golay STA. Thanks to to the ideal auto-correlation and cross-correlation properties of the binary (N, N, MN/P)-CCC sequences that we used, no axial side lobes are present as can be seen in Figure 2.12 and Figure 2.16. As for the lateral grating lobes due to the sparse array, they were not affected by coded excitation and are still visible in the anechoic inclusions either for simulation or experimental results since they highly depend on the distribution of the sparse array elements.

Furthermore, the disadvantage of using Golay codes is that 512 transmission events are required rather than 256. In fact, Golay STA and combined Hadamard-Golay STA uses two complementary codes that need to be transmitted one after another by each element of the array. This is because the two codes are not orthogonal, so in order to avoid cross-correlation interference two separate transmissions are required. Transmitting the two codes separately helps yielding a better SNR but the frame rate is divided by two compared to Conventional STA. With the proposed CCC STA, each element of the array is assigned a set of sequences from the (N, N, MN/P)-CCC used. Because the sets are cross complementary, simultaneous transmissions of the sequences are possible without cross-correlation interference during decoding. This requires only 256 transmissions to be made to increase the SNR while keeping the frame rate unchanged.

The main goal of this work was to introduce the theory of the CCC STA and verify that the improvement of the SNR with the 2D sparse arrays matches with simulations and experimentations with the Verasonics system. The proposed method gives very similar SNR gains compared to combined Hadamard-Chirp STA and combined Hadamard-Golay STA with the advantages of a better resolution as reported in Table 2.2 and the absence of correlation artifacts over Hadamard-Chirp STA and the advantage of maintaining the same frame rate as Conventional STA over Hadamard-Golay STA.

When performing 3D US imaging with sparse arrays using conventional focused transmissions, multiple elements are used to transmit and steer a focused beam at a certain depth. Therefore, they provide a higher SNR than Conventional STA where only one element is used during each transmission. Additionally, the high impedance and low sensitivity of the small element of the array leads to a very low SNR especially in STA imaging. This explains the poor image quality in Figure 2.12 (b), 2.15 (a), 2.16 (a) and 2.17 (a). However, unlike Conventional STA, focused transmissions require a very large number of transmissions in order to reconstruct the full 3D volume since a focused transmission is required for each scanline (e.g. 100x100 scanlines = 10 000 transmissions). Additionally, the 3D images produced by conventional focused transmission methods have an optimal quality only at the depth of the transmit focus and degrades out of this depth. This highlights the advantages of using CCC with sparse arrays as they allow simultaneous transmission with all the elements which highly increases the SNR and produces 3D images focused in every voxel, while keeping the number of transmissions to be the same as in Conventional STA.

As with any coded excitation technique, one must take care of the sequence length used

in CCC STA. In fact, from one side using long sequences increases the energy transmitted to the medium which in turn increases the SNR gain. However, on the other side, the problem of increasing the sequence length is that during transmission the transducer cannot receive echoes until all the bits of the sequence have been transmitted, increasing the dead zone area unless different probes are used for transmission and reception [203–205]. The size of the dead zone area is proportional to half the duration of the transmitted waveform, defined as $c \cdot \frac{t_{wv}}{2}$, where $c = 1540\,\mathrm{m/s}$ is the speed of ultrasound, and t_{wv} is the duration of the transmitted waveform. In this study, we used (N, N, MN/P)-CCC sequences of length MN/P = 16 bits with a 7.2 MHz probe. This setup results in a transmitted waveform duration (t_{wv}) of 2.22 μs, leading to a blind zone area of 1.7 mm. This blind zone remains very small, especially considering that it is the deep tissue regions that typically experience low SNR, and these regions are usually well beyond this blind zone area. Thanks to the (N, N, MN/P)-CCC codes one can construct sequences with a shorter length (e.g, 8 bits or 4 bits) to adjust the ideally short dead zone. Moreover, for a fixed number of bits, the sequences can be made longer or shorter by adjusting the number of cycles (e.g. half cycle, two cycles, ...) in the modulating pulse without affecting the ideal correlation properties of the codes. Increasing the number of cycles will produce more SNR gain since the code's frequency response will better fit in the transducer bandwidth allowing more energy to be transferred, but at the expense of reducing a little bit the axial resolution [206].

As commonly known, the transducer's bandwidth plays a significant role in the implementation and effectiveness of coded excitation techniques in ultrasound imaging [206]. Sparse arrays based on PZT have been developed in previous studies but they suffer from a relatively low bandwidth. In [142], two prototype 2D spiral arrays were designed at center frequencies 2.5MHz (low-frequency) and 5MHz (high-frequency) based piezoelectric material built directly on printed circuit boards (PZT-on-PCB). The measured -3dB one-way bandwidth of the two probes were 0.6 ± 0.3MHz ($26\% \pm 13\%$) and 1.6 ± 0.6MHz ($32\% \pm 11\%$) respectively. While these bandwidths are sufficient for fundamental mode imaging, they are too low for contrast imaging at higher harmonics and are not optimal for coded excitation. The poor impedance matching between the PZT and the PCB resulted in significant reflections within the PZT, thereby reducing the bandwidth of the probes. Designing a new PZT based sparse array with higher bandwidth would be of great benefits to coded excitation as it will allow for more transmitted energy. Additionally, As proposed in [206], bit elongation can be used to make the bandwidth of the CCC codes narrower allowing it to be well contained within the transducer's bandwidth. As an alternative approach, CCC can be used with Capacitive Micromachined Ultrasound Transducers (CMUT) which are a promising alternative to PZT transducers as they typically exhibit a large bandwidth with comparable and even improved sensitivity, enabling the transmission and reception of ultrasound waves over a broader range of frequencies [207, 208].

Additionally, simultaneously transmitting long sequences with all the elements of the probe may raise patient safety issues as introduced in section 2.1. As stated in [209], the MI limit is often the dominating constraint when scanning the tissue with conventional focused beam. In our case, no focusing is performed which helps spreading the acoustic energy over the whole scanned tissue avoiding high peak pressures that can generate cavitation. The deriving voltage should also be decreased adequately with the length of the

sequences to avoid temperature rise in both tissue and piezoelectric elements while keeping the thermal index at safe limits.This might of course reduce the theoretically achievable SNR improvement. Moreover, using low frequency probes can also help reducing the ultrasound absorption near the probe, hence limiting the tissue overheat in those areas, as well as using other probe technologies such as CMUTs which are less subject to heating.

Another aspect to consider is the decoding step of the RF signals. To obtain the fully decoded STA dataset, the RF signals need to be correlated with each transmitted sequence. For (N, N, MN/P)-CCC, which have N sets of N sequences, the conventional decoding method requires N^2 correlations, which can be time-consuming for practical applications. In this work, using the (255,255,16)-CCC, $N^2 = 256^2 = 65536$ correlations are required. The RF data acquired with the Verasonics system took around 3 minutes for decoding with conventional methods implemented in the frequency domain. However, by using the proposed GPU-optimized decoding method, only $2N = 512$ correlations need to be performed. This took around $10ms$ on an RTX 3060 NVIDIA GPU, opening the way for real-time decoding of CCC STA.

Finally, thanks to their ideal correlation properties and flexible code length, the use of CCC is not only restricted to sparse arrays, it can be applied to 1D arrays for 2D ultrasound imaging and also non-destructive testing application.

2.7 Conclusion

In this chapter, I proposed a CCC STA excitation scheme based on Complete Complementary Codes (CCC), specifically (N, N, MN/P)-CCC. These codes are known for their ideal auto-correlation and cross-correlation properties. I validated CCC STA through simulations using Field II software and experiments with a sparse array optimized on an 8 MHz Vermon 2D matrix probe. The proposed CCC STA scheme was compared against five other coded excitation schemes: Hadamard STA, Chirp STA, Golay STA, Hadamard-Chirp STA, and Hadamard-Golay STA. Compared to conventional STA, simulations demonstrated that CCC STA increased the SNR of the sparse array by approximately 36.12 dB and enhanced image contrast by nearly 24.18 dB, all while maintaining axial resolution and the same number of transmissions. Experimental results further confirmed SNR and contrast gains of 31.25 dB and 10.94 dB, respectively. The comparison with other coded excitation schemes, such as Hadamard-Chirp STA and Hadamard-Golay STA, confirms the superior performance of CCC STA in boosting SNR while preserving axial resolution and frame rate.

Chapter 3

Coded Ultrafast 3D Ultrasound Imaging with 2D Sparse Arrays

In this chapter, I will implement 3D ultrafast ultrasound imaging using 2D sparse arrays. The primary objective is to enhance the SNR in ultrafast imaging with sparse arrays, thereby improving both the frame rate and penetration depth. To achieve this goal, I will explore two advanced imaging methods: plane wave imaging (PWI) and ultrafast synthetic transmit aperture (USTA) imaging using coded excitation. For plane wave imaging, I will use complete complementary codes (CCC) to increase the SNR and penetration depth. For ultrafast STA imaging, I will introduce mutually orthogonal complementary pairs (MOCPs) to increase the frame rate of conventional STA.

3.1 Ultrafast ultrasound imaging

In chapter 2 we introduced CCC STA to increase the SNR of 2D sparse arrays while keeping the number of transmissions same as conventional STA (256 transmissions). In the context of 3D ultrasound imaging, the proposed CCC STA offers a significant advantage over focused transmission by enabling higher frame rates along with improved SNR. With focused transmission, the number of transmissions—and thus the frame rate—is directly linked to the number of scan lines in the reconstructed volume. In contrast, with CCC STA, the number of transmissions is related to the number of elements in the ultrasound probe, not the number of scan lines. However, despite providing higher frame rates than conventional focused transmission, it can still be insufficient for certain applications, such as blood flow imaging, particularly when using sparse arrays, which have usual 256 elements.

For blood flow imaging, the frame rate is a critical parameter for correctly sampling the signal according to Shannon's criterion [186]. This criterion states that to accurately sample blood flow signals, the frame rate must be at least twice the maximum Doppler frequency of the signals. For example, to image the entire brain for blood flow in a rat, where the imaging depth should be around 15mm, using CCC STA (or conventional STA) with a sparse array would require 256 transmissions to reconstruct the full brain image, resulting in a frame rate of 200Hz. However, blood flow in a rat's brain, with a velocity of 2cm/s, corresponds to a Doppler frequency of approximately 190Hz. To meet Shannon's

criterion, the frame rate should be set at 380Hz, which cannot be achieved with CCC STA.

The only way to achieve the correct frame rate for accurately sampling the blood flow signals is by reducing the number of transmissions. In this section, I will present two methods that can be used to reduce the number of transmissions and thereby achieve high frame rate ultrasound imaging with 2D sparse arrays : plane wave imaging and ultrafast STA.

3.1.1 Plane wave imaging

Plane wave imaging, when initially introduced, relied on the transmission of a plane wave instead of a focused beam. This was achieved by transmitting simultaneously with all the elements of the probe at the same time with no delays. A single Plane Wave transmission was used to insonify the entire field of view, and the resulting backscattered echoes were reconstructed into an image [210]. With only one transmission required, plane wave imaging achieves frame rates of several thousand frames per second, depending on the imaging depth. However, because no transmit focusing occurs, the image quality is considerably compromised, particularly in terms of spatial resolution and contrast, when compared to conventional focused imaging. Coherent Plane Wave Compounding (CPWC) was introduced to enhance the image quality of ultrafast plane wave imaging [211,212]. Instead of transmitting a single plane wave, this technique involves sequentially transmitting several titled plane waves at varying angles. Each plane wave is tilted by adjusting the emission time by introducing a delay to each element. After each plane wave transmission, a low quality image is beamformed and by coherently summing all the low quality images of each transmission a final image with high quality is obtained.

This techniques enabled many developments for several applications. As an example, it has been reported that, thanks to its high frame rate, ultrafast Doppler imaging using CPWC, has significantly enhanced power Doppler sensitivity, with an increase by a factor of up to 30 when compared to conventional Doppler imaging [213]. This improvement is primarily due to the fact that all the image pixels are acquired simultaneously within a short period of time with a large temporal ensemble [214]. This ensured very high temporal correlation between frames which allows the use of a singular value decomposition (SVD) clutter filter which has proven to be very effective in discriminating relatively slow blood flow in small vessels from tissue motion [215, 216]. Nevertheless, CPWC introduces a trade-off between frame rate and image quality [211, 217]. Essentially, as the number of transmitted angles increases, the image quality improves. However, concurrently, this augmentation in image quality is accompanied by a reduction in frame rate.

Coded excitation can be used to increase the transmitted energy without compromising axial resolution [218]. This technique has been proven to substantially enhance the SNR of ultrasound imaging by spatially encoding the transmitted plane waves or using long modulated signals. In the spatial encoding category, a Multiplane Wave Imaging method using Hadamard encoding (MPWI-HD) has been proposed to enhance the SNR of ultrafast images without reducing the frame rate [219]. In this technique, multiple tilted plane waves are quasi-simultaneously transmitted using short pulses encoded by a Hadamard matrix. In reception, decoding is carried out using the inverse of the Hadamard matrix. The signals from each tilted PW are decoded through simple addition and subtraction

operations, resulting in an SNR increase of $10\log_{10}(N)$ compared to CPWC, where N represents the number of PW. MPWI-HD has been applied to ultrafast power Doppler imaging of the rat brain through the skull [220]. It has demonstrated enhanced sensitivity in Doppler imaging, enabling the detection of deeper blood vessels within the brain. Nevertheless, it is worth to note that improving the SNR with MPWI-HD remains tied to the number of transmitted plane waves.

Coded excitation techniques involving long modulated excitation signals have also been investigated to increase the SNR of plane wave imaging. These methods involve a decoding step using pulse compression to restore axial resolution while increasing the SNR. In [164], a linear frequency modulated chirp was used to enhance the sensitivity of an ultrasound arthroscopic probe used for imaging meniscus vascularization during surgery. In this approach, a chirp was used as an excitation signal for CPWC combined with a mismatched filter for pulse compression to reduce axial side-lobes. Although high SNR gains in power Doppler images were achieved compared to conventional CPWC and MPWI-HD, the mismatch filtering operation does not completely suppress axial side-lobes and comes at the cost of reducing axial resolution. In [169], a phase modulation sequence based on a compound Barker code was introduced to enhance sensitivity in Transcranial power Doppler imaging. Barker codes are known for their low axial side-lobes. To suppress axial side lobes, decoding was performed using an inverse filtering approach [168]. However, while axial side lobes can be suppressed, this approach reduces SNR gains. Moreover, only 7 barker codes exist with lengths ranging from 2 to 13 bits which can restrict their use in applications requiring a larger number of diverse sequences.

Although the previous cited methods have shown promise in enhancing plane wave imaging capabilities, they also exhibit notable limitations. One of these limitations is the challenge to increase the SNR without increasing the number of transmissions or introducing sidelobe artifacts in the images. In this context, we introduce a novel approach designed to address these shortcomings and increase the SNR of 3D plane wave imaging using sparse arrays which are known for their low SNR. We propose a new coded excitation scheme for 3D ultrafast plane wave imaging with sparse arrays. This approach is based on the Multi-Plane Wave Imaging method (MPWI) [219], but instead of spatial encoding using a Hadamard matrix, a phase modulated sequence will be used. Here we propose the use of Complete Complementary Codes (CCC) [191] that we have introduced to increase the SNR in 3D synthetic transmit aperture with a sparse 2D array in the previous chapter.

CCC are known for their ideal auto-correlation (i.e., delta impulse) and ideal cross-correlation function (i.e., zero at all shifts) which makes them ideal for simultaneous sequence transmission. Consequently, during decoding, no axial sidelobes are introduced, eliminating the need for mismatch filtering or inverse filtering. Thus, ultrafast plane wave imaging using Multi-Plane Wave Imaging with Complete Complementary Codes (MPWI-3C) benefits from the quasi-simultaneous transmission of plane waves of MPWI and from the ideal correlation properties of CCC to decode the received signals. Unlike the methods suggested in [164,169], which involves transmitting a single plane wave using a modulated signal during each transmission, MPWI-3C allows for the quasi-simultaneous transmission of multiple tilted plane waves, each transmitting a different phase modulated signal. By transmitting CCC sequences, the proposed method offers the possibility to increase the SNR by increasing the length of the sequence without increasing the number of transmissions. An SNR gain of $10\log_{10}(NL)$ compared to CPWC is obtained (with L

being the length of the sequences) which is higher than the gain obtained by MPWI-HD ($10\log_{10}(N)$).

3.1.2 Ultrafast STA

STA imaging is known for its ability to produce high-resolution images, often outperforming other techniques like focused transmission and plane wave imaging. However, for certain applications, such as blood flow imaging, the frame rate achieved by STA may not be sufficient to properly sample the signals. Another challenge with STA is its inherently low SNR due to the single-element transmissions, which can significantly impact image quality, especially when using sparse arrays that are already known for their low sensitivity.

The proposed CCC STA (Chapter 2) is a coded excitation scheme designed to increase the SNR of sparse arrays in STA imaging. However, it does not enhance the imaging frame rate, as it requires the same number of transmissions as conventional STA (256 transmissions). When properly implemented, coded excitation can also significantly increase the frame rate of STA imaging while enhancing the SNR. Ideally, to maximize the frame rate in STA, all elements should transmit simultaneously in a single transmission event, rather than sequentially. To separate the contribution of each individual element, these elements would need to transmit waveforms with ideal correlation properties: each waveform should have a perfect auto-correlation function (a delta impulse), and the cross-correlation between different elements' waveforms should be zero. This would allow the decoding of each element's contribution without mutual interference, retrieving the STA dataset with higher SNR from a single transmission event.

However, waveforms with these ideal correlation properties do not exist. Various coded excitation methods have been proposed in the literature to achieve Ultrafast STA (USTA) with minimal element interference. For instance, in [221], simultaneous transmission of multiple linear chirps using multiple elements was proposed. By dividing the signal duration into multiple segments and sweeping the available bandwidth with different slopes for each segment, different linear frequency-modulated (LFM) chirps were generated and assigned to different elements. However, due to the limited bandwidth in ultrasound systems, only five chirps could be generated, allowing for the simultaneous transmission of just five elements at a time, resulting in a frame rate of 156.25 Hz. Additionally, the created chirps exhibited high cross-correlation and interference.

Another approach proposed in [203], involved using long binary sequences to mitigate interference, leveraging the property that longer sequences have lower correlation sidelobes, thus reducing element interference. However, since the transducer elements cannot switch to receive mode until the entire waveform is transmitted, these long sequences create a large blind zone. To address this, the authors suggested using separate probes for transmission and reception.

A study in [222] proposed recovering the STA dataset with a single transmission by interleaving orthogonal Hadamard sequence bits with non-repeating zero intervals. The interleaving approach, based on Golomb rulers, helped reduce correlation sidelobes. However, these codes still produced large blind zones due to their extended nature through interleaving.

In this work, we introduce a novel approach for achieving USTA imaging using Mutu-

ally Orthogonal Complementary Pairs (MOCPs). Unlike the CCC used in the proposed CCC STA, MOCPs consist of N sets of binary sequences, with each set containing only two complementary sequences (pairs) of the same length L, whereas CCC sets contain N binary sequences. Because each MOCPs set has only two sequences, this method requires just two transmission events to retrieve the entire STA dataset, whereas CCC STA requires N transmission events.

In each of the two transmission events, all elements are activated simultaneously, with each element transmitting a sequence from an MOCPs set. The received signals are then decoded using matched filtering to reconstruct the complete STA dataset. This results in a significantly higher frame rate compared to both CCC STA and conventional STA.

3.2 Proposed coded imaging methods

3.2.1 MPWI-3C

While MPWI-HD can enhance the SNR of the recovered RF signals, it is important to note that the improvement is constrained by the order of the matrix [186]. With MPWI-3C, we free this constraint by replacing the Hadamard matrix by the CCC to create the binary sequences that will be transmitted. For MPWI-3C, $(N, N, MN/P)$-CCC binary sequences are used for quasi-simultaneous plane waves transmission, where N corresponds to the number of angles (equivalently, transmissions). Each set of the $(N, N, MN/P)$-CCC is then assigned to a tilted plane wave. During each transmission, N tilted angles are quasi-simultaneously transmitted with a short time delay τ. Each tilted angle transmits a different sequence from the corresponding $(N, N, MN/P)$-CCC set assigned to it.

As described in chapter 2, the binary $(N, N, MN/P)$-CCC sequences are not transmitted directly by the transducer because the spectrum of a binary code contains high harmonics that cannot be easily transmitted and received by the transducer. Instead of directly transmitting the binary sequences, they are used to modulate a base pulse $e(t)$ by oversampling the sequence and convolving it with the base pulse. $e(t)$ is usually a sinewave at the central frequency of the transducer with a phase of 0° for a +1 bit and a phase of 180° for a -1 bit. This modulation makes good use of the transducer bandwidth and maximizes the transmitted energy [175].

Following N transmissions, and leveraging the ideal auto-correlation and cross-correlation properties of CCC, the received signals are decoded without any interference between plane waves. This decoding process allows the separation of the contribution of each plane wave. Consequently, the ultrafast plane wave data set is recovered as if a single plane wave was transmitted during each transmission event, but with a significantly higher SNR. Under the assumption of an ideal linear propagating medium, the gain in SNR would be $10\log_{10}(NL)$, where L is the number of bits in the sequences (equal to MN/P in the case of $(N, N, MN/P)$-CCC).

To illustrate the principal of MPWI-3C, we detail the example of two transmissions (N=2) with two tilted plane waves α_1 and α_2 represented in Figure 3.1. In this case $(2, 2, MN/P)$-CCC are generated using the algorithm described in Figure. 2.6 :

$$\mathcal{C} = \begin{bmatrix} s_{1,1} & s_{1,2} \\ s_{2,1} & s_{2,2} \end{bmatrix} \tag{3.1}$$

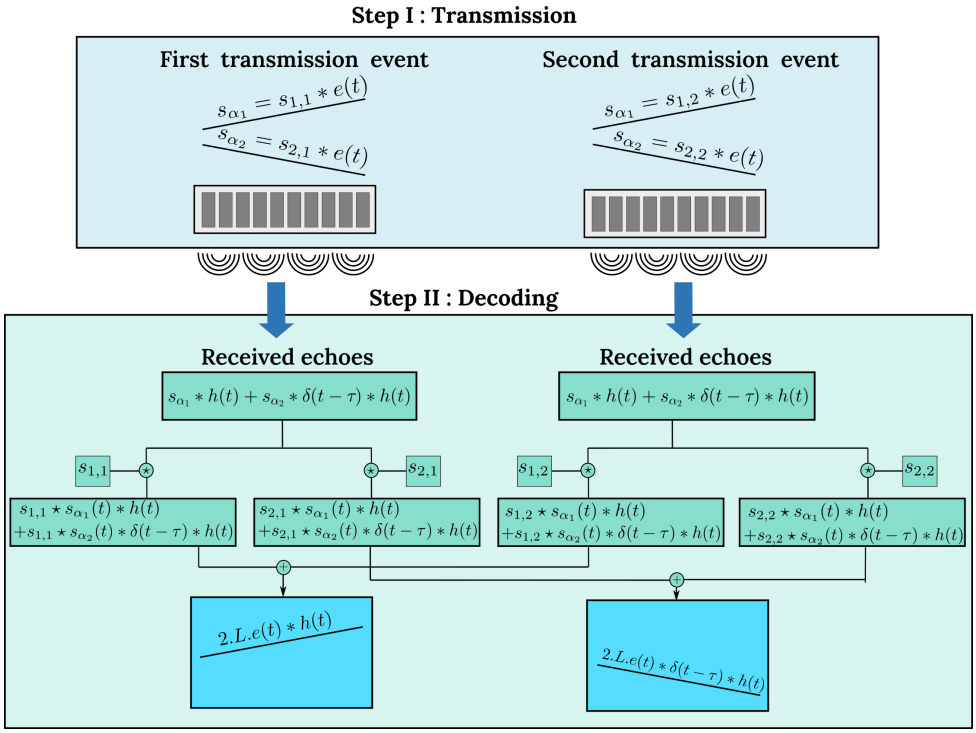

Figure 3.1: Overview of MPWI-3C imaging transmission and decoding scheme using (N, N, MN/P)-CCC.

Sequences $s_{1,1}$ and $s_{1,2}$ are assigned to the plane wave tilted with angles α_1 while sequences $s_{2,1}$ and $s_{2,2}$ are assigned to the plane wave tilted with angles α_2. During the first transmission event, the two plane waves are quasi-simultaneously transmitted by the probe, separated by a very small time delay τ that corresponds to the time required to transmit one bit to avoid overlap. The plane wave α_1 transmits the sequence $s_{1,1}$ convoluted with the base pulse $e(t)$ and the plane wave α_2 transmit the sequence $s_{2,1}$ convoluted with the base pulse $e(t)$. During the second transmission event, the plane wave α_1 transmits the sequence $s_{1,2}$ convoluted with the base pulse $e(t)$ and the plane wave α_2 transmits the sequence $s_{2,2}$ convoluted with the base pulse $e(t)$. This can be expressed as follows :

$$\begin{aligned} x_1 &= s_{1,1} * e_{\alpha_1}(t) + s_{2,1} * e_{\alpha_2}(t) * \delta(t-\tau) \\ x_2 &= s_{1,2} * e_{\alpha_1}(t) + s_{2,2} * e_{\alpha_2}(t) * \delta(t-\tau) \end{aligned} \tag{3.2}$$

The received backscattered signals after each transmission event are expressed as:

$$\begin{aligned} y_1 &= s_{1,1} * e_{\alpha_1}(t) * h(t) + s_{2,1} * e_{\alpha_2}(t) * \delta(t-\tau) * h(t) \\ y_2 &= s_{1,2} * e_{\alpha_1}(t) * h(t) + s_{2,2} * e_{\alpha_2}(t) * \delta(t-\tau) * h(t) \end{aligned} \tag{3.3}$$

Where $h(t)$ still represents the impulse response of the probe and the medium.

To separate the contribution of each tilted plane wave, the decoding operation leverages the ideal correlation properties of CCC. Following each transmission, the received signals are correlated with the sequences transmitted by each plane wave during that event. In this case, after the first transmission event, the received signals y_1 are correlated with the sequences $s_{1,1}$ and $s_{2,1}$, and after the second transmission event, the recieved

signals y_2 correlated with sequences $s_{1,2}$ and $s_{2,2}$:

$$\begin{aligned}
y_1^{\alpha_1} &= s_{1,1} \star s_{1,1} * e_{\alpha_1}(t) * h(t) + s_{1,1} \star s_{2,1} * e_{\alpha_2}(t) * \delta(t-\tau) * h(t) \\
y_1^{\alpha_2} &= s_{2,1} \star s_{1,1} * e_{\alpha_2}(t) * h(t) + s_{2,1} \star s_{2,1} * e_{\alpha_2}(t) * \delta(t-\tau) * h(t) \\
y_2^{\alpha_1} &= s_{1,2} \star s_{1,2} * e_{\alpha_1}(t) * h(t) + s_{1,2} \star s_{2,2} * e_{\alpha_2}(t) * \delta(t-\tau) * h(t) \\
y_2^{\alpha_2} &= s_{2,2} \star s_{1,2} * e_{\alpha_2}(t) * h(t) + s_{2,2} \star s_{2,2} * e_{\alpha_2}(t) * \delta(t-\tau) * h(t)
\end{aligned} \tag{3.4}$$

Given that the sum of ACF of each CCC set is a delta function (equation 2.12), and the sum of CCF between sequences at the same index in each different set is zero (equation 2.13), summing $y_1^{\alpha_1}$ and $y_2^{\alpha_1}$ suppresses the contribution of α_2 angle, keeping only signals from α_1 plane wave with a higher amplitude. Similarly, the addition of $y_1^{\alpha_2}$ and $y_2^{\alpha_2}$ suppresses the contribution of the α_1 plane wave, preserving only the contribution of α_2 plane wave with a higher amplitude. The gain in amplitude in this case is equal to $2.L$ with L being the length if the sequences. By setting $M = 2$ and $P = 1$, sequences of 4 bits can be generated leading to an SNR gain of $10\log_{10}(N.L) = 10\log_{10}(8) = 9$dB which is higher than the gain that can be obtained with MPWI-HD.

3.2.2 USTA

USTA imaging approach will be based on the use of Mutually Orthogonal Complementary Pairs (MOCPs) [223]. MOCPs refer to a collection of N sets of binary sequence, each containing two complementary sequences (pairs) of the same length (L). MOCPs sets exhibit three simultaneous properties that are interesting for USTA imaging (Figure 3.2) :

1. Ideal Aperiodic ACF : Each pairs in the MOCPs possesses an ideal ACF.
2. Ideal CCF between Adjacent Complementary Pairs: Any two adjacent pairs within the MOCPs have an ideal CCF.
3. Orthogonality of all pairs: All pairs in the MOCPs are orthogonal to each other. This means that for any two different sets in the MOCPs the cross-correlation function for zero shift is zero.

Another intriguing property of MOCPs is that the number of bits in each sequence is half the number of sets. This unique feature enables the transmission of shorter sequences compared to Hadamard orthogonal sequences. As a result, MOCPs offer an advantage in applications where shorter blind zone areas are desirable.

In the construction of MOCPs, a recursive method is employed. This iterative approach involves generating new sets of complementary sequences by using previously generated sets. The process is repeated incrementally, progressively increasing the number of pairs and the length of sequences with each iteration. Consider $\mathcal{C}^{(0)}$, an initial set of complementary pairs (N = 2). This initial set serves as a seed (0^{th} order set) for the recursion algorithm. It can be represented in a matrix form as follows:

$$\mathcal{C}^{(0)} = \begin{bmatrix} \mathcal{C}_1^{(0)} \\ \mathcal{C}_2^{(0)} \end{bmatrix} = \begin{bmatrix} \mathcal{C}_{1,1}^{(0)} & \mathcal{C}_{1,2}^{(0)} \\ \mathcal{C}_{2,1}^{(0)} & \mathcal{C}_{2,2}^{(0)} \end{bmatrix} \tag{3.5}$$

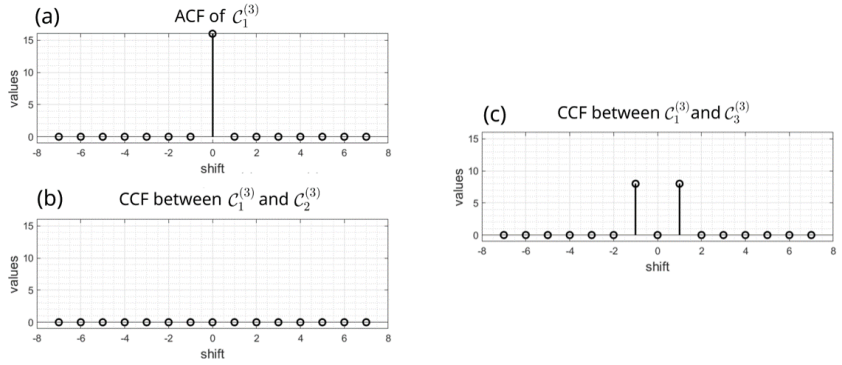

Figure 3.2: Plots of (a) ACF sum of $\mathcal{C}_1^{(3)}$ (b) CCF sum between $\mathcal{C}_1^{(3)}$ and $\mathcal{C}_2^{(3)}$ (c) CCF sum between $\mathcal{C}_1^{(3)}$ and $\mathcal{C}_3^{(3)}$.

Given that each complementary pair in $\mathcal{C}^{(0)}$ consists of two-element sequences, we use $\mathcal{C}_L^{(0)}$ and $\mathcal{C}_R^{(0)}$ to respectively represent all the first element sequences and all the second element sequences within these pairs :

$$\mathcal{C}_L^{(0)} = \begin{bmatrix} \mathcal{C}_{1,1}^{(0)} \\ \mathcal{C}_{2,1}^{(0)} \end{bmatrix} \text{and } \mathcal{C}_R^{(0)} = \begin{bmatrix} \mathcal{C}_{1,2}^{(0)} \\ \mathcal{C}_{2,2}^{(0)} \end{bmatrix} \tag{3.6}$$

The recursion method will then iteratively generate new sets of complementary pairs by building upon this initial set as follows :

$$\mathcal{C}^{(n)} = \begin{bmatrix} (e_{1,1}.\mathcal{C}_L^{(n-1)})||(e_{1,2}.\mathcal{C}_R^{(n-1)}) & (e_{1,3}.\mathcal{C}_L^{(n-1)})||(e_{1,4}.\mathcal{C}_R^{(n-1)}) \\ (e_{2,1}.\mathcal{C}_L^{(n-1)})||(e_{2,2}.\mathcal{C}_R^{(n-1)}) & (e_{2,3}.\mathcal{C}_L^{(n-1)})||(e_{2,4}.\mathcal{C}_R^{(n-1)}) \end{bmatrix} \tag{3.7}$$

Where $\mathcal{C}^{(n)}$ denotes the n^{th} order MOCPs generated by recursion, $||$ is the concatenation operation and E is matrix stisfying :

$$E = \begin{bmatrix} e_{1,1} & e_{1,2} & e_{1,3} & e_{1,4} \\ e_{2,1} & e_{2,2} & e_{2,3} & e_{2,4} \end{bmatrix} \text{ with } \sum_{k=1}^{4} e_{1,k}.e_{2,k} = 0 \tag{3.8}$$

Now, let's illustrate the construction process with an example. We begin with $\mathcal{C}^{(0)} = \begin{bmatrix} + & + \\ + & - \end{bmatrix}$ as the 0^{th} order set for the recursion construction. Additionally, we have matrix $E = \begin{bmatrix} + & + & - & + \\ + & + & + & - \end{bmatrix}$, where $+$ and $-$ represent $+1$ and -1, respectively. After undergoing the 3^{rd} order recursion construction, we successfully generate MOCPs set $\mathcal{C}^{(3)}$ consisting of 16 sets (N=16) of pairs, each having a length of 8 bits. Three complementary pairs of the generated MOCPS are shown bellow :

$$\mathcal{C}_{1,1}^{(3)} = [+,+,-,+,-,-,-,+]\, \mathcal{C}_{1,2}^{(3)} = [-,-,+,-,-,-,-,+]$$
$$\mathcal{C}_{2,1}^{(3)} = [+,-,-,-,-,+,-,-]\, \mathcal{C}_{2,2}^{(3)} = [-,+,+,+,-,+,-,-]$$
$$\mathcal{C}_{3,1}^{(3)} = [+,+,+,-,-,-,+,-]\, \mathcal{C}_{3,2}^{(3)} = [-,-,-,+,-,-,+,-]$$

Figure 3.2, shows that the constructed MOCPs adhere to the correlation conditions mentioned earlier. The ACF, CCF of two adjacent complementary pairs, and CCF of two non-adjacent complementary pairs are shown. As observed, $\mathcal{C}_1^{(3)}$ has an ideal ACF and the two adjacent complementary pairs $\mathcal{C}_1^{(3)}$ and $\mathcal{C}_2^{(3)}$ possess an ideal CCF. On the other hand, the two non-adjacent complementary pairs $\mathcal{C}_1^{(3)}$ and $\mathcal{C}_3^{(3)}$ demonstrate complete orthogonality, as their CCF is zero at zero shift, but their CCF have very high sidelobes out of the zero shift.

To perform USTA imaging with a sparse array consisting of N elements, MOCPs with N sets of sequences need to be generated. Each element in the sparse array is assigned a unique set of sequences. Since each set contains two binary sequences, only two transmission events are required, compared to the N transmission events needed in conventional STA. During each transmission event, all elements are activated simultaneously, with each element transmitting a sequence from its assigned set. The received signals are then decoded using matched filtering to reconstruct the complete STA dataset, effectively simulating individual element transmissions but with significantly fewer transmission events and improved SNR.

3.2.3 Experimental setup

The two proposed ultrafast imaging methods—MPWI-3C and USTA—were tested experimentally using the sparse array optimized on the Vermon array in section 2.3. This array has a central frequency of 7.2 MHz and was connected to the vantage Verasonics system. MPWI-3C was compared to CPWC while USTA was compared to conventional STA. To compare conventional MPWI-3C with CPWC, transmissions with 4 plane waves (-3°, -1°, 1°, 3°) were implemented. For MPWI-3C, (4, 4, 4)-CCC was used for 4 plane wave transmission.

To compare USTA with conventional STA, the sparse array can be divided into multiple sub-apertures to account for the blind zone area. In MOCPs, the number of bits in each sequence is half the number of sets. For a sparse array with 256 elements, this means 256 sets are required, leading to sequences with a length of 128 bits. With a central frequency of 7.2 MHz, this results in a blind zone area of 13 mm. Therefore, a trade-off between the achievable frame rate and the blind zone area must be considered.

In this study, to reduce the blind zone area, the sparse array was subdivided into 8 sub-apertures, each containing 32 elements (Figure 3.3). This reduces the number of required MOCPs sets to 32, with sequences of only 16 bits in length. At a central frequency of 7.2 MHz, this configuration yields a much smaller blind zone area of 1.6 mm. The decision to subdivide the sparse array into 8 sub-apertures was made as an arbitrary compromise between the frame rate and the size of the blind zone area. These sub-apertures are used only during transmission, while the entire array is used for receiving the echoes. Each sub-aperture requires two transmission events, resulting in a total of 16 transmissions, which is significantly fewer than the 256 transmissions needed for conventional STA.

After transmitting with each sub-aperture, the received RF data (captured by all elements of the array) are decoded to retrieve the contribution of each individual element. This is achieved by cross-correlating and summing the received RF data during each sub-aperture transmission with the sequence transmitted by the specific element during that event (Figure 3.4). By doing so, the complete STA dataset is decoded, simulating

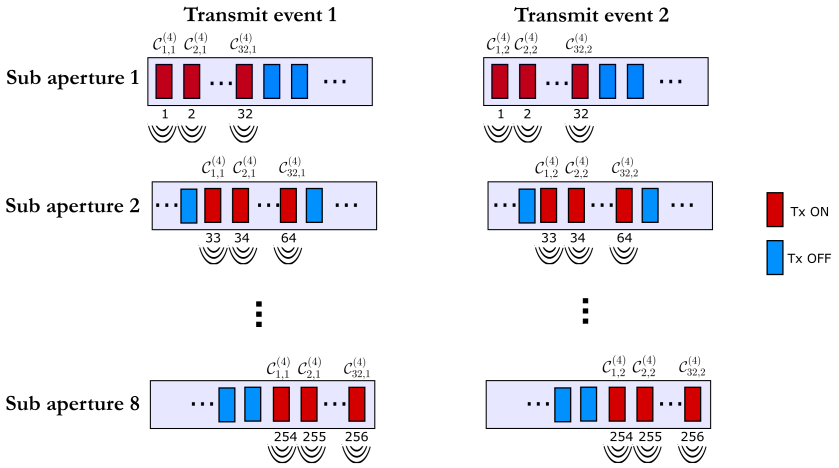

Figure 3.3: Principle of the STA imaging method with MOCPs (N=32) using 8 sub-apertures of 32 elements.

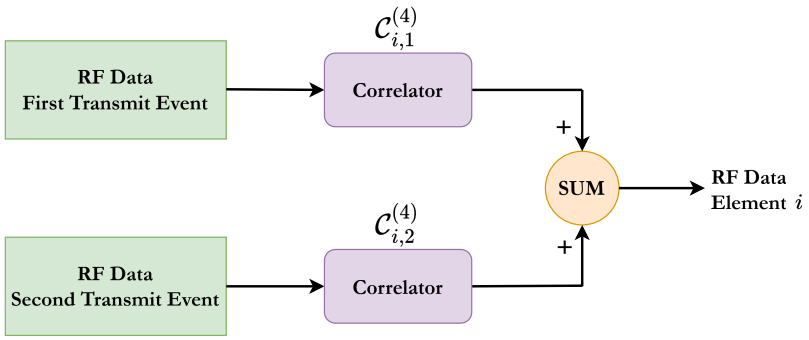

Figure 3.4: Decoding block of the received RF data to retrieve the STA dataset of Transmit element i.

individual element transmissions but with enhanced SNR and reduced interference.

For all the imaging methods, the Arbitrary Waveform Generation Toolbox (ArbWave Toolbox in Verasonics), provided by the Vantage scanner, was used to convert the binary sequences into tristate signals that can be transmitted by the scanner. The performance of the emission schemes was evaluated for B-mode imaging using a tissue-mimicking commercial phantom containing an anechoic inclusion and a nylon wire using the smae metrics introduced in chapter 2.

3.3 Results

3.3.1 MPWI-3C Results

Figure 3.5 presents the experimental beamformed images obtained using CPWC and MPWI-3C with a frame rate of 3950Hz. These images correspond to the XZ slice of the 3D beamformed volume and are displayed with a dynamic range of -60 dB. To compare the two methods under different noise level conditions, two experiments were conducted. The first experiment was performed by setting the Verasonics system voltage to 10V to

simulate high noise conditions, and the second experiment was conducted at 30V (the maximum recommended for the probe) to simulate low noise conditions.

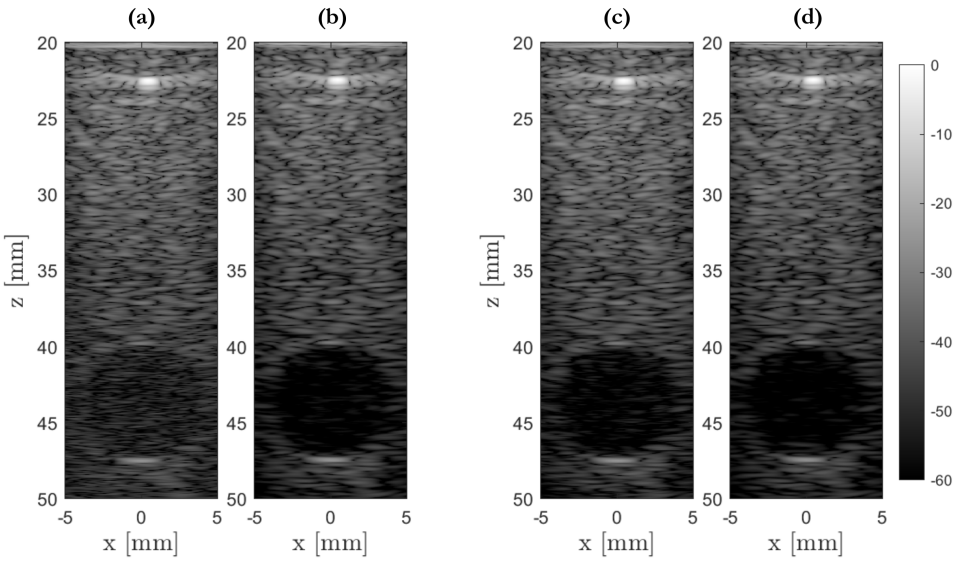

Figure 3.5: Experimental beamformed images of the tissue-mimicking phantom obtained with (a) CPWC, (b) MPWI-3C, for 10V *and (c) CPWC, (d) MPWI-3C for* 30V*.*

A qualitative visual comparison of the results shows that MPWI-3C significantly increases the SNR and image quality under both noise conditions. In the 10V experiment, the image produced by CPWC presents a high level of noise, and the anechoic inclusion is not clearly visible. Conversely, the anechoic inclusion is more visible in the image produced by MPWI-3C. In the 30V experiment, the image quality produced by CPWC improves, and the anechoic inclusion becomes more discernible. However, the MPWI-3C image still exhibit superior quality and lower noise level. Notably, the images obtained by MPWI-3C in the 10V experiment demonstrate better image quality than the images obtained with CPWC in the 30V experiment.

Table 3.1: Comparison of SNR, CR, Axial Resolution and frame rate for CWPC and MPWI-3C at 10V *and* 30V*. The gain in SNR (gSNR) obtained with MPWI-3C is also represented.*

Voltage	Method	pSNR (dB)	CR (dB)	FWHM (m)	FR (Hz)	gSNR (dB)
10V	**CPWC**	50.75	-10.55	0.34	3850	8.94
	MPWI-3C	59.70	-18.68	0.34	3850	
30V	**CPWC**	57.99	-17.80	0.34	3850	3.60
	MPWI-3C	61.59	-20.22	0.34	3850	

The visual assessment of the images is supported by quantitative analysis through PSNR calculations for both imaging methods. The PSNR was computed by determining the maximum signal on the scatterer representing the nylon wire and the RMS of the noise within the anechoic inclusion. In the 10V condition, the results indicate that the MPWI-3C method achieved a significantly higher PSNR of 59.70 dB, compared to 50.75 dB with CPWC, resulting in an SNR gain of 8.94 dB. A similar trend was observed under

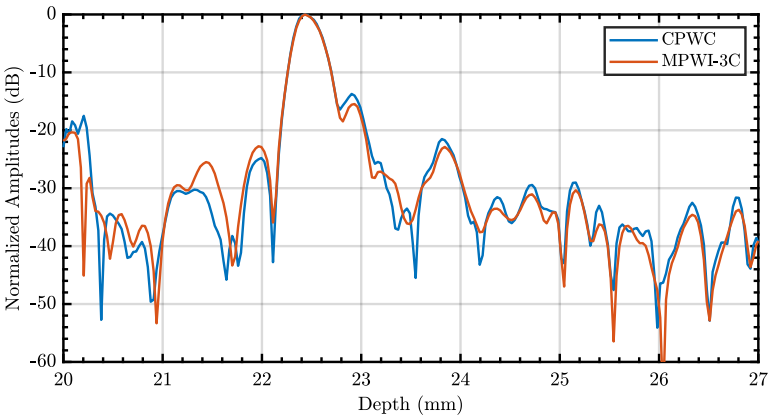

Figure 3.6: Axial line profile on the scatterer representing the nylon wire for CPWC and MPWI-3C.

the 30V condition, where MPWI-3C also outperformed CPWC, providing an SNR gain of 3.60 dB. These results confirm the visual assessment of MPWI-3C in enhancing image quality under varying noise conditions.

Figure 3.6 presents a comparison of axial line plots on the scatterer from Figure 3.5 for CPWC and MPWI-3C under the 30V condition. The plots are extremely similar, highlighting the absence of axial sidelobes in MPWI-3C, thanks to the ideal correlation properties of CCC. Notably, the axial resolution remains unaffected, with both methods having equivalent -6dB axial resolution. As shown in Table 3.1, CPWC and MPWI-3C both achieve an axial resolution of 0.34 mm. The contrast was also evaluated and the results are shown in Table 3.1. Contrast measurements were taken inside and outside the anechoic inclusion at a depth of 43 mm. MPWI-3C outperformed CPWC under both the 10V and 30V conditions, achieving a contrast gain of 8.13 dB in the 10V condition and a gain of 2.42 dB in the 30V condition.

3.3.2 USTA Results

Figure 3.7 presents B-mode images obtained from the same tissue-mimicking phantom as the one used for plane wave imaging. The figure compares conventional STA, with 256 transmissions (where each transmission involves a single element), with the USTA method. In USTA, the array was subdivided into 8 sub-apertures. Each sub-aperture requires two transmission events, resulting in a total of 16 transmissions, significantly fewer than the 256 transmissions of conventional STA (16 times less transmissions).

Both methods were tested under high noise (10V) and low noise (30V) conditions. Visual inspection of the images reveals that the USTA method produces a higher SNR compared to conventional STA in both noise scenarios. In the 10V condition, the image generated by the conventional STA method is extremely noisy, making it impossible to distinguish the anechoic inclusion from the noise, and even the tissue-mimicking speckle is dominated by noise. Conversely, the USTA image shows better quality, with the anechoic inclusion starting to become visible, although some noise remains, and the tissue-mimicking speckle is much clearer. In the 30V condition, the conventional STA image remains noisy, with the anechoic inclusion still invisible, while the tissue-mimicking

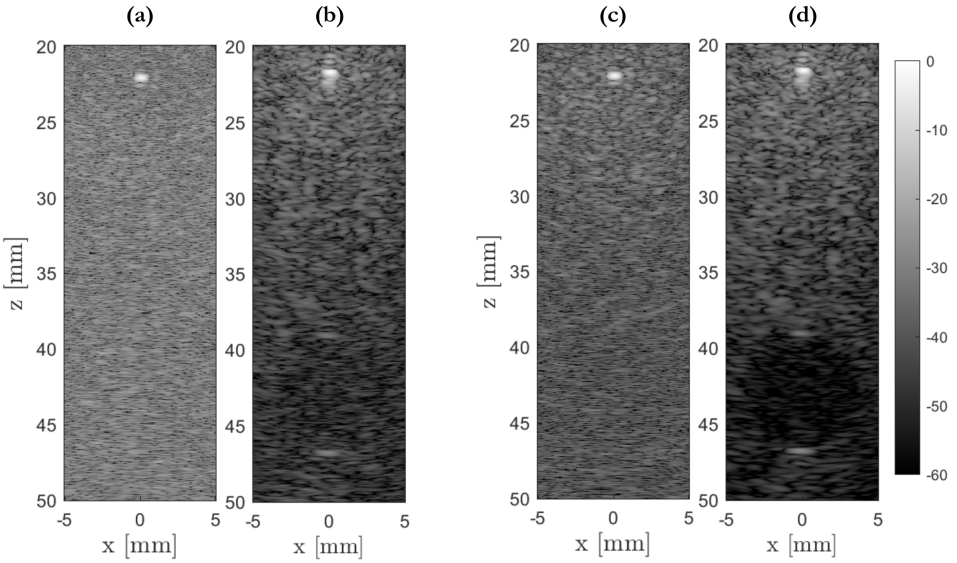

Figure 3.7: Experimental beamformed images of the tissue-mimicking phantom obtained with (a) STA, (b) USTA, for 10V *and (c) STA, (d) USTA for* 30V*.*

speckle pattern starts to appear, particularly near the probe. Meanwhile, the USTA method produces a much clearer image, with the anechoic inclusion distinctly visible and the surrounding tissue-mimicking speckle well-defined.

To further validate the results, Table 3.2 presents a comparison of PSNR and gSNR between STA and USTA under different noise conditions. The USTA method consistently demonstrated higher PSNR values than STA in both noise scenarios. Specifically, the USTA method achieved an SNR gain of 20.50 dB in the 10V experiment and 18.73 dB in the 30V experiment, compared to the STA method. This SNR improvement is reflected in enhanced image quality, particularly in terms of contrast, with gains of 5.92 dB and 11.38 dB for the 10V and 30V experiments, respectively.

Table 3.2: Comparison of SNR, CR, Axial Resolution and frame rate for STA and USTA at 10V *and* 30V*. The gain in SNR (gSNR) obtained with USTA is also represented.*

Voltage	Method	pSNR (dB)	CR (dB)	FWHM (m)	FR (Hz)	gSNR (dB)
10V	**STA**	26.51	0	0.27	60	20.50
	USTA	47.02	-5.92	0.29	962	
30V	**STA**	36.28	-1.44	0.27	60	18.73
	USTA	55.01	-12.82	0.29	962	

Although the USTA method provided superior imaging performance over STA in terms of SNR and contrast, the images exhibited axial correlation sidelobes due to the non-ideal correlation properties of MOCPs. Aditionally, a small degradation of axial sidelobes of 0.02mm is observed (Table 3.2). Figure 3.8 presents a comparison of axial line plots for both STA and USTA under the 30V condition, highlighting the presence of axial sidelobes with levels ranging between 17 dB and 20 dB. Traces of these sidelobes can also be observed inside the anechoic inclusion in Figure 3.7. Nevertheless, these artifacts are minimal in both range and magnitude.

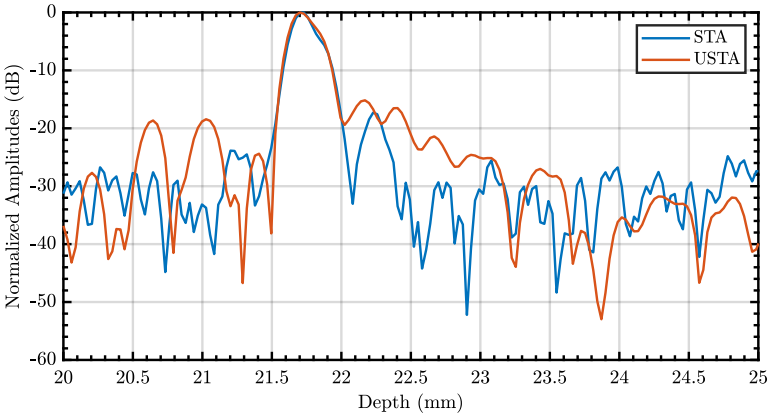

Figure 3.8: Axial line profile on the scatterer representing the nylon wire for STA and USTA.

Finally, considering an imaging depth of 50 mm and a speed of sound of 1540 m/s, the USTA method requires only 16 transmissions compared to 256 transmissions for STA, resulting in a significantly higher frame rate. As shown in Table 3.2, a frame rate of 962 Hz was achieved with USTA, compared to 60 Hz with STA.

3.4 Discussion

In this study, we focused on the implementation of ultrafast 3D ultrasound imaging using 2D sparse arrays, with the goal of increasing the frame rate and SNR of ultrafast imaging through coded excitation. Two imaging methods were investigated: plane wave imaging and STA.

For plane wave imaging, we explored the performance of a novel coded excitation scheme MPWI-3C, designed to improve SNR without compromising the frame rate. This approach utilizes (N,N,MN/P)-CCC binary sequences, which exhibit ideal correlation properties and short sequence lengths. In practice, the (N,N,MN/P)-CCC sequences are constructed so that the number of sets (N) corresponds to the number of plane waves to be transmitted, and the number of sequences in each set (also N) corresponds to the number of transmissions. The sequence length (L = MN/P) can be adjusted to produce either short or long sequences. MPWI-3C involves the quasi-simultaneous transmission of tilted plane waves during each transmission event, with each plane wave transmitting a sequence from its corresponding set. By leveraging the ideal correlation properties of these sequences, the received RF datasets are decoded to isolate the contribution of each plane wave as if they had been transmitted individually, but with significantly higher amplitude. Theoretically, this method offers an SNR increase of $10\log_{10}(NL)$ compared to conventional Plane Wave Compounding (CPWC). This approach was tested experimentally using a 256-element sparse arrays connected to the Verasonics Vantage system with 4 plane wave transmissions, employing (N,N,MN/P)-CCC sequences of 4 bits, alongside CPWC for comparison.

MPWI-3C demonstrated a significant SNR improvement, resulting in enhanced image quality compared to CPWC (Table 3.1). However, the observed SNR gain was less than the theoretical expectation. This discrepancy is attributed to the effects of frequency-

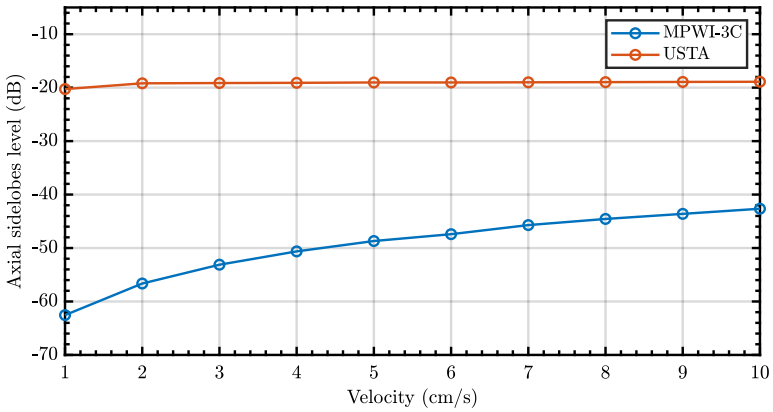

Figure 3.9: Simulated Axial sidelobes levels as a function of scatterer velocity for MPWI-3C and USTA.

dependent attenuation on the binary sequences, which reduce the SNR gains. Additionally, since the SNR was computed based on the B-mode images, the presence of aliasing artifacts arising from the high sidelobe level floor, related to the sparse array, contributed to the loss in SNR gain (Figure 3.5). Despite these factors, the SNR improvements were still high, leading to better image quality, as reflected in the improved contrast values obtained with MPWI-3C compared to CPWC (Table 3.1). This SNR gain is particularly valuable in deep tissue imaging, where electronic noise tends to dominate. Thus, the proposed sequence is especially beneficial in high-noise applications, such as imaging deep organs and highly attenuating tissues. It may also prove useful in applications requiring ultrasound probes with high central frequencies, to compensate for the rapid attenuation of ultrasonic waves and enhance penetration depth.

For the USTA imaging, we implemented an ultrafast coded excitation STA using Mutually Orthogonal Complementary Pairs (MOCPs) sequences. This coded excitation sequence was designed to increase the frame rate of STA imaging while simultaneously improving image quality in terms of SNR and contrast. Although MOCPs do not possess ideal correlation properties, they exhibit ideal correlation within each set of sequences and ideal cross-correlation properties between two adjacent sets (Figure 3.2). Additionally, their unique orthogonality between any non-adjacent sets minimizes correlation sidelobes and interference between sparse array elements.

In this work, the sparse array was subdivided into 8 sub-apertures to reduce sequences length and hence the blind zone area (Figure 3.3). Each sub-aperture performed two transmission events, resulting in a total of 16 transmissions. By dividing the sparse array into 8 sub-apertures, the generated binary sequences have only 16 bits, resulting in a very short blind zone area. However, this subdivision requires 16 transmission events to obtain the complete STA dataset. In the current study, with an imaging depth set to 50 mm, this configuration achieves a frame rate of 962 Hz, which is significantly higher than the 60 Hz typically obtained with conventional STA. Additionally, both SNR and contrast were significantly increased, as more energy is transferred to the medium.

The frame rate can be increased by reducing the number of array sub-apertures, though this comes at the cost of increasing the blind zone area. This trade-off is acceptable if the organs of interest are located in deeper regions. For example, by dividing the array

into two sub-apertures, binary sequences of 64 bits in length would be transmitted. For an array with a central frequency of 7.2 MHz, this sequence length would result in a theoretical blind zone area of 6.4 mm which, for some applications, is still within acceptable limits. The number of required transmissions would be reduced to four, yielding a frame rate of 3850 Hz.

MPWI-3C is also concerned by the blind zone area issue. The size of the dead zone area is proportional to the half of the transmitted waveform. In this study, we used (4,4,4)-CCC sequences of length 4 bits. With a 7.2MHz the duration of the transmitted waveform including the short time delay between tilted plane waves 2.64μs. This will give rise to a short blind zone area of 2.03mm. This blind zone remains reasonable especially that it is the deep tissue regions that typically experience low SNR and these regions are in most cases well beyond these area. However, when sequences with more bits are used alongside a high number of plane waves, consideration should be given to the blind zone area. An approach that we will investigate in the future is the method proposed by [204], where simultaneous plane wave transmission can be employed instead of quasi-simultaneous plane wave transmission. This approach can significantly shorten the transmitted waveform duration, thereby reducing the dead zone area in the near field.

Both MPWI-3C and USTA leverage the complementary properties of sequences to cancel out correlation sidelobes. However, these approaches require multiple transmissions, making the sequences susceptible to motion artifacts. When tissue moves between successive transmissions, the correlation function's sidelobes may not perfectly align, preventing ideal cancellation. This misalignment introduces correlation sidelobes that manifest as artifacts in the image, reducing contrast.

For example, in abdominal ultrasound applications, tissue motion due to breathing and cardiac activity can vary from 1 to 5 cm/s. Normal breathing can cause abdominal organs to move at velocities of 1 to 3 cm/s, with heavy breathing reaching up to 5 cm/s. Cardiac motion can induce tissue velocities up to 1 cm/s. These motion velocities can compromise the effectiveness of the decoding process, especially at lower frame rates. At higher frame rates, the motion-induced artifacts remain at an acceptable level.

Figure 3.9 illustrates the axial sidelobe levels resulting from a simulated moving scatterer with velocities ranging from 1 to 10 cm/s for both MPWI-3C and USTA. The frame rate was set at 3850Hz for MPWI-3C and 962Hz for USTA. As scatterer velocity increases, the axial sidelobe levels for MPWI-3C increases, but they still remain relatively low, below -40 dB. USTA, however, is less sensitive to these velocities due to the already high sidelobe levels inherent to MOCPs. Additionally, motion compensation algorithms can be employed to further mitigate the impact of tissue motion [224–226, 276–278].

3.5 Conclusion

This chapter addressed the challenge of ultrafast 3D ultrasound imaging using sparse arrays, focusing on enhancing the SNR of plane wave imaging through the introduction of MPWI-3C while maintaining high frame rates. MPWI-3C leverages the ideal correlation properties of (N,N,MN/P)-CCC binary sequences, enabling quasi-simultaneous transmission of tilted plane waves, each carrying a distinct sequence during every transmission event. The received echoes are decoded as if the plane waves were transmitted individually, resulting in higher SNR without sacrificing frame rate. Additionally, the nature

of (N,N,MN/P)-CCC allows for the generation of shorter sequences, avoiding large blind zones. Furthermore, a USTA coded sequence was proposed using MOCPs to increase the frame rate of STA with sparse arrays. A frame rate of 962 Hz was achieved using 16 coded transmissions, simultaneously improving SNR and contrast compared to conventional STA.

Experimental studies demonstrated that MPWI-3C outperforms CPWC, and USTA surpasses STA in terms of both SNR and contrast, with a minimal decrease in axial resolution. The increased frame rate and SNR offered by MPWI-3C and USTA also enhance penetration depth, offering potential benefits for various clinical applications. However, potential limitations of the proposed approachs were acknowledged, such as the impact of attenuation and motion on decoding accuracy, and the possible expansion of the blind zone area when transmitting a large number of plane waves. These issues will be the focus of future investigations.

Chapter 4

A Deep Reinforcement Learning based Region-Specific Beamformer for 2D Sparse Arrays Ultrasound Imaging

In this chapter, I introduce a newly developed reconstruction algorithm, which uses deep reinforcement learning for adaptive ultrasound beamforming, to enhance image quality with developed prototype of a sparse array. The performance of this algorithm was evaluated using both simulated and experimental datasets, with the objective of optimizing image quality. Beforehand, I will present a novel GPU-accelerated Finite Element Method (FEM) simulation model designed for realistic ultrasound imaging. This simulation model was used in the development of a 2D sparse array prototype and the generation of the dataset used to train the aforementioned reconstruction algorithm.

4.1 Design of a new 2D sparse array probe

The main goal of the SPARTECHUS ANR project is to develop a new prototype of a 2D sparse array that addresses the limitations of current sparse array technology, particularly regarding low SNR and poor image contrast. In this section, we will focus on introducing a novel GPU-accelerated FEM model that was used in the development of the prototype. Additionally, we will present examples of images obtained with the new prototype and discuss their quality.

4.1.1 Guidelines for the 2D sparse array prototype design

To increase the SNR, IMASONIC proposed increasing the size of the array elements to achieve lower impedance and, consequently, higher sensitivity. To maintain good divergence, each element in the sparse array has been equipped with an integrated lens at the front. For the elements distribution, a Fermat's spiral distribution was chosen and the central frequency was set to 1 MHz. The spiral array was chosen for its good radiated beam pattern performances, offering a good balance between main-lobe width and side-lobes level. The relatively low central frequency of 1 MHz was chosen due to technological limitations faced by IMASONIC.

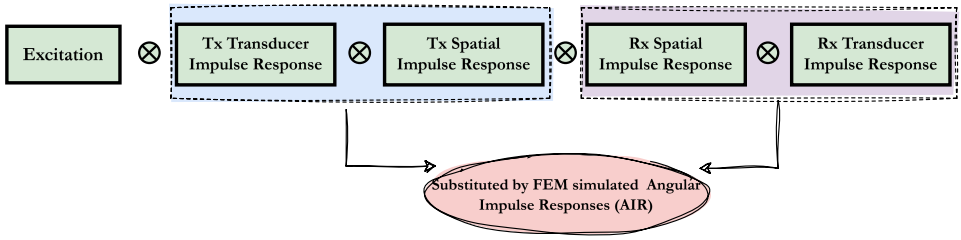

Figure 4.1: Graphical representation of the convolution model with substituted FEM AIR.

In designing the probe, various element technologies (e.g., materials, sizes) and lens technologies were combined with the CCC STA coded excitation scheme introduced in Chapter 2 to increase the SNR. These combinations were compared using simulations to select the best-performing probe model for fabrication. Several ultrasound simulation software tools, such as Field II [118, 119] and SIMUS [227, 228], were considered, with Field II being the most commonly used due to its foundation on the spatial impulse response (SIR) method. The SIR method calculates the wideband radiation pattern of an ultrasound array by solving the Rayleigh integral in the far field. By assuming the SIR has a trapezoidal shape, Field II can calculate the radiation pattern for arbitrarily shaped transducers. The pulse-echo response of the array is then calculated by convolving the excitation signal with the electromechanical impulse response of the transducer and the spatial impulse response for transmission and reception. This approach, will be called the *convolution model*, and it is illustrated in Figure 4.1.

Designing an ultrasound array using conventional software, such as Field II or SIMUS, may not produce fully accurate results due to inherent limitations in these tools. These simulators typically model the array using a finite planar baffle diffraction model, which considers the element shapes but neglects their thickness [229]. Consequently, complex phenomena occurring within the transducer layers, such as crosstalk, baffle effects, and directivity patterns, are not adequately represented. This oversight leads to inaccuracies in array design, ultimately reducing the realism and precision of the simulated results.

The most commonly used approach for designing ultrasound transducers is the Finite Element Method (FEM) [230]. Although FEM provides high accuracy in transducer design, it does not support the direct simulation of ultrasound images. FEM modeling was first applied to the design of PZT transducers in the 1990s and has since become widely adopted for analyzing ultrasound transducers due to its precision [231, 232]. The strength of FEM lies in its ability to model the complex phenomena occurring within the transducer element, including the effects of element thickness, shape, and the materials used in each layer.

4.1.2 GPU FEM based ultrasound simulation

To enhance the realism of ultrasound imaging simulations, IMASONIC proposed integrating FEM methods with the convolution model [229]. This approach replaces the convolution of the electromechanical impulse response with the spatial impulse response in both transmission and reception, with an FEM-simulated Angular Impulse Responses (AIR). Since all elements of the array share the same technology and shape, AIRs are simulated using an FEM model for a single transducer. For each elevation angle, the

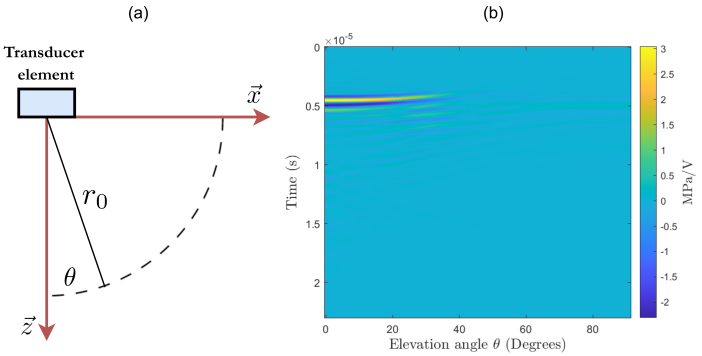

Figure 4.2: Angular impulse responses : (a) calculation setup for a single element (b) simulated transmission AIR.

model generates an angular impulse response for both transmission and reception. Figure 4.2 illustrates the various transmission AIRs simulated by the FEM model. These AIRs are then incorporated into the convolution model to enable realistic 3D ultrasound image simulations.

While certain parameters, such as the elements position following a Fermat's spiral distribution and the central frequency, remained fixed, other parameters required optimization. These included the probe size, which varied from 80 mm to 160 mm; the size of the piezoelectric elements, ranging from 1 mm to 5.5 mm; and the type of element technology employed, which influenced the probe's frequency spectrum and other parameters needing optimization. By combining these different variables, a total of 252 configurations were generated for simulation. Each configuration was simulated in 3D ultrasound imaging scenarios using the FEM simulation method with 3D tissue-mimicking phantoms.

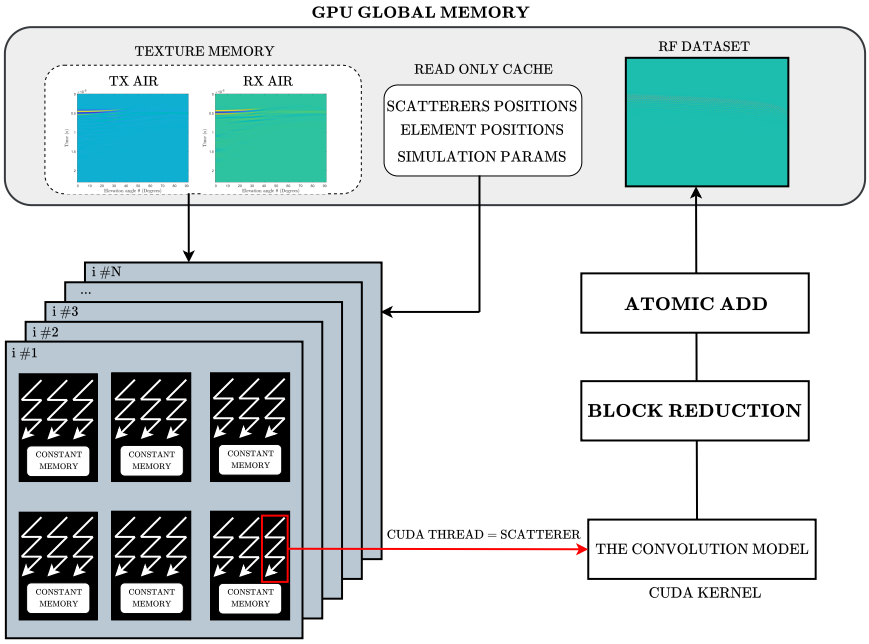

Figure 4.3: GPU Implementation of the FEM based ultrasound simulation tool.

My role in this phase was to develop an optimized simulation code to accelerate simulation times using GPUs (Graphics Processing Units). I implemented a simulation method specifically designed for Nvidia GPUs utilizing CUDA technology (Figure 4.3). The primary factor contributing to high computational cost of the simulation was the large number of scatterers in the phantoms. By assigning each scatterer to a CUDA thread, we enabled simultaneous calculations of all scatterers contributions, rather than processing them sequentially, which combined with an efficient memory access management using texture memory significantly reduced simulation times. This optimization allowed for the simulation of a phantom containing nearly 5 million scatterers in approximately 4 hours. We simulated all 252 probe configurations on the Jean Zay supercomputing platform, which provided access to 48 GPUs in parallel, enabling us to complete the simulations in about 24 hours.

After completing the simulations, we conducted a comparative study of the different configurations based on various computational metrics, such as SNR and contrast, to determine the optimal probe design for manufacturing. Following this analysis, we selected a probe with a 100 mm aperture, comprising 256 elements of 3.5 mm size and a central frequency of 1 MHz. This configuration was chosen for fabrication, and the prototype is shown in Figure 4.4. Further details on the FEM simulation model, the various probe configurations tested, and the experimental characterization of the fabricated prototype will be provided in the thesis manuscript of Jean-Baptiste Jacquet.

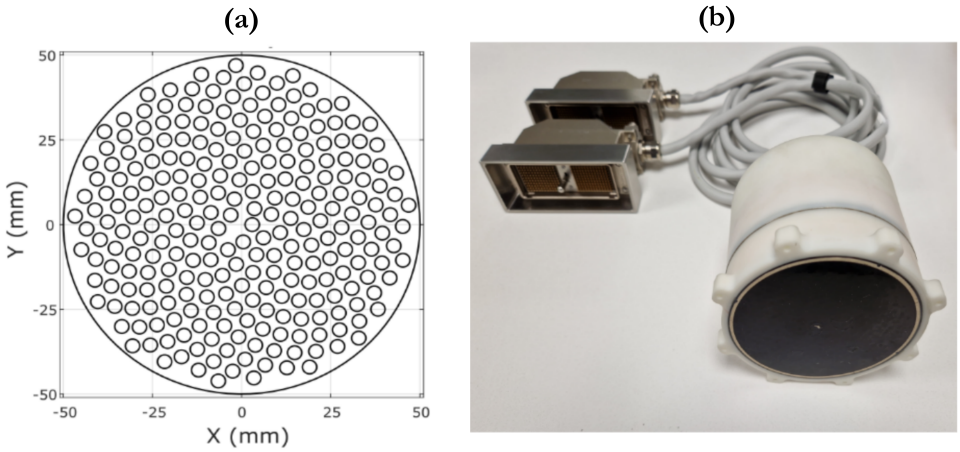

Figure 4.4: (a) Spiral Elements distribution with 256 elements of size 3.5mm (b) the fabricated probe prototype.

4.1.3 Image quality with sparse array

One of the significant drawbacks of sparse arrays is their reduced image quality. Indeed, the spatial distribution of elements on the array aperture, with inter-element spacing larger than $\lambda/2$, leads to high sidelobes level around the main lobe [7,79]. These sidelobes cause energy leakage during beamforming, severely reducing image contrast. The sidelobes level are heavily influenced by the distribution of elements across the array's aperture. As a result, much of the research on sparse arrays has focused on finding optimal element

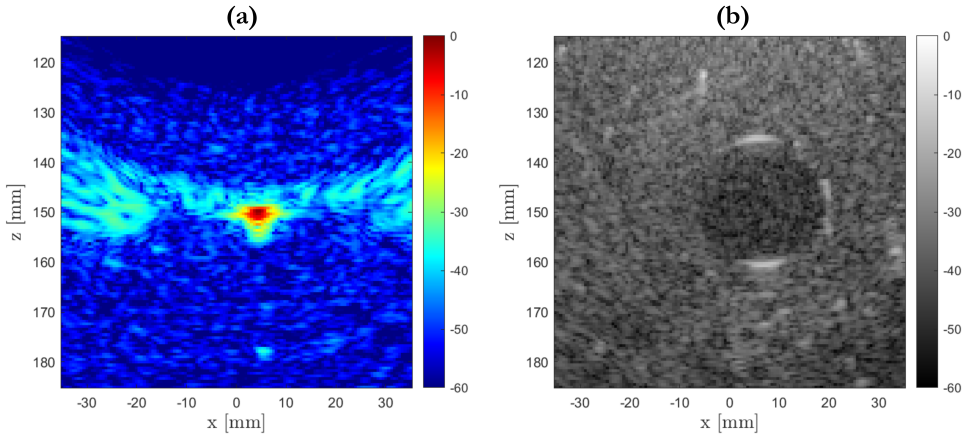

Figure 4.5: Experimental B-mode images acquired with the developed probe prototype of a (a) wire phantom, (b) home-made tissue-mimicking phantom.

distributions that minimize the number of elements while maintaining acceptable image quality [81, 108].

The prototype design presented in Figure 4.4 is based on a Fermat's spiral array, a distribution known for low sidelobes level. However, for ultrasound images typically displayed with a dynamic range of -60 dB, sidelobes-related artifacts remain visible. Figure 4.5 shows XZ slices of experimental 3D beamformed volumes obtained with the designed probe beamformed with the DAS beamformer. Figure 4.5(a) corresponds to an image of a wire phantom placed at a depth of 150 mm, which can be considered as a Point Spread Function (PSF) image. This image highlights the presence of high sidelobes level caused by the sparse array. In the case of a tissue-mimicking phantom , these sidelobes cause energy to leak from the surrounding tissue speckle into anechoic inclusion, drastically reducing the image contrast (Figure 4.5(b)).

To address this issue, my second contribution to the project was the development of a new reconstruction algorithm adapted to reconstruct high quality STA images from RF data acuired with the designed sparse array prototype. To achieve this, several ultrasound reconstruction algorithms proposed in the literature were studied. Based on this study, a novel deep learning-based reconstruction algorithm was proposed.

4.2 Ultrasound image reconstruction

4.2.1 Literature review

The DAS beamforming algorithm is the most commonly used method in ultrasound imaging [233]. This technique relies on geometric delay calculations to focus ultrasound signals and reconstruct the image. The process relies on the calculation of the time-of-flight (TOF) between each array element and a specific focal point in the imaging plane. For each pixel in the beamformed image, this TOF is used to delay the received signals from each element, aligning them as though they were originating from the same point in space. Once aligned, the delayed signals are properly weighted and summed across all the receive elements to construct the pixel values of the image. The DAS beamforming process can be mathematically represented as follows:

$$y(t) = \sum_{i=1}^{N} \omega_i s_i(t - \tau_i) \tag{4.1}$$

Where N is the number of receive elements, ω_i is the apodization weights applied to receive element i, s_i is the received signal by element i and τ_i is the time delay.

Although DAS offers a straightforward method for reconstructing ultrasound images with relatively low computational complexity, it is prone to artifacts resulting from off-axis signals [234, 235]. These artifacts can arise from grating lobes and high sidelobes level, which are particularly problematic in the beam pattern of 2D sparse arrays [236]. The images shown in Figure 4.5, reconstructed using the DAS algorithm, clearly demonstrate the limitations of DAS beamforming when dealing with the high sidelobes level of 2D sparse arrays. To overcome the limitations of DAS beamforming, several adaptive, coherence-based, and non-linear beamformers have been proposed in the literature. In this section, these techniques will be differentiated based on their category. However, for the remainder of this chapter, we will refer to all of them collectively as adaptive beamformers for simplicity.

The minimum variance (MV) beamformer is an adaptive technique introduced to enhance ultrasound image quality, particularly in terms of resolution [237,238]. Unlike DAS, which uses fixed apodization weights, the MV beamformer applies adaptive apodization weights to the delayed signals. These weights are determined based on the statistical properties of the RF data and are adjusted dynamically to minimize the output energy of the array while preserving the energy of the signal of interest. This is achieved by estimating a covariance matrix from the RF data to solve the minimization problem. However, the computational complexity of estimating and inverting the covariance matrix limits the practical application of the MV beamformer. Additionally, while MV beamforming improves resolution, it is known to have lower contrast, similar to the DAS algorithm, making it less effective in low-contrast situations, such as those encountered with sparse arrays [234, 235].

To improve the performance of the MV beamformer, several enhancements have been proposed. The eigenspace-based MV (ESBMV) beamformer, for example, was developed to improve image contrast [239]. ESBMV uses the eigenstructure of the covariance matrix to suppress off-axis signals, thereby reducing sidelobes while preserving on-axis signals. Another enhancement, the forward-backward MV beamformer, was introduced to increase the robustness of MV beamforming [235]. This technique employs spatial averaging to improve the accuracy of the covariance matrix estimation.

In addition to adaptive beamformers, coherence-based beamformers have also been introduced in the literature to improve ultrasound image quality, particularly in terms of contrast. These techniques apply pixel-wise weights to the DAS beamformed image. One of the most commonly known methods is the Coherence Factor (CF) [240, 241]. CF can be considered as a sidelobes reduction weighting technique that enhances image contrast by applying weights to the beamformed image. These weights are calculated as the ratio between the energy of the main lobe (coherent sum) and the total energy (incoherent sum) in the received signals across the array elements:

$$\mathrm{CF}(t) = \frac{\left|\sum_{i=1}^{N} s_i(t-\tau_i)\right|^2}{N\sum_{i=1}^{N}|s_i(t-\tau_i)|^2} \tag{4.2}$$

The underlying principle is that after focusing delays are applied, the on-axis signals from the main lobe are highly coherent, resulting in a higher CF value, while off-axis signals from sidelobes are incoherent, leading to a lower CF value. In regions where the received signal is dominated by sidelobes, the coherent sum energy is lower than the total incoherent energy, resulting in a low CF. By weighting the DAS beamformed image with CF, sidelobes are reduced, thereby improving the contrast.

Various variations of CF have been proposed in the literature. One such variant is the Generalized Coherence Factor (GCF), which was introduced as a spatial frequency extension of the CF [242]. Unlike the standard CF, which considers only the total coherent energy in the DC component, the GCF also accounts for the energy ratio in the low-frequency region. This approach helps preserve the speckle pattern in situations where the standard CF might not perform optimally [242].

However, both CF and GCF primarily rely on the amplitude information in the RF data. To leverage additional information, Phase Coherence Factor (PCF) beamforming was introduced [243, 244]. PCF takes into account the instantaneous phase of the time-delayed received signals. The principle behind PCF is that signals originating from the main-lobe are in phase, resulting in a PCF value close to one, while off-axis signals exhibit high phase dispersion, leading to lower PCF values. By weighting the DAS beamformed image with the PCF, artifacts due to sidelobes and grating lobes are reduced.

Delay Multiply and Sum (DMAS) is a non-linear beamforming technique developed to improve image contrast in ultrasound imaging [245]. Unlike DAS beamforming, where the TOF delayed signals are simply summed, DMAS involves multiplying the delayed signals pairwise across the receiving elements before summation. This multiplication can be viewed as a form of cross-correlation of the received signals across the aperture, enhancing the sensitivity of the DMAS to incoherent signals and thereby improving contrast. The output of the DMAS beamformer is expressed as:

$$y_{DMAS}(t) = \sum_{i=1}^{N-1}\sum_{j=i+1}^{N} \hat{s}_i(t-\tau_i)\hat{s}_j(t-\tau_j) \tag{4.3}$$

where $\hat{s}_i(t-\tau_i) = sign(s_i(t-\tau_i))\sqrt{|s_i(t-\tau_i)|}$. Multiplying the signals in this manner changes the dimensionality from volts to volts^2. To maintain the original signal dimensions and preserve the sign, the square root of the signals is taken before multiplication. Additionally, the multiplication process introduces a DC component and second harmonics, which can distort the signal. To mitigate this, a band-pass filter is applied, resulting in the Filtered DMAS (F-DMAS) technique [245, 246].

DMAS has been shown to produce images with enhanced contrast due to its higher sensitivity to incoherent signals. However, its computational cost is significantly higher than that of DAS, which can impact the achievable frame rate if limited calculation power is available. To address this, a reformulation of DMAS that reduces the computational complexity from $O(N^2)$ to $O(N)$ was proposed in [247]:

$$y_{DMAS}(t) = \frac{1}{2}\left[\left(\sum_{i=1}^{N} \hat{s}_i(t-\tau_i)\right)^2 - \sum_{i=1}^{N} |\hat{s}_i(t-\tau_i)|\right] \tag{4.4}$$

Several variations of the DMAS beamformer have been introduced in the literature to further enhance its performance for specific applications. For example, the double-stage DMAS was developed for photoacoustic imaging [248], and the Delay Weight Multiply and Sum (DwMAS) algorithm was proposed to further reduce sidelobe levels by applying a weighting window [249].

Deep learning methods have gained significant attention in recent years for ultrasound beamforming [250]. These methods can be broadly categorized into three approaches based on their focus within the ultrasound image reconstruction process.

The first category aims to enhance the quality of already DAS beamformed, low-quality images. In this category neural networks are trained to learn to map low-quality to high-quality images. In [251], a convolutional neural network (CNN) was used to transform a low-quality image obtained with only three plane waves into one that matches the quality of an image generated using 31 plane waves. Similarly, another study used a CNN to enhance the quality of images from single plane wave imaging [252]. The CNN was trained to produce image quality comparable to that of STA imaging. Although these methods have shown promising results in improving the image quality, they are still inefficient because much of the information present in the raw RF data is lost during the initial beamforming process before being fed into the network [253].

The second group of methods replaces the entire beamforming process with a neural network. In this category, the network learns to map raw RF data directly into a beamformed image. In [254], a CNN that performs joint segmentation and beamforming directly from RF data was proposed. Another approach involved training a network on raw RF data to beamform single plane wave images [255]. In [256], a self-supervised network was introduced to achieve high frame rate STA imaging. The network was trained on raw plane wave RF data to reconstruct an STA image. However, the challenge with these approaches is that the network needs to learn the complex geometric delay calculations necessary to convert temporal information into spatial information, making the training process difficult.

The third group of methods focuses on replacing only a specific step of the beamforming process with a neural network after time delay corrections have been applied. In [257] a deep neural network accelerates the MV beamformer by adaptively estimating the apodization weights has been proposed. A similar approach was taken in [258], where the network was used to directly estimate the output of the MV beamformer instead of the weights. In [259], a Frequency domain adaptative beamformer was trained on Fourier transformed delayed signals to suppress sidelobes related artifacts.

4.2.2 Problems with adaptative beamformers

While adaptive beamformers offer significant improvements in contrast and resolution, they also have several notable drawbacks that can impact the quality and reliability of ultrasound diagnostic. One major issue is the alteration of the speckle pattern, a critical feature in medical ultrasound images. Although these beamformers are designed to suppress noise and enhance contrast, they often inadvertently suppress low-reflecting

scatterers as well, resulting in changes to the natural speckle texture of the image [260]. Consequently, the reconstructed images may exhibit poor speckle quality and reduced overall brightness, particularly in low SNR conditions [261]. This degradation in speckle quality can be critical in certain applications, as the speckle pattern provides essential information about tissue characteristics.

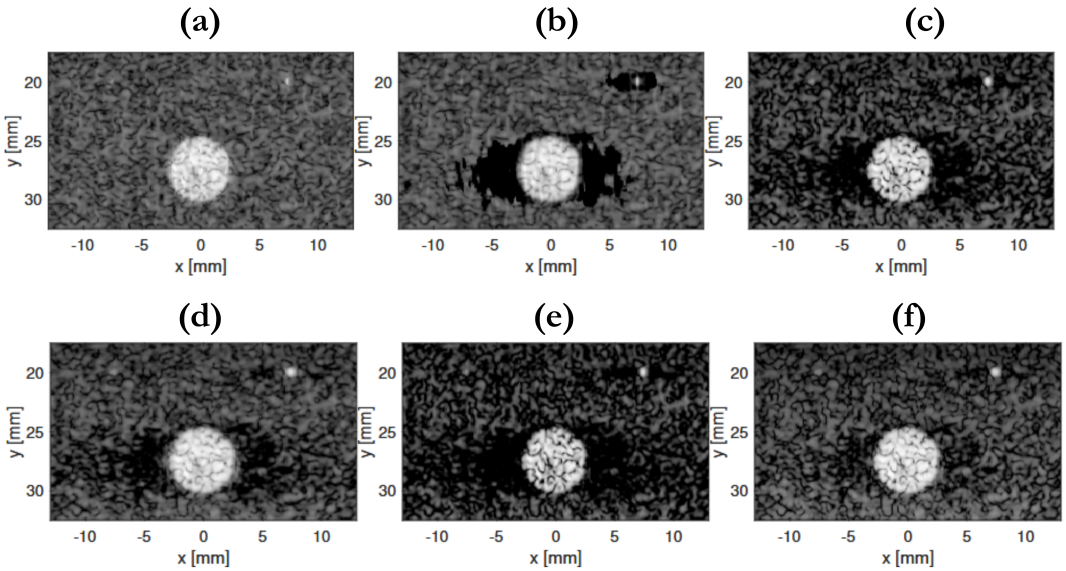

Figure 4.6: Simulated images highlighting the dark regions artifacts with (a) MV (b) EBMV (c) CF (d) GCF (e) PCF (f) DMAS. [262]

Another challenge associated with adaptive beamformers is the occurrence of dark region artifacts (DRA), especially near hyperechoic targets [261, 262]. The high sensitivity of these beamformers to partially coherent off-axis signals can lead to misinterpretation of signals, where main-lobe signals are mistaken for sidelobes signals. This results in the erroneous suppression of legitimate signals, creating artificial dark regions or severe amplitude drops that can obscure important anatomical details and give the false impression of missing tissue (Figure 4.6).

Additionally, deep learning-based beamforming methods, while promising, also present several challenges. Neural networks, despite their ability to enhance image quality, often function as black boxes, which poses significant challenges in clinical settings [250]. The opaque nature of these models makes it difficult to ensure and trust the accuracy of the results, particularly in cases where neural network hallucinations may occur [263]. These hallucinations can introduce false features into the images, appearing as hyper- or hypo-echogenic regions, potentially leading to the misidentification of lesions.

4.3 Proposed Reconstruction algorithm

In this study, we propose an innovative approach to 3D ultrasound beamforming using adaptive beamformers and deep learning to reconstruct high quality 3D images with the designed sparse array prototype from RD data obtained using a STA sequence. To mitigate the drawbacks of adaptive beamformers while leveraging their effectiveness in

reducing artifacts related to sidelobes and grating lobes, we introduce a region-specific beamforming (RSB) strategy. Instead of applying a single beamformer across the entire image, different regions or tissues will be beamformed using different beamforming techniques. Adaptive beamformers will be used in areas where sidelobes-related artifacts are dominant, while the DAS beamformer will be used in regions where preserving the natural speckle texture is essential.

To determine the most appropriate beamformer for each region, a deep reinforcement learning neural network (RSB-Net) will be trained to make these decisions dynamically. This approach aims to optimize image quality by combining the strengths of various beamforming methods, ensuring both high contrast and speckle texture preservation.

4.3.1 Overview of deep reinforcement learning

Deep reinforcement learning (DRL) is a branch of artificial intelligence that focuses on developing computer programs capable of solving complex problems using a particular machine learning approach [264]. It is a decision-making framework that has achieved super-human results in several research areas, including game playing [265], robotics [266], and self-driving cars [267]. To address a specific problem, a DRL agent is trained to make decisions by interacting with an environment. The key components of DRL are the agent, the environment, the action space, and the reward function.

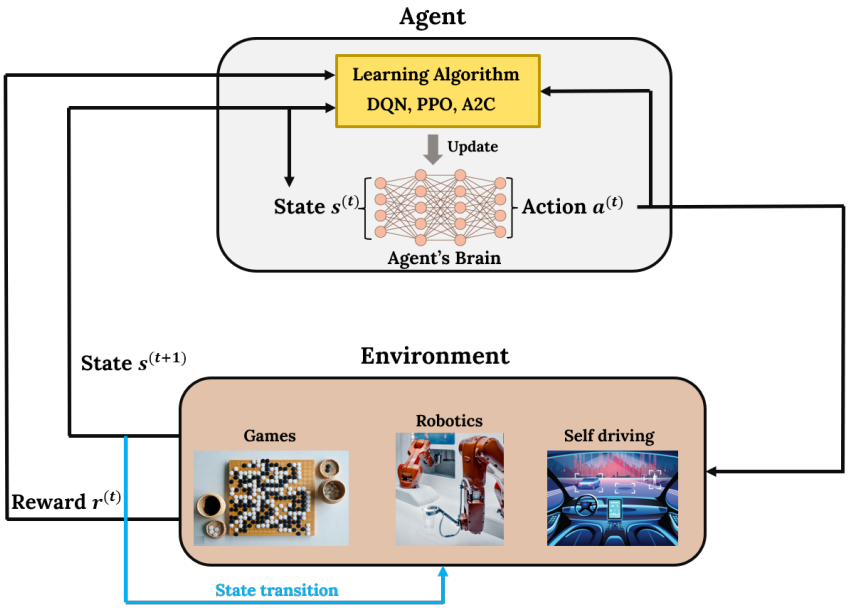

Figure 4.7: Overview of the interaction between the agent and the environment in DRL.

Figure 4.7 present an overview of the interaction between the agent and the environment. The agent is the decision-maker that learns to interact with the environment. It selects an action $a^{(t)}$ at time step (t) from an action space $\mathcal{A}$ by observing the current state $s^{(t)}$ of the environment. A DRL agent can be broken down into three main components: the interaction component, the evaluation component, and the improvement component [268]. The interaction component enables the agent to interact with the environment by taking actions and collecting data for learning. The evaluation component

assesses the behavior of the agent and identifies areas for improvement. The improvement component allows the agent to learn from past experiences and enhance its performance over time.

The environment represents the real-world problem that RL is trying to solve. It represents everything outside the agent. The complete set of variables and possible values that the environment can assume is referred to as the state $s^{(t)}$. The agent may have access to the full state of the environment or only partial access, which is referred to as an observation.

At each state, the environment presents the agent with a set of possible actions representing an action space $\mathcal{A}$. These actions can be either discrete or continuous. In discrete action spaces, only a finite set of actions is available, such as $\mathcal{A} = \{up, down, left, right\}$. In contrast, continuous action spaces involve real-valued vectors, allowing for a broader range of actions.

The core principle of RL is learning through trial and error. After each action taken by the agent, the environment transitions to a new state, and the agent receives a reward $r^{(t)}$. The rewards are determined based on a reward function, and the goal of the agent is to reinforce actions that maximize the rewards while avoiding actions that lead to lower rewards.

4.3.2 Pixel-wise adaptative beamforming : RSB-Net

We introduce RSB-Net, a novel region-specific beamforming approach for reconstructing high-quality 3D STA images. This approach involves applying different beamformers to different regions of the image: adaptive beamformers are used in areas dominated by sidelobes-related artifacts, while the DAS beamformer is used in regions where preserving speckle texture is crucial. Given that the beamforming task is formulated as a decision-making problem, DRL is an appropriate method to address this challenge. Specifically, a DRL agent is trained to select the optimal beamformer for each image pixel.

In RSB-Net, we adapt the Advantage Actor-Critic (A2C) algorithm, a well-established DRL approach that has demonstrated strong performance across a variety of reinforcement learning tasks [269]. A2C has recently been applied to several pixel-wise denoising tasks, yielding high quality results [270–272]. This algorithm belongs to the actor-critic reinforcement leaning family, which integrates both a value-based and policy-based learning methods. Therefore, the A2C algorithm employs two neural networks: the policy network (θ_p), referred to as the actor, and the value network (θ_v), known as the critic. At each time step t, both networks receive the current state $s^{(t)}$ of the environment as input. The actor is responsible for selecting actions by learning a policy $\pi(s^{(t)})$, which represents a probability distribution over possible actions given the state $s^{(t)}$. Simultaneously, the critic evaluates the action taken by the actor by estimating the value function $V(s^{(t)}, \theta_v)$, which quantifies the expected reward from the current state $s^{(t)}$. At each time step, the total discounted reward is calculated as follows:

$$R^{(t)} = \sum_{i=0}^{k-1} \gamma^i r^{(t+i)} + \gamma^k V(s^{t+k}, \theta_v) \tag{4.5}$$

where γ is the discount factor, $r^{(t)}$ is the immediate reward at state t calculated using the reward function, and θ_v represents the parameters of the value network (θ_v).

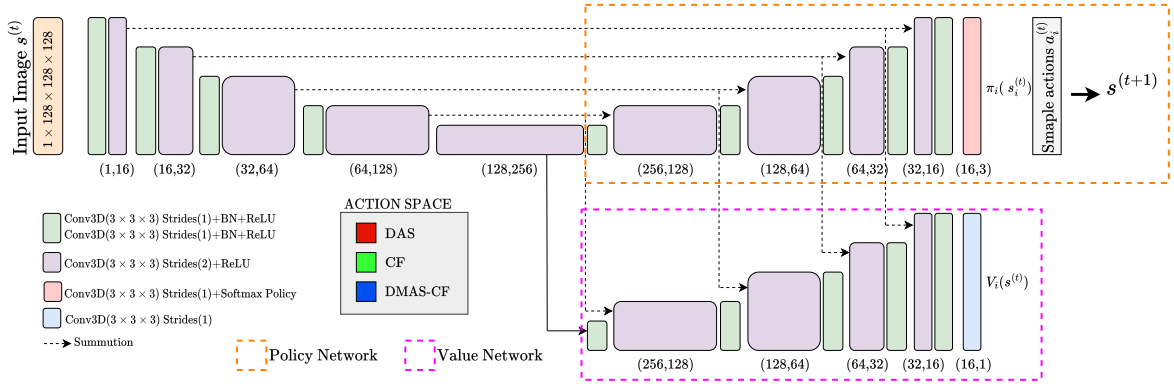

Figure 4.8: Overview of RSB-Net architecture : it corresponds to FCN adaptation of A2C algorithm with Policy Network and Value Network.

The policy network (θ_p) outputs the policy $\pi(s^{(t)})$ for selecting action $a^{(t)}$ from the action space $\mathcal{A}$, resulting in an output dimension equal to the size of the action space. The gradient for the policy network parameters is then calculated as follows:

$$d\theta_p = -\nabla_{\theta_p} \log \pi(a^{(t)}|s^{(t)}) A(a^{(t)}, s^{(t)}) \tag{4.6}$$

Where θ_p represents the actor network parameters, and $A(a^{(t)}, s^{(t)}) = R^{(t)} - V(s^{(t)})$ is known as the advantage, which measures how much better or worse an action taken in state $s^{(t)}$ is compared to the average action. Similarly, the gradients for the critic network parameters θ_v are calculated as follows:

$$d\theta_v = \nabla_{\theta_v} \left(R^{(t)} - V(s^{(t)})\right)^2 \tag{4.7}$$

To select a different beamformer for each pixel in the 3D image, in RSB-Net, each pixel i ($i = 1, 2, \ldots, N$) is treated as an individual A2C agent. The DRL environment in this study contains the received RF data and a beamformed image. However, RSB-Net only observes the beamformed image at each time step t which will represent the state $s^{(t)}$ of the environment. The initial state $s_i^{(0)}$ of the environment is a DAS beamformed image. Consequently, each one of the i agents has a policy $\pi_i(\ s_i^{(t)})$ that represents the probability of taking action $a_i^{(t)}$ by observing the state $s_i^{(t)}$ of the i^{th} pixel. Subsequently, at each time step, each agent selects a different beamformer to reconstruct the image pixel that provides the highest reward (see Section 4.4.1), resulting in an overall image with improved quality compared to the previous time step. This approach applies the A2C algorithm at the pixel level, allowing for pixel-specific beamforming rather than selecting a single action for the entire image. However, training N independent A2C agents to choose actions that maximize the total reward for each pixel is computationally expensive, particularly for 3D ultrasound images.

In this study, to avoid the computational burden of training N individual A2C agents, we adopt a strategy similar to that used in image denoising [270–272]. We propose to use a fully convolutional network (FCN) instead of N separate networks. By extending the A2C algorithm into a fully convolutional form, all N agents (pixels) can be trained simultaneously while sharing parameters. This approach effectively extends the multi-

agent deep reinforcement learning paradigm by representing all agents as a 3D image. The architecture of the proposed RSB-Net, representing a convolutional form of the A2C algorithm, is depicted in Figure 4.8.

To train the RSB-Net, at each time step, the environment provide the RSB-Net with a beamformed image representing state $\pi_i(s_i^{(t)})$. This image is processed through an encoder-decoder architecture, which constitutes both the policy network and the value network, sharing the same encoder. Each agent samples different discrete actions from the current policy, corresponding to beamforming techniques, to enhance the image quality. In this study to take into account the high image dimension in 3D ultrasound imaging, the action space is limited to three available actions—DAS, CF, and DMAS-CF (a hybrid combination of DMAS and CF which consists of weighting the DMAS image with CF)—to manage computational complexity (Figure 4.8).

4.4 Training of RSB-Net

4.4.1 Reward function

The primary objective of RSB-Net is to reconstruct an 3D ultrasound image free from artifacts associated with the high sidelobe levels inherent to sparse arrays while preserving the quality of the speckle. During training, at each time step, the image reconstructed by RSB-Net agents is compared to a high-quality target image. The reconstruction process of this high quality image will be discussed in detail in the following section. The reward for each agent is determined by the distance between the reconstructed pixel and its corresponding pixel in the target image. To consider the high dynamic range characteristic of ultrasound images, this distance is computed as :

$$\mathcal{D}_i^{(t)} = \left\| g_\alpha(s_i^{(t)}) - g_\alpha(\hat{s_i}^{(t)}) \right\|_2 \tag{4.8}$$

where $s_i^{(t)}$ represents the reconstructed pixel, and $\hat{s_i}^{(t)}$ is the corresponding pixel in the target image. The function g_α is a signed compression function used to account for the dynamic range, defined as:

$$g_\alpha(s_i) = \text{sign}(s_i) \log_\alpha \left(\frac{\alpha}{\max(\alpha, |s_i|)} \right) \tag{4.9}$$

with $\alpha \in (0, 1)$. In this study the value of alpha was chosen to take into account a dynamic range of -70dB. For further details on this function, please refer to [252]. The reward for each pixel at each time step is then calculated as:

$$r_i^{(t)} = \mathcal{D}_i^{(t)} - \mathcal{D}_i^{(t+1)} \tag{4.10}$$

This reward represents the difference between the distances $\mathcal{D}_i^{(t)}$ and $\mathcal{D}_i^{(t+1)}$ after taking action $a_i^{(t)}$. The reward value increases as $\mathcal{D}_i^{(t+1)}$ decreases, indicating that RSB-Net effectively minimizes the distance between the pixels of the reconstructed image and the target image, making them increasingly similar.

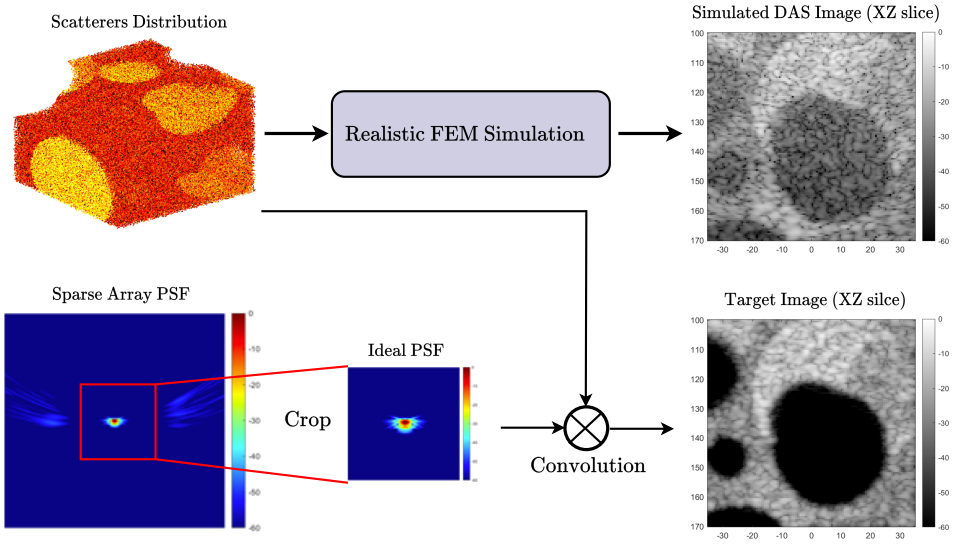

Figure 4.9: A diagram highlighting the process of generating the target image used for rewards calculation.

4.4.2 Dataset generation

To train the RSB-Net, raw STA RF datasets were generated using the realistic FEM ultrasound simulation tool developed by IMASONIC to simulate the designed sparse array prototype [229]. A dataset of 12,000 numerical phantoms was simulated, containing various phantoms with different echogenicity levels. Tissue-mimicking phantoms were created with random shapes and varying reflection levels. These phantoms, each with dimensions of 70x70x70 mm, had a scatterer density of 10 per resolution cell to ensure simulations with a fully developed speckle. Additionally, phantoms with anechoic inclusions and wire phantoms of the same size were generated. Considering that the action space comprises three beamformers—DAS, CF, and DMAS-CF—each simulated phantom was beamformed using these methods, and the resulting volumes were stored in memory, occupying a total of 358 GB. During training, instead of beamforming the pixel value with the corresponding beamformer based on the action chosen by the agent, the later simply replaces the pixel value with the corresponding pre-beamformed pixel from the selected beamformer volume. This approach significantly accelerates the training process.

To generate a high-quality target image for reward calculation during training, a 2D matrix array of the same size as the designed sparse array would ideally be used. However, to simulate images without sidelobe artifacts, the interelement spacing must be less than λ, resulting in a matrix array with 131x131 elements. Simulating thousands of phantoms with such an array is computationally infeasible. A more practical approach leverages PSF of the designed 2D sparse array prototype. The PSF consists of a main lobe, defining the scatterer positions, surrounded by high-level sidelobes, which degrade the contrast and image quality of the sparse array (Figure 4.9 and 4.5). By cropping the PSF to remove the sidelobes, an ideal high-quality PSF can be obtained. The high-quality target image is then generated by convolving this ideal PSF with the scatterer distribution, as illustrated in Figure 4.9. This 3D convolution operation is computationally inexpensive, enabling the creation of high-quality 3D ultrasound images.

4.4.3 Implementation details

The RSB-Net was implemented using PyTorch [273] and trained on STA RF dataset of 12,000 simulated phantoms. For each phantom, four volumes of size 128x128x128 pixels were reconstructed and stored in memory to accelerate the training process: a DAS volume, a CF volume, a DMAS-CF volume, and a high-quality volume. The dataset was split into 9,600 phantoms for training, 1,200 for validation, and 1,200 for testing. DRL algorithms are typically trained in an episodic manner. RSB-Net was trained for a maximum of 99,000 episodes, with the agent interacting with the environment for 10 time steps during each episode. Training was performed using the ADAM optimizer [274], with an initial learning rate of 0.001, which was scheduled to decrease according to $(1 - \frac{\text{Episode}}{\text{Max episodes}})^{0.9}$. The entire training process took approximately one week on an NVIDIA Quadro RTX 6000 GPU.

4.5 Results

In this section, we present the results obtained on the test dataset using the RSB-Net agents after training. We first discuss the overall reward curve observed during the 99,000 training episodes (Figure 4.10). The displayed overall reward is calculated as the mean reward obtained by all agents during each time step of an episode. Initially, during the first few episodes, the agents received very low rewards as the reconstructed images significantly differed from the target images. This is primarily due to the agents being in an exploration phase at the start, where the actions chosen are largely random. However, after several training episodes, the agents gradually learn a policy that enables them to select actions that maximize their rewards. As a result, the reconstructed images become increasingly similar to the target images, and the reward curve stabilizes.

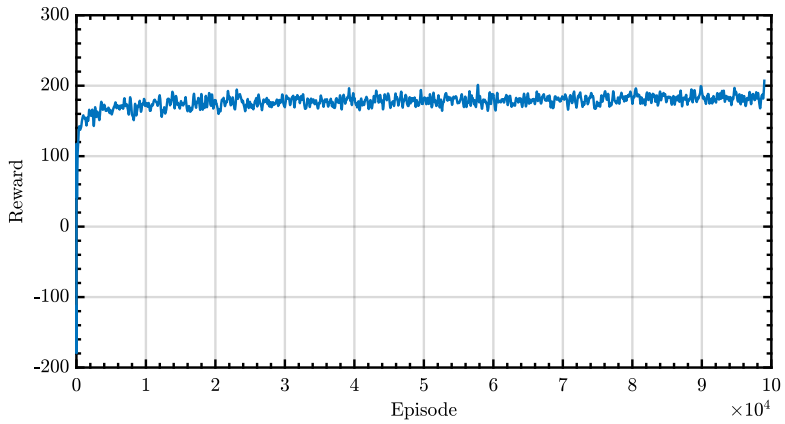

Figure 4.10: The average reward obtained by the agents during 99000 training episodes.

4.5.1 Simulated data

Figure 4.11 presents a comparison of beamformed images obtained using DAS, the target image, and RSB-Net of a simulated wire phantom with wires placed in different spatial

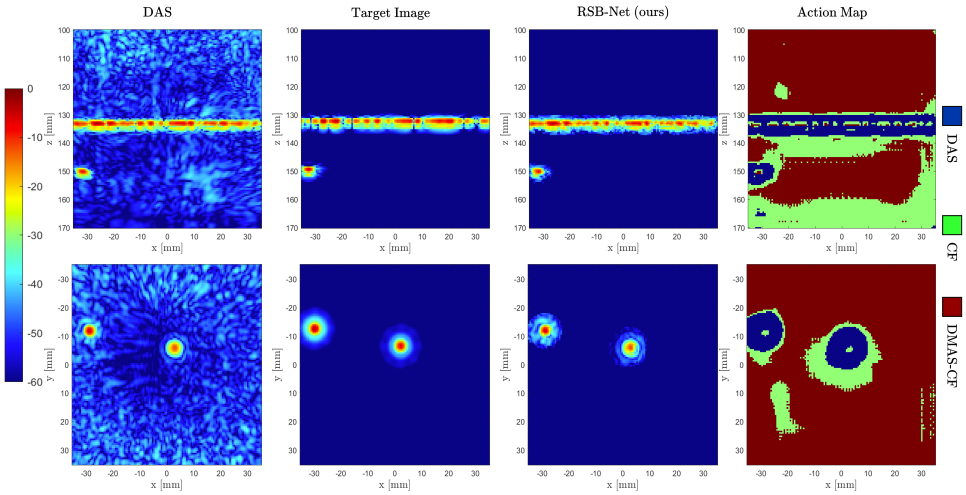

Figure 4.11: A comparison of the wire simulated reconstructed images with, DAS (First column), Target image (Second column) and RSB-Net (third column) with the action map representing the beamformer chosen for each pixel (fourth column).

directions. The first row shows XZ slices, while the second row shows XY slices from the 3D reconstructed volume displayed with a -60 dB dynamic range. A visual assessment demonstrates the superior quality of the images produced by the proposed RSB-Net compared to those generated by DAS. While the DAS images reveal the wires in both XZ and XY slices, their quality is compromised by high sidelobe artifacts from the sparse array. In contrast, RSB-Net effectively suppresses these artifacts, resulting in images with a quality comparable to that of the target images with a texture around the wires that is comparable to what is obtained with DAS.

Table 4.1: Comparison of axial resolution, lateral resolution and sidelobes level between DAS, Target Image and RSB-Net.

	δ_{ax}(mm)	δ_{lat}(mm)	Sidelobes level (dB)
DAS	1.30	2.20	-53.43
Target Image	1.20	2.30	-116.37
RSB-Net	1.20	2.10	-101.92

Figure 4.11 (fourth column) also illustrates the actions taken by the RSB-Net agents to reconstruct the images. The action maps highlight the beamformer selected for each pixel in the image. Since adaptive beamformers, such as CF and DMAS-CF, are highly effective in reducing artifacts associated with the high sidelobe levels of sparse arrays, regions where no wires are present were specifically beamformed using these adaptive methods. To preserve the speckle characteristics and ensure they match the target images, the RSB-Net agents applied DAS beamforming to regions where wires are present.

The visual assessments of the images depicted in Figure 4.11 are supported by the quantitative metrics summarized in Table 4.1. The resolution was evaluated in terms of axial and lateral -6 dB resolutions on a wire, and RSB-Net demonstrated resolutions comparable to those of both the DAS and target images. The most significant improvement was observed in artifact reduction, assessed by calculating the sidelobes level. DAS

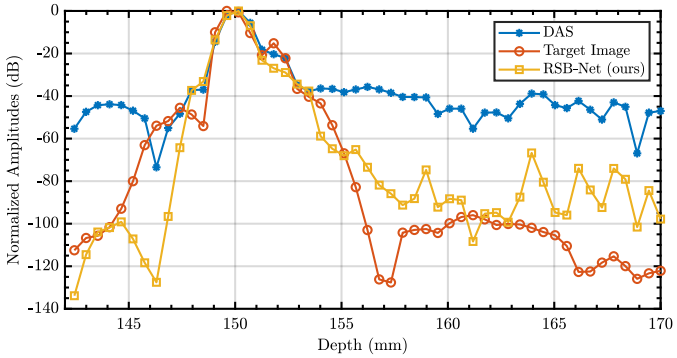

Figure 4.12: Axial line plots on a wire at 150mm highlighting the sidelobes level for the three images displayed in Figure 4.11 (DAS, Target Image, RSB-Net).

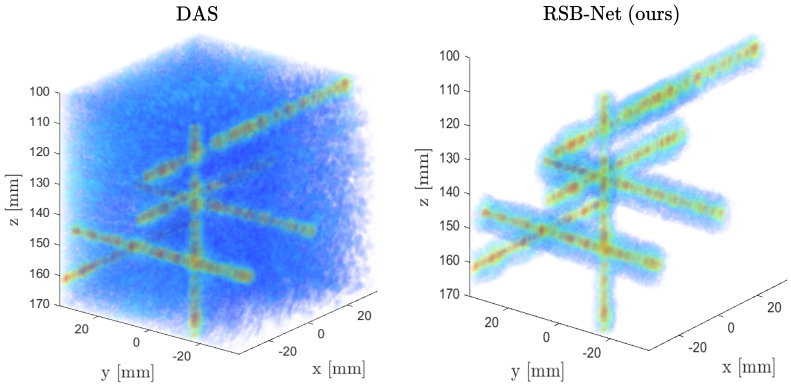

Figure 4.13: Comparison of the a 3D volumetric rendering of the simulated wires beamformed volumes with DAS and RSB-Net.

images exhibited the poorest performance, with a sidelobes level value of -53.43 dB. In contrast, RSB-Net achieved superior performance, closely matching the value obtained with the target images, with a sidelobes level of -101.92 dB, which is substantially lower than the -60 dB dynamic range typically used for displaying ultrasound images. These findings are further corroborated by plotting an axial line on an XZ slice of a wire at a depth of 150 mm, as shown in Figure 4.12. The plots confirm that all three methods exhibit similar axial resolution. Additionally, the sidelobe levels of the DAS beamformer curve are notably higher (exceeding -50 dB) compared to the target image and RSB-Net curves.

Figure 4.13 presents a comparison of the 3D renderings of the entire beamformed volume containing six wires, using DAS and RSB-Net beamforming methods. Both volumes are displayed at a -60 dB dynamic range. The high sidelobes-related artifacts in the DAS 3D volume significantly degrades the visualization quality of the individual wires. In contrast, the 3D volume reconstructed using RSB-Net effectively eliminates these sidelobes artifacts, resulting in a clear representation of the wires and greatly improving the overall visualization.

The reconstruction results for the simulated tissue-mimicking phantom with various random shapes are presented in Figure 4.14. XZ and XY slices extracted from the whole beamformed volumes using DAS beamforming, the target image, and RSB-Net are dis-

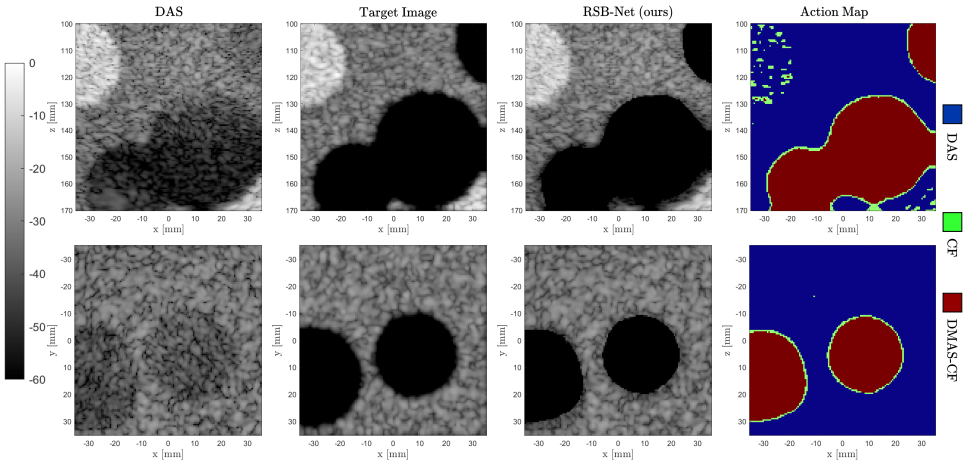

Figure 4.14: A comparison of the simulated reconstructed images with, DAS (First column), Target image (Second column) and RSB-Net (third column) with the action map representing the beamformer chosen for each pixel (fourth column).

played at a dynamic range of -60 dB. The DAS beamformed images exhibit significantly lower quality, particularly in regions containing anechoic inclusions, where sidelobe artifacts dominate, making it difficult to distinguish these inclusions from the surrounding speckle. In contrast, the images reconstructed by RSB-Net show a important quality improvement, closely matching the quality of the target image. The anechoic inclusions are clearly visible, with artifacts effectively removed.

The action maps representing each action taken by an RSB-Net agent during beamforming are displayed in Figure 4.14 (fourth column). The maps confirm the obervations made on the wires phantom results and reveal the strategy used to achieve the high quality of the reconstructed images. The DMAS-CF beamformer was applied to reconstruct pixels within the anechoic inclusions to minimize artifacts. The DAS beamformer was used in regions where speckle dominates, preserving its texture, while the CF beamformer was employed in transition zones between speckle regions and anechoic inclusions.

Table 4.2: Comparison of the CR (the lower the better) and gCNR (the higher the better) values between DAS, Target image and the RSB-Net calculated on the images in figure 4.14.

	CR (dB)	gCNR
DAS	-8.60	0.33
Target Image	-71.78	0.99
RSB-Net	-61.54	0.98

The visual comparisons are corroborated by computing the CR and gCNR [275] to assess the contrast enhancement achieved by RSB-Net. The results, summarized in Table 4.2, were obtained from an anechoic inclusion within the beamformed volumes. The CR and gCNR values show significant improvement with RSB-Net compared to DAS beamforming. Specifically, RSB-Net achieved values close to those of the target image, with a CR of -61.54 dB and a gCNR of 0.98, whereas the DAS beamformer produced a CR of -8.60 dB and a gCNR of 0.33. Additionally, a 3D rendering of the entire reconstructed volumes using DAS and RSB-Net is presented in Figure 4.15, demonstrates the superiority

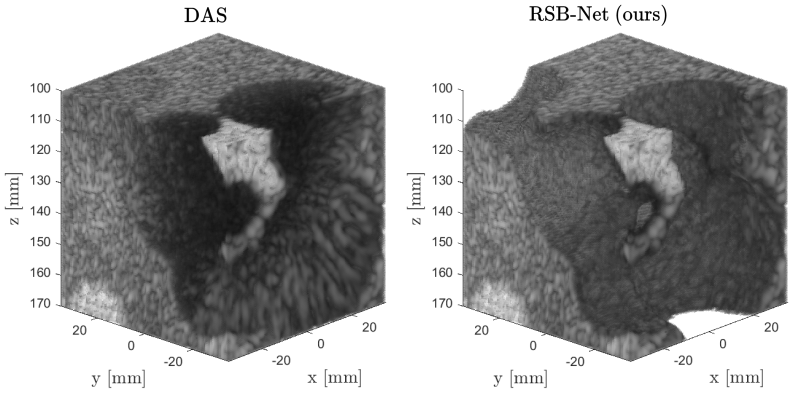

Figure 4.15: Comparison of the a 3D volumetric rendering with a dynamic range of -60dB of the simulated tissue-mimicking phantom beamformed volumes with DAS and RSB-Net.

of the proposed method. The anechoic inclusions are clearly visible in the RSB-Net volume while in the DAS volume the sidelobes artifacts make the visualization difficult.

4.5.2 Experimental data

To further validate the generalizability of RSB-Net on real-world ultrasound data, a comparative analysis was conducted with the DAS beamformer using experimental data. The experimental measurements were performed using the Verasonics Vantage 256 system (Verasonics Inc., Redmond, WA) with the designed 256-elements spiral sparse array operating at a central frequency of 1 MHz (section 4.1). Two types of experimental phantoms were used to acquire STA RF data : a nylon wire phantom positioned at a depth of approximately 140 mm and a tissue-mimicking phantom containing a cylindrical inclusion with a 30 mm diameter placed at a depth of 100 mm.

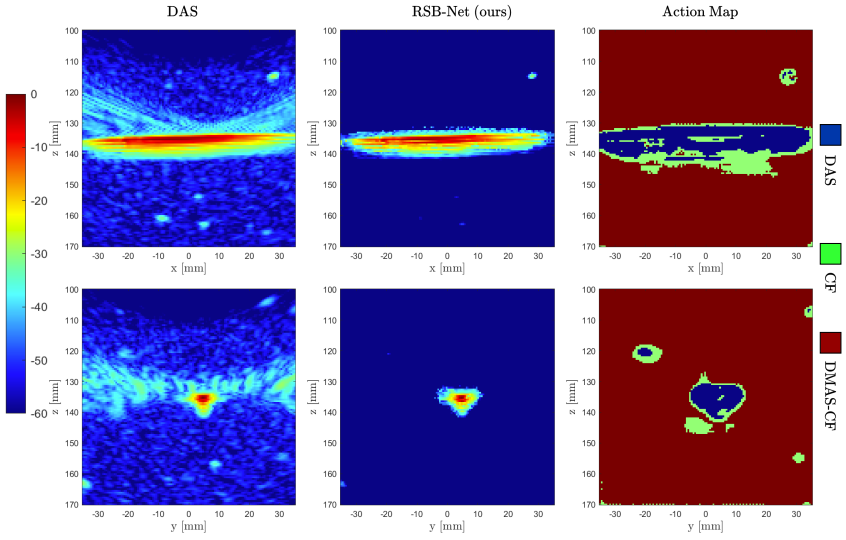

Figure 4.16: Experimental reconstructed images of a wire phantom with, DAS (First column) and RSB-Net (third column) with the action map representing the beamformer chosen for each pixel (fourth column).

Figure 4.16 presents the experimentally reconstructed images of the wire phantom using both DAS beamforming and RSB-Net agents. The images correspond to XZ and YZ slices extracted from the 3D reconstructed volume and displayed at a dynamic range of -60dB. As observed with the simulated data, the experimental DAS-reconstructed images suffer significantly from sidelobe-related artifacts. Altough the wire is still visible, the level of the sidelobe artifacts is still high especialy in the lateral direction to the wire. In contrast, the images reconstructed using RSB-Net demonstrate superior quality, with sidelobe artifacts being suppressed, and only the wire is visible. This will translate to images with high contrast for the tissue-mimicking phantom. Additionally, the action maps representing the action taken by each RSB-Net agent during the reconstruction process is shown in Figure 4.16 (third column). The maps reveal the RSB-Net agent have the same behavior as the one observed on simulated data.

Table 4.3: Comparison of axial resolution, lateral resolution and sidelobes level between DAS and RSB-Net calculated on experimental wire phantom.

	δ_{ax}(mm)	δ_{lat}(mm)	Sidelobes level (dB)
DAS	1.19	2.24	-42.94
RSB-Net	1.03	2.20	-96.80

Table 4.3 presents the quality metrics calculated for volumes beamformed using DAS and RSB-Net. The resolution comparisons yielded results consistent with those observed in the simulated wire phantom, with RSB-Net demonstrating lateral and axial resolutions comparable to those achieved by the DAS beamformer. The reduction of sidelobe-related artifacts was evaluated by calculating the sidelobes level around the wire. Compared to DAS images, RSB-Net showed significant improvements in sidelobes level by 53.86dB. Additionally, Figure 4.17 provides a comparison of the 3D renderings of the entire beamformed wire volume. RSB-Net effectively eliminates sidelobe artifacts compared to the DAS beamformer, resulting in a clear 3D representation of the wire surrounded by a number of scatterers corresponding to floating particles in water hardly visible in the DAS volumetric rendering as they are blended within the sidelobes artifacts.

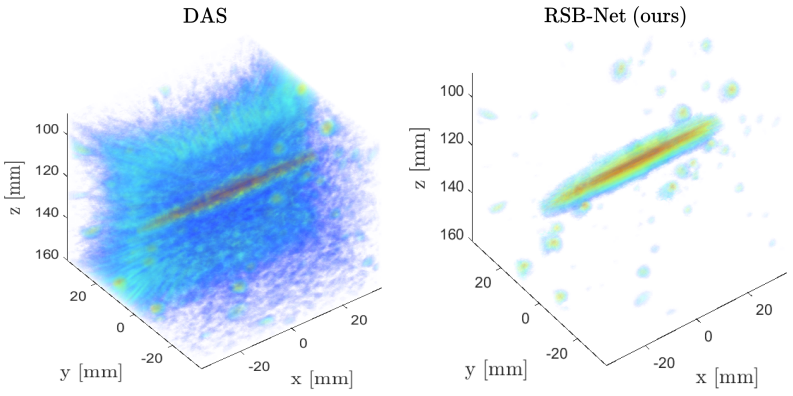

Figure 4.17: 3D volumetric rendering of the experimental wire phantom beamformed volumes with DAS and RSB-Net.

Figure 4.18 shows the reconstruction results on the experimental tissue-mimicking phantom using DAS and RSB-Net. The experimental outcomes perfectly match the

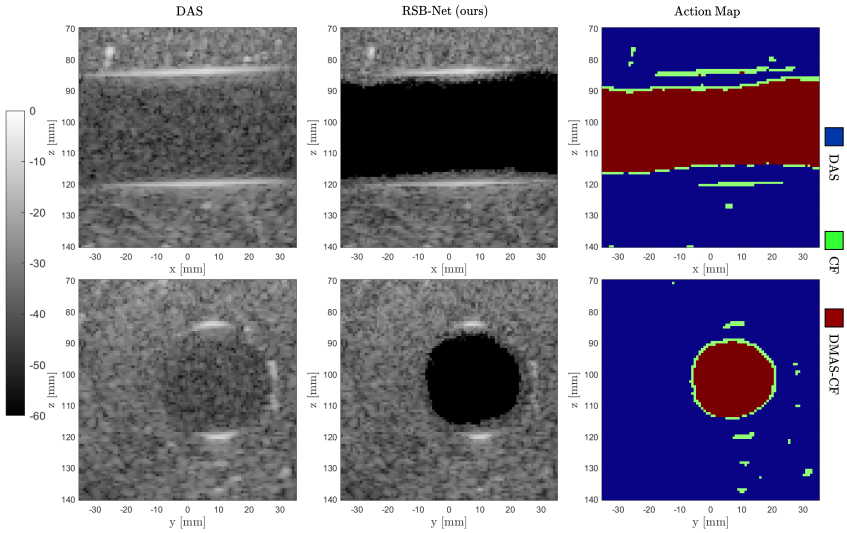

Figure 4.18: Experimental reconstructed images of a tissue-mimicking phantom with, DAS (First column) and RSB-Net (third column) with the action map representing the beamformer chosen for each pixel (fourth column).

simulation results, with RSB-Net images showing superior quality compared to those produced by the DAS beamformer. According to the action map of the RSB-Net agent, DAS beamforming was employed to reconstruct pixels in regions mimicking tissue speckle to preserve the texture, while DMAS-CF was utilized to reduce sidelobe artifacts. The sidelobes artifacts within the anechoic inclusion was entirely removed by RSB-Net, leading to improved CR and generalized gCNR values, as shown in Table 4.4. Specifically, RSB-Net achieved a CR improvement of 51.05 dB and a gCNR enhancement of 0.64 compared to the DAS beamformer.

Table 4.4: Comparison of the CR (the lower the better) and gCNR (the higher the better) values between DAS, Target image and the RSB-Net calculated on the images in figure 4.18.

	CR (dB)	gCNR
DAS	-6.66	0.34
RSB-Net	-57.71	0.98

The improvement in overall image contrast obtained with RSB-Net results in significantly better image quality, enabling high-quality 3D rendering of the entire beamformed volume, as observed in Figure 4.19. In the RSB-Net rendering, the entire cylindrical anechoic inclusion is clearly visible, while in the DAS beamformer rendering, it is difficult to differentiate the inclusion from the surrounding speckle.

4.6 Discussion

The primary objective of this study was to develop a novel reconstruction algorithm to reconstruct high quality 3D images with the designed sprase array prototype from STA imaging RF data. The prototype array was fabricated following a simulation study that compared various potential technologies. These simulations were based on the concept

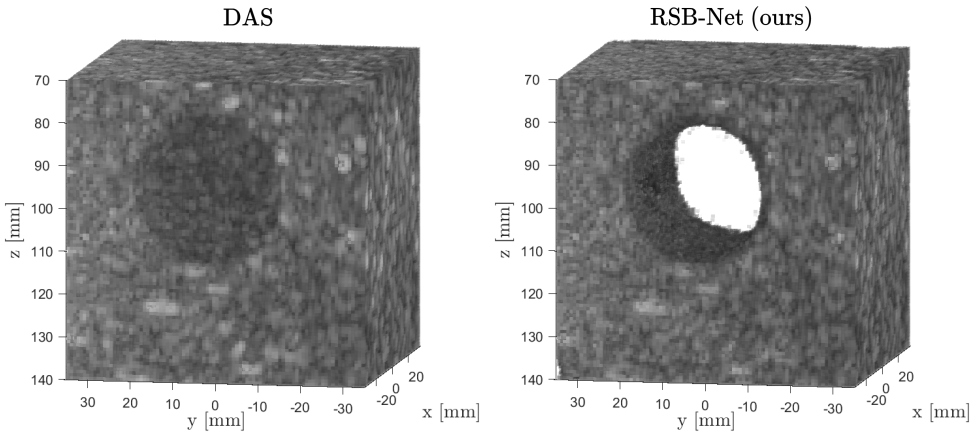

Figure 4.19: 3D volumetric rendering of the experimental tissue-mimicking phantom beamformed volumes with DAS and RSB-Net.

of angular impulse responses, calculated using a FEM model. FEM modeling provides an accurate representation of the array elements, enabling realistic 3D ultrasound image simulations.

The developed prototype features an aperture size of 10 cm, following a Fermat's spiral distribution with 256 elements operating at a central frequency of 1 MHz. Each element, with a relatively large size of 3.5mm ($\frac{7}{3}\lambda$) to enhance the SNR, is coupled with a diverging lens to improve directivity. Further details and discussions on the FEM simulation model and the experimental characterization of the fabricated prototype will be provided in the thesis manuscript of Jean-Baptiste Jacquet, as part of his PhD work.

Although the design of the array is based on Fermat's spiral distribution which is known for its good performance, especially in terms of sidelobe levels, the image quality reconstructed using the DAS beamformer still suffers from sidelobe artifacts (Figure 4.5). These artifacts can reduce the accuracy of medical diagnostics in clinical applications. To enhance the quality of the reconstructed images, the RSB-Net was developed.

RSB-Net is a deep reinforcement learning-based model that combines the performance of adaptive beamformers with the DAS beamformer within a learning framework to improve image quality. Adaptive beamformers are known for their effectiveness in reducing off-axis artifacts due to high sidelobe levels; however, they can degrade speckle texture quality and introduce dark regions in images. RSB-Net, based on the A2C deep reinforcement learning algorithm, was trained to selectively apply adaptive beamformers in regions where sidelobe artifacts are dominant and the DAS beamformer in speckle regions to preserve texture.

By implementing A2C as a fully convolutional network, RSB-Net treats each pixel of the image as an independent agent that selects actions based on a policy designed to maximize its rewards. The rewards are directly tied to the quality of the reconstructed image—the better the quality, the higher the rewards. The reward curve represented in Figure 4.10 highlights the advantage of FCN representation of A2C, the agents obtain a good policy that allows the maximization of thier rewards after just few thousands of episodes. This is due to the fact that the FCN representation allows the agent to share all the parameters, allowing them to gain N (number of pixels) experiences at a single pass [270].

In this study, the action space was limited to three beamformers: DAS, CF, and DMAS-CF. The CF and DMAS-CF adaptive beamformers were chosen for their effectiveness in reducing off-axis signals without imposing a high computational burden, which helps accelerate the training process. The realism of the FEM simulation tool enabled the generation of a high-quality dataset of RF data using the STA imaging sequence, which was used to train RSB-Net and subsequently apply it to real experimental data. In addition to its realism, the GPU implementation of the simulator enabled the rapid simulation of 3D tissue-mimicking phantoms with a large number of scatterers. Since the prototype probe was fixed to a 10 cm aperture, the tissue-mimicking phantoms were generated to fit under the probe, with dimensions of 70x70x70 mm. In this configuration, the maximum angle between a phantom scatterer and an element of the probe was 30°. This limited the number of AIR loaded into the GPU memory to 30 for transmission and 30 for reception, reducing computational overhead due to memory access.

Additionally, to ensure memory coalescing—a key optimization in CUDA programming—all scatterers were sorted by angle relative to the transmitting element before transmission. This sorting ensured that all threads in a warp accessed the AIR in contiguous memory locations, allowing for access in a single transaction. With these optimizations, the simulation of a tissue-mimicking phantom with around 5 million scatterers was completed in approximately 10 minutes and the whole training datasets in around 4 days on a cluster with multiple GPUs.

The accuracy of the simulation tool is confirmed by comparing the various metrics calculated in both the simulation study (Tables 4.1 and 4.2) and the experimental study (Tables 4.3 and 4.4). The simulation and experimental results showed similar axial and lateral resolution on the wire phantom, with values around 1.2 mm and 2.2 mm, respectively. Additionally, the contrast values were also approximately close in the DAS beamformer, with gCNR values of 0.33 and 0.34 for the simulated and experimental tissue-mimicking phantoms, respectively.

In Figure 4.11 and 4.14, we evaluated the performance of RSB-Net on simulated data, including a wire phantom and a tissue-mimicking phantom with random shapes and varying echogenicity. The results demonstrated that the agents successfully learned a policy that enables them to apply the DMAS-CF beamformer in regions with high sidelobes-related artifacts. DMAS-CF is particularly effective in reducing strong artifacts by combining the advantages of CF in suppressing incoherent signals related to sidelobes and the high sensitivity of DMAS to these signals. The reward function (Equation 4.10), which is based on the distance from the target ideal image, guided the agent to preserve speckle quality by applying the DAS beamformer in regions where the speckle is dominating. Additionally, to maintain smooth transitions between speckle regions and anechoic inclusions, the CF beamformer was applied to take into acount the shape of the PSF that was used in the generation of target images.

These simulation results were corroborated by the experimental results shown in Figures 4.16 and 4.18. Despite not being trained on an experimental dataset, RSB-Net successfully reconstructed the 3D images of the experimental wire phantom and tissue-mimicking phantom with the same accuracy as the simulated data, as validated by the metrics in Tables 4.3 and 4.4.

By applying different beamformers to distinct regions of the image, RSB-Net effectively reconstructed high-quality ultrasound images using the designed sparse array prototype.

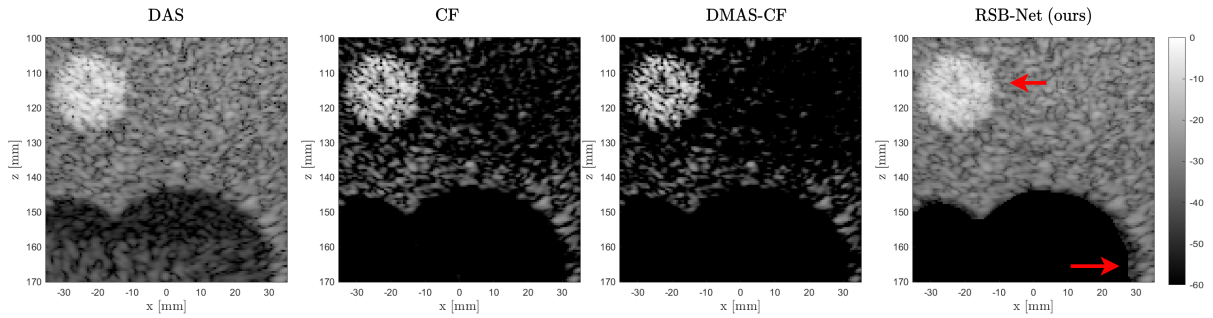

Figure 4.20: Beamfomed images from simulated tissue-mimicking volume beamformed with DAS, CF, DMAS-CF and RSB-Net highlighting the advantage of the proposed method.

This strategy leverages the advantages of adaptive beamformers in suppressing off-axis signals while avoiding their drawbacks, such as altering speckle quality. These weaknesses are evident in Figure 4.20, which compares an XZ slice from a beamformed volume using DAS, CF, DMAS-CF, and RSB-Net. The DAS image is dominated by sidelobe artifacts, which are removed by CF and DMAS-CF; however, these images exhibit a darker appearance, especially near the hyperechoic inclusion. The RSB-Net image successfully combines the benefits of CF and DMAS-CF in reducing sidelobe artifacts with the DAS beamformer and its ability to preserve speckle quality.

However, the contrast between the hyperechoic inclusion and the surrounding speckle remains unchanged from that of the DAS beamformer and has not been improved. This is still acceptable as the hyperechoic inclusion is clearly visible against the surrounding speckle, with no dark regions present. Training RSB-Net with a reward function that accounts for these regions could enhance their quality. Another potential drawback of RSB-Net is the presence of small distortions, particularly at the edges, as observed on the lower left side of the image in Figure 4.20. Including more adaptive beamformers, such as the MV beamformer, could help address this issue.

4.7 Conclusion

In this study, we introduced RSB-Net, an innovative reconstruction algorithm designed to reconstruct ultrasound images from STA RF data acquired using a newly developed 2D sparse array prototype in collaboration with IMASONIC. RSB-Net is a deep reinforcement learning-based model designed to reconstruct high-quality images by combining adaptive beamformers with the DAS beamformer. While adaptive beamformers are effective in reducing off-axis artifacts caused by high sidelobes level, they often degrade speckle texture and introduce dark regions into the image. To address this, RSB-Net employs an FCN representation of the A2C algorithm, selectively applying adaptive beamformers in regions with dominant sidelobe artifacts, while using the DAS beamformer in speckle regions to maintain texture quality.

Training of RSB-Net was performed on a large, simulated dataset generated by a GPU-accelerated FEM ultrasound simulation tool. The application of RSB-Net demonstrated a significant reduction in sidelobe-related artifacts while preserving the speckle texture. On the simulated dataset, RSB-Net showed an improvement in CR and gCNR by 52.81

dB and 0.65, respectively, compared to the DAS beamformer. Despite not being trained on experimental datasets, the realism provided by the FEM ultrasound simulation tool enabled RSB-Net to achieve similar performance when applied to experimental data. In an experimental tissue-mimicking phantom, RSB-Net achieved gains of 51.01 dB in CR and 0.64 in gCNR compared to the DAS beamformer.

While RSB-Net shows strong performance in enhancing the contrast of reconstructed images, it does have some limitations, such as challenges in improving the contrast of hyperechoic inclusions and shape distortions observed at the edges of anechoic inclusions. These issues are currently under investigation. Overall, the successful application of RSB-Net to both simulated and experimental data acquired with the developed sparse array prototype validates its robustness and effectiveness, making it a promising approach for other acquisition and imaging systems.

Summary and perspectives

In this thesis, I addressed two major challenges facing development of sparse arrays for 3D ultrasound imaging: enhancing the low signal-to-noise ratio (SNR) caused by low element sensitivity and improving the image quality affected by the inherent sparsity of the arrays. In ***chapter 1***, I introduced the concept of the beampattern, which plays a crucial role in the design and optimization of sparse arrays. I focused on two key properties of the beampattern: the main lobe width, which defines image resolution, and the sidelobes level, which is related to the image contrast. I also discussed various arrays used for 3D ultrasound image acquisition, with a focus on sparse arrays, and details on their limitations in terms of sensitivity and contrast.

In ***chapter 2***, I aimed to enhance the SNR of 2D sparse array images acquired using STA imaging methods. STA was selected to achieve high-quality 3D imaging with a higher frame rate compared to conventional focused imaging. Sparse arrays, while offering advantages in terms of reduced element count, are known for their low sensitivity due to the small element size typically used in their design. To address this limitation, I explored the use of coded excitation sequences to transmit more energy and thereby increase the SNR of the array.

I proposed a CCC STA excitation scheme based on Complete Complementary Codes (CCC), specifically (N, N, MN/P)-CCC, which are binary sequences composed of N sets, each containing N sequences of length MN/P. These codes are known for their ideal auto-correlation and cross-correlation properties. Leveraging these properties, CCC STA allows each element of the array to transmit a distinct binary sequence from a CCC set, the received RF signals are decoded through cross-correlation with the transmitted sequence. This process separates the contributions of each element and retrieves the conventional STA dataset with improved SNR, without interferences between the elements.

To validate CCC STA, I conducted simulations using the Field II software and experiments with a sparse array optimized on the 8 MHz Vermon 2D matrix probe. The proposed CCC STA scheme was compared against five well-known coded excitation schemes: Hadamard STA, Chirp STA, Golay STA, Hadamard-Chirp STA, and Hadamard-Golay STA.

Compared to conventional STA, simulations showed that the CCC STA increased the SNR of the sparse array by approximately 36.12 dB and enhanced image contrast by nearly 24.18 dB, all while maintaining axial resolution and the number of transmissions unchanged. Experimental results further demonstrated gains in SNR and contrast of 31.25 dB and 10.94 dB, respectively. The comparison with other coded excitation schemes, such

as Hadamard-Chirp STA and Hadamard-Golay STA, highlighted the superior performance of CCC STA in increasing the SNR while preserving axial resolution and frame rate.

Future work will focus on addressing the effects of frequency-dependent attenuation on the CCC STA decoding process. Such attenuation can distort the received signals, leading to deviations in the matched filter output from the autocorrelation of the coded sequence. This results in reduced SNR gains and the appearance of axial sidelobes, which in turn can decrease image contrast. Given that binary sequences are known to be sensitive to frequency-dependent attenuation, I will first investigate how CCC STA is affected and then implement strategies to reduce its impact on decoding.

Additionally, the effect of motion will be considered. The ideal auto-correlation and cross-correlation properties of CCC are based on the assumption that the medium is not moving. If targets move between CCC STA transmissions, the complementary properties of CCC will be compromised, leading to shifts between the sidelobes of each binary sequence. This shift increases axial sidelobes during decoding, proportional to the velocity of the moving medium. We will address this issue by studying the implementation of CCC STA in abdominal applications and developing motion correction algorithms to reduce the effects of motion [224–226, 276–278].

In ***chapter 3***, I addressed the challenge of achieving ultrafast 3D ultrasound imaging using 2D sparse arrays. The primary objective was to enhance the SNR in ultrafast imaging with sparse arrays, thereby improving both the frame rate and penetration depth. To achieve this, we explored two advanced imaging methods: plane wave imaging and STA imaging using coded excitation in both cases.

In the context of plane wave imaging, we introduced the MPWI-3C technique, which leverages the ideal correlation properties of (N, N, MN/P)-CCC binary sequences. This method enables quasi-simultaneous transmission of tilted plane waves, each carrying a distinct sequence during every transmission event. The received echoes are decoded as if the plane waves were transmitted individually, resulting in higher SNR without sacrificing frame rate. Additionally, the nature of (N, N, MN/P)-CCC allows for the generation of shorter sequences, avoiding the creation of large blind zones.

For STA imaging, I introduced USTA (Ultrafast Synthetic Transmit Aperture), which leverages the unique correlation properties of Mutually Orthogonal Complementary Pairs (MOCPs). MOCPs consist of sets of two binary sequences with ideal auto-correlation sums within each set and ideal cross-correlation sums between adjacent sets. USTA requires only two transmission events to retrieve the complete STA dataset. However, to mitigate the potential issue of large blind zones caused by MOCPs, we divided the sparse array into eight sub-apertures, resulting in a total of 16 transmissions—significantly fewer than the 256 transmissions required for conventional STA. Using the 16 coded USTA transmissions, we achieved a frame rate of 962 Hz while simultaneously improving SNR and contrast compared to conventional STA.

Experimental studies demonstrated that MPWI-3C outperformed CPWC, and USTA surpassed conventional STA in terms of both SNR and contrast, with only a minimal decrease in axial resolution with USTA. The increased frame rate and SNR provided by MPWI-3C and USTA also enhanced penetration depth, offering potential benefits for various clinical applications.

However, I will be investigating potential limitations of the proposed approaches, such as the impact of attenuation and motion on decoding accuracy, which represent similar

challenges to those discussed in Chapter 2. Additionally, the possible expansion of the blind zone area when transmitting a large number of plane waves with MPWI-3C will be considered. To address this, I plan to develop simultaneous transmission of all plane waves in a superposition manner instead of quasi-simultaneous transmission, which would result in a very short blind zone corresponding to the blind zone of the plane wave with the highest tilt angle [203–205].

In ***chapter 4***, I focused on developing a new reconstruction algorithm to produce high-quality ultrasound images from STA RF data acquired using a new 2D sparse array prototype developed in collaboration with IMASONIC. I introduced a region-specific beamformer RSB-Net, a deep reinforcement learning-based model designed to reconstruct high-quality images by combining adaptive beamformers with the DAS beamformer within a deep learning reconstruction framework. While adaptive beamformers are effective in reducing off-axis artifacts caused by high sidelobe levels, they often degrade speckle texture and introduce dark regions into the image. On the other hand, the DAS beamformer preserves speckle quality but suffers from sidelobe-related artifacts. To get the best of the two worlds (adaptive beamformers and DAS), RSB-Net uses a Fully Convolutional Network (FCN) representation of the Advantage Actor-Critic (A2C) algorithm, a deep reinforcement learning approach. RSB-Net selectively applies adaptive beamformers in regions with dominant sidelobe artifacts while using the DAS beamformer in speckle regions to maintain texture quality.

RSB-Net was trained on a large, simulated dataset generated using my GPU-accelerated version of the FEM ultrasound simulation tool proposed by IMASONIC. The application of RSB-Net demonstrated a significant reduction in sidelobe-related artifacts while preserving speckle texture. On the simulated dataset, RSB-Net showed an improvement in CR and gCNR by 52.81 dB and 0.65, respectively, compared to the DAS beamformer. Despite not being trained on experimental datasets, the realism provided by the FEM ultrasound simulation tool enabled RSB-Net to achieve similar performance when applied to experimental data. In an experimental tissue-mimicking phantom, RSB-Net achieved gains of 51.01 dB in CR and 0.64 in gCNR compared to the DAS beamformer.

While RSB-Net shows strong performance in reconstructing images with high contrast by removing sidelobe artifacts, particularly in anechoic inclusions, the contrast between hyperechoic inclusions and surrounding speckle remains almost the same as that produced by DAS, which is still acceptable since DAS provides decent image quality in these regions. Improving contrast in these situations will be considered in future work by proposing a new reward function to train RSB-Net. Additionally, RSB-Net produces small shape distortions, especially at the edges between anechoic inclusions and speckle regions. This issue arises from the failure to apply the coherence factor (CF) beamformer in these regions. Future studies will focus on incorporating more adaptive beamformers, such as minimum variance (MV) beamformer and phase coherence factor (PCF), to reduce these effects. Finally, RSB-Net will also be trained on MPWI-3C and USTA data to reconstruct high-quality images with ultrafast imaging sequences using sparse arrays.

Although there is still room for improvement, all the objectives set for my PhD thesis project have been met. I successfully proposed and validated new imaging sequences that enhance the SNR of sparse arrays and enable ultrafast imaging, significantly increasing the frame rate. Additionally, I developed a reconstruction algorithm capable of producing high-quality 3D images with a designed sparse array, which has been rigorously tested on

both simulated and experimental data. Building on these achievements, future research will focus on exploring and testing these contributions in more complex imaging scenarios. A key area of investigation will be the application of the developed techniques in *in vivo* imaging, to evaluate their robustness and effectiveness in real biological environments, where factors such as tissue heterogeneity and physiological noise can impact the imaging performance. Furthermore, the compatibility of these methods with advanced parametric ultrasound imaging techniques, such as blood flow imaging and elastography, will be examined to ensure their broader applicability in clinical and experimental settings.

List of publications

Journal papers

- **M. Tamraoui**, H. Liebgott and E. Roux, "Complete Complementary Coded Excitation Scheme for SNR Improvement of 2D Sparse Array Ultrasound Imaging," in IEEE Transactions on Biomedical Engineering, vol. 71, no. 3, pp. 1043-1055, March 2024, doi: 10.1109/TBME.2023.3325657.

- D. Garcia, **M. Tamraoui**, F. Varray, "Think twice before f-numbering", Ultrasonics. (Dec. 2023), Ultrasonics, Volume 138, 2024, 107222, ISSN 0041-624X, https://doi.org/10 .1016/j.ultras.2023.107222.

- (Under Review) **M. Tamraoui**, E. Roux and H. Liebgott, "Complementary Coded Multiplane Wave Sequences For SNR Increase in Ultrafast Power Doppler Ultrasound Imaging," in IEEE Transactions on Ultrasonics, Ferroelectrics, and Frequency Control.

- (Under Review) Jacquet, Jean-Baptiste; Guey, Jean-Luc; Kauffmann, Pierre; **TAMRAOUI, Mohamed**; Roux, Emmanuel; Nicolas, Barbara; Coffy, Etienne; Liebgott, Herve, "Simulation, Design and Field Analysis of a Large Divergent Element Sparse Array (LDESA) for 3D Ultrasound Imaging," in IEEE Transactions on Ultrasonics, Ferroelectrics, and Frequency Control.

Conference papers

- **M. Tamraoui**, E. Roux and H. Liebgott, "Hyperuniform Disordered Sparse Array For 3D Ultrasound Imaging," 2023 IEEE International Ultrasonics Symposium (IUS), Montreal, QC, Canada, 2023, pp. 1-4, doi: 10.1109/IUS51837.2023.10308368.

- **M. Tamraoui**, E. Roux and H. Liebgott, "Zero interleaved mutually orthogonal sequences for high frame rate synthetic transmit aperture," 2023 IEEE International Ultrasonics Symposium (IUS), Montreal, QC, Canada, 2023, pp. 1-4, doi: 10.1109/IUS51837. 2023.10308095.

- J-B., Jacquet, **M. Tamraoui**, P. Kauffmann, J-L. Guey, E. Roux, B. Nicolas, H. Liebgott, "Integrating Finite-Element Model of Probe Element in GPU Accelerated Ultrasound Image Simulation," 2023 IEEE International Ultrasonics Symposium (IUS), Montreal, QC, Canada, 2023, pp. 1-4, doi: 10.1109/IUS51837.2023.10306556.

- E. Roux, **M. Tamraoui**, H. Liebgott "Reaction-Diffusion Algorithm for Element Shaping in 2-D Sparse Array Beam Pattern Optimization," XXIXème Colloque Francophone de Traitement du Signal et des Images. GRETSI'23. Grenoble, France

Résumé en francais

Introduction générale

Selon l'Organisation mondiale de la santé, jusqu'à deux tiers de la population mondiale n'ont pas un accès facile aux équipements d'imagerie diagnostique. Parmi les modalités disponibles, l'échographie médicale est probablement la seule technologie qui pourrait être largement accessible à cette population mal desservie, ce qui en fait la modalité d'imagerie ayant le plus grand potentiel pour améliorer la santé à l'avenir. L'imagerie par échographie offre un outil diagnostique rapide et précis, fournissant des images en temps réel du corps humain à faible coût et sans recourir aux rayonnements ionisants. Actuellement, les systèmes d'échographie 2D conventionnels sont la norme dans les pratiques cliniques, capturant des tranches en temps réel du corps humain à l'aide de sondes 1D. Cependant, le principal inconvénient de l'échographie 2D conventionnelle est qu'elle utilise des techniques d'imagerie 2D pour capturer des images d'une anatomie 3D. Par conséquent, la précision du diagnostic dépend en grande partie de la capacité des cliniciens à reconstruire mentalement l'anatomie 3D à partir des images 2D, ce qui peut être particulièrement difficile lors des diagnostics ou des interventions chirurgicales. En revanche, l'imagerie par échographie 3D offre des avantages significatifs par rapport aux modalités 2D traditionnelles en révolutionnant la manière dont les professionnels de la santé visualisent et interprètent les structures anatomiques. L'un des principaux avantages de l'imagerie 3D est qu'elle fournit une représentation complète de l'anatomie, éliminant ainsi le besoin de reconstruction mentale. Cette visualisation complète réduit la dépendance à l'expertise de l'opérateur et permet de réexaminer l'organe sous différents angles, même après le départ du patient, facilitant ainsi le partage des acquisitions pour obtenir l'avis de spécialistes situés dans des hôpitaux éloignés. Malgré les nombreux avantages de l'imagerie 3D, elle n'est pas encore devenue la norme clinique. Cela est probablement dû à deux facteurs principaux : soit la qualité d'image fournie par les systèmes actuels est insuffisante, soit les systèmes sont prohibitivement coûteux. Un élément clé de la qualité d'image en imagerie échographique 3D est la sonde utilisée pour acquérir le volume. Idéalement, des sondes matriciels 2D sont utilisés pour scanner l'ensemble du volume anatomique. Le balayage du volume avec ces réseaux nécessite généralement un contrôle individuel de chaque élément transducteur de la sonde ce qui nécessite le même nombre de voies de beamforming dans le système d'ultrason. Cependant, la plupart des systèmes d'échographie actuels ne sont équipés que de 256 voies. D'un point de vue technique, la fabrication d'une sonde matricielle avec des milliers d'éléments est très complexe et coûteuse. De plus, con-

necter plusieurs milliers d'éléments a chaque voies augmente la complexité des systèmes électroniques, du transfert de données et des exigences de stockage.

Les sondes sparses ont été proposées comme une solution prometteuse pour l'imagerie échographique 3D en relevant les défis liés au grand nombre d'éléments des sondes matriciels 2D. En optimisant la répartition d'un nombre réduit d'éléments sur l'ouverture de la sonde, ils permettent de réduire le nombre de voies de beamforming nécessaires pour la formation des faisceaux, rendant ainsi possible l'utilisation de systèmes d'échographie existants, tout en offrant une flexibilité accrue dans la formation et le pilotage des faisceaux. Bien que cette approche simplifie considérablement la complexité et le coût de fabrication des sondes, elle se heurte à deux défis majeurs : une faible sensibilité et une qualité d'image réduite, notamment en termes de contraste. Pour remédier à ces problèmes, cette thèse se concentre sur l'amélioration de la sensibilité et du contraste des sondes sparses. D'une part, j'ai développé des séquences d'excitations codées pour améliorer le rapport signal sur bruit (SNR), et d'autre part, j'ai conçu un nouvel algorithme de reconstruction basé sur des réseaux d'apprentissage profond, spécifiquement développé pour un prototype de sonde sparse, afin de produire des images échographiques de haute qualité. Ces contributions visent à surmonter les principaux obstacles des sondes sparses, ouvrant ainsi la voies à des innovations significatives pour faire de l'imagerie échographique 3D la nouvelle norme en pratique clinique.

Chapitre 1 : Sondes pour l'imagerie ultrasonore 3D

Le chapitre 1 représente un état de l'art des différentes sondes utilisées pour l'imagerie ultrasonore 3D. Dans ce chapitre, nous explorerons d'abord les aspects théoriques du champ de rayonnement émis par les sondes ultrasonores. Comprendre le champ de rayonnement est essentiel pour optimiser la résolution et la qualité des images en imagerie échographique 3D. Par la suite, nous examinerons les différents types de sondes utilisées pour l'imagerie échographique 3D. Pour réaliser une imagerie ultrasonore 3D, un réseau 2D est généralement utilisé pour balayer l'ensemble du volume sans qu'il soit nécessaire de déplacer mécaniquement la sonde ultrasonore. L'université de Duke a été la première à introduire un système d'imagerie 3D en temps réel utilisant des matrices 2D composées de 20×20 éléments [12, 13]. Le système était limité par le nombre de voies de formation de faisceau disponibles, ce qui ne permettait d'utiliser que 32 éléments pour l'émission et la réception afin de créer un balayage pyramidal en 3D. La formation parallèle de faisceaux a ensuite été utilisée pour atteindre une cadence d'imagerie élevé [14]. Pour éviter les artefacts tels que les lobes secondaires et les lobes de réseau dans les images reconstruites, la configuration de la sonde matricielle doit respecter le critère de Nyquist. Ce critère stipule que la distance entre les éléments de la sonde ne doit pas être supérieur à la moitié de la longueur d'onde. Le respect de cette condition est essentiel pour maintenir le contraste de l'image et minimiser les artefacts. En outre, pour obtenir la même résolution que celle fournie par une sonde 1D conventionnelle, la sonde 2D doit contenir un nombre suffisant d'éléments dans les deux dimensions. Par exemple, pour obtenir la même qualité d'image qu'avec une sonde linéaire de 128 éléments, il faut une sonde matricielle de $128 \times 128 = 16384$ éléments. Étant donné que chaque élément doit être contrôlé individuellement afin de diriger librement le faisceau ultrasonore, le même nombre de voies que le nombre d'éléments est nécessaire. La plupart des systèmes à ultrasons actuels ne

disposent que de 256 voies, il faudrait donc 64 systèmes pour contrôler une telle sonde. D'un point de vue technique, la connexion de plusieurs milliers d'éléments augmente la complexité de l'électronique nécessaire pour contrôler la sonde et produit un câble de sonde de taille énorme, ce qui le rend inadapté aux pratiques cliniques. Pour surmonter les limitations associées aux matrices 2D, diverses techniques ont été proposées pour réduire le nombre d'éléments ou le nombre de signaux transférés au système d'échographie. Les techniques les plus importantes comprennent le micro-beamforming, le multiplexage, l'adressage ligne-colonne et les sondes sparses.

Le micro-beamforming, a été proposé pour réduire la quantité de données transférées de la sonde au système d'échographie et, par conséquent, diminuer le nombre de voies de formation de faisceau nécessaires [20–23]. Cette technique consiste à effectuer une étape initiale de formation de faisceau directement dans la sonde, ce qui réduit le nombre de signaux transmis par le câble de connexion au système d'échographie. L'implémentation du micro-beamforming dans les sondes pose plusieurs défis principaux : la complexité élevée des circuits intégrés (ASIC) nécessaire pour gérer les délais et les amplifications à l'intérieur de la sonde et la gestion de la consommation d'énergie pour éviter la surchauffe des tissus.

Le multiplexage est une solution efficace pour réduire le nombre de voies de beamforming nécessaires tout en conservant tous les éléments d'une sonde matricielle 2D. Dans ce système, un ensemble d'éléments est connecté à une même voies par un multiplexeur, ce qui permet d'activer uniquement un élément à la fois lors de la transmission ou de la réception. Des exemples incluent le réseau 32x35 de Vermon (Vermon, Tours, France), qui utilise un multiplexeur externe 4:1 pour connecter quatre éléments de sous-ouverture différentes à une même voies. Bien que ces sondes aient montré de bonnes performances, les éléments multiplexés ne sont pas connectés en continu au système d'échographie, ce qui affecte la formation des faisceaux et limite la cadence d'imagerie.

Une technique récente de réduction de nombre de voies est l'adressage lignes et colonnes (RCA) [52]. Cette méthode permet de piloter une sonde matriciel 2D en adressant des lignes ou des colonnes entières plutôt que chaque élément individuellement. Cela réduit le nombre de voies de beamforming nécessaires à $2N$ pour une sonde $N \times N$ au lieu de N^2. Les sondes RCA présentent plusieurs inconvénients majeurs : l'absence de contrôle électronique sur la longueur des éléments engendre des effets de bord importants, dégradant la qualité de l'image en produisant des artefacts [52, 55]. De plus, la focalisation bidirectionnelle limitée à un seul plan spatial crée des artefacts en forme de croix et détériore la résolution [77, 78].

L'approche des sondes sparses se présente come un candidat intéressant pour l'imagerie ultrasonore 3D. Cette approche s'attaque aux limitations associées au grand nombre d'éléments des sondes matricielles 2D en distribuant de manière optimale un nombre réduit d'éléments sur l'ouverture de la sonde, ce qui permet d'utiliser un nombre réduit de voies de beamforming [79, 80]. Les premières études sur les sondes sparses 2D ont été présentées par Turnbull en [79] et ont montré que les éléments d'une sonde matricielle 2D peuvent être réduits jusqu'à 1/6 du nombre initial tout en préservant une bonne qualité d'image. Dans la plupart des cas, les sondes à 256 éléments sont conçues pour correspondre au nombre de voies disponibles dans la plupart des systèmes à ultrasons, ce qui permet à chaque élément d'être contrôlé en permanence. Par conséquent, le système d'échographie peut transmettre et recevoir des faisceaux focalisés à différents

angles, ce qui permet une grande flexibilité dans la formation des faisceaux et les capacités d'orientation [81]. En outre, la réduction du nombre d'éléments diminue les coûts de fabrication et d'instrumentation.

Malgré les avantages proposés par les sondes sparses, elles rencontrent deux défis : une sensibilité faible et un contraste d'image réduit. En raison de la petite taille des éléments, les sondes sparses ont souvent une faible sensibilité et une impédance électrique élevée, ce qui diminue le SNR. Bien que l'augmentation de la taille des éléments puisse améliorer la sensibilité, cela réduit la divergence du faisceau. De plus, le grand espacement entre les éléments entraîne une dégradation du champs de rayonnement avec des lobes secondaires élevés, réduisant le contraste de l'image. Les principaux objectifs de cette thèse sont donc, d'augmenter le SNR des sondes sparses et d'améliorer le contraste des images obtenues avec ces sondes. Ce travail s'inscrit dans le cadre du projet ANR SPARTECHUS, visant à développer la prochaine génération de sondes sparses pour l'imagerie ultrasonore 3D. Ma première contribution a consisté à proposer des séquences d'excitations codées, dans le but d'améliorer le SNR. Ensuite, j'ai amélioré le contraste des images reconstruites à partir des signaux acquises par les sondes sparses en développant un nouvel algorithme de reconstruction basé sur des réseaux d'apprentissage profond, spécifiquement développé pour un prototype de sonde sparse, afin de produire des images échographiques de haute qualité.

Chapitre 2 : Augmentation du rapport signal-bruit des sondes sparses par émissions codées

Dans ce chapitre, j'ai cherché à augmenter le SNR des images de sondes sparses acquises à l'aide de méthodes d'imagerie par synthèse d'ouverture (STA). La technique STA a été choisie pour obtenir une imagerie 3D de haute qualité avec une cadence d'images plus élevée comparé à l'imagerie focalisée conventionnelle. Les sondes sparses, bien qu'offrant des avantages en termes de réduction du nombre d'éléments, sont connues pour leur faible sensibilité due à la petite taille des éléments généralement utilisés dans leur conception. Pour remédier à cette limitation, j'ai exploré l'utilisation de séquences d'excitations codées afin de transmettre plus d'énergie et ainsi augmenter le SNR de la sonde.

J'ai proposé un schéma d'excitation CCC STA basé sur les Codes Complètement Complémentaires (CCC), spécifiquement des CCC de type (N, N, MN/P), qui sont des séquences binaires composées de N ensembles, chacune contenant N séquences de longueur MN/P. Ces codes sont réputés pour leurs propriétés idéales d'auto-corrélation et de corrélation croisée. En tirant parti de ces propriétés, le CCC STA permet à chaque élément de la sonde de transmettre une séquence binaire distincte provenant d'un ensemble CCC, les signaux RF reçus étant décodés par corrélation croisée avec la séquence transmise (Figure 4.21). Ce processus sépare les contributions de chaque élément et récupère l'ensemble de données de la STA conventionnelle avec un SNR amélioré, sans interférences entre les éléments.

Pour valider le CCC STA, j'ai mené des simulations en utilisant le logiciel Field II ainsi que des expériences avec une sonde sparse optimisée sur la sonde matricielle 2D Vermon de 8 MHz. Le schéma CCC STA proposé a été comparé à cinq autres schémas d'excitations codées bien connus : Hadamard STA, Chirp STA, Golay STA, Hadamard-Chirp STA et

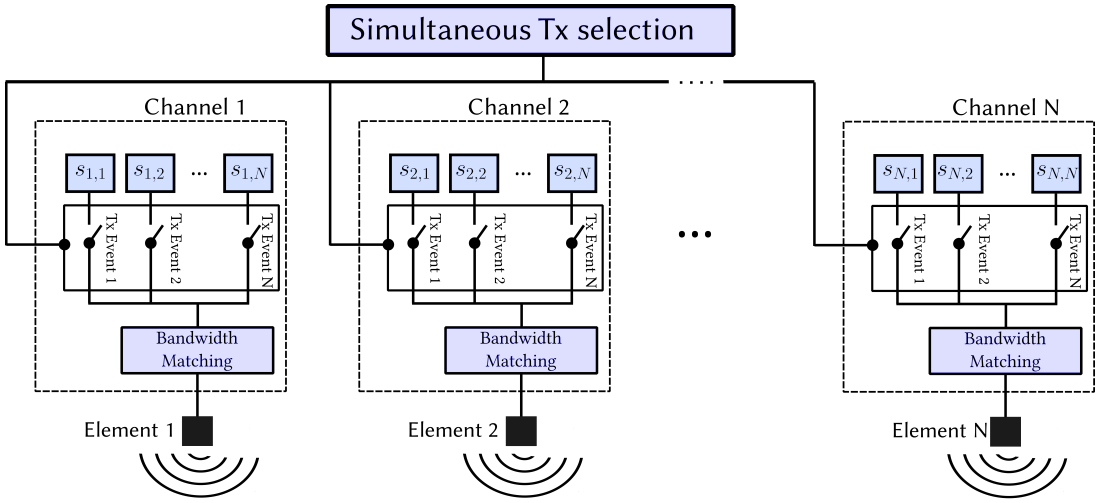

Figure 4.21: Schéma de transmission en imagerie CCC STA utilisant (N, N, MN/P)-CCC.

Hadamard-Golay STA.

Comparé à la STA conventionnelle, les simulations ont montré que le CCC STA augmente le SNR du réseau parcimonieux d'environ 36,12 dB et améliore le contraste de l'image de près de 24,18 dB, tout en maintenant la résolution axiale et le nombre de transmissions inchangés. Les résultats expérimentaux ont également démontré des gains de SNR et de contraste de 31,25 dB et 10,94 dB respectivement. La comparaison avec d'autres schémas d'excitations codées, tels que Hadamard-Chirp STA et Hadamard-Golay STA, a mis en évidence la performance supérieure du CCC STA en matière d'augmentation du SNR tout en préservant la résolution axiale et la cadence d'imagerie.

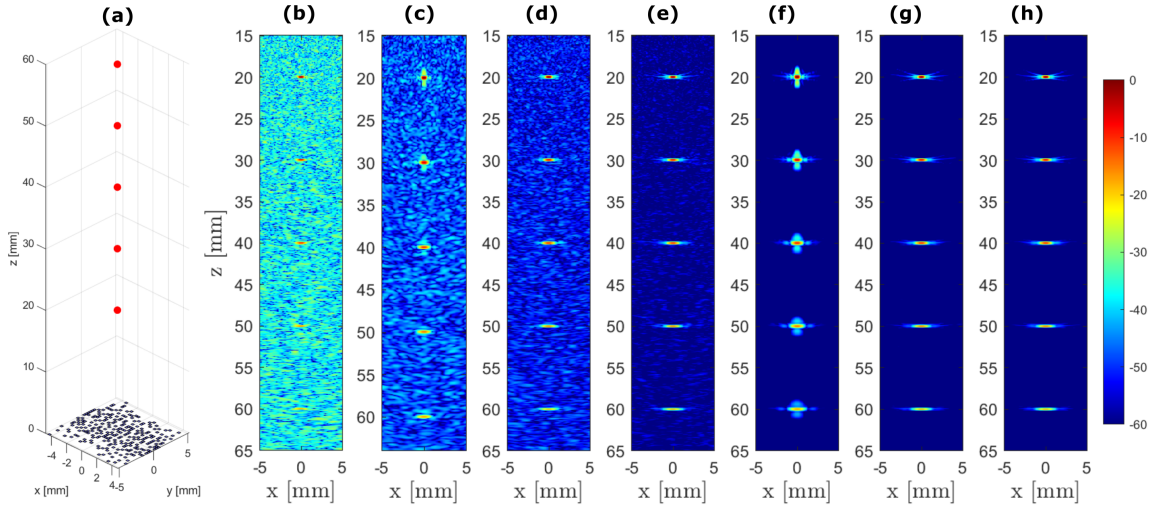

Figure 4.22: Images de PSFs simulées obtenues avec (b) STA *conventionnelle, (c)* STA *Hadamard, (d)* STA *Chirp, (e)* STA *Golay, (f)* STA *Hadamard-Chirp, (g)* STA *Hadamard-Golay, (h)* CCC-*STA proposé.*

Les images simulées des PSFs obtenues avec la STA conventionnelle et les différentes techniques d'excitations codées sont présentées dans la figure 4.22. Les images montrent

les coupes XZ (Y=0) extraites du volume 3D reconstruit. L'image produite par la STA conventionnelle est très bruitée, ce qui rend difficile la distinction des diffuseurs par rapport au bruit en raison du faible SNR des sondes sparses. Comparé à l'image de la STA conventionnelle, il est visuellement évident que toutes les techniques d'excitations codées ont réduit le bruit dans les images, confirmant la capacité de ces techniques à améliorer le SNR. Malgré une forte réduction du bruit, le fond reste légèrement bruité dans le cas d'un premier groupe de méthodes : Hadamard STA, Chirp STA et, dans une moindre mesure, Golay STA. En revanche, une amélioration plus significative du SNR est obtenue avec le second groupe de méthodes : Hadamard-Chirp STA, Hadamard-Golay STA, et CCC STA proposé, où le bruit semble complètement éliminé des images. La figure 4.22 (f), montres la présences des lobes secondaires axiaux sur les images obtenues avec Hadamard-Chirp STA, tandis que les images obtenues avec Hadamard-Golay STA nécessitent deux fois plus de transmissions que le CCC STA proposé .

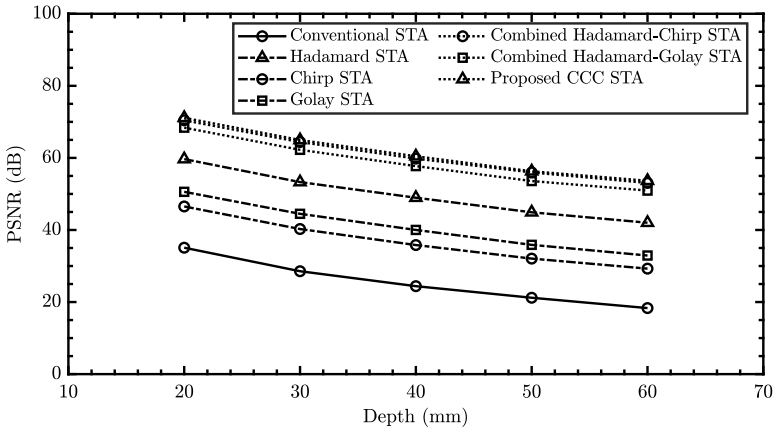

Figure 4.23: Comparaison du PSNR des schémas d'excitations en fonction de la profondeur des 5 diffuseurs.

De plus, la figure 4.23 montre une comparaison des PSNRs calculés pour chacun des 5 diffuseurs placés axialement, tels qu'affichés dans les images de la figure 4.22. Encore une fois, on distingue deux groupes de méthodes performantes. D'une part, le Hadamard STA montre un gain d'environ 24 dB, tandis que Chirp STA et Golay STA offrent respectivement un gain de 11 dB et 15 dB en SNR. D'autre part, Hadamard-Chirp STA et Hadamard-Golay STA atteignent respectivement un gain de SNR de 34,60 dB et 40,29 dB, tandis que la méthode proposée, CCC STA, réalise un gain de SNR de 35,95 dB sans présence de lobes secondaires axiaux ni de réduction de la cadence d'imagerie.

Les travaux réalisés dans ce chapitre ont permis d'augmenter le SNR des sondes sparses dans un cadre d'imagerie par synthèse d'ouverture. Les travaux futurs se concentreront sur la réduction des effets de l'atténuation dépendante de la fréquence et du mouvement sur le processus de décodage du CCC STA. L'atténuation pourrait diminuer les gains de SNR et introduire des lobes secondaires axiaux, affectant ainsi le contraste de l'image. Le mouvement du milieu entre les transmissions pourrait également compromettre les propriétés de corrélation des CCC, augmentant les lobes secondaires. Pour y remédier, des stratégies de correction pour ces deux problèmes seront étudiées et développées.

Chapitre 3 : Imagerie ultrasonore 3D ultrarapide codée avec des sondes sparses 2D

Dans ce chapitre j'ai abordé le défi de réaliser une imagerie ultrasonore 3D ultrarapide en utilisant des sondes sparses. L'objectif principal est d'améliorer le SNR dans l'imagerie ultrarapide avec des sondes sparses, afin d'augmenter à la fois la cadence d'imagerie et la profondeur de pénétration. Pour y parvenir, j'ai exploré deux méthodes d'imagerie avancées : l'imagerie par ondes planes et l'imagerie STA utilisant une excitation codée.

Dans le cadre de l'imagerie par ondes planes, j'ai introduit la technique MPWI-3C, qui tire parti des propriétés idéales de corrélation des séquences binaires (N, N, MN/P)-CCC que j'ai développé dans le chapitre 2 pour améliorer le SNR des sondes sparses. Cette méthode permet la transmission quasi-simultanée d'ondes planes inclinées, chacune portant une séquence distincte lors de chaque événement de transmission (Figure 4.24). Les échos reçus sont décodés comme si les ondes planes avaient été transmises individuellement, ce qui permet d'obtenir un SNR plus élevé sans sacrifier la cadence d'imagerie. De plus, la nature des séquences (N, N, MN/P)-CCC permet de générer des séquences plus courtes, évitant ainsi la création de grandes zones mortes devant la sonde.

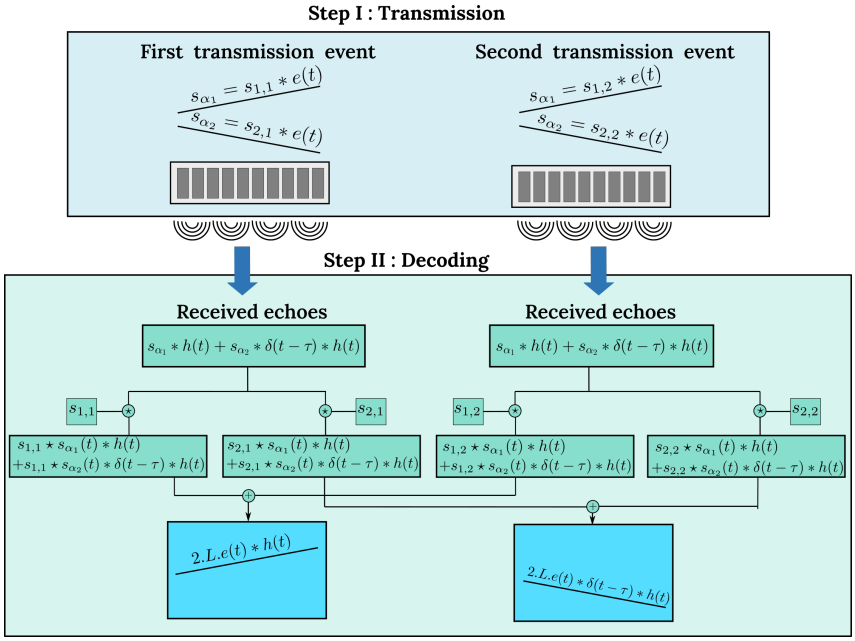

Figure 4.24: Schéma de transmission et de décodage de l'imagerie MPWI-3C utilisant (N, N, MN/P)-CCC.

Pour l'imagerie STA, j'ai introduit l'USTA (Ultrafast Synthetic Transmit Aperture), qui exploite les propriétés de corrélation uniques des Paires Complémentaires Mutuellement Orthogonales (MOCPs). Les MOCPs se composent de groupes de deux séquences binaires avec des sommes d'auto-corrélations idéales au sein de chaque groupe et des sommes de corrélations croisées idéales entre les groupes adjacentes. l'USTA nécessite seulement deux événements de transmission pour récupérer l'ensemble des données RF STA. Cependant, pour limiter le problème potentiel des grandes zones mortes causées par les MOCPs, j'ai divisé la sonde sparse en huit sous-ouvertures, ce qui a donné un

total de 16 transmissions (Figure 4.25)—beaucoup moins que les 256 transmissions nécessaires pour la STA conventionnelle et le CCC STA développé dans le chapitre 2. Avec ces 16 transmissions codées l'USTA, j'ai atteint une cadence d'imagerie de 962 Hz tout en améliorant le SNR et le contraste par rapport à la STA conventionnelle.

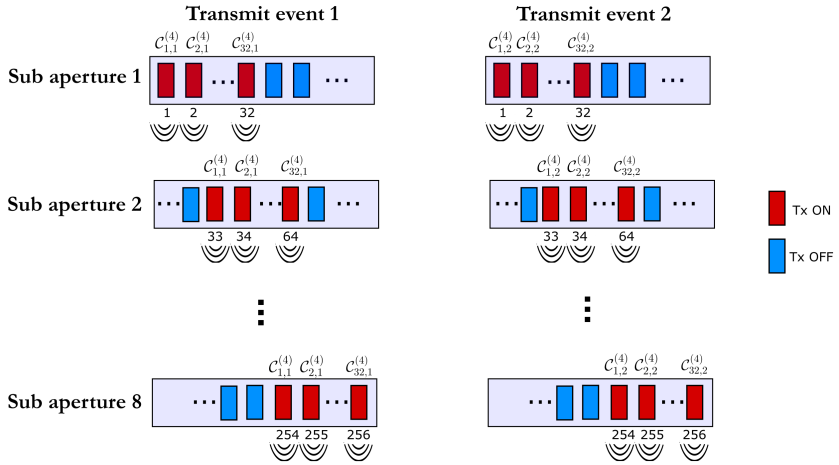

Figure 4.25: Principe de la méthode d'imagerie STA avec MOCPs (M=32) utilisant 8 sous-ouvertures de 32 éléments.

Le MPWI-3C a été comparé au CPWC et l'USTA a été comparé à la STA conventionnelle en menant des expériences sur la même sonde sparse utilisée au chapitre 2 dans deux conditions de bruit en réglant la tension Verasonics à 10V et 30V.

La figure 4.26 compare les images obtenues avec les méthodes CPWC et MPWI-3C à un taux de rafraîchissement de 3950 Hz, sous des conditions de bruit élevé (10v) et faible (30v). Les résultats montrent que MPWI-3C améliore significativement le SNR et la qualité de l'image dans les deux cas. Même à 10V, MPWI-3C produit des images de meilleure qualité que CPWC à 30V, avec une meilleure visibilité des inclusions anéchoïques et moins de bruit.

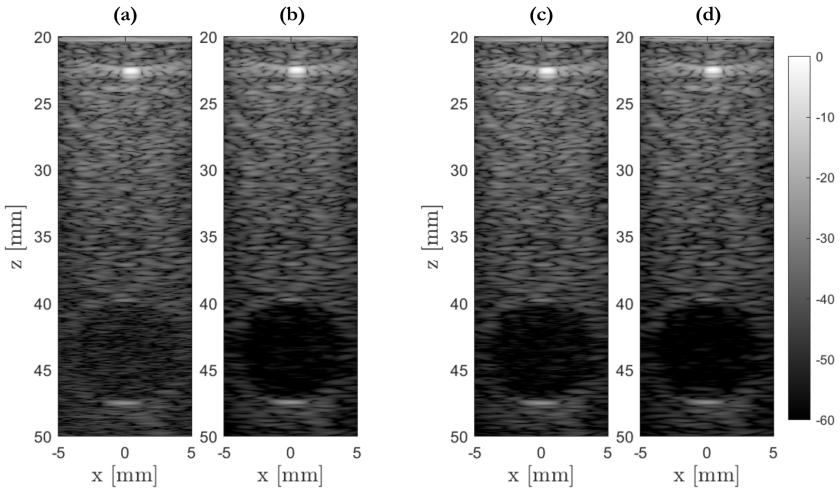

Figure 4.26: Images expérimentales d'un fantôme de speckle obtenues avec (a) CPWC, (b) MPWI-3C, pour 10V *et (c) CPWC, (d) MPWI-3C pour* 30V*.*

La figure 4.27 compare les images B-mode obtenues avec la méthode STA conventionnelle (256 transmissions) et la méthode USTA (16 transmissions) sur un fantôme de speckle, dans des conditions de bruit élevé (10V) et faible (30V). Les résultats montrent que la méthode USTA produit des images avec un SNR supérieur dans les deux scénarios. À 10V, l'image STA conventionnelle est très bruité et les inclusions anéchoïques sont indiscernables, tandis que l'image USTA montre une meilleure qualité avec une inclusion partiellement visible. À 30V, l'USTA offre une image beaucoup plus définie, avec des inclusions anéchoïques bien définies et un motif de speckle net.

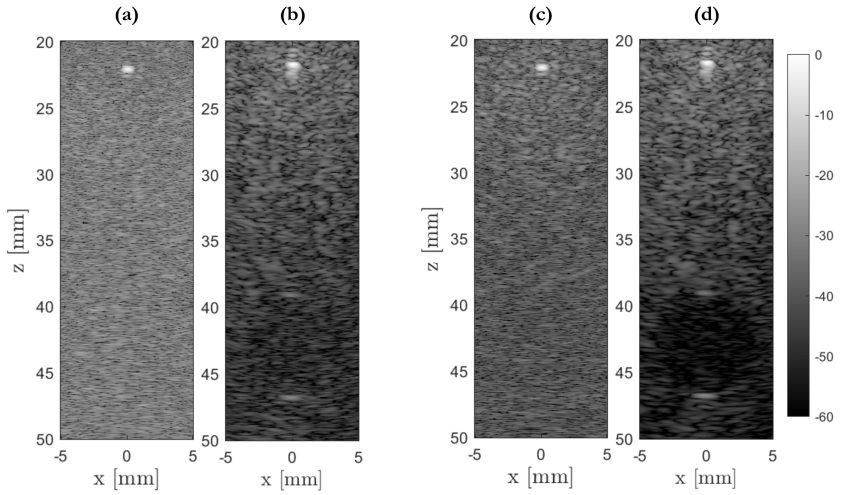

Figure 4.27: Images expérimentales d'un fantôme de speckle obtenues avec (a) STA, (b) USTA, pour 10V *et (c) STA, (d) USTA pour* 30V*.*

Les études expérimentales ont montré que MPWI-3C surpasse CPWC, et USTA dépasse la STA conventionnelle en termes de SNR et de contraste, avec seulement une diminution minimale de la résolution axiale pour l'USTA. Le taux de rafraîchissement et le SNR accrus fournis par MPWI-3C et l'USTA ont également amélioré la profondeur de pénétration, offrant des avantages potentiels pour diverses applications cliniques.

Cependant, dans les futurs travaux, je vais examiner les limitations potentielles des approches proposées, telles que l'impact de l'atténuation et du mouvement sur la précision du décodage, qui représentent des défis similaires à ceux discutés dans le Chapitre 2. De plus, l'expansion possible de la zone mortes lors de la transmission d'un grand nombre d'ondes planes avec MPWI-3C sera prise en compte. Pour y remédier, je prévois de développer une transmission simultanée de toutes les ondes planes de manière superposées plutôt qu'une transmission quasi-simultanée, ce qui entraînerait une zone morte très courte correspondant à celle de l'onde plane avec l'angle d'inclinaison le plus élevé.

Chapitre 4 : Reconstruction adaptative d'image basé sur l'apprentissage profond par renforcement pour l'imagerie ultrasonore 3D avec des sondes sparses

L'objectif principal de ce chapitre était de développer un nouvel algorithme de reconstruction pour obtenir des images 3D de haute qualité à partir des données RF STA

en utilisant le prototype de sonde sparse développé en collaboration avec IMASONIC. Le prototype a été fabriqué à la suite d'une étude de simulation qui a comparé diverses technologies potentielles. Ces simulations étaient basées sur le concept de réponses impulsionnelles angulaires, calculées à l'aide d'un modèle FEM. La modélisation FEM fournit une représentation précise des éléments de la sonde, permettant des simulations réalistes d'images échographiques 3D.

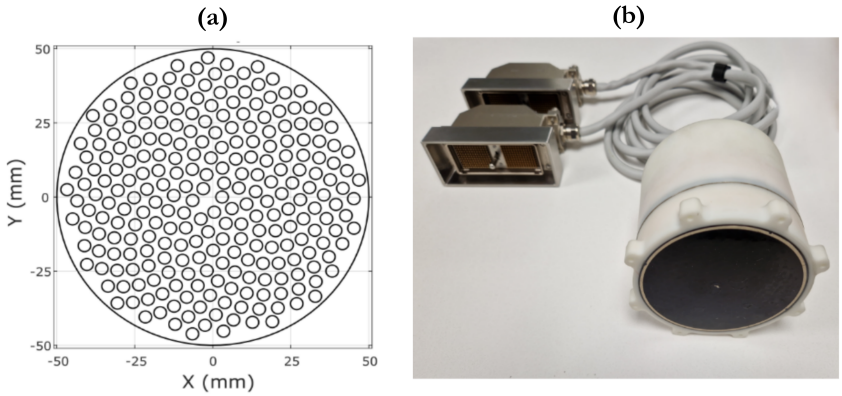

Figure 4.28: (a) Distribution des éléments en spirale avec 256 éléments de taille 3,5 mm (b) prototype de sonde fabriqué.

Le prototype développé (Figure 4.28(b)) possède une ouverture de 10 cm, suivant une distribution en spirale de Fermat avec 256 éléments (Figure 4.28(a)) fonctionnant à une fréquence centrale de 1 MHz. Chaque élément, de taille relativement grande de 3,5 mm pour améliorer le SNR, est couplé à une lentille divergente pour améliorer sa directivité. Bien que la conception de la sonde soit basée sur la distribution en spirale de Fermat, reconnue pour ses bonnes performances, notamment en termes de niveaux de lobes secondaires, la qualité des images reconstruites à l'aide du DAS souffre encore d'artefacts de lobes secondaires (Figure 4.29). Ces artefacts peuvent réduire la précision des diagnostic médical dans les applications cliniques.

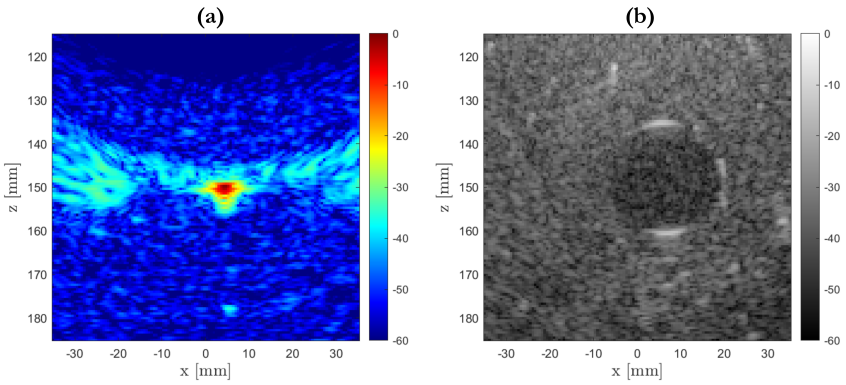

Figure 4.29: Images acquises avec le prototype de sonde développé d'un (a) fantôme de fil, (b) fantôme de speckle.

Pour améliorer la qualité des images reconstruites, le modèle RSB-Net a été développé. RSB-Net est un modèle basé sur l'apprentissage par renforcement profond qui combine les

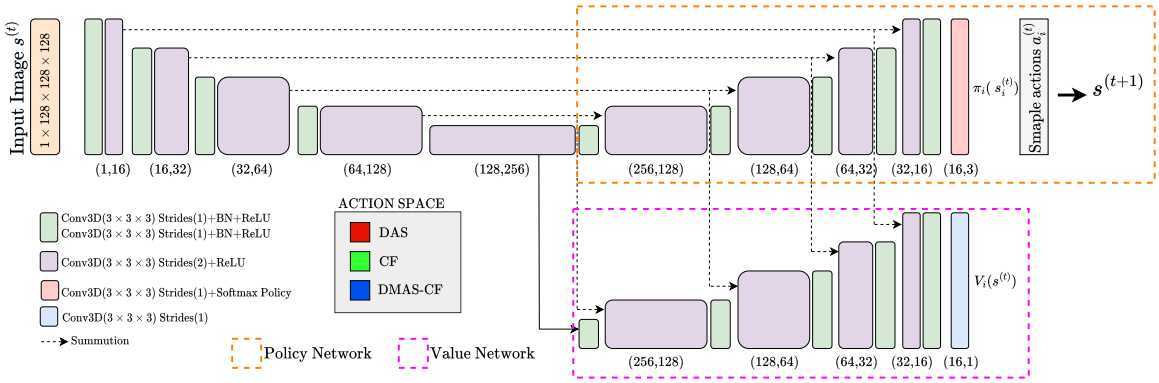

Figure 4.30: Architecture de RSB-Net : il s'agit d'une adaptation en FCN de l'algorithme A2C.

performances des beamformers adaptatifs avec le DAS au sein d'un cadre d'apprentissage pour améliorer la qualité des images. Les beamformers adaptatifs sont connus pour leur efficacité à réduire les artefacts hors axe dus à des niveaux élevés de lobes secondaires ; cependant, ils peuvent dégrader la qualité de la texture du speckle et introduire des zones sombres dans les images. RSB-Net, basé sur l'algorithme d'apprentissage par renforcement profond A2C, a été entraîné à appliquer de manière sélective des beamformers adaptatifs dans les régions où les artefacts de lobes secondaires sont dominants et le DAS dans les régions de speckle pour préserver la texture.

En implémentant A2C comme un réseau entièrement convolutionnel (FCN), RSB-Net traite chaque pixel de l'image comme un agent indépendant qui sélectionne des actions en fonction d'une politique conçue pour maximiser ses récompenses (Figure 4.30). Les récompenses sont directement liées à la qualité de l'image reconstruite : plus la qualité est élevée, plus les récompenses sont importantes. Dans cette étude, l'espace d'action a été limité à trois beamformers — DAS, CF, et DMAS-CF — afin de réduire la charge de calcul. Le réalisme et l'implémentation sur GPU de l'outil de simulation FEM ont permis de générer un ensemble de données RF de haute qualité en utilisant la séquence d'imagerie STA, qui a été utilisée pour entraîner RSB-Net. Enfin il a été appliquer à des données expérimentales réelles.

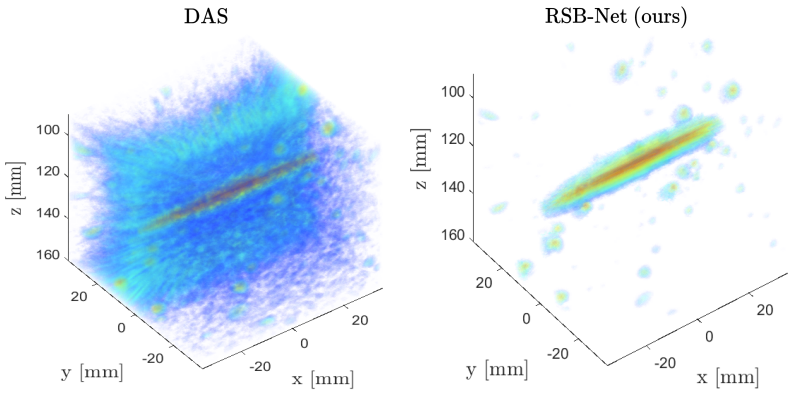

Figure 4.31: Rendu volumétrique 3D des volumes du fantôme de fil expérimental avec DAS et RSB-Net.

Sur l'ensemble de données simulées, RSB-Net a montré une amélioration du CR et du gCNR de 52,81 dB et 0,65, respectivement, par rapport au DAS. Bien qu'il n'ait pas été entraîné sur des ensembles de données expérimentales, le réalisme fourni par l'outil de simulation par FEM a permis à RSB-Net d'atteindre des performances similaires lorsqu'il a été appliqué à des données expérimentales. La Figure 4.31 présente un exemple de comparaison des rendus 3D du volume des images formées par DAS et par RSB-Net d'un fantôme de fil expérimental. RSB-Net élimine efficacement les artefacts de lobes secondaires par rapport au DAS, ce qui donne une représentation 3D claire du fil entouré d'un certain nombre de diffuseurs correspondant à des particules en suspension dans l'eau. Dans un fantôme simulant des tissus expérimentaux, RSB-Net a obtenu des gains de 51,01 dB en CR et de 0,64 en gCNR par rapport au DAS.

Conclusion

Dans cette thèse, j'ai abordé deux défis majeurs dans le développement des sondes sparses pour l'imagerie ultrasonore 3D : l'amélioration du SNR faible dû à la faible sensibilité des éléments et l'amélioration de la qualité d'image affectée par la sparsité des sondes. Dans le ***chapitre 1***, j'ai introduit le concept du champs de rayonnement, essentiel pour la conception et l'optimisation des sondes sparses. J'ai mis l'accent sur deux propriétés clés du diagramme de faisceau : la largeur du lobe principal, qui définit la résolution de l'image, et le niveau des lobes secondaires, qui est lié au contraste de l'image. J'ai également discuté des différents réseaux utilisés pour l'acquisition d'images ultrasonores 3D, en me concentrant sur les sondes sparses et leurs limitations en termes de sensibilité et de contraste.

Dans le ***chapitre 2***, j'ai travaillé sur l'amélioration du SNR des images obtenues avec des sondes sparses 2D en utilisant l'imagerie STA. Pour surmonter la faible sensibilité des sondes sparses, j'ai introduit un schéma d'excitations codées basé sur les Codes Complémentaires Complets (CCC). Ce schéma améliore le SNR des images en transmettant plus d'énergie sans interférences entre les éléments de la sonde.

Les résultats ont montré que le CCC STA augmente le SNR de 36,12 dB en moyenne et améliore le contraste des images de 24,18 dB, tout en maintenant la résolution axiale. Les prochaines étapes incluront l'étude des effets de l'atténuation de fréquence et du mouvement sur le CCC STA, ainsi que le développement de stratégies pour atténuer ces effets.

Dans le ***chapitre 3***, j'ai amélioré l'imagerie 3D ultrarapide avec des sondes sparses 2D en utilisant deux techniques : MPWI-3C pour les ondes planes et USTA pour l'imagerie STA avec excitation codée. MPWI-3C améliore le SNR en transmettant quasi-simultanément des ondes planes, tandis que USTA réduit le nombre de transmissions nécessaires et augmente la cadence d'imagerie à 962 Hz. Les deux méthodes ont montré des améliorations significatives en SNR et contraste par rapport aux techniques conventionnelles, mais des recherches futures devront traiter l'impact de l'atténuation et du mouvement sur la qualité des images.

Dans le ***chapitre 4***, j'ai développé un nouvel algorithme de reconstruction pour améliorer la qualité des images ultrasonores à partir des données RF STA, en utilisant un prototype de sonde sparse 2D créé en collaboration avec IMASONIC. J'ai introduit RSB-Net, un modèle basé sur l'apprentissage par renforcement profond, qui combine des

beamformers adaptatifs avec le beamformer DAS pour améliorer la qualité des images. RSB-Net applique des beamformers adaptatifs dans les zones avec des artefacts de lobes secondaires et utilise le beamformer DAS dans les zones avec du speckle pour préserver la qualité de la texture.

RSB-Net, entraîné sur un grand jeu de données simulé, a montré une réduction significative des artefacts de lobes secondaires et une amélioration de la qualité des images par rapport au DAS. Bien que le contraste des inclusions hyperéchogènes soit similaire à celui du DAS, le futur travail visera à améliorer ce contraste et à réduire les distorsions de forme. Des beamformers supplémentaires seront intégrés et RSB-Net sera également testé avec des données MPWI-3C et USTA pour optimiser l'imagerie ultrarapide avec des sondes sparses.

Bien qu'il reste encore des améliorations possibles, tous les objectifs fixés pour mon projet de thèse ont été atteints. De nouvelles séquences d'imagerie permettant d'augmenter le SNR des sondes sparses et de réaliser une imagerie ultrarapide avec ces sondes, augmentant ainsi la cadence d'imagerie, ont été proposées et validées expérimentalement. De plus, un algorithme de reconstruction capable de produire des images 3D de haute qualité avec une sonde sparse a été développé et testé sur des données simulées et expérimentales.

Bibliography

[1] F. Padilla, M. A. Roubidoux, C. Paramagul, S. P. Sinha, M. M. Goodsitt, G. L. Le Carpentier, H.-P. Chan, L. M. Hadjiiski, J. B. Fowlkes, A. D. Joe, *et al.*, "Breast mass characterization using 3-dimensional automated ultrasound as an adjunct to digital breast tomosynthesis: A pilot study," *Journal of Ultrasound in Medicine*, vol. 32, no. 1, pp. 93–104, 2013.

[2] D. Barbosa, T. Dietenbeck, B. Heyde, H. Houle, D. Friboulet, J. D'hooge, and O. Bernard, "Fast and fully automatic 3-d echocardiographic segmentation using b-spline explicit active surfaces: Feasibility study and validation in a clinical setting," *Ultrasound in medicine & biology*, vol. 39, no. 1, pp. 89–101, 2013.

[3] M. Tanter and M. Fink, "Ultrafast imaging in biomedical ultrasound," *IEEE transactions on ultrasonics, ferroelectrics, and frequency control*, vol. 61, no. 1, pp. 102–119, 2014.

[4] C. Papadacci, M. Tanter, M. Pernot, and M. Fink, "Ultrasound backscatter tensor imaging (bti): analysis of the spatial coherence of ultrasonic speckle in anisotropic soft tissues," *IEEE transactions on ultrasonics, ferroelectrics, and frequency control*, vol. 61, no. 6, pp. 986–996, 2014.

[5] M. Wang, B. Byram, M. Palmeri, N. Rouze, and K. Nightingale, "Imaging transverse isotropic properties of muscle by monitoring acoustic radiation force induced shear waves using a 2-d matrix ultrasound array," *IEEE transactions on medical imaging*, vol. 32, no. 9, pp. 1671–1684, 2013.

[6] J. W. Goodman, *Introduction to Fourier optics*. Roberts and Company publishers, 2005.

[7] R. S. Cobbold, *Foundations of biomedical ultrasound*. Oxford university press, 2006.

[8] L. Ziomek, *Fundamentals of acoustic field theory and space-time signal processing*. CRC press, 2020.

[9] R. W. Prager, U. Z. Ijaz, A. H. Gee, and G. M. Treece, "Three-dimensional ultrasound imaging," vol. 224.

[10] E. D. Light and S. W. Smith, "Two Dimensional Arrays for Real Time 3D Intravascular Ultrasound,"

[11] S. W. Smith and G. E. Trahey, "TWO-DIMENSIONAL ARRAYS FOR MEDICAL ULTRASOUND,"

[12] S. W. Smith and H. G. Pavy, "High-speed Ultrasound Volumetric Imaging System- Part I: Transducer Design and Beam Steering,"

[13] O. von Ramm, S. Smith, and H. Pavy, "High-speed ultrasound volumetric imaging system. ii. parallel processing and image display," *IEEE Transactions on Ultrasonics, Ferroelectrics, and Frequency Control*, vol. 38, no. 2, pp. 109–115, 1991.

[14] D. P. Shattuck, M. D. Weinshenker, and S. W. Smith, "Explososcan: A parallel processing technique for high speed ultrasound imaging with linear phased arrays," vol. 75, no. 4.

[15] V. T. Rathod, "A Review of Electric Impedance Matching Techniques for Piezoelectric Sensors, Actuators and Transducers," *Electronics*, vol. 8, p. 169, Feb. 2019.

[16] R. Wodnicki, H. Kang, D. Li, D. N. Stephens, H. Jung, Y. Sun, R. Chen, L.-M. Jiang, N. E. Cabrera-Munoz, J. Foiret, Q. Zhou, and K. W. Ferrara, "Highly Integrated Multiplexing and Buffering Electronics for Large Aperture Ultrasonic Arrays," *BME Frontiers*, vol. 2022, p. 9870386, Jan. 2022.

[17] T. R. Gururaja, "Composite piezoelectric transducer arrays with improved acoustical and electrical impedance," May 1 2001. US Patent 6,225,728.

[18] K. Hynynen and J. Song, "Ultrasound transducer and method for making the same," May 3 2016. US Patent 9,327,317.

[19] E. Roux, *2D sparse array optimization and operating strategy for real-time 3D ultrasound imaging.* PhD thesis, Université de Lyon; Università degli Studi di Firenze, 2016.

[20] J. D. Larson III, "2-d phased array ultrasound imaging system with distributed phasing," July 20 1993. US Patent 5,229,933.

[21] B. Savord and R. Solomon, "Fully sampled matrix transducer for real time 3d ultrasonic imaging," in *IEEE Symposium on Ultrasonics, 2003*, vol. 1, pp. 945–953, IEEE, 2003.

[22] Z. Yu, S. Blaak, Z.-Y. Chang, J. Yao, J. G. Bosch, C. Prins, C. T. Lancée, N. de Jong, M. A. Pertijs, and G. C. Meijer, "Front-end receiver electronics for a matrix transducer for 3-d transesophageal echocardiography," *IEEE transactions on ultrasonics, ferroelectrics, and frequency control*, vol. 59, no. 7, pp. 1500–1512, 2012.

[23] G. Matrone, A. S. Savoia, M. Terenzi, G. Caliano, F. Quaglia, and G. Magenes, "A volumetric cmut-based ultrasound imaging system simulator with integrated reception and μ-beamforming electronics models," *IEEE transactions on ultrasonics, ferroelectrics, and frequency control*, vol. 61, no. 5, pp. 792–804, 2014.

[24] U.-W. Lok and P.-C. Li, "Improving micro-beamforming by error compensation," in *2016 IEEE International Ultrasonics Symposium (IUS)*, pp. 1–4, IEEE, 2016.

[25] H. Philips, "An imaging revelation: Philips ie33 xmatrix echocardiography system overview."

[26] H. GE, "Vivid e9 4d cardiovascular ultrasound system."

[27] T. Kim and S. Kim, "A 12.1mw, 60db snr, 8-channel beamforming embedded sar adc for ultrasound imaging systems," in *2017 IEEE Asian Solid-State Circuits Conference (A-SSCC)*, pp. 141–144, 2017.

[28] J. V. Hatfield and K. S. Chai, "A beam-forming transmit asic for driving ultrasonic arrays," *Sensors and Actuators A: Physical*, vol. 92, no. 1-3, pp. 273–279, 2001.

[29] C. Chen, Z. Chen, D. Bera, S. B. Raghunathan, M. Shabanimotlagh, E. Noothout, Z.-Y. Chang, J. Ponte, C. Prins, H. J. Vos, *et al.*, "A front-end asic with receive sub-array beamforming integrated with a 32x32 pzt matrix transducer for 3-d transesophageal echocardiography," *IEEE Journal of Solid-State Circuits*, vol. 52, no. 4, pp. 994–1006, 2017.

[30] C. Chen, "Front-end asics for 3-d ultrasound: From beamforming to digitization," 2018.

[31] C. Chen, S. B. Raghunathan, Z. Yu, M. Shabanimotlagh, Z. Chen, Z.-y. Chang, S. Blaak, C. Prins, J. Ponte, E. Noothout, *et al.*, "A prototype pzt matrix transducer with low-power integrated receive asic for 3-d transesophageal echocardiography," *IEEE transactions on ultrasonics, ferroelectrics, and frequency control*, vol. 63, no. 1, pp. 47–59, 2015.

[32] J. N. Hilberath, D. A. Oakes, S. K. Shernan, B. E. Bulwer, M. N. D'Ambra, and H. K. Eltzschig, "Safety of transesophageal echocardiography," *Journal of the American Society of Echocardiography*, vol. 23, no. 11, pp. 1115–1127, 2010.

[33] D. Bera, "Beamforming for 3d transesophageal echocardiography," 2018.

[34] M. Sautto, D. Leone, A. Savoia, D. Ghisu, F. Quaglia, G. Caliano, and A. Mazzanti, "A cmut transceiver front-end with 100-v tx driver and 1-mw low-noise capacitive feedback rx amplifier in bcd-soi technology," in *ESSCIRC 2014-40th European Solid State Circuits Conference (ESSCIRC)*, pp. 407–410, IEEE, 2014.

[35] A. Bhuyan, J. W. Choe, B. C. Lee, I. O. Wygant, A. Nikoozadeh, Ö. Oralkan, and B. T. Khuri-Yakub, "Integrated circuits for volumetric ultrasound imaging with 2-d cmut arrays," *IEEE transactions on biomedical circuits and systems*, vol. 7, no. 6, pp. 796–804, 2013.

[36] K. Chen, H.-S. Lee, and C. G. Sodini, "A column-row-parallel asic architecture for 3-d portable medical ultrasonic imaging," *IEEE Journal of Solid-State Circuits*, vol. 51, no. 3, pp. 738–751, 2016.

[37] K. Latham, "A miniature high resolution endoscope for 3d ultrasound imaging," 2020.

[38] N. Wang, Y. Qiang, C. Qiu, Y. Chen, X. Wang, Y. Pan, R. Liu, W. Wu, H. Zheng, W. Qiu, and Z. Zhang, "A multiplexed 32×32 2d matrix array transducer for flexible sub-aperture volumetric ultrasound imaging," *IEEE Transactions on Biomedical Engineering*, vol. 71, no. 3, pp. 831–840, 2024.

[39] P. A. Hager, *Design of Fully-Digital Medical Ultrasound Imaging Systems*. PhD thesis, ETH Zurich, 2019.

[40] J. Yen and S. Smith, "Real-time rectilinear 3-d ultrasound using receive mode multiplexing," *IEEE Transactions on Ultrasonics, Ferroelectrics, and Frequency Control*, vol. 51, no. 2, pp. 216–226, 2004.

[41] J. Yu, H. Yoon, Y. M. Khalifa, and S. Y. Emelianov, "Design of a volumetric imaging sequence using a vantage-256 ultrasound research platform multiplexed with a 1024-element fully sampled matrix array," *IEEE Transactions on Ultrasonics, Ferroelectrics, and Frequency Control*, vol. 67, no. 2, pp. 248–257, 2020.

[42] J. Provost, C. Papadacci, C. Demene, J.-L. Gennisson, M. Tanter, and M. Pernot, "3-d ultrafast doppler imaging applied to the noninvasive mapping of blood vessels in vivo," *IEEE transactions on ultrasonics, ferroelectrics, and frequency control*, vol. 62, no. 8, pp. 1467–1472, 2015.

[43] J. Provost, C. Papadacci, J. E. Arango, M. Imbault, M. Fink, J.-L. Gennisson, M. Tanter, and M. Pernot, "3d ultrafast ultrasound imaging in vivo," *Physics in Medicine & Biology*, vol. 59, no. 19, p. L1, 2014.

[44] S. Holbek, C. Ewertsen, H. Bouzari, M. J. Pihl, K. L. Hansen, M. B. Stuart, C. Thomsen, M. B. Nielsen, and J. A. Jensen, "Ultrasonic 3-d vector flow method for quantitative in vivo peak velocity and flow rate estimation," *IEEE Transactions on Ultrasonics, Ferroelectrics, and Frequency Control*, vol. 64, no. 3, pp. 544–554, 2016.

[45] L. Petrusca, F. Varray, R. Souchon, A. Bernard, J.-Y. Chapelon, H. Liebgott, W. A. N'Djin, and M. Viallon, "Fast volumetric ultrasound b-mode and doppler imaging with a new high-channels density platform for advanced 4d cardiac imaging/therapy," *Applied Sciences*, vol. 8, no. 2, p. 200, 2018.

[46] B. Heiles, M. Correia, V. Hingot, M. Pernot, J. Provost, M. Tanter, and O. Couture, "Ultrafast 3d ultrasound localization microscopy using a 32x32 matrix array," *IEEE Transactions on Medical Imaging*, vol. 38, no. 9, pp. 2005–2015, 2019.

[47] A. Chavignon, B. Heiles, V. Hingot, C. Orset, D. Vivien, and O. Couture, "3d transcranial ultrasound localization microscopy in the rat brain with a multiplexed matrix probe," *IEEE Transactions on Biomedical Engineering*, vol. 69, no. 7, pp. 2132–2142, 2021.

[48] J. Yan, B. Wang, K. Riemer, J. Hansen-Shearer, M. Lerendegui, M. Toulemonde, C. J. Rowlands, P. D. Weinberg, and M.-X. Tang, "Fast 3d super-resolution ultrasound with adaptive weight-based beamforming," *IEEE Transactions on Biomedical Engineering*, 2023.

[49] B. Heiles, A. Chavignon, A. Bergel, V. Hingot, H. Serroune, D. Maresca, S. Pezet, M. Pernot, M. Tanter, and O. Couture, "Volumetric ultrasound localization microscopy of the whole rat brain microvasculature," *IEEE Open Journal of Ultrasonics, Ferroelectrics, and Frequency Control*, vol. 2, pp. 261–282, 2022.

[50] C. Vallecilla and J. D'hooge, "Design of a multiplexing array for 3d cardiac imaging," in *2016 Computing in Cardiology Conference (CinC)*, pp. 877–879, 2016.

[51] H. De Hoop, M. Vermeulen, H.-M. Schwab, and R. G. Lopata, "Coherent bistatic 3-d ultrasound imaging using two sparse matrix arrays," *IEEE transactions on ultrasonics, ferroelectrics, and frequency control*, vol. 70, no. 3, pp. 182–196, 2022.

[52] J. A. Jensen, M. Schou, L. T. Jørgensen, B. G. Tomov, M. B. Stuart, M. S. Traberg, I. Taghavi, S. H. Øygaard, M. L. Ommen, K. Steenberg, *et al.*, "Anatomic and functional imaging using row–column arrays," *IEEE transactions on ultrasonics, ferroelectrics, and frequency control*, vol. 69, no. 10, pp. 2722–2738, 2022.

[53] M. F. Rasmussen, T. L. Christiansen, E. V. Thomsen, and J. A. Jensen, "3-d imaging using row-column-addressed arrays with integrated apodization-part i: apodization design and line element beamforming," *IEEE transactions on ultrasonics, ferroelectrics, and frequency control*, vol. 62, no. 5, pp. 947–958, 2015.

[54] T. L. Christiansen, M. F. Rasmussen, J. P. Bagge, L. N. Moesner, J. A. Jensen, and E. V. Thomsen, "3-d imaging using row–column-addressed arrays with integrated apodization—part ii: Transducer fabrication and experimental results," *IEEE transactions on ultrasonics, ferroelectrics, and frequency control*, vol. 62, no. 5, pp. 959–971, 2015.

[55] H. Bouzari, M. Engholm, S. I. Nikolov, M. B. Stuart, E. V. Thomsen, and J. A. Jensen, "Imaging performance for two row–column arrays," *IEEE transactions on ultrasonics, ferroelectrics, and frequency control*, vol. 66, no. 7, pp. 1209–1221, 2019.

[56] C. E. Morton and G. R. Lockwood, "Theoretical assessment of a crossed electrode 2-d array for 3-d imaging," in *IEEE Symposium on Ultrasonics, 2003*, vol. 1, pp. 968–971, IEEE, 2003.

[57] C. E. Demore, A. W. Joyce, K. Wall, and G. R. Lockwood, "Real-time volume imaging using a crossed electrode array," *IEEE transactions on ultrasonics, ferroelectrics, and frequency control*, vol. 56, no. 6, pp. 1252–1261, 2009.

[58] C. H. Seo and J. T. Yen, "5a-5 64x64 2-d array transducer with row-column addressing," in *2006 IEEE Ultrasonics Symposium*, pp. 74–77, IEEE, 2006.

[59] C. H. Seo and J. T. Yen, "A 256 x 256 2-d array transducer with row-column addressing for 3-d rectilinear imaging," *IEEE transactions on ultrasonics, ferroelectrics, and frequency control*, vol. 56, no. 4, pp. 837–847, 2009.

[60] A. S. Logan, L. L. Wong, and J. T. Yeow, "2-d cmut wafer bonded imaging arrays with a row-column addressing scheme," in *2009 IEEE International Ultrasonics Symposium*, pp. 984–987, IEEE, 2009.

[61] A. S. Logan, L. L. Wong, A. I. Chen, and J. T. Yeow, "A 32 x 32 element row-column addressed capacitive micromachined ultrasonic transducer," *IEEE transactions on ultrasonics, ferroelectrics, and frequency control*, vol. 58, no. 6, pp. 1266–1271, 2011.

[62] R. J. Zemp, W. Zheng, and P. Zhang, "Feasibility of top-orthogonal-to-bottom electrode (tobe) 2d cmut arrays for low-channel-count 3d imaging," in *2011 IEEE International Ultrasonics Symposium*, pp. 498–502, IEEE, 2011.

[63] A. Sampaleanu, P. Zhang, A. Kshirsagar, W. Moussa, and R. J. Zemp, "Top-orthogonal-to-bottom-electrode (tobe) cmut arrays for 3-d ultrasound imaging," *IEEE transactions on ultrasonics, ferroelectrics, and frequency control*, vol. 61, no. 2, pp. 266–276, 2014.

[64] R. K. Chee, A. Sampaleanu, D. Rishi, and R. J. Zemp, "Top orthogonal to bottom electrode (tobe) 2-d cmut arrays for 3-d photoacoustic imaging," *IEEE transactions on ultrasonics, ferroelectrics, and frequency control*, vol. 61, no. 8, pp. 1393–1395, 2014.

[65] M. Engholm, A. S. Havreland, E. V. Thomsen, C. Beers, B. G. Tomov, and J. A. Jensen, "A row-column-addressed 2d probe with an integrated compound diverging lens," in *2018 IEEE International Ultrasonics Symposium (IUS)*, pp. 1–4, IEEE, 2018.

[66] M. Engholm, C. Beers, H. Bouzari, J. A. Jensen, and E. V. Thomsen, "Increasing the field-of-view of row–column-addressed ultrasound transducers: implementation of a diverging compound lens," *Ultrasonics*, vol. 88, pp. 97–105, 2018.

[67] M. Engholm, H. Bouzari, T. L. Christiansen, C. Beers, J. P. Bagge, L. N. Moesner, S. E. Diederichsen, M. B. Stuart, J. A. Jensen, and E. V. Thomsen, "Probe development of cmut and pzt row–column-addressed 2-d arrays," *Sensors and Actuators A: Physical*, vol. 273, pp. 121–133, 2018.

[68] J. Sauvage, M. Flesch, G. Ferin, A. Nguyen-Dinh, J. Poree, M. Tanter, M. Pernot, and T. Deffieux, "A large aperture row column addressed probe for in vivo 4d ultrafast doppler ultrasound imaging," *Physics in Medicine & Biology*, vol. 63, no. 21, p. 215012, 2018.

[69] M. Flesch, M. Pernot, J. Provost, G. Ferin, A. Nguyen-Dinh, M. Tanter, and T. Deffieux, "4d in vivo ultrafast ultrasound imaging using a row-column addressed matrix and coherently-compounded orthogonal plane waves," *Physics in Medicine & Biology*, vol. 62, no. 11, p. 4571, 2017.

[70] J. Sauvage, J. Porée, C. Rabut, G. Férin, M. Flesch, B. Rosinski, A. Nguyen-Dinh, M. Tanter, M. Pernot, and T. Deffieux, "Ultrafast 4d doppler imaging of the rat brain with a large aperture row column addressed probe," in *2018 IEEE International Ultrasonics Symposium (IUS)*, pp. 1–4, IEEE, 2018.

[71] J. Sauvage, J. Porée, C. Rabut, G. Férin, M. Flesch, B. Rosinski, A. Nguyen-Dinh, M. Tanter, M. Pernot, and T. Deffieux, "4d functional imaging of the rat brain using a large aperture row-column array," *IEEE transactions on medical imaging*, vol. 39, no. 6, pp. 1884–1893, 2019.

[72] J. A. Jensen, M. Schou, M. L. Ommen, S. H. Øygard, T. Sams, M. B. Stuart, E. V. Thomsen, N. B. Larsen, C. Beers, and B. G. Tomov, "3-d super resolution imaging using a 62+ 62 elements row-column array," in *2019 IEEE International Ultrasonics Symposium (IUS)*, pp. 1838–1841, IEEE, 2019.

[73] I. Taghavi, M. Schou, N. S. Panduro, S. B. Andersen, B. G. Tomov, C. M. Sørensen, M. B. Stuart, and J. A. Jensen, "In vivo 3d super-resolution ultrasound imaging of a rat kidney using a row-column array," in *2022 IEEE International Ultrasonics Symposium (IUS)*, pp. 1–3, IEEE, 2022.

[74] A. I. Chen *et al.*, "Row-column capacitive micromachined ultrasonic transducers for medical imaging," 2016.

[75] I. Ben Daya, "Compensated row-column ultrasound imaging system," 2020.

[76] T. L. Christiansen, M. F. Rasmussen, J. A. Jensen, and E. V. Thomsen, "Row-column addressed 2-d cmut arrays with integrated apodization," in *2014 IEEE International Ultrasonics Symposium*, pp. 600–603, 2014.

[77] I. Ben Daya, A. I. Chen, M. J. Shafiee, A. Wong, and J. T. Yeow, "Compensated row-column ultrasound imaging system using multilayered edge guided stochastically fully connected random fields," *Scientific reports*, vol. 7, no. 1, p. 10644, 2017.

[78] J. Hansen-Shearer, M. Lerendegui, M. Toulemonde, and M.-X. Tang, "High contrast ultrafast 3d ultrasound imaging using row column specific frame multiply and sum," *arXiv preprint arXiv:2102.07746*, 2021.

[79] D. Turnbull and F. Foster, "Beam steering with pulsed two-dimensional transducer arrays," *IEEE Transactions on Ultrasonics, Ferroelectrics, and Frequency Control*, vol. 38, no. 4, pp. 320–333, 1991.

[80] A. Ramalli, E. Boni, E. Roux, H. Liebgott, and P. Tortoli, "Design, implementation, and medical applications of 2-d ultrasound sparse arrays," *IEEE Transactions on Ultrasonics, Ferroelectrics, and Frequency Control*, vol. 69, no. 10, pp. 2739–2755, 2022.

[81] B. Diarra, M. Robini, P. Tortoli, C. Cachard, and H. Liebgott, "Design of optimal 2-d nongrid sparse arrays for medical ultrasound," *IEEE Transactions on Biomedical Engineering*, vol. 60, no. 11, pp. 3093–3102, 2013.

[82] X. Li, "Design of 2d sparse array transducers for anomaly detection associated with a transcranial ultrasound system," 2020.

[83] H. Favre, M. Pernot, M. Tanter, and C. Papadacci, "Boosting transducer matrix sensitivity for 3d large field ultrasound localization microscopy using a multi-lens diffracting layer: a simulation study," *Physics in Medicine & Biology*, vol. 67, no. 8, p. 085009, 2022.

[84] H. Favre, M. Pernot, M. Tanter, and C. Papadacci, "Transcranial 3d ultrasound localization microscopy using a large element matrix array with a multi-lens diffracting layer: an in vitro study," *Physics in Medicine & Biology*, vol. 68, no. 7, p. 075003, 2023.

[85] S. W. Smith, K. Chu, S. F. Idriss, N. M. Ivancevich, E. D. Light, and P. D. Wolf, "Feasibility study: Real-time 3-d ultrasound imaging of the brain," *Ultrasound in medicine & biology*, vol. 30, no. 10, pp. 1365–1371, 2004.

[86] D. Turnbull and F. Foster, "Beam steering with pulsed two-dimensional transducer arrays," *IEEE Transactions on Ultrasonics, Ferroelectrics and Frequency Control*, vol. 38, pp. 320–333, July 1991.

[87] R. E. Davidsen, J. A. Jensen, and S. W. Smith, "Two-dimensional random arrays for real time volumetric imaging," *Ultrasonic Imaging*, vol. 16, no. 3, pp. 143–163, 1994.

[88] W. J. Hendricks, "The totally random versus the bin approach for random arrays," *IEEE Transactions on antennas and propagation*, vol. 39, no. 12, pp. 1757–1762, 1991.

[89] A. Austeng and S. Holm, "Sparse 2-d arrays for 3-d phased array imaging-design methods," *IEEE transactions on ultrasonics, ferroelectrics, and frequency control*, vol. 49, no. 8, pp. 1073–1086, 2002.

[90] P. Weber, R. Schmitt, B. Tylkowski, and J. Steck, "Optimization of random sparse 2-d transducer arrays for 3-d electronic beam steering and focusing," in *1994 Proceedings of IEEE Ultrasonics Symposium*, vol. 3, pp. 1503–1506, IEEE, 1994.

[91] S. Holm, A. Austeng, K. Iranpour, and J.-F. Hopperstad, "Sparse sampling in array processing," *Nonuniform Sampling: Theory and Practice*, pp. 787–833, 2001.

[92] B. Diarra, H. Liebgott, P. Tortoli, and C. Cachard, "Sparse array techniques for 2d array ultrasound imaging," in *Acoustics 2012*, 2012.

[93] C. Wang, Y. He, and C. Qi, "Analysis of grating lobe effects on geo dsc distributed antennas," *Applied Sciences*, vol. 13, no. 19, p. 10912, 2023.

[94] A. Ramalli, E. Boni, A. S. Savoia, and P. Tortoli, "Density-tapered spiral arrays for ultrasound 3-d imaging," *IEEE Transactions on ultrasonics, ferroelectrics, and frequency control*, vol. 62, no. 8, pp. 1580–1588, 2015.

[95] C. Boni, M. Richard, and S. Barbarossa, "Optimal configuration and weighting of nonuniform arrays according to a maximum islr criterion," in *Proceedings of ICASSP'94. IEEE International Conference on Acoustics, Speech and Signal Processing*, pp. V–157, IEEE, 1994.

[96] J. O. Erstad and S. Holm, "An approach to the design of sparse array systems," in *1994 Proceedings of IEEE Ultrasonics Symposium*, vol. 3, pp. 1507–1510, IEEE, 1994.

[97] S. Holm and B. Elgetun, "Optimization of the beampattern of 2d sparse arrays by weighting," in *1995 IEEE Ultrasonics Symposium. Proceedings. An International Symposium*, vol. 2, pp. 1345–1348, IEEE, 1995.

[98] S. Holm, B. Elgetun, and G. Dahl, "Properties of the beampattern of weight-and layout-optimized sparse arrays," *IEEE Transactions on Ultrasonics, Ferroelectrics, and Frequency Control*, vol. 44, no. 5, pp. 983–991, 1997.

[99] J. F. DeFord and O. P. Gandhi, "Phase-only synthesis of minimum peak sidelobe patterns for linear and planar arrays," *IEEE transactions on antennas and propagation*, vol. 36, no. 2, pp. 191–201, 1988.

[100] G. Zames, "Genetic algorithms in search, optimization and machine learning," *Inf Tech J*, vol. 3, no. 1, p. 301, 1981.

[101] K. A. De Jong, *An analysis of the behavior of a class of genetic adaptive systems.* University of Michigan, 1975.

[102] A. H. Wright, "Genetic algorithms for real parameter optimization," in *Foundations of genetic algorithms*, vol. 1, pp. 205–218, Elsevier, 1991.

[103] S. Kirkpatrick, C. D. Gelatt Jr, and M. P. Vecchi, "Optimization by simulated annealing," *science*, vol. 220, no. 4598, pp. 671–680, 1983.

[104] R. Chibante, *Simulated annealing: theory with applications.* BoD–Books on Demand, 2010.

[105] J. E. Gubernatis, "Marshall rosenbluth and the metropolis algorithm," *Physics of plasmas*, vol. 12, no. 5, 2005.

[106] A. Trucco, "Thinning and weighting of large planar arrays by simulated annealing," *IEEE transactions on ultrasonics, ferroelectrics, and frequency control*, vol. 46, no. 2, pp. 347–355, 1999.

[107] R. L. Haupt, "Thinned arrays using genetic algorithms," *IEEE transactions on antennas and propagation*, vol. 42, no. 7, pp. 993–999, 1994.

[108] E. Roux, A. Ramalli, H. Liebgott, C. Cachard, M. C. Robini, and P. Tortoli, "Wideband 2-d array design optimization with fabrication constraints for 3-d us imaging," *IEEE transactions on ultrasonics, ferroelectrics, and frequency control*, vol. 64, no. 1, pp. 108–125, 2016.

[109] P. Weber, A. Austeng, S. Holm, and N. Aakvaak, "1d-and 2d-sparse-array-optimization," *Instrumentation science & technology*, vol. 27, no. 4, pp. 235–246, 1999.

[110] J. W. Choe, Ö. Oralkan, and P. T. Khuri-Yakub, "Design optimization for a 2-d sparse transducer array for 3-d ultrasound imaging," in *2010 IEEE International Ultrasonics Symposium*, pp. 1928–1931, IEEE, 2010.

[111] P. Chen, Y. Zheng, and W. Zhu, "Optimized simulated annealing algorithm for thinning and weighting large planar arrays in both far-field and near-field," *IEEE journal of Oceanic Engineering*, vol. 36, no. 4, pp. 658–664, 2011.

[112] B. Diarra, H. Liebgott, M. Robini, P. Tortoli, and C. Cachard, "Optimized 2d array design for ultrasound imaging," in *2012 Proceedings of the 20th European Signal Processing Conference (EUSIPCO)*, pp. 2718–2722, IEEE, 2012.

[113] B. Diarra, M. Robini, H. Liebgott, C. Cachard, and P. Tortoli, "Variable-size elements in 2d sparse arrays for 3d medical ultrasound," in *2013 IEEE International Ultrasonics Symposium (IUS)*, pp. 508–511, IEEE, 2013.

[114] B. Diarra, M. Robini, E. Roux, H. Liebgott, C. Cachard, and P. Tortoli, "Optimization of free-moving elements in 2d ultrasound sparse arrays," in *2014 IEEE International Ultrasonics Symposium*, pp. 2189–2192, IEEE, 2014.

[115] B. Diarra, M. Robini, P. Tortoli, C. Cachard, and H. Liebgott, "Design of optimal 2-d nongrid sparse arrays for medical ultrasound," *IEEE Transactions on Biomedical Engineering*, vol. 60, no. 11, pp. 3093–3102, 2013.

[116] E. Roux, B. Diarra, M. Robini, C. Cachard, P. Tortoli, and H. Liebgott, "Realistic acoustic simulation of 2-d probe elements in simulated annealing sparse array optimization," in *2014 IEEE International Ultrasonics Symposium*, pp. 2125–2128, IEEE, 2014.

[117] E. Roux, A. Ramalli, P. Tortoli, C. Cachard, M. C. Robini, and H. Liebgott, "2-d ultrasound sparse arrays multidepth radiation optimization using simulated annealing and spiral-array inspired energy functions," *IEEE transactions on ultrasonics, ferroelectrics, and frequency control*, vol. 63, no. 12, pp. 2138–2149, 2016.

[118] J. A. Jensen and N. B. Svendsen, "Calculation of pressure fields from arbitrarily shaped, apodized, and excited ultrasound transducers," *IEEE transactions on ultrasonics, ferroelectrics, and frequency control*, vol. 39, no. 2, pp. 262–267, 1992.

[119] J. A. Jensen, "Field: A program for simulating ultrasound systems," *Medical & Biological Engineering & Computing*, vol. 34, no. sup. 1, pp. 351–353, 1997.

[120] E. Roux, A. Ramalli, P. Tortoli, C. Cachard, M. Robini, and H. Liebgott, "Speed-up of acoustic simulation techniques for 2d sparse array optimization by simulated annealing," in *2015 IEEE International Ultrasonics Symposium (IUS)*, pp. 1–4, IEEE, 2015.

[121] S. W. Smith, H. G. Pavy, and O. T. von Ramm, "High-speed ultrasound volumetric imaging system. i. transducer design and beam steering," *IEEE transactions on ultrasonics, ferroelectrics, and frequency control*, vol. 38, no. 2, pp. 100–108, 1991.

[122] J. T. Yen, J. P. Steinberg, and S. W. Smith, "Sparse 2-d array design for real time rectilinear volumetric imaging," *IEEE transactions on ultrasonics, ferroelectrics, and frequency control*, vol. 47, no. 1, pp. 93–110, 2000.

[123] G. Lookwood and F. S. Foster, "Optimizing the radiation pattern of sparse periodic two-dimensional arrays," *IEEE transactions on ultrasonics, ferroelectrics, and frequency control*, vol. 43, no. 1, pp. 15–19, 1996.

[124] S. S. Brunke and G. R. Lockwood, "Broad-bandwidth radiation patterns of sparse two-dimensional vernier arrays," *IEEE transactions on ultrasonics, ferroelectrics, and frequency control*, vol. 44, no. 5, pp. 1101–1109, 1997.

[125] G. Lockwood and F. S. Foster, "Optimizing sparse two-dimensional transducer arrays using an effective aperture approach," in *1994 Proceedings of IEEE Ultrasonics Symposium*, vol. 3, pp. 1497–1501, IEEE, 1994.

[126] A. Tweedie, "Spiral 2d array designs for volumetric imaging," 2011.

[127] T. S. Sumanaweera, J. Schwartz, and D. Napolitano, "A spiral 2d phased array for 3d imaging," in *1999 IEEE Ultrasonics Symposium. Proceedings. International Symposium (Cat. No. 99CH37027)*, vol. 2, pp. 1271–1274, IEEE, 1999.

[128] O. Martínez-Graullera, C. J. Martín, G. Godoy, and L. G. Ullate, "2d array design based on fermat spiral for ultrasound imaging," *Ultrasonics*, vol. 50, no. 2, pp. 280–289, 2010.

[129] M. C. Viganó, G. Toso, G. Caille, C. Mangenot, and I. E. Lager, "Sunflower array antenna with adjustable density taper," *International Journal of Antennas and Propagation*, vol. 2009, no. 1, p. 624035, 2009.

[130] H. Yoon and T.-K. Song, "Sparse rectangular and spiral array designs for 3d medical ultrasound imaging," *Sensors*, vol. 20, no. 1, p. 173, 2019.

[131] J. H. Song, J. Lee, S. Yeo, G.-D. Kim, and T.-K. Song, "An analytical approach to designing optimal sparse 1-d phased arrays for handheld ultrasound imaging," *IEEE Transactions on Ultrasonics, Ferroelectrics, and Frequency Control*, vol. 67, no. 7, pp. 1354–1365, 2020.

[132] L. Peralta, A. Ramalli, K. Christensen-Jeffries, S. Harput, P. Tortoli, and J. V. Hajnal, "Feasibility of 3-d coherent multi-transducer ultrasound imaging with two sparse arrays," in *2021 IEEE International Ultrasonics Symposium (IUS)*, pp. 1–4, IEEE, 2021.

[133] L. Peralta, A. Gomez, Y. Luan, B.-H. Kim, J. V. Hajnal, and R. J. Eckersley, "Coherent multi-transducer ultrasound imaging," *IEEE transactions on ultrasonics, ferroelectrics, and frequency control*, vol. 66, no. 8, pp. 1316–1330, 2019.

[134] M. H. Masoumi, T. Kaddoura, and R. J. Zemp, "Costas sparse 2-d arrays for high-resolution ultrasound imaging," *IEEE Transactions on Ultrasonics, Ferroelectrics, and Frequency Control*, vol. 70, no. 5, pp. 460–472, 2023.

[135] E. Roux, F. Varray, L. Petrusca, C. Cachard, P. Tortoli, and H. Liebgott, "Experimental 3-d ultrasound imaging with 2-d sparse arrays using focused and diverging waves," *Scientific reports*, vol. 8, no. 1, p. 9108, 2018.

[136] A. Ramalli, E. Boni, C. Giangrossi, P. Mattesini, A. Dallai, H. Liebgott, and P. Tortoli, "Real-time 3-d spectral doppler analysis with a sparse spiral array," *IEEE Transactions on Ultrasonics, Ferroelectrics, and Frequency Control*, vol. 68, no. 5, pp. 1742–1751, 2021.

[137] A. Ramalli, S. Harput, S. Bézy, E. Boni, R. J. Eckersley, P. Tortoli, and J. D'Hooge, "High-frame-rate tri-plane echocardiography with spiral arrays: From simulation to real-time implementation," *IEEE Transactions on Ultrasonics, Ferroelectrics, and Frequency Control*, vol. 67, no. 1, pp. 57–69, 2020.

[138] S. Harput, K. Christensen-Jeffries, A. Ramalli, J. Brown, J. Zhu, G. Zhang, C. H. Leow, M. Toulemonde, E. Boni, P. Tortoli, R. J. Eckersley, C. Dunsby, and M.-X. Tang, "3-d super-resolution ultrasound imaging with a 2-d sparse array," *IEEE Transactions on Ultrasonics, Ferroelectrics, and Frequency Control*, vol. 67, no. 2, pp. 269–277, 2020.

[139] P. Tortoli, L. Bassi, E. Boni, A. Dallai, F. Guidi, and S. Ricci, "Ula-op: An advanced open platform for ultrasound research," *IEEE transactions on ultrasonics, ferroelectrics, and frequency control*, vol. 56, no. 10, pp. 2207–2216, 2009.

[140] L. Peralta, D. Mazierli, A. Gomez, J. V. Hajnal, P. Tortoli, and A. Ramalli, "3-d coherent multitransducer ultrasound imaging with sparse spiral arrays," *IEEE Transactions on Ultrasonics, Ferroelectrics, and Frequency Control*, vol. 70, no. 3, pp. 197–206, 2023.

[141] O. Martínez-Graullera, V. Yagüe-Jiménez, A. Blanco Paetsch, M. Parrilla Romero, A. Ibáñez Rodríguez, and T. Gómez Álvarez-Arenas, "Prototyping sparse arrays of ultrasonic transducers for 3d image generation," in *Proceedings of Meetings on Acoustics*, vol. 38, AIP Publishing, 2019.

[142] L. Wei, E. Boni, A. Ramalli, F. Fool, E. Noothout, A. F. Van Der Steen, M. D. Verweij, P. Tortoli, N. De Jong, and H. J. Vos, "Sparse 2-d pzt-on-pcb arrays with density tapering," *IEEE Transactions on Ultrasonics, Ferroelectrics, and Frequency Control*, vol. 69, no. 10, pp. 2798–2809, 2022.

[143] J. McCall, R. Jones, F. Santibanez, K. Latham, J. Zou, P. Dayton, and G. Pinton, "The development of a 1.25 mhz 1024-channel sparse array for human transcranial imaging: in vitro characterization," *Measurement Science and Technology*, vol. 35, no. 3, p. 034003, 2023.

[144] A. S. Savoia, B. Mauti, L. Fanni, A. Bagolini, E. Boni, A. Ramalli, F. Guanziroli, S. Passi, M. Sautto, G. Matrone, *et al.*, "A 256-element spiral cmut array with integrated analog front end and transmit beamforming circuits," in *2018 IEEE International Ultrasonics Symposium (IUS)*, pp. 206–212, IEEE, 2018.

[145] R. Maffett, E. Boni, A. J. Chee, B. Y. Yiu, A. S. Savoia, A. Ramalli, P. Tortoli, and C. Alfred, "Unfocused field analysis of a density-tapered spiral array for high-volume-rate 3-d ultrasound imaging," *IEEE Transactions on Ultrasonics, Ferroelectrics, and Frequency Control*, vol. 69, no. 10, pp. 2810–2822, 2022.

[146] M. Bernal, B. Cunitz, D. Rohrbach, and R. Daigle, "High-frame-rate volume imaging using sparse-random-aperture compounding," *Physics in Medicine & Biology*, vol. 65, no. 17, p. 175002, 2020.

[147] S. Rossi, A. Ramalli, F. Fool, and P. Tortoli, "High-frame-rate 3-d vector flow imaging in the frequency domain," *Applied Sciences*, vol. 10, no. 15, p. 5365, 2020.

[148] D. Mazierli, A. Ramalli, E. Boni, F. Guidi, and P. Tortoli, "Architecture for an ultrasound advanced open platform with an arbitrary number of independent channels," *IEEE Transactions on Biomedical Circuits and Systems*, vol. 15, no. 3, pp. 486–496, 2021.

[149] A. Fenster, *3D Ultrasound: Devices, Applications, and Algorithms*. CRC Press, 2023.

[150] J. R. Klauder, A. Price, S. Darlington, and W. J. Albersheim, "The theory and design of chirp radars," *Bell System Technical Journal*, vol. 39, no. 4, pp. 745–808, 1960.

[151] M. O'Donnell, "Coded excitation system for improving the penetration of real-time phased-array imaging systems," *IEEE transactions on ultrasonics, ferroelectrics, and frequency control*, vol. 39, no. 3, pp. 341–351, 1992.

[152] M. O'Donnell and Y. Wang, "Coded excitation for synthetic aperture ultrasound imaging," *IEEE transactions on ultrasonics, ferroelectrics, and frequency control*, vol. 52, no. 2, pp. 171–176, 2005.

[153] P. M. Woodward, *Probability and information theory, with applications to radar: international series of monographs on electronics and instrumentation*, vol. 3. Elsevier, 2014.

[154] A. Misaridis, "Ultrasound imaging using coded signals," 2001.

[155] M. H. Pedersen, T. X. Misaridis, and J. A. Jensen, "Clinical evaluation of chirp-coded excitation in medical ultrasound," *Ultrasound in medicine & biology*, vol. 29, no. 6, pp. 895–905, 2003.

[156] T. Misaridis and J. Jensen, "Use of modulated excitation signals in medical ultrasound. part i: basic concepts and expected benefits," *IEEE Transactions on Ultrasonics, Ferroelectrics, and Frequency Control*, vol. 52, no. 2, pp. 177–191, 2005.

[157] T. Misaridis and J. Jensen, "Use of modulated excitation signals in medical ultrasound. part ii: design and performance for medical imaging applications," *IEEE Transactions on Ultrasonics, Ferroelectrics, and Frequency Control*, vol. 52, no. 2, pp. 192–207, 2005.

[158] T. Misaridis and J. Jensen, "Use of modulated excitation signals in medical ultrasound. part iii: high frame rate imaging," *IEEE Transactions on Ultrasonics, Ferroelectrics, and Frequency Control*, vol. 52, no. 2, pp. 208–219, 2005.

[159] V. Behar and D. Adam, "Parameter optimization of pulse compression in ultrasound imaging systems with coded excitation," *Ultrasonics*, vol. 42, no. 10, pp. 1101–1109, 2004.

[160] B. Lashkari, K. Zhang, and A. Mandelis, "High-frame-rate synthetic aperture ultrasound imaging using mismatched coded excitation waveform engineering: A feasibility study," *IEEE Transactions on Ultrasonics, Ferroelectrics, and Frequency Control*, vol. 63, no. 6, pp. 828–841, 2016.

[161] B. Lashkari, K. Zhang, E. Dovlo, and A. Mandelis, "Coded excitation waveform engineering for high frame rate synthetic aperture ultrasound imaging," *Ultrasonics*, vol. 77, pp. 121–132, 2017.

[162] F. Gran and J. A. Jensen, "Frequency division transmission imaging and synthetic aperture reconstruction," *ieee transactions on ultrasonics, ferroelectrics, and frequency control*, vol. 53, no. 5, pp. 900–911, 2006.

[163] F. Gran and J. A. Jensen, "Directional velocity estimation using a spatio-temporal encoding technique based on frequency division for synthetic transmit aperture ultrasound," *IEEE transactions on ultrasonics, ferroelectrics, and frequency control*, vol. 53, no. 7, pp. 1289–1299, 2006.

[164] B. Pialot, A. Bernard, H. Liebgott, and F. Varray, "Sensitivity enhancement using chirp transmission for an ultrasound arthroscopic probe," *IEEE Transactions on Ultrasonics, Ferroelectrics, and Frequency Control*, vol. 69, no. 10, pp. 2776–2784, 2022.

[165] R. H. Barker, "Group synchronization of binary digital system," *Communication theory*, pp. 273–287, 1953.

[166] S. Zhou, X.-C. Wang, J. Yang, J.-J. Ji, and Y.-Q. Wang, "Barker-coded excitation in ophthalmological ultrasound imaging," *International Journal of Clinical and Experimental Medicine*, vol. 7, no. 9, p. 2413, 2014.

[167] H. Zhao, L. Y. Mo, and S. Gao, "Barker-coded ultrasound color flow imaging: Theoretical and practical design considerations," *IEEE transactions on ultrasonics, ferroelectrics, and frequency control*, vol. 54, no. 2, pp. 319–331, 2007.

[168] F. Gran, J. Udesen, M. B. Nielsen, and J. A. Jensen, "Coded ultrasound for blood flow estimation using subband processing," *IEEE transactions on ultrasonics, ferroelectrics, and frequency control*, vol. 55, no. 10, pp. 2211–2220, 2008.

[169] E. Vienneau, A. Weeks, and B. Byram, "Coded excitation for increased sensitivity in transcranial power doppler imaging," in *2022 IEEE International Ultrasonics Symposium (IUS)*, pp. 1–4, IEEE, 2022.

[170] E. P. Vienneau and B. C. Byram, "A coded excitation framework for high snr transcranial ultrasound imaging," *IEEE Transactions on Medical Imaging*, vol. 42, no. 10, pp. 2886–2898, 2023.

[171] B. Kiranmai and P. R. Kumar, "Performance evaluation of compound barker codes using cascaded mismatched filter technique," *International Journal of Computer Applications*, vol. 121, no. 19, 2015.

[172] E. Vienneau and B. Byram, "Compound barker-coded excitation for increased signal-to-noise ratio and penetration depth in transcranial ultrasound imaging," in *2020 IEEE International Ultrasonics Symposium (IUS)*, pp. 1–4, IEEE, 2020.

[173] M. J. Golay, "Multi-slit spectrometry," *JOSA*, vol. 39, no. 6, pp. 437–444, 1949.

[174] M. Golay, "Complementary series," *IRE transactions on information theory*, vol. 7, no. 2, pp. 82–87, 1961.

[175] R. Y. Chiao and X. Hao, "Coded excitation for diagnostic ultrasound: A system developer's perspective," *IEEE transactions on ultrasonics, ferroelectrics, and frequency control*, vol. 52, no. 2, pp. 160–170, 2005.

[176] A. Nowicki, W. Secomski, J. Litniewski, I. Trots, and P. A. Lewin, "ON THE APPLICATION OF SIGNAL COMPRESSION USING GOLAY'S CODES SEQUENCES IN ULTRASOUND DIAGNOSTIC," p. 12.

[177] A. Nowicki, I. Trots, W. Secomski, and J. Litniewski, "GOLAY'S CODES SEQUENCES IN ULTRASONOGRAPHY," p. 10.

[178] C. Jin, S.-p. Chen, Z.-d. Qin, and T.-f. Wang, "A new scheme of coded ultrasound using Golay codes," *Journal of Zhejiang University SCIENCE C*, vol. 11, pp. 476–480, June 2010.

[179] I. Trots, Y. Tasinkevych, A. Nowicki, and M. Lewandowski, "Golay Coded Sequences in Synthetic Aperture Imaging Systems," *Archives of Acoustics*, vol. 36, Jan. 2011.

[180] M. Yang and C. Chakrabarti, "Design of orthogonal coded excitation for synthetic aperture imaging in ultrasound systems," in *2012 IEEE International Symposium on Circuits and Systems*, (Seoul, Korea (South)), pp. 113–116, IEEE, May 2012.

[181] D. Romero-Laorden, O. Martinez-Graullera, C. J. Martin-Arguedas, and M. Parrilla-Romero, "Application of Golay codes to improve SNR in coarray based synthetic aperture imaging systems," in *2012 IEEE 7th Sensor Array and Multichannel Signal Processing Workshop (SAM)*, (Hoboken, NJ, USA), pp. 325–328, IEEE, June 2012.

[182] D. DJokovic, "Equivalence classes and representatives of golay sequences," *Discrete Mathematics*, vol. 189, no. 1-3, pp. 79–93, 1998.

[183] R. Y. Chiao, L. J. Thomas, and S. D. Silverstein, "Sparse array imaging with spatially-encoded transmits," in *1997 IEEE Ultrasonics Symposium Proceedings. An International Symposium (Cat. No. 97CH36118)*, vol. 2, pp. 1679–1682, IEEE, 1997.

[184] P. Gong, A. Moghimi, M. C. Kolios, and Y. Xu, "Delay-encoded transmission in synthetic transmit aperture (de-sta) imaging," in *2014 IEEE International Ultrasonics Symposium*, pp. 1005–1008, IEEE, 2014.

[185] P. Gong, M. C. Kolios, and Y. Xu, "Delay-encoded transmission and image reconstruction method in synthetic transmit aperture imaging," *IEEE transactions on ultrasonics, ferroelectrics, and frequency control*, vol. 62, no. 10, pp. 1745–1756, 2015.

[186] E. Tiran, T. Deffieux, M. Correia, D. Maresca, B.-F. Osmanski, L.-A. Sieu, A. Bergel, I. Cohen, M. Pernot, and M. Tanter, "Multiplane wave imaging increases signal-to-noise ratio in ultrafast ultrasound imaging," *Physics in Medicine & Biology*, vol. 60, no. 21, p. 8549, 2015.

[187] S. Nikolov and J. A. Jensen, "Comparison between different encoding schemes for synthetic aperture imaging," in *Medical Imaging 2002: Ultrasonic Imaging and Signal Processing*, vol. 4687, pp. 1–12, SPIE, 2002.

[188] N. Suehiro and M. Hatori, "N-shift cross-orthogonal sequences," *IEEE Transactions on Information Theory*, vol. 34, pp. 143–146, Jan. 1988.

[189] C.-C. Tseng and C. Liu, "Complementary sets of sequences," *IEEE Transactions on Information Theory*, vol. 18, pp. 644–652, Sept. 1972. Conference Name: IEEE Transactions on Information Theory.

[190] C. Han, N. Suehiro, and T. Imoto, "A generation method of length of MN complete complementary code," *IEICE Transactions on Fundamentals (in Japanese)*, vol. 88, no. 3, pp. 357–363, 2005.

[191] Chenggao Han and N. Suchiro, "A generation method for constructing (N,N,MN/P) complete complementary sequences," in *SympoTIC '04. Joint 1st Workshop on Mobile Future & Symposium on Trends In Communications (IEEE Cat. No.04EX877)*, (Bratislava, Slovakia), pp. 70–73, IEEE, 2004.

[192] M. Dávideková, M. Greguš Ml., P. Farkaš, and M. Rákus, "Applications of Complete Complementary Codes and Propositions for Future Research Areas of these Codes," *Procedia Computer Science*, vol. 83, pp. 592–599, 2016.

[193] Hsiao-Hwa Chen, Jun-Feng Yeh, and N. Suehiro, "A multicarrier CDMA architecture based on orthogonal complementary codes for new generations of wideband wireless communications," *IEEE Communications Magazine*, vol. 39, pp. 126–135, Oct. 2001.

[194] N. Suehiro, "A signal design without co-channel interference for approximately synchronized CDMA systems," *IEEE Journal on Selected Areas in Communications*, vol. 12, pp. 837–841, June 1994.

[195] N. Suehiro and N. Kuroyanagi, "Binary signal design for approximately synchronized CDMA systems without detection sidelobe nor co-channel interference using auto- and cross-complementary codes," in *ICUPC '98. IEEE 1998 International Conference on Universal Personal Communications. Conference Proceedings (Cat. No.98TH8384)*, vol. 2, (Florence, Italy), pp. 1097–1102, IEEE, 1998.

[196] C.-Y. Pai, Z. Liu, Y.-Q. Zhao, Z.-M. Huang, and C.-Y. Chen, "Designing Two-Dimensional Complete Complementary Codes for Omnidirectional Transmission in Massive MIMO Systems," May 2022. arXiv:2108.06863 [cs, math].

[197] "A Complete Complementary Coded MIMO System and Its Performance in Multipath Channels," *IEEE Wireless Communications Letters*, vol. 3, pp. 181–184, Apr. 2014.

[198] J. Tang, Z. Ma, and C. Han, "The application of complete complementary codes in MIMO radar," in *2012 International Waveform Diversity & Design Conference (WDD)*, (Kauai, HI, USA), pp. 271–276, IEEE, Jan. 2012.

[199] A. Brenner, K. Eck, W. Wilhelm, and T. Noll, "Improved resolution and dynamic range in medical ultrasonic imaging using depth-dependent mismatched filtering," in *1997 IEEE Ultrasonics Symposium Proceedings. An International Symposium (Cat. No.97CH36118)*, vol. 2, (Toronto, Ont., Canada), pp. 1475–1480, IEEE, 1997.

[200] G. Jeng, S. Huang, P. Li, and J. Tsao, "A novel pulse compression technique using inverse filtering in frequency domain," in *2001 IEEE Ultrasonics Symposium. Proceedings. An International Symposium (Cat. No.01CH37263)*, vol. 2, (Atlanta, GA, USA), pp. 1535–1538, IEEE, 2001.

[201] A. Ramalli, F. Guidi, E. Boni, and P. Tortoli, "A real-time chirp-coded imaging system with tissue attenuation compensation," *Ultrasonics*, vol. 60, pp. 65–75, July 2015.

[202] Ping Gong, A. Moghimi, M. C. Kolios, and Yuan Xu, "Delay-encoded transmission in synthetic transmit aperture (DE-STA) imaging," in *2014 IEEE International Ultrasonics Symposium*, (Chicago, IL, USA), pp. 1005–1008, IEEE, Sept. 2014.

[203] F. Nicolet, E. Carcreff, H. Liebgott, and B. Nicolas, "Synthetic Transmit Aperture Imaging Using Orthogonal Coded Sequences With Separate Transmitters-Receivers," in *2022 IEEE International Ultrasonics Symposium (IUS)*, pp. 1–4, Oct. 2022. ISSN: 1948-5727.

[204] F. Nicolet, D. Bujoreanu, E. Carcreff, H. Liebgott, D. Friboulet, and B. Nicolas, "Simultaneous Coded Plane-Wave Imaging Using an Advanced Ultrasound Forward Model," *Applied Sciences*, vol. 12, p. 12809, Dec. 2022.

[205] A. Adam, B. Nicolas, A. Basarab, and H. Liebgott, "Continuous emission ultrasound: A new paradigm to ultrafast ultrasound imaging," *IEEE Transactions on Biomedical Engineering*, pp. 1–14, 2024.

[206] A. Nowicki, I. Trots, P. Lewin, W. Secomski, and R. Tymkiewicz, "Influence of the ultrasound transducer bandwidth on selection of the complementary Golay bit code length," *Ultrasonics*, vol. 47, pp. 64–73, Dec. 2007.

[207] O. Oralkan, B. Bayram, G. Yaralioglu, A. Ergun, M. Kupnik, D. Yeh, I. Wygant, and B. Khuri-Yakub, "Experimental characterization of collapse-mode CMUT operation," *IEEE Transactions on Ultrasonics, Ferroelectrics and Frequency Control*, vol. 53, pp. 1513–1523, Aug. 2006.

[208] R. P. Zangabad, J. G. Bosch, F. Mastik, R. H. S. H. Beurskens, V. A. Henneken, J. W. Weekamp, A. F. W. Van Der Steen, and G. Van Soest, "Real-Time Coded Excitation Imaging Using a CMUT-Based Side Looking Array for Intravascular Ultrasound," *IEEE Transactions on Ultrasonics, Ferroelectrics, and Frequency Control*, vol. 68, pp. 2048–2058, June 2021.

[209] P. Kaczkowski, "Arbitrary Waveform Generation with the Verasonics Research Ultrasound Platform,"

[210] J. Bercoff, M. Tanter, and M. Fink, "Supersonic shear imaging: a new technique for soft tissue elasticity mapping," *IEEE Transactions on Ultrasonics, Ferroelectrics and Frequency Control*, vol. 51, pp. 396–409, Apr. 2004.

[211] G. Montaldo, M. Tanter, J. Bercoff, N. Benech, and M. Fink, "Coherent plane-wave compounding for very high frame rate ultrasonography and transient elastography," *IEEE Transactions on Ultrasonics, Ferroelectrics and Frequency Control*, vol. 56, pp. 489–506, Mar. 2009.

[212] M. Tanter and M. Fink, "Ultrafast imaging in biomedical ultrasound," *IEEE Transactions on Ultrasonics, Ferroelectrics, and Frequency Control*, vol. 61, pp. 102–119, Jan. 2014.

[213] E. Mace, G. Montaldo, B.-F. Osmanski, I. Cohen, M. Fink, and M. Tanter, "Functional ultrasound imaging of the brain: theory and basic principles," *IEEE Transactions on Ultrasonics, Ferroelectrics and Frequency Control*, vol. 60, pp. 492–506, Mar. 2013.

[214] J. Bercoff, G. Montaldo, T. Loupas, D. Savery, F. Mézière, M. Fink, and M. Tanter, "Ultrafast compound doppler imaging: providing full blood flow characterization," *IEEE Transactions on Ultrasonics, Ferroelectrics and Frequency Control*, vol. 58, pp. 134–147, Jan. 2011.

[215] C. Demene, T. Deffieux, M. Pernot, B.-F. Osmanski, V. Biran, J.-L. Gennisson, L.-A. Sieu, A. Bergel, S. Franqui, J.-M. Correas, I. Cohen, O. Baud, and M. Tanter, "Spatiotemporal Clutter Filtering of Ultrafast Ultrasound Data Highly Increases Doppler and fUltrasound Sensitivity," *IEEE Transactions on Medical Imaging*, vol. 34, pp. 2271–2285, Nov. 2015.

[216] B. Pialot, L. Augeul, L. Petrusca, and F. Varray, "A simplified and accelerated implementation of SVD for filtering ultrafast power Doppler images," *Ultrasonics*, vol. 134, p. 107099, Sept. 2023.

[217] R. Paridar and B. M. Asl, "Frame rate improvement in ultrafast coherent plane wave compounding," *Ultrasonics*, vol. 135, p. 107136, Dec. 2023.

[218] T. X. Misaridis, K. Gammelmark, C. H. Jørgensen, N. Lindberg, A. H. Thomsen, M. H. Pedersen, and J. A. Jensen, "Potential of coded excitation in medical ultrasound imaging," *Ultrasonics*, vol. 38, pp. 183–189, Mar. 2000.

[219] E. Tiran, T. Deffieux, M. Correia, D. Maresca, B.-F. Osmanski, L.-A. Sieu, A. Bergel, I. Cohen, M. Pernot, and M. Tanter, "Multiplane wave imaging increases signal-to-noise ratio in ultrafast ultrasound imaging," *Physics in Medicine and Biology*, vol. 60, pp. 8549–8566, Nov. 2015.

[220] E. Tiran, J. Ferrier, T. Deffieux, J.-L. Gennisson, S. Pezet, Z. Lenkei, and M. Tanter, "Transcranial Functional Ultrasound Imaging in Freely Moving Awake Mice and Anesthetized Young Rats without Contrast Agent," *Ultrasound in Medicine & Biology*, vol. 43, pp. 1679–1689, Aug. 2017.

[221] B. Lashkari, K. Zhang, E. Dovlo, and A. Mandelis, "Coded excitation waveform engineering for high frame rate synthetic aperture ultrasound imaging," *Ultrasonics*, vol. 77, pp. 121–132, May 2017.

[222] T. Kaddoura and R. J. Zemp, "Hadamard Aperiodic Interval Codes for Parallel-Transmission 2D and 3D Synthetic Aperture Ultrasound Imaging," *Applied Sciences*, vol. 12, p. 4917, May 2022.

[223] Z. Zhang, F. Tian, F. Zeng, L. Ge, and G. Xuan, "Mutually orthogonal complementary pairs for OFDM-CDMA systems," in *2014 12th International Conference on Signal Processing (ICSP)*, (Hangzhou, Zhejiang, China), pp. 1761–1765, IEEE, Oct. 2014.

[224] C. Cannon, J. Hannah, and S. McLaughlin, "Segmented motion compensation for complementary coded ultrasonic imaging," *IEEE transactions on ultrasonics, ferroelectrics, and frequency control*, vol. 57, no. 5, pp. 1039–1050, 2010.

[225] C.-C. Shen and J.-G. Yu, "Slow-time golay decoding for doppler detection of high-velocity blood flow," in *2013 IEEE International Ultrasonics Symposium (IUS)*, pp. 1488–1491, IEEE, 2013.

[226] C.-C. Shen, J.-G. Yu, and G. Jeng, "Implementation and evaluation of slow-time golay decoding for pre-clinical high-frequency color doppler imaging in mice," in *2015 IEEE International Ultrasonics Symposium (IUS)*, pp. 1–4, IEEE, 2015.

[227] D. Garcia, "Simus: an open-source simulator for medical ultrasound imaging. part i: theory & examples," *Computer Methods and Programs in Biomedicine*, vol. 218, p. 106726, 2022.

[228] D. Garcia and F. Varray, "Simus3: An open-source simulator for 3-d ultrasound imaging," *Computer Methods and Programs in Biomedicine*, vol. 250, p. 108169, 2024.

[229] J. Jacquet, M. Tamraoui, P. Kauffmann, J. Guey, E. Roux, B. Nicolas, and H. Liebgott, "Integrating finite-element model of probe element in gpu accelerated ultrasound image simulation," in *2023 IEEE International Ultrasonics Symposium (IUS)*, pp. 1–4, IEEE, 2023.

[230] Q. B. Wang, *Design and optimization of ultrasonic array transducers for medical imaging applications*. PhD thesis, 2005.

[231] R. Lerch, "Simulation of piezoelectric devices by two-and three-dimensional finite elements," *IEEE transactions on ultrasonics, ferroelectrics, and frequency control*, vol. 37, no. 3, pp. 233–247, 1990.

[232] G. L. Wojcik, D. Vaughan, N. Abboud, and J. J. Mould, "Electromechanical modeling using explicit time-domain finite elements," in *1993 Proceedings IEEE Ultrasonics Symposium*, pp. 1107–1112, IEEE, 1993.

[233] V. Perrot, M. Polichetti, F. Varray, and D. Garcia, "So you think you can das? a viewpoint on delay-and-sum beamforming," *Ultrasonics*, vol. 111, p. 106309, 2021.

[234] Y. Wang, Y. Wang, M. Liu, Z. Lan, C. Zheng, and H. Peng, "Minimum variance beamforming combined with covariance matrix-based adaptive weighting for medical ultrasound imaging," *BioMedical Engineering OnLine*, vol. 21, no. 1, p. 40, 2022.

[235] B. M. Asl and A. Mahloojifar, "Contrast enhancement and robustness improvement of adaptive ultrasound imaging using forward-backward minimum variance beamforming," *IEEE transactions on ultrasonics, ferroelectrics, and frequency control*, vol. 58, no. 4, pp. 858–867, 2011.

[236] M. F. Schiffner and G. Schmitz, "Frequency-dependent f-number suppresses grating lobes and improves the lateral resolution in coherent plane-wave compounding," *IEEE Transactions on Ultrasonics, Ferroelectrics, and Frequency Control*, 2023.

[237] J. F. Synnevag, A. Austeng, and S. Holm, "Adaptive beamforming applied to medical ultrasound imaging," *IEEE transactions on ultrasonics, ferroelectrics, and frequency control*, vol. 54, no. 8, pp. 1606–1613, 2007.

[238] J.-F. Synnevag, A. Austeng, and S. Holm, "Benefits of minimum-variance beamforming in medical ultrasound imaging," *IEEE transactions on ultrasonics, ferroelectrics, and frequency control*, vol. 56, no. 9, pp. 1868–1879, 2009.

[239] B. M. Asl and A. Mahloojifar, "Eigenspace-based minimum variance beamforming applied to medical ultrasound imaging," *IEEE transactions on ultrasonics, ferroelectrics, and frequency control*, vol. 57, no. 11, pp. 2381–2390, 2010.

[240] R. Mallart and M. Fink, "Adaptive focusing in scattering media through sound-speed inhomogeneities: The van cittert zernike approach and focusing criterion," *The Journal of the Acoustical Society of America*, vol. 96, no. 6, pp. 3721–3732, 1994.

[241] K. Hollman, K. Rigby, and M. O'donnell, "Coherence factor of speckle from a multi-row probe," in *1999 IEEE Ultrasonics Symposium. Proceedings. International Symposium (Cat. No. 99CH37027)*, vol. 2, pp. 1257–1260, IEEE, 1999.

[242] P.-C. Li and M.-L. Li, "Adaptive imaging using the generalized coherence factor," *IEEE transactions on ultrasonics, ferroelectrics, and frequency control*, vol. 50, no. 2, pp. 128–141, 2003.

[243] J. Camacho, M. Parrilla, and C. Fritsch, "Phase coherence imaging," *IEEE transactions on ultrasonics, ferroelectrics, and frequency control*, vol. 56, no. 5, pp. 958–974, 2009.

[244] C. Fritsch, J. Camacho, and M. Parrilla, "New ultrasound imaging techniques with phase coherence processing," *Ultrasonics*, vol. 50, no. 2, pp. 122–126, 2010.

[245] G. Matrone, A. S. Savoia, G. Caliano, and G. Magenes, "The delay multiply and sum beamforming algorithm in ultrasound b-mode medical imaging," *IEEE transactions on medical imaging*, vol. 34, no. 4, pp. 940–949, 2014.

[246] F. Prieur, O. M. H. Rindal, and A. Austeng, "Signal coherence and image amplitude with the filtered delay multiply and sum beamformer," *IEEE transactions on ultrasonics, ferroelectrics, and frequency control*, vol. 65, no. 7, pp. 1133–1140, 2018.

[247] A. Ramalli, M. Scaringella, G. Matrone, A. Dallai, E. Boni, A. S. Savoia, L. Bassi, G. E. Hine, and P. Tortoli, "High dynamic range ultrasound imaging with real-time filtered-delay multiply and sum beamforming," in *2017 IEEE International Ultrasonics Symposium (IUS)*, pp. 1–4, IEEE, 2017.

[248] M. Mozaffarzadeh, A. Mahloojifar, M. Orooji, S. Adabi, and M. Nasiriavanaki, "Double-stage delay multiply and sum beamforming algorithm: Application to linear-array photoacoustic imaging," *IEEE Transactions on Biomedical Engineering*, vol. 65, no. 1, pp. 31–42, 2017.

[249] A. Vayyeti and A. K. Thittai, "A filtered delay weight multiply and sum (f-dwmas) beamforming for ultrasound imaging: Preliminary results," in *2020 IEEE 17th International Symposium on Biomedical Imaging (ISBI)*, pp. 312–315, IEEE, 2020.

[250] B. Luijten, N. Chennakeshava, Y. C. Eldar, M. Mischi, and R. J. van Sloun, "Ultrasound signal processing: from models to deep learning," *Ultrasound in medicine & biology*, vol. 49, no. 3, pp. 677–698, 2023.

[251] M. Gasse, F. Millioz, E. Roux, D. Garcia, H. Liebgott, and D. Friboulet, "High-quality plane wave compounding using convolutional neural networks," *IEEE transactions on ultrasonics, ferroelectrics, and frequency control*, vol. 64, no. 10, pp. 1637–1639, 2017.

[252] D. Perdios, M. Vonlanthen, F. Martinez, M. Arditi, and J.-P. Thiran, "Cnn-based image reconstruction method for ultrafast ultrasound imaging," *IEEE Transactions on Ultrasonics, Ferroelectrics, and Frequency Control*, vol. 69, no. 4, pp. 1154–1168, 2021.

[253] B. W. Ossenkoppele, B. Luijten, D. Bera, N. De Jong, M. D. Verweij, and R. J. Van Sloun, "Improving lateral resolution in 3-d imaging with micro-beamforming through adaptive beamforming by deep learning," *Ultrasound in Medicine & Biology*, vol. 49, no. 1, pp. 237–255, 2023.

[254] A. A. Nair, K. N. Washington, T. D. Tran, A. Reiter, and M. A. L. Bell, "Deep learning to obtain simultaneous image and segmentation outputs from a single input of raw ultrasound channel data," *IEEE transactions on ultrasonics, ferroelectrics, and frequency control*, vol. 67, no. 12, pp. 2493–2509, 2020.

[255] Z. Li, A. Wiacek, and M. A. L. Bell, "Beamforming with deep learning from single plane wave rf data," in *2020 IEEE International Ultrasonics Symposium (IUS)*, pp. 1–4, IEEE, 2020.

[256] Y. Chen, J. Liu, J. Luo, and X. Luo, "A data-driven approach for high frame rate synthetic transmit aperture ultrasound imaging," in *Medical Image Computing and Computer Assisted Intervention–MICCAI 2021: 24th International Conference, Strasbourg, France, September 27–October 1, 2021, Proceedings, Part VI 24*, pp. 412–420, Springer, 2021.

[257] B. Luijten, R. Cohen, F. J. De Bruijn, H. A. Schmeitz, M. Mischi, Y. C. Eldar, and R. J. Van Sloun, "Adaptive ultrasound beamforming using deep learning," *IEEE Transactions on Medical Imaging*, vol. 39, no. 12, pp. 3967–3978, 2020.

[258] F. Vignon, J. S. Shin, F. C. Meral, I. Apostolakis, S.-W. Huang, and J.-L. Robert, "Resolution improvement with a fully convolutional neural network applied to aligned per-channel data," in *2020 IEEE International Ultrasonics Symposium (IUS)*, pp. 1–4, IEEE, 2020.

[259] A. C. Luchies and B. C. Byram, "Deep neural networks for ultrasound beamforming," *IEEE transactions on medical imaging*, vol. 37, no. 9, pp. 2010–2021, 2018.

[260] K. Esmailian and B. M. Asl, "Correlation-based modified delay-multiply-and-sum beamforming applied to medical ultrasound imaging," *Computer methods and programs in biomedicine*, vol. 226, p. 107171, 2022.

[261] M. Xu, X. Yang, M. Ding, and M. Yuchi, "Spatio-temporally smoothed coherence factor for ultrasound imaging [correspondence]," *IEEE transactions on ultrasonics, ferroelectrics, and frequency control*, vol. 61, no. 1, pp. 182–190, 2014.

[262] O. M. H. Rindal, A. Rodriguez-Molares, and A. Austeng, "The dark region artifact in adaptive ultrasound beamforming," in *2017 IEEE International Ultrasonics Symposium (IUS)*, pp. 1–4, IEEE, 2017.

[263] S. Bhadra, V. A. Kelkar, F. J. Brooks, and M. A. Anastasio, "On hallucinations in tomographic image reconstruction," *IEEE Transactions on Medical Imaging*, vol. 40, no. 11, pp. 3249–3260, 2021.

[264] M. Lapan, *Deep Reinforcement Learning Hands-On: Apply modern RL methods, with deep Q-networks, value iteration, policy gradients, TRPO, AlphaGo Zero and more*. Packt Publishing Ltd, 2018.

[265] D. Silver, A. Huang, C. J. Maddison, A. Guez, L. Sifre, G. Van Den Driessche, J. Schrittwieser, I. Antonoglou, V. Panneershelvam, M. Lanctot, *et al.*, "Mastering the game of go with deep neural networks and tree search," *nature*, vol. 529, no. 7587, pp. 484–489, 2016.

[266] E. F. Morales, R. Murrieta-Cid, I. Becerra, and M. A. Esquivel-Basaldua, "A survey on deep learning and deep reinforcement learning in robotics with a tutorial on deep reinforcement learning," *Intelligent Service Robotics*, vol. 14, no. 5, pp. 773–805, 2021.

[267] B. R. Kiran, I. Sobh, V. Talpaert, P. Mannion, A. A. Al Sallab, S. Yogamani, and P. Pérez, "Deep reinforcement learning for autonomous driving: A survey," *IEEE Transactions on Intelligent Transportation Systems*, vol. 23, no. 6, pp. 4909–4926, 2021.

[268] M. Morales, *Grokking deep reinforcement learning*. Manning Publications, 2020.

[269] V. Mnih, A. P. Badia, M. Mirza, A. Graves, T. Lillicrap, T. Harley, D. Silver, and K. Kavukcuoglu, "Asynchronous methods for deep reinforcement learning," in *International conference on machine learning*, pp. 1928–1937, PMLR, 2016.

[270] R. Furuta, N. Inoue, and T. Yamasaki, "Pixelrl: Fully convolutional network with reinforcement learning for image processing," *IEEE Transactions on Multimedia*, vol. 22, no. 7, pp. 1704–1719, 2019.

[271] Y. Guo, Y. Gao, B. Hu, X. Qian, and D. Liang, "Cmid: Crossmodal image denoising via pixel-wise deep reinforcement learning," *Sensors*, vol. 24, no. 1, p. 42, 2023.

[272] P. Jarosik, M. Lewandowski, Z. Klimonda, and M. Byra, "Pixel-wise deep reinforcement learning approach for ultrasound image denoising," in *2021 IEEE International Ultrasonics Symposium (IUS)*, pp. 1–4, IEEE, 2021.

[273] A. Paszke, S. Gross, F. Massa, A. Lerer, J. Bradbury, G. Chanan, T. Killeen, Z. Lin, N. Gimelshein, L. Antiga, *et al.*, "Pytorch: An imperative style, high-performance deep learning library," *Advances in neural information processing systems*, vol. 32, 2019.

[274] D. P. Kingma, "Adam: A method for stochastic optimization," *arXiv preprint arXiv:1412.6980*, 2014.

[275] A. Rodriguez-Molares, O. M. H. Rindal, J. D'hooge, S.-E. Måsøy, A. Austeng, M. A. L. Bell, and H. Torp, "The generalized contrast-to-noise ratio: A formal definition for lesion detectability," *IEEE Transactions on Ultrasonics, Ferroelectrics, and Frequency Control*, vol. 67, no. 4, pp. 745–759, 2019.

[276] C. Cannon, J. Hannah, and S. McLaughlin, "Mirrored motion compensation for complementary-coded ultrasonic imaging," in *2008 IEEE Ultrasonics Symposium*, pp. 467–470, 2008.

[277] K. L. Gammelmark and J. Jensen, "2-d tissue motion compensation of synthetic transmit aperture images," *IEEE Transactions on Ultrasonics, Ferroelectrics, and Frequency Control*, vol. 61, no. 4, pp. 594–610, 2014.

[278] J. Porée, D. Posada, A. Hodzic, F. Tournoux, G. Cloutier, and D. Garcia, "High-frame-rate echocardiography using coherent compounding with doppler-based motion-compensation," *IEEE transactions on medical imaging*, vol. 35, no. 7, pp. 1647–1657, 2016.